

Numerical Wind Potential Analysis in Urban Environments

A thesis accepted by the Faculty of Aerospace Engineering and Geodesy of the University of Stuttgart in partial fulfilment of the requirements for the degree of Doctor of Engineering Sciences (Dr.-Ing.)

by

Maximilian Siegfried Ulrich von der Grün

born in Rosenheim

Main referee: Prof. Dr.-Ing. Ewald Krämer

Co-referee: Prof. Dr. Ursula Voß

Date of defense: 29.09.2023

Institute of Aerodynamics and Gas Dynamics
University of Stuttgart
2024

*I dedicate this thesis to my family and my friends,
none of this would have been possible without their love, patience and support.*

Acknowledgements

During my PhD candidature I had the pleasure to be supported by numerous friends, colleagues, students and my family. At this point I would like to thank these people for making this work possible.

I wish to express my gratitude to my supervisors, Prof. Dr. Ursula Voß and Prof. Dr. Ewald Krämer, for their incredible amount they have taught me during the course of this thesis, their professional guidance and assistance.

My thanks also go to Pradip Zamre and Dr. Thorsten Lutz for the excellent and inspiring discussions and they always came up with new ideas.

It was a great honor being part of the interdisciplinary Joint Graduate Research Training Group "Windy Cities" in corporation with the University of Stuttgart, the Hochschule für Technik Stuttgart and the Hochschule Esslingen, meeting and working together with people from all over the world.

I would like to thank the Stuttgart Wind Energy @ Institute of Aircraft Design (SWE), University of Stuttgart, in particular Yiyin Chen for conducting the Lidar measurement campaign and providing the wind measurement data.

The computational resources were provided by the bwUniCluster funded by the Ministry of Science, Research and Arts and the universities of Baden-Württemberg, Germany, within the framework program bwHPC.

Abstract

Due to the global warming, the man-made CO₂ emissions have to be reduced. A possible role can play the switch of fossil energies towards electric energy. The increasing trend to urbanism rises the energy demand in urban areas. Short power supply distances in urban areas, where the most energy is needed, reduce the total energy costs and the power loss in long distance grids. A local renewable power generation, such as by small wind turbines, which are mounted in urban areas, can help to overcome these problems and meet the increasing demand in electric energy.

It is not substantially investigated how urban areas can be used economically for small wind turbines. The influences of environmental and atmospheric parameters, such as atmospheric turbulence intensities or vegetational properties, on the flow field and the energy yield of small wind turbines are still unknown. Usually, the evaluation of suitable positions for small wind turbines is based on wind speed. For that measurement data from metmasts or sonic measurement devices are used which do not sufficiently consider local wind effects. But the measurement data is just valid within a short range since local effects, for example induced by buildings, complex terrain structures or vegetation, can strongly influence the wind field and are not represented in calculation methods of the AEP. Furthermore, an extensive three-dimensional validation of urban wind field simulations with on-site measurement data is still lacking. So far only punctual sonic data are used to validate simulation data.

The objective of this work is the numerical investigation of the urban wind field at the university campus Morgenstelle in Tübingen (southern Germany) which is chosen as a test site for this study. This is done using CFD and highly resolved DES simulations with ANSYS Fluent in this work. The simulations include complex terrain and vegetation with the focus on the energy yield of small wind turbines. The building geometries used in the simulations are based on a real 3D city model geometry. A workflow is used to prepare the city models for urban CFD simulations from geometry optimisation to meshing requirements. An already existing vegetation model is extended to consider local tree heights. A sensitivity analysis is performed to study the influence of different meshing parameters and domain sizes. Additionally, the effect of the vegetation in general and the effects of various environmental parameters such as the atmospheric turbulence intensity, different tree heights and foliage densities to simulate the wind flow in summer and winter times are investigated. The numerical setup and the vegetation modelling are compared

with on-site LiDAR measurement data in Tübingen. A new method is presented how to use planar on-site wind measurement data as an inflow boundary condition.

Since the AEP is one of the most important key parameters defining suitable locations for wind turbines, a procedure for calculating local AEP values and local wind statistics is presented. For that the wind flow is simulated from four evenly distributed wind directions with and without buildings which surround the buildings of interest. For that, a new building model is presented which models the buildings by means of a volume force and an indicator function. That allows a faster preparation and a simplified meshing of complex building geometries. The calculation of the AEP is based on large scale synthetic wind statistics which have been already available. The simulations of the four wind directions are used in the method to achieve local frequencies of wind directions and wind speeds. The AEP is calculated for each building using a real horizontal and vertical axis wind turbine. An already existing approach for correcting the AEP by the atmospheric turbulence intensity and the angle of attack of the wind turbines is implemented in the procedure to obtain a more realistic and precise prediction of the energy yield. Finally, suitable locations for small wind turbines are evaluated and discussed.

Especially, the local wind statistics and the approach for correcting the AEP by the atmospheric turbulence intensity lead to a significant difference in the calculated AEP values. The study further shows a potential of small wind turbines at the university campus Morgenstelle in Tübingen, e.g., the highest AEP value is reached on the highest building on the campus when a horizontal axis wind turbine is used.

Kurzzusammenfassung

Aufgrund der globalen Erwärmung müssen die menschengemachten Emissionen reduziert werden. Eine mögliche Rolle kann dabei der Umstieg von fossilen Energien auf elektrische Energie spielen. Der zunehmende Trend zur Urbanisierung erhöht den Energieverbrauch in urbanen Gegenden. Kurze Stromversorgungswege in städtischen Gebieten, wo die meiste Energie benötigt wird, reduzieren die Gesamtenergiekosten und den Leistungsverlust in Fernnetzen. Eine dezentrale regenerative Stromerzeugung, beispielsweise durch Kleinwindkraftanlagen, die in städtischen Gebieten aufgestellt werden, kann helfen, diese Probleme zu überwinden und den steigenden Bedarf an elektrischer Energie zu decken. Es ist bislang nicht ausreichend untersucht, inwiefern städtische Gebiete für Kleinwindkraftanlagen wirtschaftlich genutzt werden können. Die Einflüsse von Umweltparametern und atmosphärischen Parametern, wie z.B. atmosphärische Turbulenzintensitäten oder Vegetationsparameter, auf das Strömungsfeld und den Energieertrag von Kleinwindkraftanlagen sind bislang noch unbekannt. Normalerweise basiert die Auswertung von geeigneten Standorten für Kleinwindkraftanlagen auf der Windgeschwindigkeit. Dafür werden Messdaten von Messmasten oder Anemometerdaten verwendet, welche lokale Windeffekte nicht ausreichend berücksichtigen. Aber die Messdaten gelten nur innerhalb eines kleinen Bereichs, weil lokale Effekte, z.B. induziert durch Gebäude, komplexe Bodenstrukturen oder Vegetation, das Windfeld stark beeinflussen können und nicht in den Berechnungsmethoden des Jahresenergieertrags abgebildet sind. Darüber hinaus fehlt noch eine umfassende dreidimensionale Validierung urbaner Windfeldsimulationen mit Messdaten vor Ort. Bisher werden nur punktuelle Anemometerdaten zur Validierung von Simulationsdaten verwendet.

Ziel dieser Arbeit ist die numerische Untersuchung des städtischen Windfeldes auf dem Universitätscampus Morgenstelle in Tübingen (Süddeutschland), der als Testgelände für diese Studie ausgewählt wurde. Das soll in dieser Arbeit mit Hilfe von CFD und hoch aufgelösten DES Simulationen mit ANSYS Fluent geschehen. Die Simulationen umfassen komplexes Terrain und Vegetation mit dem Fokus auf den Energieertrag von Kleinwindkraftanlagen. Die Gebäudegeometrien, die in den Simulationen verwendet werden, basieren auf einer realen 3D-Stadtmodellgeometrie. Es wird ein Workflow verwendet, um die Stadtmodelle für urbane CFD-Simulationen vorzubereiten, von der Geometrieoptimierung bis hin zu den Anforderungen an die Vernetzung. Ein bereits bestehendes Vegetationsmodell wird erweitert, um lokale Baumhöhen zu berücksichtigen. Es wird eine

Sensitivitätsanalyse durchgeführt, um den Einfluss verschiedener Vernetzungsparameter und Domaingrößen zu untersuchen. Zusätzlich werden die Auswirkungen der Vegetation im Allgemeinen und die Auswirkungen verschiedener Umweltparameter wie die atmosphärische Turbulenzintensität, verschiedene Baumhöhen und Laubdichten zur Simulation der Windströmung im Sommer und im Winter untersucht. Der numerische Aufbau und die Vegetationsmodellierung werden mit LiDAR-Messdaten vor Ort in Tübingen verglichen. Es wird ein neues Verfahren vorgestellt, wie man flächige Vor-Ort-Windmessdaten als Einlassrandbedingung verwenden kann.

Da der Jahresenergieertrag einer der wichtigsten Schlüsselparameter zur Bestimmung geeigneter Standorte für Windkraftanlagen ist, wird ein Verfahren zur Berechnung lokaler Jahresenergieerträge und lokaler Windstatistiken vorgestellt. Dafür wird die Windströmung aus vier gleichmäßig verteilten Windrichtungen mit und ohne Gebäude simuliert, welche die Gebäude, die von Interesse sind, umgeben. Dazu wird ein neues Gebäudemodell vorgestellt, das die Gebäude mittels Volumenkraft und einer Indikatorfunktion modelliert. Dies ermöglicht eine schnellere Vorbereitung und eine vereinfachte Vernetzung von komplexen Gebäudegeometrien.

Die Berechnung des Jahresenergieertrags basiert auf großskaligen synthetischen Windstatistiken, die bereits verfügbar sind. Die Simulationen der vier Windrichtungen werden im Verfahren verwendet, um lokale Häufigkeiten von Windrichtungen und Windgeschwindigkeiten zu erhalten. Der Jahresenergieertrag wird für jedes Gebäude mit einer realen Horizontal- und Vertikalachsenwindkraftanlage berechnet. Ein bereits vorhandener Ansatz zur Korrektur des Jahresenergieertrags durch die atmosphärische Turbulenzintensität und den Anstellwinkel der Windturbinen wird in das Verfahren implementiert, um eine realistischere und genauere Vorhersage des Energieertrags zu erhalten. Abschließend werden geeignete Standorte für Kleinwindkraftanlagen diskutiert und bewertet.

Insbesondere die lokale Windstatistik und der Ansatz zur Korrektur des Jahresenergieertrags um die atmosphärische Turbulenzintensität führen zu einem signifikanten Unterschied in den berechneten Jahresenergieertragswerten. Die Studie zeigt weiterhin ein Potential von Kleinwindkraftanlagen auf dem Universitätscampus Morgenstelle in Tübingen, z.B. der höchste Jahresenergieertrag auf dem höchsten Gebäude auf dem Campus erreicht, wenn eine Horizontalachsenwindkraftanlage verwendet wird.

Contents

List of Symbols	IV
List of Subscripts	XI
List of Abbreviations	XII
List of Figures	XV
List of Tables	XXI
1 Introduction	1
1.1 Previous studies about urban wind field simulations	2
1.2 Objective	9
2 Fundamental Equations and Numerical Approach	11
2.1 Governing equations	11
2.2 Methodology of simulations	12
2.3 Generation and injection of atmospheric turbulence	15
3 Testcase Validation: Flow around a High-rise Building Structure	18
3.1 Description of the experiment	18
3.2 Numerical setup	19
3.3 Results and validation	21
3.3.1 Turbulence model and shielding function	22
3.3.2 Turbulence generation method	25
3.4 Summary	26
4 Geometry Preparation and Meshing for Urban Simulations	28
4.1 Site information	29
4.2 Building preparation	30
4.3 Terrain modelling	32
4.4 Vegetation modelling details	32
4.5 Modelling of surrounding buildings	36
4.6 Meshing of the urban domain	40

5	Evaluation: Sensitivity Analysis	42
5.1	Mesh convergence study	42
5.1.1	Simulation setup	42
5.1.2	Influence of meshing parameters	43
5.2	Domain size analysis	47
5.2.1	Simulation setup	47
5.2.2	Domain height	48
5.2.3	Domain width	52
5.3	Influence of environmental conditions	54
5.3.1	Simulation setup	54
5.3.2	Investigation of different atmospheric turbulence intensities	57
5.3.3	Investigation of different vegetation modelling	61
5.3.4	Summer - winter comparison	63
5.3.5	Investigation of different tree heights	67
5.4	Simulation of surrounding buildings	71
5.4.1	Site information	71
5.4.2	Simulation setup	72
5.4.3	Wake flow analysis	73
5.5	Summary	78
6	Evaluation against LiDAR Measurement Data	80
6.1	Preparation and filtering of LiDAR measurement data	80
6.2	Numerical setup and inflow conditions	82
6.3	Comparison with on-site LiDAR data	83
6.4	Summary	85
7	Windfield Evaluation and local Annual Energy Production	87
7.1	Local site information	87
7.2	Numerical setup and inflow conditions	88
7.3	Flow analysis of the simulated wind directions	89
7.4	Procedure for calculating the local AEP	96
7.4.1	Interpolation of the synthetic wind statistics onto the grid	97
7.4.2	Calculation of local wind statistics	99
7.4.3	Calculation of the local AEP	101
7.4.4	Correction of the local AEP	102
7.5	Local wind statistics and local AEP	104
7.6	Influence of surrounding buildings on local AEP	110
7.7	Evaluation of locations for small wind turbines	112
7.8	Summary	118
8	Conclusion and Outlook	120

Bibliography	124
A Appendix	137
A.1 Data sheet of horizontal axis wind turbine [5]	137
A.2 Data sheet of vertical axis wind turbine [6]	138

List of Symbols

Symbol	Description	Unit
A_{in}	Area of inflow plane	$[\text{m}^2]$
A_{cs}	Cross-sectional area of the domain	$[\text{m}^2]$
B_{WS}	Wind speed bins in synthetic wind statistics	$[\frac{\text{m}}{\text{s}}]$
B_{sim}	Wind speed bins in simulations	$[\frac{\text{m}}{\text{s}}]$
C_{DES}	Constants in the IDDES model	$[-]$
C_{DES1}	Constants in the IDDES model	$[-]$
C_{DES2}	Constants in the IDDES model	$[-]$
C_w	Constant in equ. 2.17	$[-]$
C_μ	Constant in the k -production term	$[-]$
Co	Courant number	$[-]$
D_w	Diameter of wind turbine	$[\text{m}]$
F_1	Blending function in the k - ω SST model	$[-]$
F_2	Blending function in the k - ω SST model	$[-]$
$F_{b,i}$	Building drag force	$[\frac{\text{kg}}{\text{ms}^2}]$
$F_{w,i}$	Forest drag force	$[\frac{\text{kg}}{\text{m}^2\text{s}^2}]$
$G(x, x')$	LES filter operation	$[-]$
H_b	Building height	$[\text{m}]$
H_c	Height of cube	$[\text{m}]$
H_t	Tree height	$[\text{m}]$
$H_{t,\text{av}}$	Average tree height	$[\text{m}]$

H_w	Height of wind turbine	[m]
I	Turbulence intensity	[-]
L	Turbulent length scale	[m]
L_{11}	Longitudinal integral length scale	[m]
LAI	Leaf area index	[-]
$L_{b,x}$	Length of building in x -direction	[m]
L_D	Domain length	[m]
L_d	Downwind length of the domain	[m]
L_u	Upwind length of the domain	[m]
L_γ	Constant in equ. 7.10	[m]
$M(i)$	Measurement signal	[-]
N	Number of vortex points	[-]
N_{il}	Number of inflation layers	[-]
P	Power of wind turbine	[W]
$P_{10\%TI}$	Wind turbine power with 10 % turbulence intensity	[W]
P_w	Wind power	[W]
P_{corr}	Corrected wind turbine power	[W]
P_K	k production term in equ. 2.14	$\left[\frac{\text{kg}}{\text{s}^3 \cdot \text{m}} \right]$
\tilde{P}_K	k production term in equ. 2.7	$\left[\frac{\text{kg}}{\text{s}^3 \cdot \text{m}} \right]$
$P_{l,i}$	Wind turbine power according to the lower wind speed bin limit	[W]
P_{max}	Rated power of wind turbine	[W]
P_{simTI}	Wind turbine power with simulated I	[W]
$P_{u,i}$	Wind turbine power according to the upper wind speed bin limit	[W]
Re	Reynolds number	[-]

Re_λ	Taylor-scale Reynolds number	$[-]$
Ri	Richardson number	$[-]$
S	Strain rate magnitude	$[\frac{1}{s}]$
S_{ij}	Strain rate tensor	$[\frac{1}{s}]$
V_c	Cell volume	$[m^3]$
a	Local foliage density	$[\frac{1}{m}]$
a_1	Constant in equ. 2.16	$[-]$
c	Threshold value in median filter	$[-]$
c_d	Drag coefficient	$[-]$
c_p	Pressure coefficient	$[-]$
$c_{p,b}$	Pressure coefficient for buildings	$[-]$
c_r	Resistance coefficient	$[-]$
c_{VM}	Constant in the Vortex Method	$[-]$
d	Side length of cube	$[m]$
d_w	Wall distance	$[m]$
\tilde{f}_d	Blending function in equ. 2.17	$[-]$
f_e	Elevating function in equ. 2.17	$[-]$
$f_{G10\%}$	Gaussian distribution function (TI= 10 %)	$[-]$
f_{Gsim}	Gaussian distribution function (TI from the simulations)	$[-]$
g	Gravitational acceleration	$[\frac{m}{s^2}]$
$g(x)$	Value in median filter	$[-]$
$g'(x)$	Median value in median filter	$[-]$
h_{max}	Maximum edge length of a cell	$[m]$
k	Turbulent kinetic energy	$[\frac{m^2}{s^2}]$
l	Filtered length scale	$[m]$
l_g	Local grid scale	$[m]$

l_{EI}	Demarcation length scale between the energy-containing range of eddies ($l > l_{EI}$) and smaller eddies ($l < l_{EI}$)	[m]
l_{IDDES}	IDDES length scale	[m]
l_{LES}	LES length scale	[m]
l_{RANS}	RANS length scale	[m]
p	Pressure	[Pa]
p_{∞}	Atmospheric pressure	[Pa]
q	Induction factor of HAWT	[—]
r	Radius in building model	[m]
s	Skewness of a numerical cell	[—]
t	Time	[s]
u	Wind speed	$[\frac{m}{s}]$
u'	Fluctuating velocity field	$[\frac{m}{s}]$
u_i	Velocity component ($u_i = \bar{u}_i + u'_i$)	$[\frac{m}{s}]$
u'_i	Fluctuating velocity component	$[\frac{m}{s}]$
$u' *_i$	Fluctuating velocity in the Vortex Method	$[\frac{m}{s}]$
\bar{u}_i	Time-averaged velocity component	$[\frac{m}{s}]$
u_{ref}	Reference velocity in velocity profile	$[\frac{m}{s}]$
\bar{u}_{sim}	Time-averaged and wind-direction averaged simulated wind speed	$[\frac{m}{s}]$
\bar{u}_{WS}	Yearly-averaged wind speed in synthetic wind statistics	$[\frac{m}{s}]$
u_{60}	Wind speed from 60° wind direction	$[\frac{m}{s}]$
u_{90}	Wind speed from 90° wind direction	$[\frac{m}{s}]$
u_{150}	Wind speed from 150° wind direction	$[\frac{m}{s}]$

w	Raster width in building model	[m]
w_m	Weighting factor in median filter	[-]
w_1, w_2	Weightings in the bilinear interpolation method	[-]
x	x -coordinate of the domain	[-]
y	y -coordinate of the domain	[-]
y^+	Normalized wall distance	[-]
z	z -coordinate of the domain	[-]
z_{hom}	Demarcation height between lateral homogeneous velocity profile ($z > z_{hom}$) and lateral inhomogeneous velocity profile ($z < z_{hom}$)	[m]
z_{ref}	Reference height in velocity profile	[m]
Γ	Circulation	$\left[\frac{m^2}{s}\right]$
Δ	Cell size	[m]
Δ_{be}	Cell size of building edges	[m]
Δ_{bs}	Cell size of building surfaces	[m]
Δ_t	Cell size terrain surfaces	[m]
Θ	Virtual potential temperature	[K]
Φ_{sim}	Frequency based on the simulations	[-]
Φ_{WS}	Frequency in the synthetic wind statistics	[-]
Ψ	Load factor	[-]
α	Exponent in velocity profile	[-]
α_ω	Constant in ω -equation 2.9	[-]
β	Constant in ω -equation 2.9	[-]
β^*	Constant in k -equation 2.7	[-]
$\beta_\gamma, \beta_{\gamma 0}$	Constants in equ. 7.10	[-]
γ	Angle of attack	[°]

δ	Angle of local wind direction	$[\circ]$
ϵ	Dissipation rate	$\left[\frac{\text{m}^2}{\text{s}^3}\right]$
ζ	Blocking ratio	$[-]$
η	Spatial distribution of vortex points	$[-]$
θ_e	Angle for an equiangular face or cell	$[\circ]$
θ_{\max}	Largest angle in a face or cell	$[\circ]$
θ_{\min}	Smallest angle in a face or cell	$[\circ]$
κ	Wavenumber	$\left[\frac{1}{\text{m}}\right]$
κ_c	Filter cutoff wavenumber	$\left[\frac{1}{\text{m}}\right]$
λ_2	Second eigenvalue of $(\mathbf{S}^2 + \mathbf{\Omega}^2)$	$\left[\frac{1}{\text{m}}\right]$
μ	Dynamic viscosity	$\left[\frac{\text{kg}}{\text{m s}}\right]$
μ_t	Modelled turbulent viscosity	$\left[\frac{\text{kg}}{\text{m s}}\right]$
ν	Kinematic viscosity	$\left[\frac{\text{m}^2}{\text{s}}\right]$
ξ	Vortex size	$[\text{m}]$
ρ	Density	$\left[\frac{\text{kg}}{\text{m}^3}\right]$
σ	Standard deviation	$[-]$
σ_k	Constant in k -equation 2.7	$[-]$
$\sigma_\omega, \sigma_{\omega 2}$	Constants in ω -equation 2.9	$[-]$
τ_{ij}	Shear stress tensor	$\left[\frac{\text{kg}}{\text{m s}^2}\right]$
τ_{ij}^{sgs}	Subgrid stress tensor	$\left[\frac{\text{kg}}{\text{m s}^2}\right]$
ϕ	Scalar quantity	$[-]$
$\bar{\phi}$	Filtered quantity	$[-]$
ψ	Ratio of \bar{u}_{sim} to \bar{u}_{WS}	$[-]$
ω	Specific dissipation rate	$\left[\frac{1}{\text{s}}\right]$
\vec{C}_c	Cell coordinates	$[\text{m}]$
\vec{R}_{1-4}	Coordinates of synthetic wind statistics	$[\text{m}]$

\vec{n}	Normal vector of the gradient of the streamwise mean velocity in equ. 2.21	[m]
\vec{n}_{nord}	Vector of the northern wind direction	[m]
\vec{n}_x	Vector in x -direction	[m]
\vec{u}	Velocity vector	$[\frac{\text{m}}{\text{s}}]$
\vec{u}_h	Horizontal velocity vector	$[\frac{\text{m}}{\text{s}}]$
\vec{u}_{xz}	Velocity vector in x - z -plane	$[\frac{\text{m}}{\text{s}}]$
\vec{v}'	Planar fluctuating velocity field	$[\frac{\text{m}}{\text{s}}]$
\vec{x}	Location vector	[m]
\vec{z}	Unit vector in equ. 2.21	[-]
\mathbf{S}	Symmetric tensor of the velocity gradient	$[\frac{1}{\text{s}}]$
$\mathbf{\Omega}$	Asymmetric tensor of the velocity gradient	$[\frac{1}{\text{s}}]$

List of Subscripts

Subscript	Description
av	average
max	maximum
rms	root mean square
x	x -coordinate
y	y -coordinate
z	z -coordinate
∞	freestream
0	origin

List of Abbreviations

Abbreviation	Description
ABL	Atmospheric Boundary Layer
AEP	Annual Energy Production
CFD	Computational Fluid Dynamics
DDES	Delayed Detached Eddy Simulation
DES	Detached Eddy Simulation
DNS	Direct Numerical Simulation
HAWT	Horizontal Axis Wind Turbine
IDDES	Improved Delayed Detached Eddy Simulation
LAI	Leaf Area Index
LES	Large Eddy Simulation
LGL	Landesamt für Geoinformation und Landentwicklung (State Agency for Spatial Information and Rural Development)
LiDAR	Light Detection And Ranging
LKM	Linear Kinematic Model
LoD	Level of Detail
PANS	Partially-Averaged Navier-Stokes
pdf	probability density function
RANS	Reynolds-Averaged Navier-Stokes
SDES	Shielded Detached Eddy Simulation

sgs	subgrid stress
SpS	Spectral Synthesizer
SST	Shear Stress Tensor
TI	Turbulence Intensity
TIN	Triangulated Irregular Network
URANS	Unsteady Reynolds-Averaged Navier-Stokes
VAWT	Vertical Axis Wind Turbine
VM	Vortex Method

List of Figures

3.1	Computational domain of the validation case [104] (modified).	20
3.2	Time-averaged first- and second-order velocity profiles in x -direction and elements of the Reynolds stress tensor	23
3.3	Iso-surface of λ_2 for the DDES shielding function.	24
3.4	Iso-surface of λ_2 for the IDDES shielding function.	24
3.5	Time-averaged first- and second-order velocity profiles in x -direction and elements of the Reynolds stress tensor	26
4.1	Model of the campus Morgenstelle of the University of Tübingen (Germany). Relative height (z) of the complex terrain with all buildings included.	30
4.2	Optimized building geometries (blue) and original geometries (green). . . .	31
4.3	Profiles of a over the dimensionless tree height H_t for different LAI, based on [115].	33
4.4	Seasonal LAI-values for pedunculate oaks in different vegetation times [23] (modified).	33
4.5	Forested zones (dark green) in the computational model.	34
4.6	Local dimensionless tree heights in the domain.	34
4.7	Probability density functions and tree height distributions for $\sigma/H_{t,av} = 0.05, 0.1, 0.15$ and the local forested zone in Tübingen.	35
4.8	Influence of the local tree height standard deviation σ on $ \bar{u} $ for different distances ($z/H_{t,av}$) to the ground.	35
4.9	Influence of the local tree height standard deviation σ on k for different distances ($z/H_{t,av}$) to the ground.	35
4.10	Schematic view of a mesh to check, if the cell is inside the building: A red cross must be captured by the green circle with radius r	37
4.11	Time-averaged streamwise velocity with different c_r	38
4.12	Time-averaged streamwise rms velocity $u_{x,rms}$ with different c_r	38
4.13	Streamwise velocity with different raster widths w and corresponding r . . .	39
4.14	Velocity cross section: the flow infiltrates the cube at the black arrows because r is chosen too small.	39
4.15	Meshed geometry with buildings, terrain and forested zones (light areas). .	40

5.1	Computational domain of the simulations used in the mesh convergence study. Relative height (z) of the complex terrain with the buildings.	43
5.2	Iso-surfaces of the λ_2 criterion, obtained from the simulations with different cell sizes Δ and coloured by the velocity magnitude from blue (0 m/s) to red (11 m/s).	44
5.3	$c_{p,b}$ values averaged over all buildings for different meshing parameters. . .	45
5.4	Computational domain used in the domain height study. The vertical evaluation lines are highlighted in red. Relative height (z) of the complex terrain with all buildings included.	48
5.5	Blockage ratio ζ of the computational domain with a height of $6 H_{b,\max}$, $12 H_{b,\max}$ and $18 H_{b,\max}$ over the domain length L_D	49
5.6	Computational domain used in the domain height study with the horizontal evaluation line which is highlighted in blue. Largest cross-sectional area of the domain $A_{cs,\max}$ is indicated by the dashed line.	50
5.7	Time-averaged velocity magnitude $ \bar{u} $ evaluated at the horizontal line 4 indicated as blue line in fig. 5.6 which is perpendicular to the main wind direction.	51
5.8	Time-averaged velocity magnitude $ \bar{u} $ evaluated at vertical lines 1 - 3 using different domain heights, wherein line 1 is above building A and line 2 is above building B. Blue: $6 H_{b,\max}$, red: $12 H_{b,\max}$, green: $18 H_{b,\max}$	51
5.9	Computational domain with a width of $10 H_{b,\max}$. The vertical evaluation lines are highlighted in red. Relative height (z) of the complex terrain with all buildings included.	52
5.10	Computational domain with the horizontal evaluation lines highlighted in blue.	53
5.11	Time-averaged velocity magnitude evaluated at vertical lines 1 - 3 using different domain widths, wherein line 1 is above building A, line 2 is above building B and line 3 is above building C. Blue: $10 H_{b,\max}$ and red: $16 H_{b,\max}$	53
5.12	Time-averaged velocity magnitude evaluated at horizontal lines in y -direction as shown by the blue lines in fig. 5.9 in a height of 70 m. Blue: $10 H_{b,\max}$ and red: $16 H_{b,\max}$	54
5.13	Computational domain for the simulations of different environmental conditions.	55
5.14	Vertical evaluation lines in front of building B at $y=80 \text{ m}$ (blue) and in front of building A at $y=-4.5 \text{ m}$ (red).	57
5.15	Time-averaged velocity magnitude evaluated in front of building B at $y=80 \text{ m}$ with an inlet turbulence intensity of 10 % (green), 20 % (blue) and 30 % (red).	58
5.16	Turbulent kinetic energy evaluated in front of building B at $y=80 \text{ m}$ with an inlet turbulence intensity of 10 % (green), 20 % (blue) and 30 % (red). .	59

5.17	Time-averaged velocity magnitude evaluated in front of building A at $y=-4.5$ m with an inlet turbulence intensity of 10 % (green), 20 % (blue) and 30 % (red).	59
5.18	Turbulent kinetic energy evaluated in front of building A at $y=-4.5$ m with an inlet turbulence intensity of 10 % (green), 20 % (blue) and 30 % (red).	60
5.19	Time-averaged streamwise velocities u_x plotted over height with different types of forests: volume force modelled forest (black), solid body modelled forest (green) and without forest (red), based on [50].	62
5.20	Time averaged velocity magnitude of the wind field with summer foliation in the forested zone (LAI=3.5).	63
5.21	Time averaged velocity magnitude of the wind field with winter foliation in the forested zone (LAI=0.5).	63
5.22	Time-averaged velocity magnitude evaluated in front of building B at $y=80$ m with summer foliation (blue) and winter foliation (red).	64
5.23	Turbulent kinetic energy evaluated in front of building B at $y=80$ m with summer foliation (blue) and winter foliation (red).	65
5.24	Time-averaged velocity magnitude evaluated in front of building A at $y=-4.5$ m with summer foliation (blue) and winter foliation (red).	65
5.25	Turbulent kinetic energy evaluated in front of building A at $y=-4.5$ m with summer foliation (blue) and winter foliation (red).	66
5.26	Time-averaged velocity magnitude of the wind field with 50 % of the tree height.	67
5.27	Time-averaged velocity magnitude of the wind field with 150 % of the tree height.	67
5.28	Time-averaged velocity magnitude in front of building B at $y=80$ m with tree heights of 50 % (blue), 100 % (green) and 150 % (red) related to the original tree heights.	69
5.29	Turbulent kinetic energy evaluated in front of building B at $y=80$ m with tree heights of 50 % (blue), 100 % (green) and 150 % (red) related to the original tree heights.	69
5.30	Time-averaged velocity magnitude in front of building A at $y=-4.5$ m with tree heights of 50 % (blue), 100 % (green) and 150 % (red) related to the original tree heights.	70
5.31	Turbulent kinetic energy evaluated in front of building A at $y=-4.5$ m with tree heights of 50 % (blue), 100 % (green) and 150 % (red) related to the original tree heights.	70
5.32	University campus Tübingen with modelled surrounding buildings (left) and surrounding buildings with solid geometries (right).	72

5.33	Time-averaged velocity magnitude with a simulated wind direction of 240° , evaluated at $z=15$ m with surrounding buildings included (left) and without surrounding buildings (right).	74
5.34	Time-averaged velocity magnitude with a simulated wind direction of 330° , evaluated at $z=15$ m with surrounding buildings included (left) and without surrounding buildings (right).	75
5.35	Time-averaged velocity magnitude on building A with surrounding buildings (red) and without surrounding buildings (blue).	77
5.36	Time-averaged velocity magnitude on building B with surrounding buildings (red) and without surrounding buildings (blue).	78
6.1	Velocity in streamwise direction u over time - unfiltered and filtered by the original median filter, von der Grün et al. [50].	81
6.2	Velocity in streamwise direction u over time - unfiltered and filtered by the extended version of the median filter, von der Grün et al. [50].	81
6.3	Height(z) of the complex terrain with forested zones, buildings and instantaneous streamwise velocity u_x from the simulation, von der Grün et al. [50].	83
6.4	Simulated time-averaged velocity magnitude (red) compared with LiDAR data (black), see also [50].	84
6.5	Section of the domain showing the locations of the evaluated lines, see also [50].	84
7.1	Computational domain with forested zones and buildings used for the calculation of the annual energy production. The four simulated wind directions are illustrated by the arrows.	88
7.2	Time-averaged velocity magnitude (left) and turbulent kinetic energy (right) with a simulated wind direction of 60° and evaluated at $z=15$ m.	89
7.3	Time-averaged velocity magnitude (left) and turbulent kinetic energy (right) with a simulated wind direction of 150° and evaluated at $z=15$ m.	91
7.4	Time-averaged velocity magnitude (left) and turbulent kinetic energy (right) with a simulated wind direction of 240° and evaluated at $z=15$ m.	93
7.5	Time-averaged velocity magnitude (left) and turbulent kinetic energy (right) with a simulated wind direction of 330° and evaluated at $z=15$ m.	95
7.6	One of the 14 used synthetic large scale wind statistics with frequencies (%) for wind direction sectors ($^\circ$) and wind speeds (m/s) at the university campus in Tübingen [3].	98
7.7	Large scale synthetic wind statistics at the university campus in Tübingen [3] (dashed lines) and the computational domain (black lines).	99
7.8	Pressure coefficient for the HAWT and the VAWT in dependence of γ	103
7.9	Power loss of the HAWT with increasing γ	103

7.10	HAWT power curve with a pdf with $I=20\%$ and 70%	104
7.11	HAWT power curve affected by turbulence intensity.	104
7.12	Frequencies Φ of local wind directions based on the simulations and synthetic wind statistics on building 12 with surrounding buildings in the simulations.	105
7.13	Frequencies Φ of local wind speeds based on the simulations and synthetic wind statistics on building 12 with surrounding buildings in the simulations.	106
7.14	Calculated AEP associated to buildings at the university campus Morgenstelle in Tübingen for VAWT.	107
7.15	Calculated AEP associated to buildings at the university campus Morgenstelle in Tübingen for HAWT.	108
7.16	Calculated AEP associated to buildings at the university campus Morgenstelle in Tübingen for VAWT when the surrounding buildings are included in the simulations.	111
7.17	Calculated AEP associated to buildings at the university campus Morgenstelle in Tübingen for HAWT when the surrounding buildings are included in the simulations.	112
7.18	Local wind statistics including frequencies of wind directions and wind speeds compared to synthetic wind statistics for building 12.	113
7.19	Local wind statistics including frequencies of wind directions and wind speeds compared to synthetic wind statistics for building 13.	114
7.20	Local wind statistics including frequencies of wind directions and wind speeds compared to synthetic wind statistics for building 19.	115
7.21	Local wind statistics including frequencies of wind directions and wind speeds compared to synthetic wind statistics for building 21.	117

List of Tables

5.1	Mesh properties of the simulations with various cell sizes.	44
5.2	Mesh properties of the simulations with various cell resolutions of the terrain and building surfaces and building edges.	46
5.3	Mesh properties of the simulations with various numbers of inflation layers.	46
7.1	Comparison of the horizontal and vertical wind turbines used in the calculation of the local AEP.	101
7.2	Comparison of the corrected and uncorrected AEP values using the VAWT.	109

1 Introduction

The human-induced climate change is one of the most important issues the humanity has to face. Compared to the preindustrial time the global temperature is increased by 1.2°C until now and the annual rise even accelerated. To limit the increase in temperature to 1.5°C , the CO_2 emissions have to be reduced by 50% by 2030 compared to 1990 and eliminated by 2050 [99]. In the Paris Agreement all nations commonly agreed to limit the global warming well below 2°C . An increase in temperature of 2°C could be already a threshold value which leads to irreversible changes in the ecosystem, stronger increase in global warming than anticipated and impacts on human societies and economies [124]. The European Union set the objective to limit global warming to 1.5°C in his climate legislation. That means that 40 percent of the emissions have to be reduced by 2030 compared to 1990 and eliminated by 2050 which is transferred in national laws.

The world population increased from 2015 to 2020 by 78 million people per year and 9.7 billion people are expected to live on the planet by 2050, projected by the UN Department of Economics and Social Affairs [8]. Worldwide 56.2 percent of the population live in urban areas, in the US this ratio already increased from 65% in 1950 to 83% until now. This trend will continue in the future, so the design and the supply of urban areas become more important. Due to the increase in urban population and industry, the urban energy consumption will rise in future. The climate legislation makes it necessary to switch the primary energy to electric energy. Short power supply distances in urban areas, where the most energy is needed, reduce the total energy costs and the power loss in long distance grids. The additional lack of people's acceptance delays the implementations of small wind turbines. A local renewable power generation, such as by small wind turbines, which are mounted in urban areas, can reduce the total energy costs and the power loss in long distance grids and meet the increasing demand in electric energy.

There is a presumed potential for small wind turbines in cities. For example, in Munich the technical potential for small wind turbines for buildings with flat roofs and a height above 20 m is estimated to be 27.000 MWh/year corresponding to 6750 households [4]. To estimate the yield potential, a geo-information system based approach was used, which combines wind data, exemplary system characteristics and building-specific characteristics such as roof shape and height. The wind data were taken from the German Weather Service based on test reference years, while the building-specific parameters are taken from a 3D model of the city of Munich. Based on the performance curve of a wind turbine, yields

were calculated at various hub heights for each square kilometre of the test reference years and assigned to the respective buildings or roof areas. In Surakarta, the yearly available energy of buildings with a height above 50 m is assumed to be 1221 kWh/m²/year [127]. In this study, the assessment of the wind energy potential was analyzed using a Weibull distribution in a period from 2011 to 2015 on the height of 50 m. The wind speed data were taken from a meteorological station nearby and extrapolated to the intended location and height. In a next step, the average wind velocity and the standard deviation of the extrapolating result of the wind data were calculated.

Varying wind directions are not considered when calculating the annual energy yield. Another weakness of the studies regarding the wind potential in Munich and Surakarta is that local flow effects around single buildings and the vegetation are not taken into account. However, the latter are considered to be of great importance for an accurate prediction of the annual energy yield and the potential for small wind turbines [41].

This work is part of the interdisciplinary Joint Graduate Research Training Group "Windy Cities" which investigate the economic use of small wind turbines in urban areas. That also includes the research about new web-based visualisation, new energy storage technologies and intelligent load management of small wind turbines [7].

1.1 Previous studies about urban wind field simulations

Computational Fluid Dynamics (CFD) is a widely used and appropriate tool for wind field simulations with increasing significance [24]. For instance, the aerodynamics and loads of wind turbine blades [45], the wake [101], the performance [119] or the layout of wind farms [67] can be studied with CFD. In the last years CFD has established as a common tool in architecture and urban planning [24, 133, 136, 128]. Blocken [24] gave an overview of the development of CFD for computational wind engineering and pointed out the advantage of CFD compared to on-site measurements. CFD provides detailed information on the relevant flow variables in the whole computational domain, especially when using scale resolving simulations. But CFD still needs high-quality measurements for solution verification and validation studies. In addition, the results of CFD simulations can be very sensitive to the computational parameters. Valger et al. [136] provide studies, in which influences of turbulence models, thermal stratification regimes or concentration of gaseous emissions are investigated with CFD. Moreover, CFD is used to optimize building-roof shapes for the wind energy exploitation and to simulate and optimize real geometries of vertical axis wind turbines on building roofs [128].

An urban wind field is mainly affected by buildings, vegetation and urban terrain [41]. A study using generic buildings and an artificial vegetation layout shows a large impact of

even small vegetation obstacles like hedges [87]. This effect is also confirmed by studies in built-up areas and open terrain simulations [73]. Recent studies with isolated mountain islands in the sea show topographic speed-up effects when complex terrain is considered in the simulations [57, 135]. These effects have to be taken into account for a precise wind flow prediction.

Urban wind field simulations are not only performed with focus on wind energy but also include a wide range of urban related topics. For example, Yoshie et al. [146] did some validation studies with generic and real urban building geometries compared to wind tunnel experiments to investigate the wind flow at pedestrian level and proposed that the results can be improved with scale-resolved simulations. The simulation of the Amsterdam ArenA stadium by van Hooff et al. [56] showed large differences in the air change rate of up to 42% depending on the wind direction. This rate can be improved by increasing the size of openings near the roof of the stadium.

In new urban areas and new buildings, wind safety and wind comfort studies for pedestrians are required by some authorities. Thus, Blocken et al. [26] investigated the wind flow around the Eindhoven University campus at pedestrian level and concluded that the local wind speed and the wind direction can be totally different compared to the inflow parameters and have to be simulated individually for each location. The wind in passages between high buildings may be perceived as uncomfortable by pedestrians. Blocken et al. [27] developed a control system, controlled by local wind measurements, with sliding doors to modify the wind climate in passages.

Due to the climate change and rising temperatures, the effect of urban heat islands has come more into the focus of the research in the recent years. Toparlar et al. [133] investigated the design of climate adaptive urban areas in a case study of a quarter in Rotterdam. By means of urban greening and evaporative cooling the effect of a heat storage mechanism and wind pattern on the temperature field is analysed. Besides vegetational evaporation, radiation plays a big role in an urban microclimate. Thus, Qu et al. [97] showed the importance of a 3D radiation model to consider the non-uniform radiation by the sun position and shadows which causes asymmetrical wall heating of buildings. The microclimate in urban areas can also be influenced by the layout and the morphologies of the buildings [18]. The temperatures of building facades depend on the distance to other buildings with non-uniform heights. Near complex geometries the facade temperatures are reduced due to increased shadowing effects. A higher ventilation between the buildings cool down the facades.

Water surfaces can also lower the temperatures in urban areas as shown by Tominaga et al. [131]. At pedestrian level the maximum temperature is decreased by the evaporation of the water surface by approximately 2°C. The wind propagates the cooling effect to an unobstructed distance of 100 m. The transpirational cooling effect of different types of vegetation during a heat wave in the Netherlands was investigated by Gromke et al. [48]. The vegetation lowers the urban temperature by 1.6°C and a facade greening by 0.3°C

while a roof greening does not change the temperature in the street canyons.

Urban air pollution comes into the focus of research in the last recent years. Traffic is one of the main contributors to air pollution. The polluted air is also distributed to streets with lower traffic, not just limited to busy roads. The degree of pollution is locally influenced by buildings and vegetation, as shown by a concentration map for Madrid [108]. However, tree alleys which can be mostly found in every city, significantly changes the flow in street canyons and can have an adverse effect on the pollution since they increase the concentration near the walls of buildings [38]. Jeanjean et al. [61] investigated the effectiveness of trees to disperse road traffic emissions in Leicester City Centre. At pedestrian level the pollution is decreased by 7% by tree alleys due to increased turbulence and mixing effects. Trees show the biggest effect on reduction in emissions when they are planted in open areas.

Another topic related to urban wind field simulations is the investigation of gas or other chemical dispersions in populated areas. When gas is released due to terrorist attacks or accidental events, the simulation could be used as a decision support system which indicates the affected areas. Pontiggia et al. [95] simulated a real gas event and found out that the presence of buildings leads to a different cloud footprint than in a free field dispersion. Hanna et al. [53] investigated the release of chlorine gas from a railroad tank car. The released chlorine cloud could initially extend a hundred meters or more in the upwind and crosswind directions and follows the terrain drainage, e.g. river channels or valleys. The buildings slow down the gas distribution and can locally increase the gas concentration.

The three-dimensional building geometry used in this study is obtained from a CityGML model. The availability of these city models, which are provided for whole Germany [49] strongly has increased over the last years. The CityGML models are categorized into different Levels of Details (LoD) from 0 to 4: LoD0 is actually just a 2D geometry containing the ground area of buildings, LoD1 is the extruded geometry of LoD0 by the mean building height. In LoD2, the simplified roof shapes, such as a flat roof or a gabled roof, are included. The LoD3 contains more exterior details, e.g. balconies, dormers, windows etc.. The highest Level of Detail LoD4 further includes interior rooms which can be used for indoor ventilation studies. For urban CFD simulations usually LoD1 or LoD2 buildings are sufficient. With CityGML models different urban topics can be investigated. For instance, Jang et al. [60] used these geometries to simulate the flooding status, the degree of flooding and the level of building damage after heavy rainfall in a case study in Korea. Furthermore, the loss of human life and property damage is estimated in this study. Trometer et al. [134] simulated scenarios in which detected unexploded bombs have to be defused or detonated. This can be used for a more precise prediction of which areas must be evacuated for the deactivation. One of the most important scenarios happening

in complex and tall buildings is the evacuation of people. Atila et al. [19] combined CityGML buildings with an individual evacuation model to find the shortest path with safety in case of disasters such as fire. Besides the heat demand forecast of single buildings or city districts [88], CityGML models are applied in photovoltaic potential estimation. Rodriguez et al. [100] determined their potential in urban and regional scale and also the fraction of electricity demand that can be covered. Lu et al. [77] investigated a 3D noise propagation on building facade level with different heights by using a 3D city model and integrating all the noise coming from individual traffic such as cars or motorcycles as well as planes and railroad based vehicles. Furthermore, studies based on 3D city models or architectural proposal embedded in an existing city model can be used for decision support in cities and communities.

Basically, two different approximate forms of the Navier-Stokes-equations can be used for urban wind simulations: the Large Eddy Simulation (LES) in which the larger eddies are solved directly and the smaller ones are modelled and the Reynolds Averaged Navier-Stokes (RANS) simulation in which all eddies are modelled. In Detached Eddy Simulations (DES), also called hybrid methods, the wall boundary layers in a domain are modelled with RANS and the remaining flow field with LES. Blocken et al. [25] compared both methods for the use of outdoor and indoor building simulations. In general, LES shows more precise results, but more computational resources and higher requirements for the grid generation are needed. Due to the high simulation complexity of LES a lack of knowledge to set up such a simulation can yield to less accurate and less reliable results than those by RANS [25]. Depending on the problem to be solved, RANS simulations can be sufficiently accurate. Back to the basic bluff body flow simulation, Bourdreau et al. [28] compared unsteady RANS (URANS) and DES simulations by performing simulations of the wake of a bluff body. In that, the DES approach tends to overestimate the time-averaged streamwise velocity component, especially in the near wake. The velocity fluctuations agree better with experimental data and better than the URANS results. For a more detailed overview about bluff body flow it is referred to chapter 3.1. Krajnovic et al. [68] also investigated the bluff body flow with Partially Averaged Navier Stokes (PANS) simulations. They found out that the simulation results with LES and DES show more details and fluctuations than PANS and RANS. Moreover, LES and DES tend to be more accurate and more suitable for bluff body flow simulations. Liu et al. [75] also confirmed the superiority of LES and DDES over RANS models when they simulated an isolated high-rise building. LES and DDES predicted similar results in the wake region, but the DDES approach has a lower overall mesh requirement. Thus, it is recommended to use DDES for building simulations, since instantaneous wind characteristics can be useful for a more accurate analysis of wind comfort [75].

The wind field in the atmospheric boundary layer is affected by the structure of the ground surface which is complex terrain, vegetation and buildings. The effects of complex terrain on the wind field under various wind directions were investigated by Huang et al. [57]. A hilly island in the sea is taken as a test site and the simulations are validated using wind tunnel experiments. The island strongly influences the wind flow in terms of wind speed and higher turbulent kinetic energy. Another study of topographic speed-up effects in complex terrain using a hilly island in the sea was performed by Uchida et al. [135]. The wind field with different locations for high wind turbines is investigated. Behind the island a recirculation area of eight times the height of the island is formed. The wind flow is mainly affected by the terrain instead of the inflow shear boundary condition. Letzgus et al. [73] performed highly resolved DDES simulations including complex terrain and forested zones. A real inflow boundary condition with velocity fluctuations is used provided by a previous mesoscale simulation. The comparison with on-site met mast data shows a good agreement regarding the power spectra and the mean velocity values.

For a precise prediction of the wind flow atmospheric wind properties have to be considered in the simulations. The properties have to be applied as inflow conditions. A synthetic turbulence generator is crucial for scale resolving simulations like DES. Li et al. [74] compared two different inflow conditions: the first is a classical logarithmic/exponential law to define the velocity profile without generating atmospheric turbulence at the inlet. The second is to interpolate the velocities and turbulence properties provided by a previous simulation of the upstream region. The last boundary condition shows a better prediction, but also needs more computational resources. Schulz et al. [114] investigated the power response of a wind turbine to inflow turbulence and terrain effects, and confirmed the importance of applying atmospheric turbulence at the inflow plane. That leads to an increase in load and power fluctuations and to a decrease of the tower blockage.

An approach for a more universal predication of urban wind field studies is to categorize buildings and city quarters. Therefore, morphological indicators can be defined which potentially correlate with the wind environment. The parameters such as building density, building coverage in terms of the aspect ratio, variation level of the building volumes or porosity of the city (street canyons, parks, etc.) have a large correlation with the wind potential [140]. For example, the impact of the building length on the wind potential on roofs is much more important than the building width [139].

The urban windfield is influenced by the arrangement of street canyons, the arrangements and the shape of buildings. Wang et al. [141] defined various urban morphologies and categorized urban quarters. They defined seven typical urban forms from the city of Beijing and made a cross analysis of the wind potential over the rooftops of the highest build-

ings in each urban form, wherein just the local dominant wind direction is simulated and the wind energy density is evaluated. The determination of suitable locations for wind turbines requires the use of real-scale urban geometries. Juan et al. [64] investigated the wind resource assessment around high-rise buildings in real urban areas based on real urban geometries. The domain includes roof geometries, upstream obstacles, arrangements of integrated building complexes and parallel high-rise buildings. Possible locations have been evaluated depending on distances from rooftop sidewalls or lowest mounting heights above rooftops. These zones indicate high wind power densities and acceptable turbulence intensities for wind turbines.

A common approach evaluating wind turbine locations is calculating the mean wind speed, for example in the above-mentioned studies from Wang et al. [141], Sunderland et al. [126] and Balduzzi et al. [21]. Additionally, the turbulence intensity or the wind power density can be considered, as for example in the studies of Ledo et al. [69] and Juan et al. [64]. Toja-Silva et al. [129] used the threshold value of the turbulent intensity of 0.15 according to the European Wind Turbine Standards II [2] to define heights for installing HAWTs. Another approach evaluating wind turbine locations is to calculate local Weibull distributions of the wind field based on wind roses as annual wind speed distributions can be approximated by a Weibull distribution [126]. To represent wind turbines in the evaluation approach, the wind turbine power curve can be included in the approach [32, 43].

Kalmikov et al. [65] calculated the probability distribution of an urban wind flow which is described by the parameters of the Weibull distribution. They used the MIT campus to study and validate the mean wind speed and wind power density by integrating local wind measurements and observations of near reference sites in their simulations. The micro-climate around the campus was analysed and optimal locations for small wind turbines were studied. Sunderland et al. [126] used Weibull distributions for a more accurate power prediction of wind turbines than current wind turbine power output measurements which are based on average wind speeds over an observation period. Two models were developed which are based on the normal and Weibull distributions, respectively. Both models predicted the mean wind speed, the standard deviation within a 10 min time interval and the turbulence intensity. The validation shows that the Weibull based model shows a more accurate prediction of the energy production under realistic conditions. However, Toja-Silva et al. claims that Weibull distributions of wind statistics would be incorrect in urban settings [128].

The installation site has a great influence on the potential energy yield. Balduzzi et al. [21] did a study with generic buildings which vary in shapes, geometrical proportions and various arrangements. The skew angle of the flow, which may change near the roof top, is considered in the wind turbine power curve. As a result, a vertical axis wind turbine (VAWT) shows better performances with the skewed flow than a horizontal axis wind turbine (HAWT), so that a VAWT may be more recommended for urban wind flow. Gagliano et al. [43] assessed the feasibility of building integrated micro wind turbines and

calculated the wind distribution within urban areas and the yearly energy yield. That allows a possible owner of a wind turbine to evaluate its effective potentiality of wind energy generation in urban areas. A large number of building integrated micro wind turbines, will make a large contribution to local energy production [43].

Dadioti did an extensive research about urban wind field simulation with the focus on small wind turbines [33, 32]. In this study, the university campus in Leicester (UK) is used as a test site for the DES simulations. After detailed validation studies with bluff body flows and local anemometer data, the optimum location for micro wind turbines installation was investigated based on the calculation of the annual energy production. This study concludes and recommends that DES offers robustness and accuracy over a range of wind conditions and is well suited to the analysis of wind energy potentials in complex urban environments.

But one of the most interesting questions regarding small wind turbines in urban areas is the question if it is worth to mount a small wind turbine on a specific building. To answer this question, different micro-siting processes were applied in the literature. For example Wang et al. [142] performed CFD simulations of wind flow in built environment under the urban atmospheric boundary layer inflow condition. Their simulations have been compared to wind lidar measurements. They concluded that the wind turbine should be installed at the height of 1.3 to 1.5 of a building height. An overview of existing studies gives the review paper of Toja-Silva et al. [128]. The studies considering several real buildings and mentioned therein use mostly RANS simulations, a real-scale geometry and isolated or several generic buildings. Toja-Silva et al. [128] emphasized the influence and the importance of surrounding buildings and figured out that it is not legitimate to conclude from the flow around one isolated building to the wind field around several buildings. The few studies mentioned in the review paper did not consider a combination of vegetation, the flow from more than one wind direction, and any kind of evaluation of the suitable positions for small wind turbines based on AEP values on buildings or local wind statistics as a whole in one study.

But only the minority of the studies used the power curve of a wind turbine to determine the possible energy output such as Gagliano et al. [43] or Dadioti [32]. As Toja-Silva et al. mentioned in their review paper there is a lack of studies which determine the local frequencies of the wind speed and show the expected great potential of LES for accurate turbine performance evaluation [128].

The energy yield of a wind turbine strongly depends on the wind flow around its position. This wind flow is affected by the building itself on which the wind turbine is mounted. As compared to typical rectangular roofs, a rounded roof design produces a lower turbulence intensity and higher power density which is increased up to 86.5% [145]. Furthermore, high-rise buildings tend to block the incoming wind in the upstream direction and induce

higher turbulence intensities [145]. Another approach to improve the wind flow towards building integrated wind turbines are ducted openings. Their aerodynamic design is optimized for wind energy harvesting by Ruiz et al. [16]. Rounded openings suppress the flow separation, enhance the magnitude and uniformity in the wind, and tend to lower the turbulent kinetic energy. With an optimized design the wind speed can be increased up to 78%. Ledo et al. [69] found out that the power density above flat roofs is increased compared to pyramidal roofs, independently of the wind direction. In general, the wind velocity decelerates above pitched and pyramidal roofs when the inclination angle of the roof exceeds 55° in the pitched case and 67° in the pyramidal roof. With a domed, vaulted and a wedged roof shape an increase of energy yield of more than 45% can be reached [9]. The lowest increase of power is obtained with a pyramidal roof [9]. Moreover, Lu et al. [78] mentioned that the concentration effect of buildings and the heights of buildings could enhance wind power utilization by increasing the wind speed by a factor of 1.5 – 2. Thus, not only the type of roof affects the wind flow but also the interaction between adjacent buildings.

It is well known that numerical simulations still rely on experimental data sets to validate numerical setups, turbulence models, or any kind of new implementation in the source code. For urban wind simulations many on-site measurement devices are needed to capture the wind flow in urban domains. Due to the large influence of local conditions the measured wind data is only valid within a short range. Wind tunnel experiments can help to overcome these problems. For simple validation purposes, wind tunnel data with simple building geometries are preferred. Yoshie et al. [146] from the Architectural Institute of Japan proposed a workflow with different validation steps based on comparative studies. In the first step, the flow around two types of single high-rise buildings is simulated. The second step includes a high-rise building surrounded by an array of equal simplified buildings. Just the last step is based on actual urban areas with two types of building complexes. But in all stages the complex terrain and the vegetation is not included [146]. To include complex terrain, vegetation and real scale buildings in the validation process, on-site measurements are crucial but still lacking for validation purposes.

1.2 Objective

The objective of this work is to investigate the urban wind field at the university campus Morgenstelle in Tübingen (southern Germany) with the focus on the energy yield of small wind turbines. Highly resolved DES simulations are performed which include building geometries, complex terrain and vegetation using the ANSYS Fluent software [1]. The building geometries are based on a real 3D city model geometry. A method for using 3D city models for urban CFD simulations from geometry optimisation to meshing

requirements is presented. An already existing vegetation model from Shaw and Schumann [115] is extended to consider local tree heights and seasonal effects of the vegetation. A sensitivity analysis is performed to study the influences of different meshing parameters and domain sizes. Additionally, the effect of various environmental parameters such as turbulence intensity at the inlet, different tree heights and foliage densities to simulate a summer and winter wind flow are investigated. The wind flow is evaluated with and without buildings which surround the target zone. The numerical setup and the vegetation model are validated with on-site LiDAR measurement data in Tübingen. A new method for using planar on-site wind measurement data as an inflow boundary condition is introduced.

To investigate if it is worth to install small wind turbines on one of the buildings, the wind fields from four different wind directions are simulated and evaluated. A new method for calculating local wind statistics for each numerical cell is introduced using large-scale synthetic wind statistics. The local wind statistics are used to determine the maximal annual energy production associated to each building using a real vertical and horizontal axis wind turbine. The annual energy production values are corrected according to local turbulence intensities and angles of attack. Finally, the annual energy production is taken as the main parameter to evaluate suitable locations on the buildings for small wind turbines.

2 Fundamental Equations and Numerical Approach

The simulations in this work were performed with the commercial CFD program ANSYS Fluent in the versions 18.1 [12] and 2019R3 [13]. For the highly resolved Detached Eddy Simulation (DES) an incompressible solver is used with the Improved Delayed DES (IDDES) shielding function combined with the $k-\omega$ SST turbulence model. At the inflow plane the atmospheric turbulence is synthetically generated. Their governing equations and the methodologies are described in the following chapter.

2.1 Governing equations

A Newtonian fluid can be described by the Navier-Stokes equations which include the conservation equations for mass, momentum and energy. The simulations in this work are performed assuming incompressible flow only. Hence, the continuity equation [111] is described by

$$\frac{\partial u_i}{\partial x_i} = 0 \quad (2.1)$$

where $i = 1, 2$ and 3 which corresponds to the x, y, z -direction in the computational domain and u_i is the velocity in i -direction. The momentum equation is defined by [123]

$$\rho \frac{Du_i}{Dt} = \rho g_i - \frac{\partial p}{\partial x_i} + \mu \frac{\partial^2 u_i}{\partial x_j \partial x_j}, \quad (2.2)$$

where j and $i = 1, 2$ and 3 , ρ is the density, p is the pressure, t is the time, g_i is the gravitational acceleration in i -direction and μ is the dynamic viscosity. According to Pope [96] the material derivative is defined by

$$\frac{D}{Dt} \equiv \frac{\partial}{\partial t} + u_j \frac{\partial}{\partial x_j}. \quad (2.3)$$

Since the air temperature is not considered in this work, the energy conservation equation is not listed here. The Navier-Stokes equations are solved numerically which is described in the following.

2.2 Methodology of simulations

CFD simulations can be basically divided into three major categories according to the degree of modelling: Reynolds-Averaged Navier–Stokes simulations (RANS), Large Eddy Simulation (LES) and Direct Numerical Simulations (DNS). In RANS simulations the variables are time-averaged and no information about fluctuating velocities is available. The entire flow and all turbulent eddies are modelled. Due to low computational costs RANS simulations are widely used in industrial applications. In LES small scale eddies are filtered out by a filter operation in order to be modelled by a turbulence model. However, the remaining large scale eddies are resolved directly. Since the large scale eddies are the most energy containing eddies and are mainly affected by the geometry [96], e.g. in urban areas which are mostly affected by buildings and vegetation zones [40, 96], LES simulation results are assumed to be more accurate [25]. In DNS simulations 100 % of the turbulence is resolved directly, down to the smallest scales, also known as the Kolmogorov scales [96]. That makes DNS simulations the most expensive type of simulation and is especially used for validation purposes. In general, the degree of modelling increases the computational costs, but also the accuracy of the results [96].

In a hybrid simulation, both RANS and LES are involved simultaneously, also called Detached Eddy Simulation (DES). The basic idea behind DES is that the near-wall region is simulated with the RANS method and the outer, i.e. detached flow, with the LES method. The transition from RANS to LES is coupled by the length scale and the viscosity. When the boundary layer is modelled, the cell layers inside the boundary layer can be thicker compared to when the boundary layer is solved directly because the small turbulent eddies within a boundary layer do not have to be resolved in LES mode. That increases temporal resolution in the detached regions and reduces computational costs [122]. Hence, DES can be seen as a preferable compromise for urban wind field simulations, since the focus is on the directly resolved outer region where wind turbines are mounted on buildings and unsteady turbulence information can be provided with reasonable costs.

Before the LES method and the transition between RANS and LES is explained, the RANS approximation of Navier-Stokes equations is described briefly. A velocity u is decomposed as the sum of a time-averaged velocity \bar{u} and a fluctuating velocity u' . After inserting $u = \bar{u} + u'$ in equ. 2.2 and time-averaging this equation yields to

$$\rho \frac{\partial \bar{u}_i}{\partial t} + \rho \bar{u}_j \frac{\partial \bar{u}_i}{\partial x_j} = -\frac{\partial \bar{p}}{\partial x_i} + \frac{\partial}{\partial x_j} \left(\mu \frac{\partial \bar{u}_i}{\partial x_j} - \overline{\rho u'_i u'_j} \right), \quad (2.4)$$

where the term $-\overline{\rho u'_i u'_j}$ is the unknown Reynolds stress tensor. Defining a conservation equation for $-\overline{\rho u'_i u'_j}$ would lead to further unknown terms in this equation. More equations would lead again to more unknown terms resulting in an endless loop which cannot be closed [96].

The starting point for solving the closure problem is Boussinesq's analogy to the law of viscosity. The turbulent shear stress is directly proportional to the mean deformation rate. In tensor notation, this analogy results

$$\tau_{ij} = -\overline{\rho u_i u_j} = \mu_t \left(\frac{\partial \bar{u}_i}{\partial x_j} + \frac{\partial \bar{u}_j}{\partial x_i} \right) - \frac{2}{3} \rho \delta_{ij} k, \quad (2.5)$$

where τ_{ij} is the shear stress tensor and μ_t the modelled turbulent viscosity. Thus, the modelling of the turbulent stresses is reduced to the modelling of μ_t . In this work, the k - ω SST approach by Menter et al. [83] is used as the RANS model for DES simulation [10, 11]. Accordingly, the turbulent viscosity is modelled by the following term

$$\mu_t = C_\mu \frac{k}{\omega} \quad (2.6)$$

Since μ_t is a function of k and ω , the Reynolds stress tensor is modelled by defining two additional transport equations, one for the turbulent kinetic energy k and one for the specific dissipation rate ω . The original k - ω SST approach, developed by Menter [84], uses the k - ω model by Wilcox [143] in the sub- and log-layer and gradually switches to the k - ε model in the outer part of the boundary layer [84], wherein ε is the dissipation rate. The governing equation for k implemented in ANSYS according to the formulation of Menter et al. [83] is

$$\frac{\partial(\rho k)}{\partial t} + \frac{\partial(\rho u_i k)}{\partial x_i} = \tilde{P}_k - \beta^* \rho k \omega + \frac{\partial}{\partial x_j} \left[\left(\mu + \frac{\mu_t}{\sigma_k} \right) \frac{\partial k}{\partial x_j} \right] \quad (2.7)$$

with the limited production term \tilde{P}_k

$$\tilde{P}_k = \min \left(\tau_{ij} \frac{\partial u_i}{\partial x_j}, 10 \cdot \beta^* \rho k \omega \right), \quad (2.8)$$

where μ is the dynamic viscosity and β^* and σ_k are constants. The transport equation for ω implemented in ANSYS is

$$\frac{\partial(\rho \omega)}{\partial t} + \frac{\partial(\rho u_i \omega)}{\partial x_i} = \alpha_\omega \rho S^2 - \beta \rho \omega^2 + \frac{\partial}{\partial x_j} \left[\left(\mu + \frac{\mu_t}{\sigma_\omega} \right) \frac{\partial \omega}{\partial x_j} \right] + 2(1 - F_1) \cdot \frac{\rho \sigma_{\omega 2}}{\omega} \frac{\partial k}{\partial x_i} \frac{\partial \omega}{\partial x_i} \quad (2.9)$$

with the strain rate magnitude S and the constants α_ω , β , σ_ω and $\sigma_{\omega 2}$ [83]. The blending function F_1 ensures that the k - ω model gradually switches to the k - ε model with increasing wall distance.

The outer region in DES is simulated with LES. Herein, the eddies are filtered in the computational domain so that large scale eddies can be resolved directly, while smaller scales can be represented by simple models [96]. The general filtering operation $G(x, x')$

applied to a quantity $\phi(x')$ is introduced by Leonard [72] and is defined by

$$\bar{\phi}(x) = \int G(x, x') \phi(x') dx' \quad (2.10)$$

to obtain the filtered quantity $\bar{\phi}(x)$ [96]. The filter width determines the filtered length scale l which is not necessarily the cell size Δ but the condition $l > \Delta$ is always valid [40]. In ANSYS Fluent, the filtered length scale is based on the local grid scale l_g and is calculated by $l_g = V_c^{1/3}$, where V_c is the volume of the computational cell [10, 11]. By introducing the subgrid stress (sgs) tensor τ_{ij}^{sgs} [96] based on the filtered velocities in equ. 2.10

$$\tau_{ij}^{sgs} = -\rho \overline{u'_i u'_j}, \quad (2.11)$$

the filtered momentum equation for LES yields [40]:

$$\frac{\partial(\rho \bar{u}_i)}{\partial t} + \frac{\partial(\rho \bar{u}_i \bar{u}_j)}{\partial x_j} = \frac{\partial}{\partial x_j} \left[\mu \left(\frac{\partial \bar{u}_i}{\partial x_j} + \frac{\partial \bar{u}_j}{\partial x_i} \right) \right] - \frac{\partial \tau_{ij}^{sgs}}{\partial x_j} - \frac{\partial \bar{p}}{\partial x_i}. \quad (2.12)$$

Similar to the Reynolds stress tensor, the sgs tensor has to be modelled to close the equations, similar to the RANS formulation. In ANSYS Fluent, the Boussinesq hypothesis is applied to the subgrid models to compute the subgrid-scale stresses with the strain-rate tensor S_{ij} [10, 11]

$$\tau_{ij}^{sgs} - \frac{1}{3} \tau_{bb}^{sgs} \delta_{ij} = \mu_t \left(\frac{\partial \bar{u}_i}{\partial x_j} + \frac{\partial \bar{u}_j}{\partial x_i} \right) = 2\mu_t S_{ij}, \quad (2.13)$$

where b, i and $j = 1, 2$ and 3 . Finally, the turbulent viscosity μ_t is the only left quantity which has to be modelled.

In the newer version of DES by Spalart et al [121], also called the Delayed DES (DDES), a shielding function is introduced to protect the outer LES region to fall back into the RANS modelled boundary layer. When an undesired LES-fallback into the boundary layer occurs, velocity fluctuations cannot be resolved properly because the grid of the boundary layer is too coarse. But providing velocity fluctuations for the LES mode is crucial. It is achieved by Menter et al [83] by using the F_1 and F_2 functions of the $k-\omega$ SST RANS model to identify the boundary layer and the transition to LES since the thickness of the boundary layer is unknown during the grid generation process.

Since the simulations in this work are performed with the IDDES $k-\omega$ SST model, this model is described briefly. An overview of all tested DES turbulence models and their different results is given in the next chapter. The IDDES model in ANSYS Fluent is based on the $k-\omega$ SST model [84] and the IDDES approach by Shur et al [118] including the modifications proposed by Gritskevich et al. [47]. This model provides shielding against the LES-fallback and includes wall-modelled LES capabilities in the attached flow regions [47]. The following governing equations are extracted from the publication of Gritskevich

et al. [47]. The equation for k is defined as

$$\frac{\partial(\rho k)}{\partial t} + \frac{\partial(\rho u_i k)}{\partial x_i} = \frac{\partial}{\partial x_j} \left[\left(\mu + \frac{\mu_t}{\sigma_k} \right) \frac{\partial k}{\partial x_j} \right] + P_k - \rho \frac{\sqrt{k^3}}{l_{\text{IDDES}}}, \quad (2.14)$$

where l_{IDDES} is the IDDES length scale, and with the limited production term P_k

$$P_k = \min(\mu_t^2 S^2, 10 \cdot C_\mu \rho k \omega) \quad (2.15)$$

and the constant C_μ . The turbulent viscosity is modelled as

$$\mu_t = \rho \frac{a_1 \cdot k}{\max(a_1 \cdot \omega, F_2 \cdot S)} \quad (2.16)$$

with the constant a_1 and the blending function F_2 . While the ω -equation 2.9 and the blending functions F_1 and F_2 remain unmodified, the sink term of the k -equation is modified using the IDDES length scale l_{IDDES} which is defined as follows

$$\begin{aligned} l_{\text{IDDES}} &= \tilde{f}_d \cdot (1 + f_e) \cdot l_{\text{RANS}} + (1 - \tilde{f}_d) \cdot l_{\text{LES}} \\ l_{\text{LES}} &= C_{\text{DES}} \cdot \min\{C_w \cdot \max[d_w, h_{\text{max}}], h_{\text{max}}\} \\ l_{\text{RANS}} &= \frac{\sqrt{k}}{C_\mu \omega} \\ C_{\text{DES}} &= C_{\text{DES1}} \cdot F_1 + C_{\text{DES2}} \cdot (1 - F_1) \end{aligned} \quad (2.17)$$

with the constants C_{DES} , C_{DES1} , C_{DES2} , C_w , the wall distance d_w , the LES length scale l_{LES} and the RANS length scale l_{RANS} . The variable h_{max} is the maximum edge length of a cell and its definition includes only hexahedral cells [47]. This formulation is adapted to other cell types in ANSYS Fluent [10, 11]. For the empiric blending function \tilde{f}_d and the elevating function f_e it is referred to the work of Gritskevich et al. [47].

2.3 Generation and injection of atmospheric turbulence

In order to simulate the atmospheric turbulence in the wind field, the turbulent structures have to be generated synthetically at the inflow plane of the domain in scale-resolving simulations. ANSYS Fluent provides two different methods to generate turbulent velocity fluctuations: the Vortex Method (VM) and the Spectral Synthesizer (SpS) [10, 11]. In most of the simulations of this work the Vortex Method is used, thus only the algorithm of this method is described in the following chapter which is mainly related to the ANSYS Fluent Theory Guide [10, 11]. This approach is originally published and validated in several cases by Mathey et al. [81, 80] and is a relatively inexpensive and precise way to

generate random fluctuations at the inlet since it is temporally and spatially correlated [81].

To consider perturbations of a turbulent inlet velocity profile, a time-dependent 2D vortex method is applied. The fluctuating velocities are added to the mean velocity profile at the inflow plane. A vorticity field is created randomly on the two-dimensional boundary inlet plane. This approach is based on the Lagrangian form of the 2D evolution equation of the vorticity written in the Biot-Savart law form [11, 123]. This equation is solved by a particle discretization representing the vortex points. Taking the number of vortex points N and the area of the inflow plane A_{in} into account, the amount of vorticity carried by a given particle i is represented by the circulation $\Gamma_i(x, y)$

$$\Gamma_i(x, y) = 4\sqrt{\frac{\pi A_{\text{in}} k(x, y)}{3N[2\ln(3) - 3\ln(2)]}} \quad (2.18)$$

and a spatial distribution η depending on the location vector \vec{x}

$$\eta(\vec{x}) = \frac{1}{2\pi\xi^2} \left(2e^{-|\vec{x}|^2/2\xi^2} - 1 \right) 2e^{-|\vec{x}|^2/2\xi^2}. \quad (2.19)$$

The quantity ξ specifies the size of a vortex by a turbulent mixing length hypothesis to ensure a wide applicability. Using k and the dissipation rate ε it yields

$$\xi = \frac{c_{\text{VM}} k^{3/2}}{2\varepsilon}, \quad (2.20)$$

where the constant c_{VM} amounts to 0.16. The discretization of the velocity field is given by

$$\vec{u}(\vec{x}) = \frac{1}{2\pi} \sum_{i=1}^N \Gamma_i \frac{((\vec{x}_i - \vec{x}) \times \vec{z}) \left(1 - e^{|\vec{x} - \vec{x}_i|^2/2\xi^2} \right)}{|\vec{x} - \vec{x}_i|^2} \quad (2.21)$$

with the unit vector \vec{z} in streamwise direction. The sign of the circulation of each vortex changes randomly every characteristic time scale which is the time for a vortex to travel 100 times the mean vortex size ξ with the velocity in streamwise direction [81]. The minimum size of the vortex is bounded by the cell width which ensures that it belongs to resolved turbulent scales which is important for partially resolved simulations as LES or DES.

A simplified Linear Kinematic Model (LKM) is used based on the work of Mathey et al. [10, 11, 81]. This model imitates the influences of the vortices in the streamwise mean velocity field. The fluctuating velocity field u' in streamwise direction is given by

$$u' = -\vec{v}' \cdot \vec{n}, \quad (2.22)$$

where \vec{v}' is the planar fluctuating velocity field and \vec{n} is the normal vector of the gradient of the streamwise mean velocity. The perturbations are equally distributed among the velocity components. In the case normal fluctuations are known, e.g. from previous simulations or defining the Reynolds stresses for isotropic turbulence, they can be applied to the flow field in order to fulfil the normal statistic fluctuations $\overline{u_i u_i}$ [10, 11]. The resulting velocity fluctuations are then calculated by

$$u_i'^* = u_i' \frac{\sqrt{\overline{u_i u_i}}}{\sqrt{2/3k}}. \quad (2.23)$$

3 Testcase Validation: Flow around a High-rise Building Structure

In this chapter different setups and turbulence models with various shielding functions were tested and validated. Since no real-scale measurements for buildings are available, a surface mounted cube in a boundary flow profile was chosen which is similar to a single high-rise building. The results are validated with wind tunnel experiments by Bourgeois et al. [29] and DNS simulations by Saeedi et al. [104].

3.1 Description of the experiment

Bluff body flows are very common for testing simulation setups and turbulence models. Both can be validated by wind tunnel experiments and DNS simulations. For instance, Yakhot et al.[144] performed a DNS simulation of a wall mounted cube in a fully developed channel flow and analysed the wake and the vortex structure. Also Saeedi et al. [104] used DNS simulations to investigate the wake of a surface mounted slim cube and studied the Reynolds stresses and velocity fluctuations in the wake. Valger et al.[137] simulated the flow around a surface mounted cube and discovered an over-prediction of k in RANS with $k-\epsilon$ and $k-\omega$ turbulence models. Elkhoury et al. [37] did a bluff body flow study with different RANS models. They came to the conclusion that the Spalart-Allmaras turbulence model and the $k-\omega$ Scale Adaptive Simulation best reproduce the separation region in front of the cube and the Spalart-Allmaras model predicts the best velocity profile of the roof of the cube. But the length of the separation region behind the bluff body is overpredicted by all models used in the study. Due to the complex flow around bluff bodies a scale resolving simulation is highly recommended and shows a higher accuracy in the results than using RANS [28, 75, 68]. Roy et al.[102] showed in their simulations that RANS over-predicted the length of the recirculation zone in comparison to LES. Paik et al.[92] simulated the flow around two wall-mounted cubes in tandem. Herein, URANS fails to capture key features such as single vortices while good agreements with various DES and DDES models are achieved. Robertson et al.[98] observed similar results testing the DDES and the IDDES shielding function.

The flow around an array of several cubes was simulated using LES by Stoesser et al.[125]

who achieved a good agreement with wind tunnel experiments. Hanna et al.[54] simulated various arrangements of several obstacles using LES to investigate street canyon effects. Both Hang et al.[52] and Santiago et al.[107] investigated the flow around cube arrays, validated their results with wind tunnel data and obtained a good agreement. The importance of a synthetic turbulence generator to capture the atmospheric turbulence in LES simulations is confirmed by Shi et al.[116].

Also on the experimental side there are some studies which are worth to mention. Hajimirzaie et al.[51] used particle image velocimetry in the wind tunnel to investigate the wake behind two different ellipsoid bodies and observed counter-rotating distributions of vorticity inducing downwash (tip structures), upwash (base structures), and horseshoe vortices in the wake. Bourgeois et al.[29] investigated the large scale structures behind a wall mounted square cylinder. They observed a strong interaction between the free end and the wall and a resulting deformation of the vortex structures with a principal core behind the cube. Two zones in the flow around a surface mounted cube are detected by Sattari et al.[109]. While the first and windward zone is dominated by alternate formation and vortex shedding, the second and lee side zone is characterized by two co-existing vortices throughout the shedding cycle.

The wind tunnel experiments by Bourgeois et al. [29] and Sattari et al. [109], who investigated a small-scale high-rise building in a wind tunnel, and DNS simulations by Saeedi et al. [104] are taken to validate the numerical setup which is used for the simulations in this work. The building with an aspect ratio of 4:1 in height to width is placed in a boundary layer flow. A schematic view of this geometry is shown in fig. 3.1. The side length d and the height of the cube H_c is 0.0127 m and 0.0508 m. The computational domain is 0.31496 m long, 0.17018 m wide and 0.1143 m high. Saeedi et al. [104] also mentioned differences in the blockage ratio and in the domain size between the wind tunnel experiments and their DNS simulation. Since the results in this work are compared in particular with the results of Saeedi et al. [104], the size of the domain is according to the DNS domain of Saeedi et al. [104]. The cube is located $4d$ downstream behind the inflow plane and in the centre of the z -direction as shown in fig. 3.1. The boundary layer flow enters the domain on the left with a free stream velocity u_∞ of 15 m/s. The Reynolds number is 12.000, based on u_∞ and d as the characteristic length scale. The centre of origin is located at the ground area of the cube in its centre as illustrated in fig. 3.1.

3.2 Numerical setup

In order to exactly match the thickness of the boundary layer of 0.184 when it hits the obstacle, the same formulation for the mean inlet velocity $u(y)$ is used as Saeedi et al.

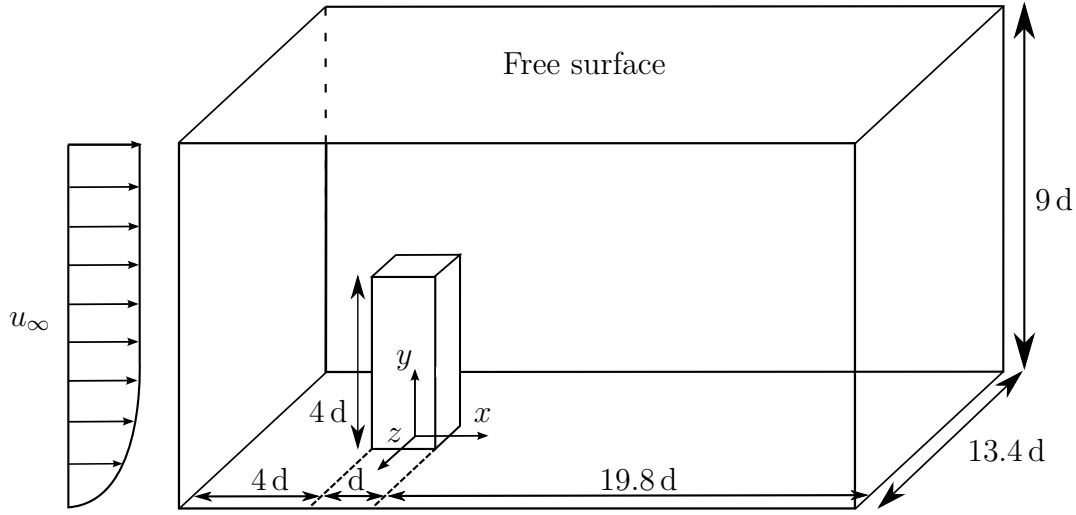


Figure 3.1: Computational domain of the validation case [104] (modified).

[104]

$$u(y) = \begin{cases} u_{\infty} \cdot \left(\frac{y}{0.15H_c}\right)^{0.16} & \text{for } y < 0.15H_c \\ u_{\infty} & \text{for } y \geq 0.15H_c \end{cases} \quad (3.1)$$

A synthetic turbulence generator is applied to the inlet plane using a turbulent intensity of 0.8% and a zero mean of the velocity fluctuations to reproduce equal turbulence structures as in the DNS simulations. The velocity fluctuations are added to the mean velocity profile of $u(y)$ at the inlet plane, as mentioned in chapter 2.3. In ANSYS Fluent two methods are implemented modelling fluctuating velocities at the inlet, the Vortex Method and the Spectral Synthesizer [10, 11]. Both of them are tested to study their influences on the results. The free surfaces are modelled as zero gradient boundary conditions, and a no-slip boundary condition is applied to all solid surfaces. The outlet plane is modelled as a pressure-outlet boundary condition. In the vortex method (VM) the number of vortices has to be defined a priori, but is not published by Saeedi et al. [104] and by Bourgeois et al. [29]. Thus, the value of 200 as the number of vortices is taken from a similar bluff body flow simulation performed by Mathey et al. [81]. In order to investigate the sensitivity of the vortex number, also 150 and 250 vortices considered. In contrast, the Spectral synthesizer method does neither require any additional input quantities nor a specific vortex number.

Pope [96] proposed that 80% of the turbulent scales in a flow have to be resolved in scale-resolving simulations. The cell size has to be determined carefully since it limits the minimal size of turbulent scales [40]. It determines the degree of modelled turbulent structures and influences the simulation accuracy [96].

The following approach to calculate the cell width in an LES grid is proposed by Pope [96]. According to Pope, 80% of the energy is contained in motions of length scales $1/6L_{11} < l < 6L_{11}$ where L_{11} is the longitudinal integral length scale. Regarding a

cumulative turbulent kinetic energy spectra, approximately 80 % of the energy is resolved in the range until $l_{\text{EI}} = 1/6L_{11}$ where l_{EI} is the demarcation length scale between the energy containing range of eddies ($l > l_{\text{EI}}$) and smaller eddies. Considering the Reynolds number of 12.000 in the validation case, the Taylor-scale Reynolds number Re_λ is 155, estimated from the relation

$$\text{Re}_\lambda \approx \sqrt{2\text{Re}}. \quad (3.2)$$

The ratio of L_{11}/L , wherein L is the turbulent length scale $L = k^{3/2}/\varepsilon$, depends on the Reynolds number of the model spectrum Re_λ , which is 155 in this case, and L_{11}/L is 0.51 [96]. For 80 % of the resolved turbulent kinetic energy, the product κL_{11} is 15 [96] where κ is the wave number. Considering the definition of the cut-off wave number

$$\kappa_c = \frac{\pi}{\Delta}, \quad (3.3)$$

the cell width is

$$\Delta_{0.80} = \frac{\pi}{\kappa_c} = \frac{\pi \cdot L_{11}}{15} = \frac{\pi \cdot 0.51L}{15} = 0.107L. \quad (3.4)$$

With $L = 0.009$ m obtained in a previous RANS simulation the cell width is 0.001 m for an 80 % resolution. In the simulation of the surface mounted cube, only tetragonal cells are used. This strongly simplifies the meshing process of urban domains including buildings, vegetation and terrain. The grid has a total number of 6.235.529 tetragonal cells. In comparison to that, the grid, which Saeedi et al. [104] used in their simulations, has 35.5 million cells. The boundary layer consists of 25 inflation layers with the first cell layer height of 0.0000175 m, fulfilling the requirement $y^+ = 1$ for an entirely resolved boundary layer at the wall, where y^+ is the normalized wall distance. The growth rate of the cells in the boundary layer towards the outer flow is 1.2. For a better comparison, the total runtime of the simulations is eight flow-through times which consists of two and a half times for stabilizing the flow and five and a half times for sampling unsteady statistics according to the times used by Saeedi et al. [104]. The time step is chosen according to the stability criteria of the Courant number $\text{Co} < 1$ [40, 111].

3.3 Results and validation

For the validation of the numerical setup, the flow around a surface mounted cube is simulated with different turbulence generators and DES turbulence models combined with various shielding functions. Regarding synthetic turbulence generation, the Spectral Synthesizer and the Vortex Method with 150, 200 and 250 vortices are applied. In the case no turbulence generation method is explicitly mentioned, the Spectral Synthesizer is used in the simulations. On the turbulence model side, the k - ω SST [84], the realizable k - ϵ [117] and the one-equation Spalart-Allmaras [120] turbulence model are used for the in-

vestigation. To study the effect of the shielding functions on the flow field, the following shielding functions are used in the validation study: DDES [121], IDDES [47, 118] and the Shielded Detached Eddy Simulation (SDES) [10, 11].

3.3.1 Turbulence model and shielding function

In fig. 3.2a the dimensionless time-averaged velocity in streamwise direction, located at $x/d = 3.5$ and $y/d = 3$ is plotted against the dimensionless z -axis. All evaluation lines are located in the wake behind the cube. The best agreement with the DNS simulations is achieved with the SDES and the IDDES model, while the velocities obtained with the first model are closer to the measured velocity at $z = 0$. The other turbulence models with the DDES shielding function, show an insufficient performance and underestimate the measured velocity by 0.3 at $z=0$. The models with the DDES shielding function predicted a wider and longer wake behind the cube which leads to a higher blockage and consequently to higher velocity peaks at the edge of the wake. Roy et al. [102] made a similar observation in their study. Herein, good agreements between LES simulations and experiments were achieved, while with RANS the recirculation zone was predicted too long. A thicker RANS boundary layer around the cube in the DDES shielding function could be an explanation for the longer recirculation zone. The deviation between the numerics and the experiments in the outer regions of the domain can be traced back to the slightly different domains and the higher blockage ratio in the simulations [104], as mentioned in the description of the experiment.

The $\overline{u'_x u'_z}$ element of the Reynolds stress tensor, evaluated along a line at $x/d = 3.5$ and $y/d = 3$, is shown in fig. 3.2b. The best agreement is obtained with the IDDES model. In the left peak in fig. 3.2b, the $\overline{u'_x u'_z}$ -stresses are almost identical to the DNS data. The DDES $k-\omega$ SST and the SDES models show an overshoot in the results, while the DDES $k-\epsilon$ realizable model basically struggles to resolve the turbulent fluctuations in the wake. The right peak in fig. 3.2b is over-predicted by almost all turbulence models except the DDES $k-\epsilon$ realizable model. With the Spalart-Allmaras and the $k-\epsilon$ realizable models the peak is narrower and is located more outside in spanwise direction.

In fig. 3.2c the time-averaged velocity u_x is plotted in downstream direction at $y/d = 1$ and $z = 0$. The best results compared to the DNS simulation are obtained with the DDES Spalart-Almaras and the IDDES model. Both turbulence models fail to predict the location of the negative peak velocity correctly. The recirculation zone is predicted to be shorter with the IDDES model, but longer with the DDES Spalart-Almaras model. However, with increasing distance to the cube the simulated velocity with the IDDES model is closer to the velocity in the DNS simulations than the velocity with the DDES Spalart-Almaras model.

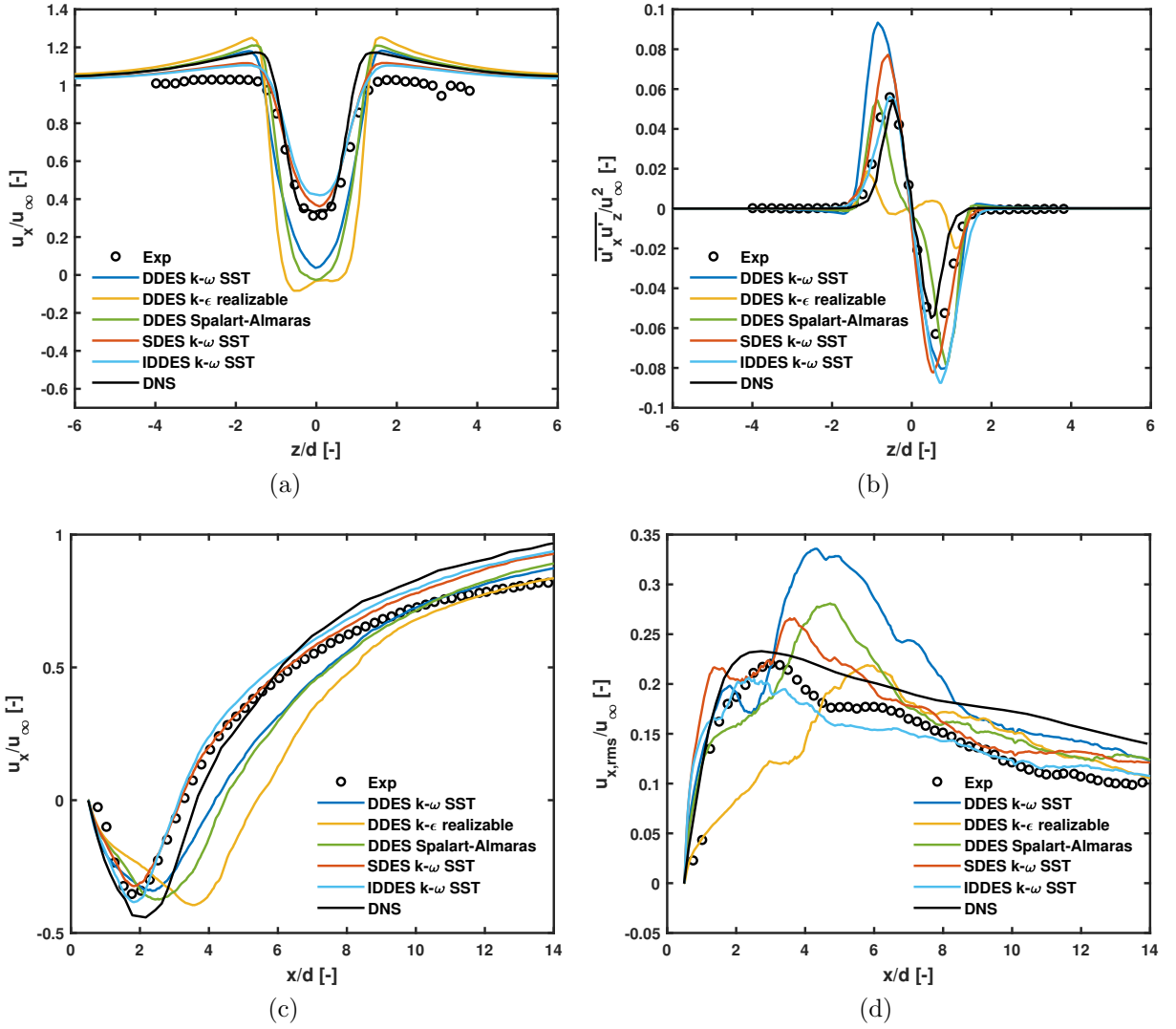


Figure 3.2: Time-averaged first- and second-order velocity profiles in x -direction and elements of the Reynolds stress tensor: (a) u_x/u_∞ at $x/d = 3.5$ and $y/d = 3$, (b) $\overline{u'_x u'_z}/u_\infty^2$ at $x/d = 3.5$ and $y/d = 3$, (c) u_x/u_∞ at $y/d = 1$ and $z = 0$, (d) $u_{x,rms}/u_\infty$ at $y/d = 1$ and $z = 0$ in comparison to the wind tunnel experiments by Bourgeois et al. [29] and the DNS simulations by Saeedi et al. [104].

Fig. 3.2d shows the dimensionless root mean square velocity in streamwise direction $u_{x,rms}$. The best qualitative and quantitative agreement with the DNS data is obtained with the IDDES model. The $u_{x,rms}$ values almost reach the maximal peak value and further decrease slightly towards the outlet with the same slope as in the DNS simulations. The DDES $k-\epsilon$ realizable model completely fails to predict the initial slope of $u_{x,rms}$ behind the cube currently due to the over-prediction of the length of the recirculation zone which is also confirmed by the streamwise velocity distribution in fig. 3.2c. In the simulation with the DDES $k-\omega$ SST model, the maximum value of $u_{x,rms}$ is over-estimated by 50% and by 25% with the SDES and the DDES Spalart-Allmaras model. The peak of $u_{x,rms}$ in fig. 3.2d indicates the reunion of the flow which is separated by the cube after the recirculation zone. The location of the peak is moved downstream using the turbulence

models with the DDES shielding functions. The value of $u_{x,rms}$ at the outlet is quite similar independently of the used turbulence models.

To analyse the entire vortex structure in the domain, the vortices are visualized using iso-surfaces of the λ_2 -criterion for the DDES (in fig. 3.3) and the IDDES shielding function (in fig. 3.4) with the same $k-\omega$ SST turbulence model. The λ_2 -criterion was developed by Jeong and Hussain [63] and is a method to visualize vortex structures from a three-dimensional velocity field. The variable λ_2 defines the second eigenvalue of the tensor $\mathbf{S}^2 + \mathbf{\Omega}^2$, where \mathbf{S} and $\mathbf{\Omega}$ are the symmetric and antisymmetric tensor of the velocity gradient, respectively.

In the figs. 3.3 and 3.4, the horseshoe vortex is a characteristic vortex which is formed

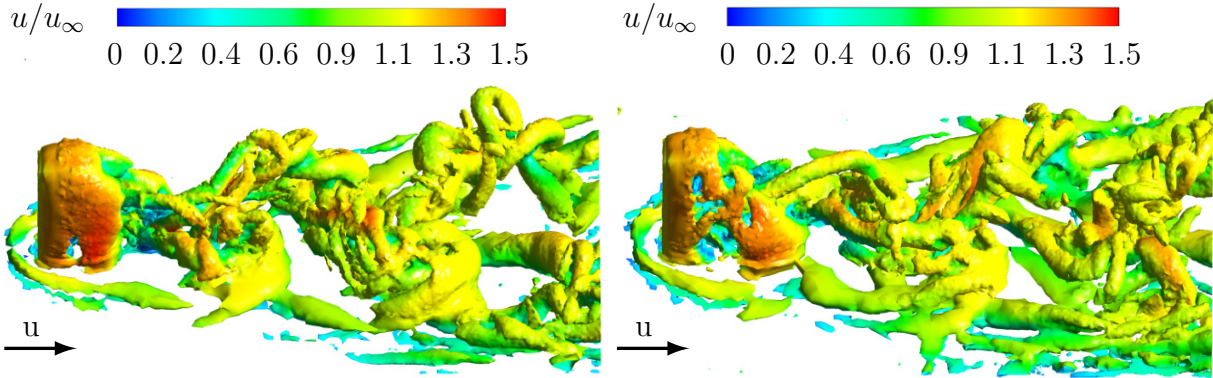


Figure 3.3: Iso-surface of λ_2 for the DDES shielding function.

Figure 3.4: Iso-surface of λ_2 for the IDDES shielding function.

near a surface mounted cube at the ground wall [58]. It is generated by the backflow of the flow which hits the wall pointing against the streamwise direction and the flow which passes the cube at its sidewalls. The flow in front of the cylinder is subjected to a pressure increase. As a result, the boundary layer in front of the cylinder detaches immediately from the bottom and rolls up into a vortex, which wraps around the cylinder like a horseshoe [58]. In the IDDES simulation, the horseshoe vortex is developed more precisely.

The IDDES model is more capable to resolve finer turbulent structures which is especially visible in the downstream part of the flow and in the boundary layer near the ground wall. The vortices in the separation zones near the cube show more detailed structures and finer resolved eddies in the IDDES simulation, since the IDDES model includes wall-modelled LES capabilities in the near wall regions and provides better shielding against the LES fallback into the RANS modelled boundary layer. For more detailed information about the IDDES model it is referred to the literature [47, 118].

3.3.2 Turbulence generation method

In this subchapter the bluff body flow is simulated with different synthetic turbulence generation methods which is crucial to represent the atmospheric turbulence in scale resolving simulations at the inlet [116]. These simulations are performed with the DDES $k-\omega$ SST turbulence model using the same grid. In fig. 3.5a the dimensionless time-averaged velocity in streamwise direction, located at $x/d = 3.5$ and $y/d = 3$ is plotted over the dimensionless z -axis. A qualitative agreement with the experimental data and the DNS data is obtained with all turbulence generators, but they under-estimate the negative peak velocity. A higher number of vortices applied at the inlet plane in the VM leads to lower velocities and a wider recirculation zone behind the cube as shown in fig. 3.5a. Since the size of the inflow area is constant and all vortices are distributed equally over the area, a higher vortex number leads to smaller generated eddies which dissipate faster with lower fluctuations in downstream direction. If these fluctuations are too small to be resolved by the LES near the boundary layer, this part is likely to be modelled in RANS. The lower fluctuations correlated with increasing vortex numbers are also observed in the $\overline{u'_x u'_z}$ -stresses in fig. 3.5b. When 200 vortices are applied, the peak values are predicted the best while the Spectral Synthesizer and the VM with 150 vortices show 50% higher stresses. When 250 vortices are applied, around 50% lower values correlating with thinner peaks are obtained which is a sign for smaller developed horseshoe vortices.

In fig. 3.5c the time-averaged velocity u_x is plotted in downstream direction at $y/d = 1$ and $z = 0$. Although none of the turbulence models reaches the negative peak value of the DNS simulations, the best agreement with DNS data is obtained with the VM and 150 vortices followed by the Spectral Synthesizer. Independent of the turbulence generator, the negative velocity of the peak is obtained as in the experiments. However, the number of vortices in the VM increases the length of the recirculation zone from $x/d = 1.9$ to $x/d = 3.0$. Due to the lower turbulent structures as shown in fig. 3.5b, the recirculation zone is wider developed and the two separated flows need a longer distance to reunite behind the wake. Fig. 3.5d shows the dimensionless root mean square velocity in streamwise direction $u_{x,\text{rms}}$ and illustrates also the differences in simulated wake lengths. The maximum value is over-predicted in all simulations, especially when the Spectral Synthesizer and the VM with 150 vortices are used. All simulations with the VM reaches the value as in the DNS simulations at $x/d = 6.5$ while the Spectral Synthesizer reaches the value at $x/d = 8$. The initial slope of $u_{x,\text{rms}}$ is best captured in the simulations with the lowest number in the VM, whereas the peak slope in the other simulations is interrupted by a wavelike behaviour before the peak.

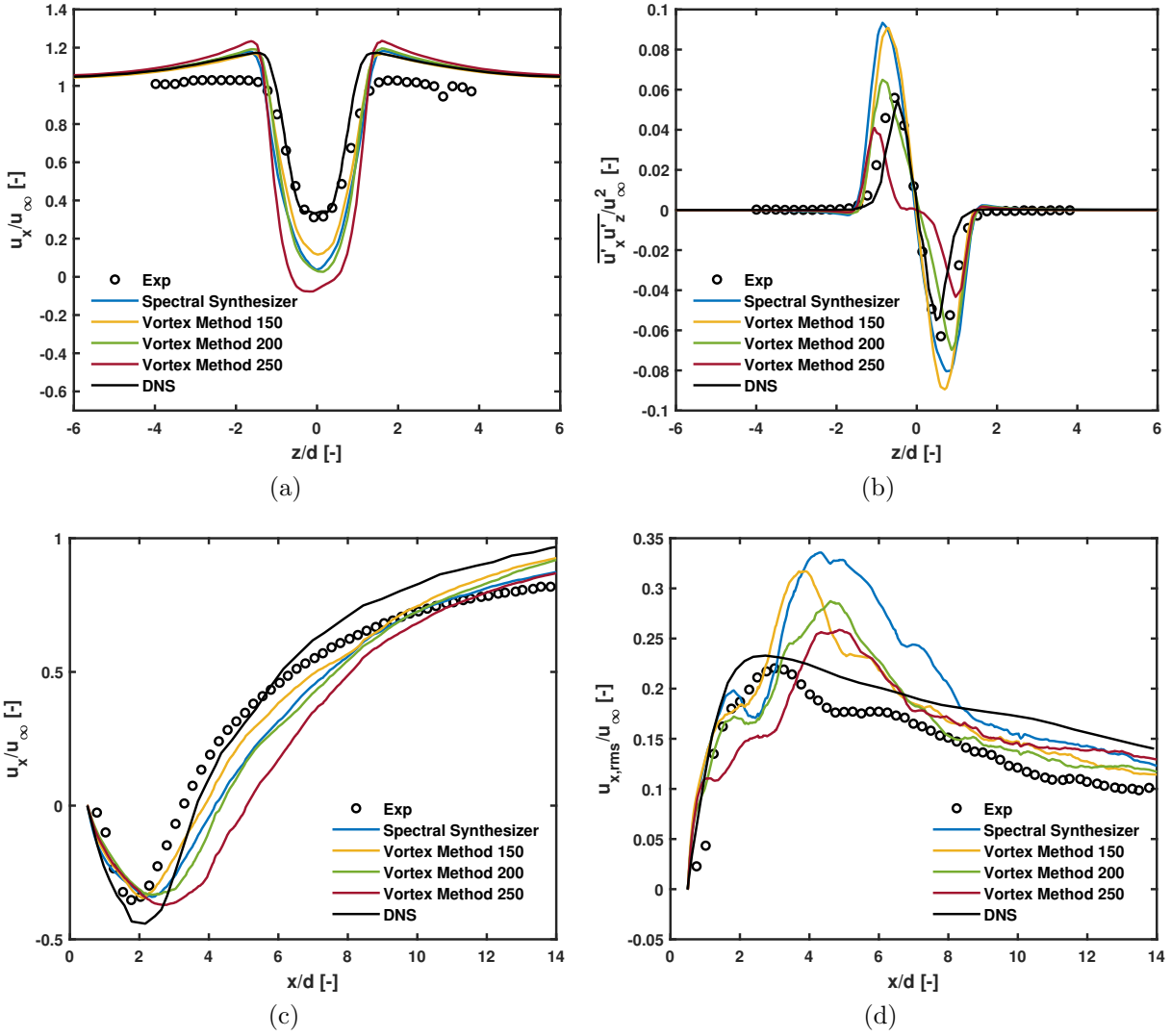


Figure 3.5: Time-averaged first- and second-order velocity profiles in x -direction and elements of the Reynolds stress tensor: (a) u_x/u_∞ at $x/d = 3.5$ and $y/d = 3$, (b) $\overline{u'_x u'_z} / u_\infty^2$ at $x/d = 3.5$ and $y/d = 3$, (c) u_x/u_∞ at $y/d = 1$ and $z = 0$, (d) $u_{x,rms}/u_\infty$ at $y/d = 1$ and $z = 0$ in comparison to the wind tunnel experiments by Bourgeois et al. [29] and the DNS simulations by Saeedi et al. [104].

3.4 Summary

Several variants of the numerical setup using different turbulence models, shielding functions and synthetic turbulence generators have been simulated and validated in simulations of a surface mounted cube in a boundary flow. The numerical results have been compared with wind tunnel data by Bourgeois et al. [29], and DNS simulations by Saeedi et al. [104]. The results have shown the importance to choose the shielding functions and the turbulence models properly. The shielding function has a large influence on the time-averaged velocity and the dimensions of the recirculation zone because the shielding function prevents that the LES falls back into the RANS modelled boundary layer where the grid is too coarse to sufficiently resolve velocity fluctuations for LES.

Regarding turbulence models, the best results are obtained with the $k-\omega$ SST turbulence model and the IDDES shielding function. The validation study also indicates the dependency of the number of vortices in the VM which are applied at the inflow plane. Due to the constant size of the inflow area, more vortices lead to smaller turbulent structures which dissipate faster in the flow and increase the size of the recirculation zone behind the cube.

Further simulations will be performed with the combination of the IDDES shielding function and the $k-\omega$ SST turbulence model, since it shows the best agreement with the DNS data. In the turbulence generation category, the VM performed the best and is chosen for future numerical setups. The number of vortices have to be adapted to the atmospheric boundary layer for urban wind flow.

4 Geometry Preparation and Meshing for Urban Simulations

The domain for the urban wind field simulations contains building geometries, complex terrain and vegetation. The building geometries in the area of interest are based on a CityGML model. They are prepared and optimized for CFD simulations and used as solid bodies. The buildings surrounding the buildings in the area of interest are represented by a new model which is based on a volume resistance force and modelled as a source term. The vegetation model by Shaw and Schumann [115] is adapted to include local tree heights for a better representation of the vegetation. Finally, the mesh properties which are used to mesh the urban domain are described.

The 3D building geometry of the urban site is based on a CityGML model. The availability of these city models has been strongly increased over the last years, e.g. they are provided in whole Germany [49] or in selected cities as Helsinki [103], Vienna [71] and Zürich [113]. These models are not suitable for CFD simulations due to geometrical errors, e.g. leaky geometries, misalignments, small overlapping buildings etc. This can lead to distorted cells and expensive meshing processes. Depending on the problem statement, a more detailed geometry does not always improve the results. Lee et al. [70] investigated the impact of the geometric details in a heat flux simulation. Herein, the consideration of balconies and windows did not improve the simulation results, they just increased the computational time. However, balconies on the building facade can change the wind flow and the pressure distribution on building surfaces and can improve the results, as in the study of Monatazeri et al. [89]. Also the roof type can change the wind flow drastically and also affect the prediction of the energy yield [9].

The optimization of a CityGML based geometry requires mainly manual work which is based on personal experience and know-how of a user. Saeedraashed et al. [105] compared software tools for the validation and healing process. Due to the high complexity of the validation and healing workflow, no fully automated solution is available to handle 3D buildings data with all types of errors and defects. It still requires a lot of manual work. Pieperit et al. [93, 94] developed a sweep plane algorithm to simplify city models automatically. It eliminates the edges which are smaller than a given threshold value, e.g. windows, balconies, roof overhangs and chimneys. The definition of a prepared building

relates to the problem statement to be investigated and the zone of interest. Thus, the level of detail can even change within a domain and still requires manual effort. Deininger et al. used the sweep plane algorithm for a continuous semi-automated workflow to accelerate the preparation process by 85% compared to pure manual work. Additionally, this leads to a simplified meshing process and better computational meshes [35].

Surrounding buildings can have a considerable impact on the wind flow near the target buildings, wherein the impact depends on the height and the layout of the surrounding buildings [147]. A minimal radius of $3H_{b,\max}$ of detailed building geometries have to be considered in the simulations, where $H_{b,\max}$ is the maximum building height in the domain [76]. Tong et al. [132] proposed that a sufficient amount of buildings near the target building has to be included in the domain for an accurate prediction of the urban ventilation. They recommended three layers of surrounding buildings for regular street canyons or two layers for wide street canyons. The downstream buildings do not have to be represented in the domain due to low impacts on the upstream flow [132]. In these studies, the complex terrain is not included. Since surrounding buildings and complex terrain can have a considerable impact on the wind flow, a site depending study has to be performed.

Furthermore, the vegetation can have an additional impact on the local wind field [73]. Mohamed et al. [87] recommended to consider even smaller vegetation objects, such as hedges or bushes, in the wind flow simulation. Basically, vegetation models can be distinguished in canopy and roughness models. In canopy models, the vegetation is represented by a resistance force and added as a source term to the governing equations [115]. Better results are obtained with the canopy model, while the roughness model just slightly changes the wind flow [106]. The canopy models are categorized depending to which equation the source term is added: the momentum equation [62, 115], the conservation equation for k [55, 90] or the equation for the turbulent dissipation rate [48, 85]. In this work the source term is added to the momentum equation.

4.1 Site information

The campus Morgenstelle of the University of Tübingen (Germany) is chosen as a test site in this work for on-site validation and to investigate the potential of small wind turbines. The campus is located on a hill with mostly box-shaped high-rise buildings with a maximum height of 50 m. The campus is surrounded by smaller forested zones and a large forested zone on the west side. Residential areas are located on the eastern and southern side. Fig. 4.1 shows a model of the campus site with terrain and real building geometries. The iso-lines at the ground represent the different heights of the terrain with a maximum difference in altitude of 115 m, thus it is crucial to include the terrain in the simulations. The building geometry and the terrain are provided by the Landesamt für

Geoinformation und Landentwicklung (LGL) (State Agency for Spatial Information and Rural Development) Baden-Württemberg. The CityGML model (also called "city model" in the following) contains an LoD2 (Level of Detail) geometry which means that buildings are extruded from their ground area and include their original type of roof. The city model of the campus site includes 300 buildings and building parts. The area of interest contains only 25 buildings. The main wind direction is from south-west with a frequency of more than 40 % and a mean annual wind speed of 2.1 m/s [3].

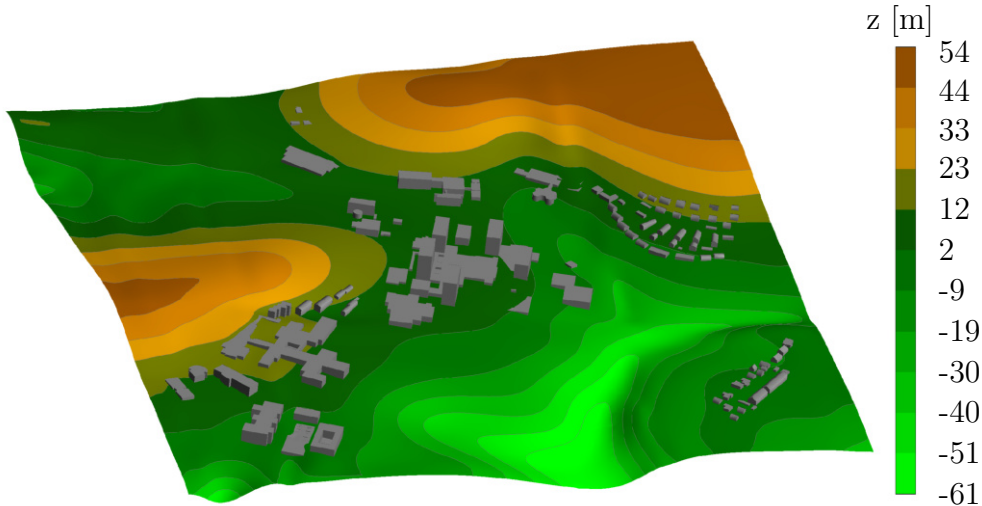


Figure 4.1: Model of the campus Morgenstelle of the University of Tübingen (Germany). Relative height (z) of the complex terrain with all buildings included.

4.2 Building preparation

The use of city models for urban CFD simulations requires a couple of preprocessing steps which are explained in the following subchapter. Since CFD software programs need CAD data formats, the CityGML file has to be converted into a CAD data format at first. The CityDoctor tool [138] sufficiently converts CityGML based geometries into solid CAD geometries and removes typical geometrical failures such as gaps between surfaces, detached surfaces, duplicated points, non-planar and overlapping polygons in the CityGML geometries[35].

In the present study, the CityDoctor tool is first applied to convert the CityGML geometry to solid bodies. In a next step, building geometries are optimized for CFD simulations to ensure high quality meshing and to avoid grid induced unphysical results. In the building geometry, all details and edges smaller than 0.2 m are consequently removed and incoherent surfaces are merged to solid volume bodies. Fig 4.2 shows the final optimized buildings which are used in the simulations and some examples of how the geometries are simplified. The buildings in green show the original geometries in comparison to the final geometries in blue. In example A, the jutting on the lateral surface is removed, since a low

impact on the flow is assumed. The jutting would just rise the required number of cells for a sufficient meshing. The roof height of building B is levelled for an equal roof height. A typical defect in city models is that one surface is split into two single planar surfaces as in case C which have to be merged. This reduces complexity and reduces the meshing effort since the numerical cells are always aligned to the edge of a surface in the meshing process. Case D shows a typical example of how a building is simplified, that means removing small details, gaps and corner offsets. Many residential buildings are equipped with balconies encapsulated by two vertical walls. But as shown in example E, unlike the two vertical walls the balconies are not included in LoD2 geometries. The walls are removed in the optimization process because otherwise many tiny cells are required to resolve the turbulence generated by the walls. A similar case, recessed balconies in residential houses, is illustrated in example F. These notches are filled up to ensure continuous surfaces. A characteristic feature in city models is the representation of curved surfaces by a large number of connected narrow polygons. The meshing of these polygons would drastically increase the number of cells because in the meshing process the cells are aligned to the edges of these polygons. Thus, these walls have to be manually replaced by a curved surface as shown in case G.

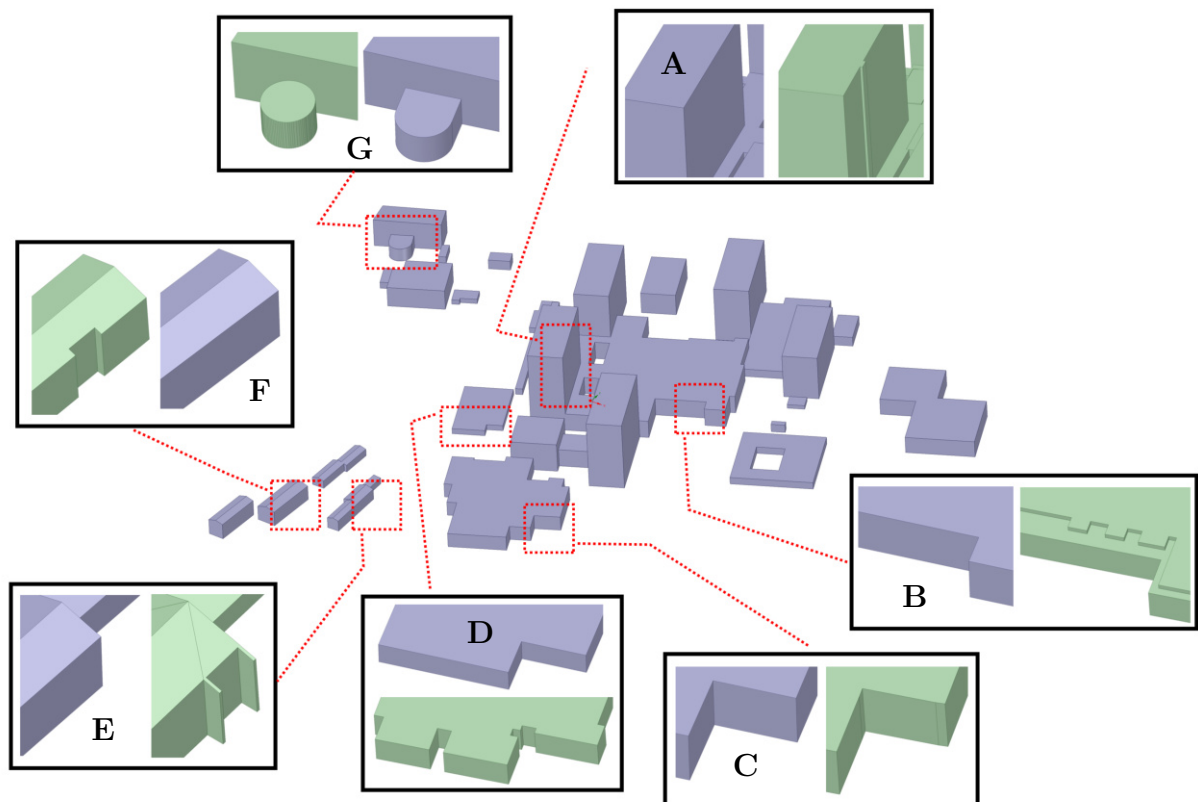


Figure 4.2: Optimized building geometries (blue) and original geometries (green).

4.3 Terrain modelling

The terrain data is provided by the LGL as a point cloud and is not included in the building model. The spatial resolution of the terrain is 1 m. The terrain is approximated by existing CityGML TIN elements. The abbreviation TIN stands for triangulated irregular network. In this work, the terrain point cloud is thinned out and triangulated again with a surface tolerance of 2 m. Afterwards, the terrain is modelled with a free-form surface which just captures the main characteristic elements of the terrain. That reduces the meshing effort and avoids distorted cells with high aspect ratio in the boundary layer. The terrain surface is matched with the building model based on the geo-reference of the coordinate systems of the terrain surface and the building model.

4.4 Vegetation modelling details

The following subchapter is extracted from a previous publication of von der Grün et al. [50] and partially modified .

Regarding the main wind direction, the inflow region towards the buildings is mainly covered with a forested zone. To include forested zones in the simulation, a vegetation model based on the approach of Shaw and Schumann [115] is added to the solver. That enables the implementation of any kind of forest structure in the simulations. The model is specified by source terms in a spatially porous media which are added to the momentum equation of the Navier-Stokes equations. The volume force for the source terms in i -direction represent the drag caused by the forest. The force is defined by

$$F_{w,i}(z) = -\rho c_d a(z) |u| u_i, \quad (4.1)$$

where $i = 1, 2, 3$, ρ is the density and c_d is the drag coefficient which is set to 0.15 [115]. The variable $|u|$ describes the velocity magnitude and u_i the velocity component in i -direction. The height-depending function $a(z)$ represents the drag induced by the local foliage density of the trees leading to different velocity profiles within the forested zone and in the wake behind the trees. As a consequence, the source term $F_{w,i}(z)$ is also depending on the height z . The Leaf Area Index (LAI) describes the forest density and is defined by

$$\text{LAI} = \int_0^{H_t} a(z) dz, \quad (4.2)$$

where H_t is the height of trees or of any kind of vegetation, respectively. That means that every tree species has its own LAI according to its degree of foliation and its own

a -profile. Fig. 4.3 shows profiles for different values of LAI where LAI=2 represents a sparsely covered forest canopy and LAI=5 a very dense forest canopy in summer. Here, the LAI is given and the qualitative profile shape of a . The forest in the inflow region at the test site in Tübingen is a mixed forest with 56 % conifers and 44 % deciduous trees. The averaged LAI value according to this ratio is 3 which is taken for the simulation and the associated profile of a is shown as the red line in fig. 4.3. Bequet et al. [23] investigated the seasonal variation of LAI over the year for oaks and peaches which is shown for oaks in fig. 4.4. According to that study the LAI of oaks changes from 0.7 during the winter time to 2.7 in the summer time and that of peaches from 0.6 to 3.5 over the year [23]. However, for spruce and pines the seasonal LAI variation remains quite constant at 6 and 3, respectively [44]. For a detailed prediction of the (seasonal) wind flow, the proper LAI has to be considered in the vegetation model.

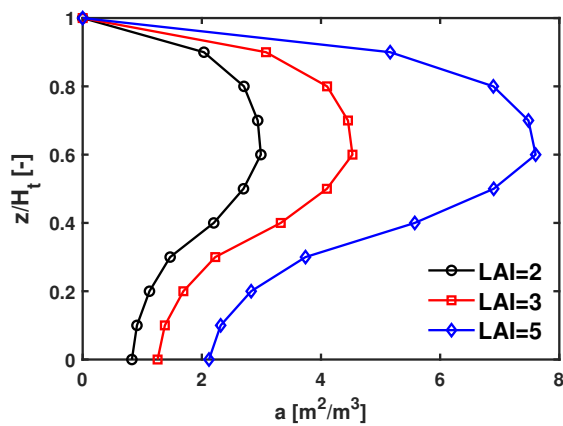


Figure 4.3: Profiles of a over the dimensionless tree height H_t for different LAI, based on [115].

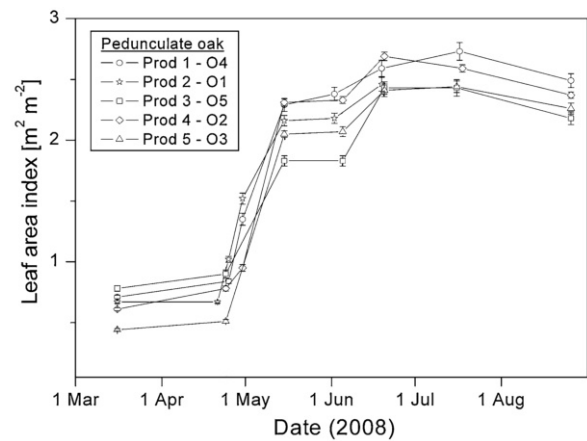


Figure 4.4: Seasonal LAI-values for pedunculate oaks in different vegetation times [23] (modified).

The coordinates of the forested zones are obtained from OpenStreetMap data and directly projected onto the terrain. The coordinates were used to generate 3D forest volume bodies which are highlighted in dark green in fig 4.5. The vegetation model is only activated in these bodies. The local tree height of the forest is obtained from Laser scan data from the LGL. The Laser scan point cloud is split up into vegetation and ground marks which are divided into 10 m x 10 m tiles. The values within one tile are averaged and the mean values are fed into the simulation. Fig. 4.6 shows the location of the forest and the distribution of the local tree height H_t which are used in the simulations. It shows a large deviation of H_t in the forested zones.

Influence of local tree heights

The tree height in a forest is not equal. But when vegetation is considered in urban or rural wind field simulations, usually one uniform tree height is set in the vegetation

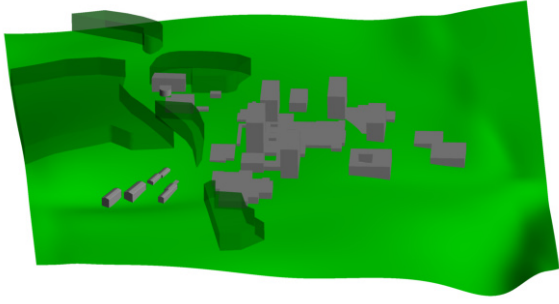


Figure 4.5: Forested zones (dark green) in the computational model.

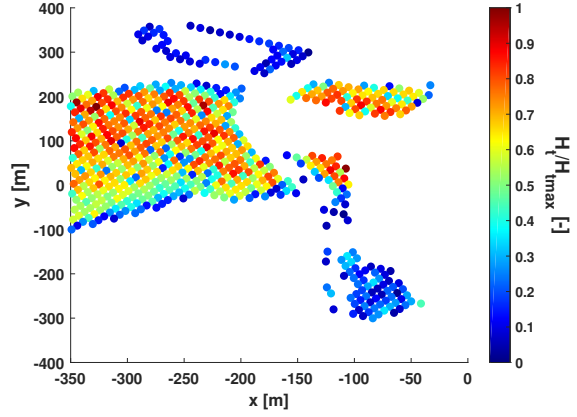


Figure 4.6: Local dimensionless tree heights in the domain.

model. In this subchapter, the difference of local tree heights compared to a uniform tree height is investigated. A parameter to describe the variation in local tree heights is the standard deviation σ . For that, a generic forested zone is generated in a box ($700 \text{ m} \times 175 \text{ m} \times 200 \text{ m}$ in length, width and height) and simulated in a boundary layer flow, wherein the ground wall of the box is covered with the forested zone. The forested zone is simulated with different standard deviations of the tree heights which is $\sigma/H_{t,av}$ is 0 (uniform tree height), 0.05, 0.1 and 0.15. The average tree height $H_{t,av}$ amounts to 20 m which corresponds to the main forest on the test site in Tübingen.

The simulations are performed with the IDDES $k-\omega$ SST turbulence model, described in chapter 2.2. To consider the atmospheric turbulence, synthetic turbulence is generated by the VM. Since the wall is totally covered with forest, the velocity inlet boundary condition for forests is taken according to Niemann et al. [91]. They assumed that the wind speed within forests is quite low. Therefore, the zero point of the wind profile can be shifted upwards by a so-called offset height. Niemann et al. specified an offset height of $0.9 H_{t,av}$ for forests so that the following velocity power law starts at $0.9 H_{t,av}$:

$$u(z) = \begin{cases} 0 & \text{for } z < 0.9 H_{t,av} \\ 2.95 \text{ m/s} \cdot \left(\frac{z-0.9H_{t,av}}{10 \text{ m}-0.9H_{t,av}} \right)^{0.21} & \text{for } z \geq 0.9 H_{t,av} \end{cases} \quad (4.3)$$

The forest is artificially generated with the assumption that the tree heights are Gaussian distributed. Fig 4.7 shows the distribution of the artificially generated tree heights and the Gaussian probability density functions (pdf) according to their σ . For comparison, the real distribution of the forested zones in Tübingen, which seems to be log-normal distributed, is also presented in fig 4.7.

The time-averaged velocity magnitude $|\bar{u}|$ (fig. 4.8) and the turbulent kinetic energy (fig. 4.9) are plotted over the dimensionless standard deviation $\sigma/H_{t,av}$ for different heights $z/H_{t,av}$. The values of $|\bar{u}|$ and k are spatially averaged in the last 100 m of the computa-

tional domain since these values are expected to represent the most steady-state values. The values in fig. 4.8 and k 4.9 are normalized with the values obtained for a zero standard deviation σ_0 . Both figures show a strong dependency of the tree height variation σ . Especially at $z/H_{t,av}=1$, the velocity is strongly reduced, e.g. for $\sigma/H_{t,av}=0.15$ it decreases by 50%. Even for smaller σ , the speed is decreased by 15%. At $z/H_{t,av}=2$, the difference between local tree heights and a uniform tree height is not noticeable.

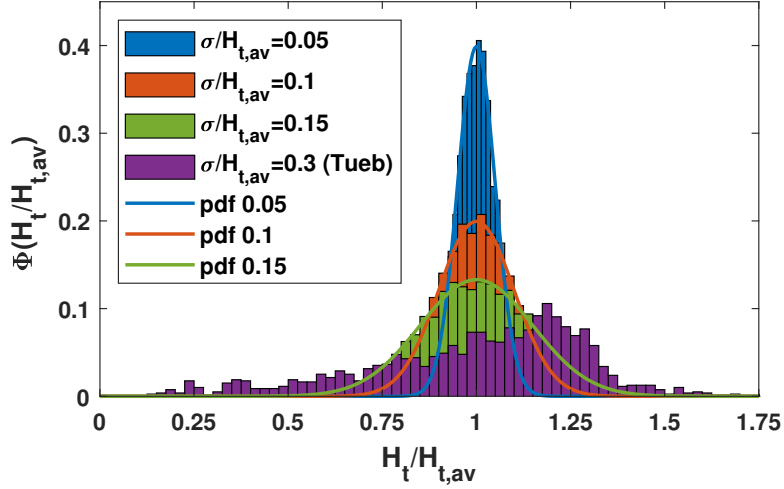


Figure 4.7: Probability density functions and tree height distributions for $\sigma/H_{t,av} = 0.05, 0.1, 0.15$ and the local forested zone in Tübingen.

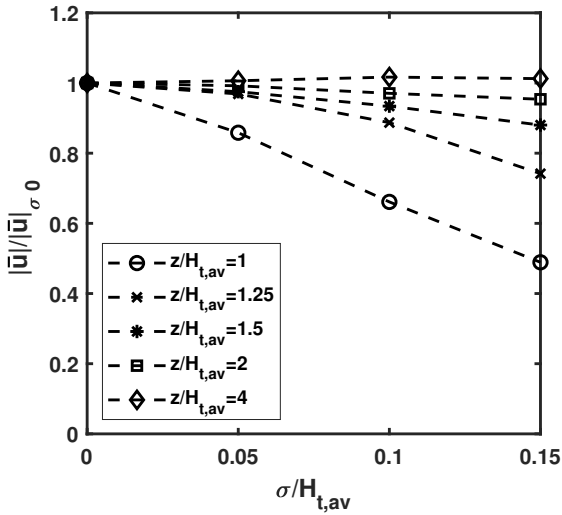


Figure 4.8: Influence of the local tree height standard deviation σ on $|\bar{u}|$ for different distances ($z/H_{t,av}$) to the ground.

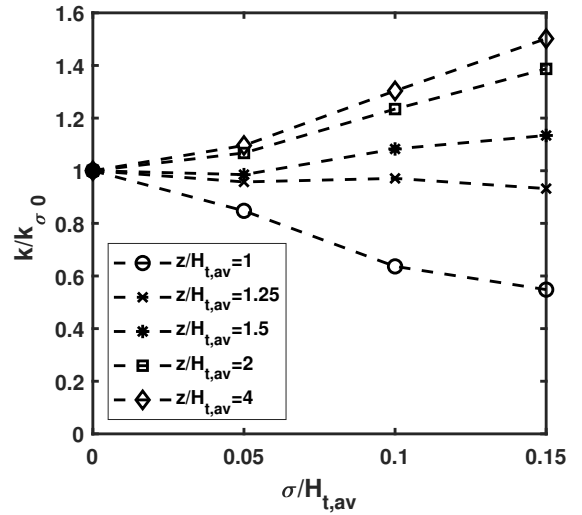


Figure 4.9: Influence of the local tree height standard deviation σ on k for different distances ($z/H_{t,av}$) to the ground.

But at $z/H_{t,av}=4$ a small increase in $|\bar{u}|$ is observed for strong tree height variations due to a higher blockage of the flow by the trees using local tree heights. The distribution of k shows an ambivalent behaviour. Below $z/H_{t,av}=1.25$ the turbulent kinetic energy

decreases, while above $z/H_{t,av}=1.25$ k strongly increases. A zone with increased k values is generated above the forest, as observed in higher $z/H_{t,av}$ -values. This phenomenon is also confirmed by Letzgus et al. [73] and Adipe et al. [15]. With an increasing standard variation of the tree height, the surface representing the top of the forested zone is getting rougher and consequently generates more turbulence and leads to higher k values. For $z/H_{t,av}$ smaller than 1.25 k is decreased by 40% for $\sigma/H_{t,av}=0.15$. In this zone the velocity fluctuations are damped more and more by the forest. The threshold value of $z/H_{t,av}=1.25$ for k can be explained by the fact that only a few trees in the forest are higher than the threshold value as shown in fig 4.9.

In this subchapter the implementation of the vegetation model of Shaw and Schumann in ANSYS Fluent is explained and how vegetation zones are defined. The vegetation model is extended by a local tree height adaption. In simulations with a generic forest it was shown that the further above the forest, the lower the influence of the standard deviation on u and k .

4.5 Modelling of surrounding buildings

As mentioned in chapter 1.1, buildings outside the target zone can influence the flow. The influence has to be investigated for each site individually, since layout, type and height of buildings may be different at each site. When more surrounding buildings are considered in the simulations, the flow towards the target zone becomes more realistic, leading to more precise results and a better energy yield prediction. Since the wind energy yield depends on the velocity in the third power, an error of 10% in the velocity means an error of 33% in the prediction of the power output of the wind turbine. The question is, whether the additional effort to preprocess the building geometries is worth it. Including more buildings in the domain increases the preprocessing effort including complex meshing and makes simulations more expensive. Thus, a new building model is developed which represents buildings not by real solid body geometries but by a resistance force, similar to the vegetation model. The methodology and the validation of the building model with IDDES simulations are presented in this subchapter.

The inner volumes of the buildings are entirely meshed and represented by an indicator function. A value larger than zero means, the cell is inside the building and a value of zero means, the cell is outside the building. Considering equ. 4.1, the volume force in i -direction for $i = 1, 2, 3$ makes sure that the flow passes around the building and not through it. The force is defined by

$$F_{b,i} = -\rho c_r |u| u_i. \quad (4.4)$$

Herein, the resistance in the vegetation is replaced by one resistance coefficient c_r . This value represents the flow resistance inside the buildings and consequently the value has to be artificially high to prevent the flow from penetrating the building. Its validation and the influence on the flow are described later on. The volume forces $F_{b,i}$ are added as source terms to the momentum equation, as in the vegetation model.

To define the buildings, OpenStreetMap data and the point cloud from LGL as used in the vegetation model are required. The point cloud contains ground marks and surface marks of vegetation, buildings and other urban elements. The OpenStreetMap data includes positions of buildings, vegetation, streets etc. The data is used to extract the points associated to buildings. The extracted point cloud is processed similar to the vegetation model process: the point cloud is divided into tiles with a predefined raster width w . The building heights are averaged within each tile and are fed into the simulations. The determination if a numerical cell is part of a building is shown in a schematic view of a mesh for a 2D case in fig 4.10. The red crosses are central coordinates of each tile with the

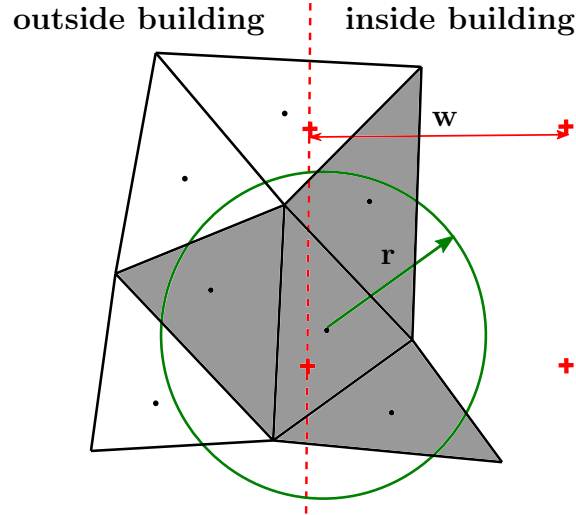


Figure 4.10: Schematic view of a mesh to check, if the cell is inside the building: A red cross must be captured by the green circle with radius r .

raster width w . The red dotted line marks the boundary of the building, the right part of the plane is inside the building and the left is outside. In a next step, the building heights stored in the extracted point cloud are interpolated on the numerical cells. This step also includes the indication which numerical cell is inside the building. The interpolation is based on the shortest distance method between the numerical cell centre and the raster cells. Herein, a radius r is defined by

$$r = \sqrt{2} \frac{w}{2}. \quad (4.5)$$

Hence, all numerical cells inside the circle with the radius r , that contains a red cross, are identified as inside the buildings. These cells are marked in grey in fig. 4.10. If the raster width w is chosen too high, less building details are resolved, and the building size

is artificially increased. The resolution of the building details in the simulations is further affected by the numerical cell size. Using a smaller radius r , not all building data (red crosses) can be captured so that the algorithm falsely associate the cell to „outside the building“.

Validation and influence studies

For the validation and determination of c_r the flow around a single high-rise building is simulated. The size of the bounding box is $248\text{ m} \times 120\text{ m} \times 90\text{ m}$ with the building size of $30\text{ m} \times 10\text{ m} \times 20\text{ m}$ in length, width and height, respectively. The length of the domain is divided into an upwind length L_u of 55 m , which is the distance from the inlet to the centre of the building, and a downwind length L_d of 193 m which is the length of the centre of the building to the outlet. The building is streamed in x -direction by a boundary layer flow with the following inlet velocity profile

$$u(z) = u_{\text{ref}} \cdot \left(\frac{z}{10\text{ m}} \right)^{0.21}, \quad (4.6)$$

where u_{ref} is 2.95 m/s . All solid walls are modelled with a zero velocity boundary condition and all free surfaces with a zero gradient boundary condition. Since the IDDES with the $k-\omega$ SST turbulence model is chosen, the atmospheric turbulence is synthetically generated by the VM at the inlet plane. The simulations with the modelled building are all compared to the solid body simulation as a reference. Herein, the influence of various c_r and various w are investigated.

To demonstrate the influence of different c_r values, the results of the simulations with

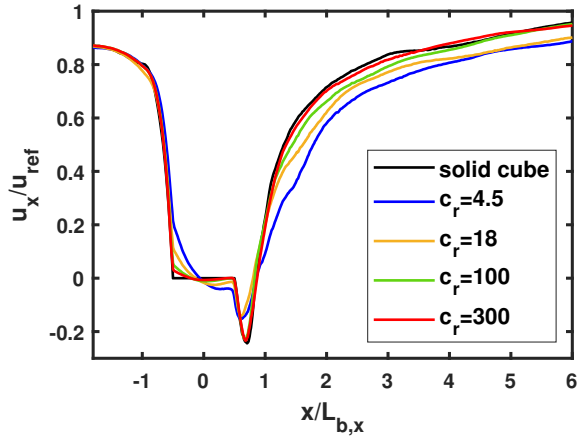


Figure 4.11: Time-averaged streamwise velocity with different c_r .

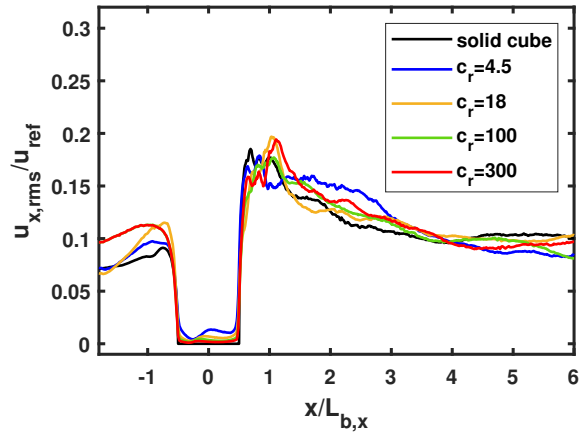


Figure 4.12: Time-averaged streamwise rms velocity $u_{x,\text{rms}}$ with different c_r .

c_r values of 4.5, 18, 100 and 300 are shown. Higher values led to convergence issues. The raster width is $w/L_{b,x} = 0.0275$ and r is 0.58 m according to equ. 4.5. The time-averaged velocity is plotted in x -direction in fig 4.11, where $L_{b,x}$ is the length of the building in

x -direction. The z -value of the evaluation line is 0 m and the y -value is 10 m, thus it is behind the centre of the cube. It shows a strong dependency on the resistance coefficient. With lower c_r values the flow needs a longer distance to decelerate, once it hits the cube. The length of the wake decreases with higher c_r and the corners of the building are more defined. That leads to more sharply bent streamlines around the edges, smaller reattachment lengths and shorter wakes. The negative velocities within the modelled cube are obtained with the lowest c_r value as a result of weak surface walls, since the recirculation zone enters the cube at its backside. With a c_r of 300 a good agreement is achieved in comparison with the results of the solid body simulation. The difference between 100 and 300 is almost negligible but still better than 100, so it is assumed that higher c_r values do not lead to better results. Thus, the value of 300 is sufficient and c_r is set to 300 in this work. A comparison of $u_{x,rms}$ in fig. 4.12 shows a good agreement with the solid body results. In the simulation with the highest c_r value, the velocity fluctuations are damped to zero within the cube. In the wake the maximum value of $u_{x,rms}$ is reached in all simulations, followed by an over-prediction when c_r is 4.5. The effect of a raster width w that is too coarse and a corresponding large radius r is illustrated in fig 4.13. According to equ. 4.5 the radius has to be increased for a larger w , otherwise not all cells can be captured by the radius properly. Due to that, the building size is artificially increased which is indicated by the displacement of the curve using $w/L_{b,x}=0.151$. The displacement is exactly the increased radius in front and behind the building. Another simulation failure can occur, when the radius r is chosen too small. Not all numerical cells inside the building are marked as a building, thus the flow infiltrates the cube, indicated by the black arrows in fig 4.14. The velocity field shows a dot pattern, which is caused by circles due to a small radius, and the building becomes more porous.

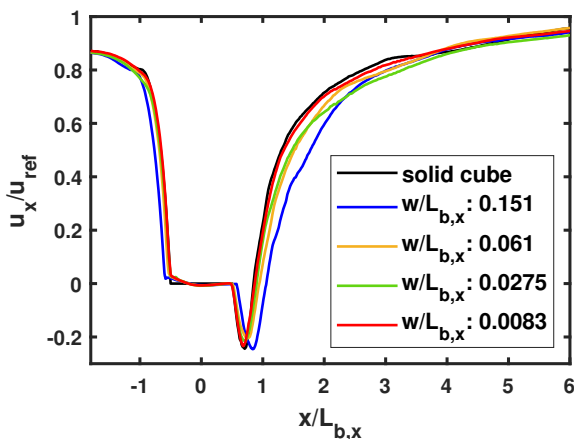


Figure 4.13: Streamwise velocity with different raster widths w and corresponding r .

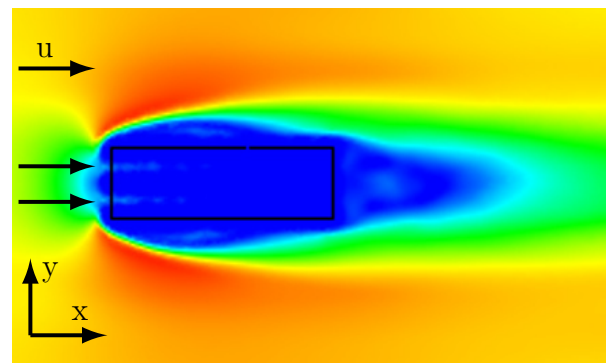


Figure 4.14: Velocity cross section: the flow infiltrates the cube at the black arrows because r is chosen too small.

A time efficient method to include buildings in urban wind simulations is developed and validated. Herein, the buildings are marked by an indicator function and modelled by a

volume resistance force which is added to the momentum equations.

4.6 Meshing of the urban domain

The mesh of urban geometries has to meet a lot of requirements. Some of them are listed in the best practice guides of Franke et al. [41]. Requirements due to the IDDES turbulence model, terrain and vegetation come in addition. The mesh itself is divided into several blocks. In all blocks including terrain, vegetation or buildings, tetrahedral cells are used while in other blocks hexahedral cells are used. This method drastically reduces the meshing effort since tetrahedral cells are more flexible and can be applied in a non-structured mesh. All wall-modelled surfaces are equipped with so-called inflation

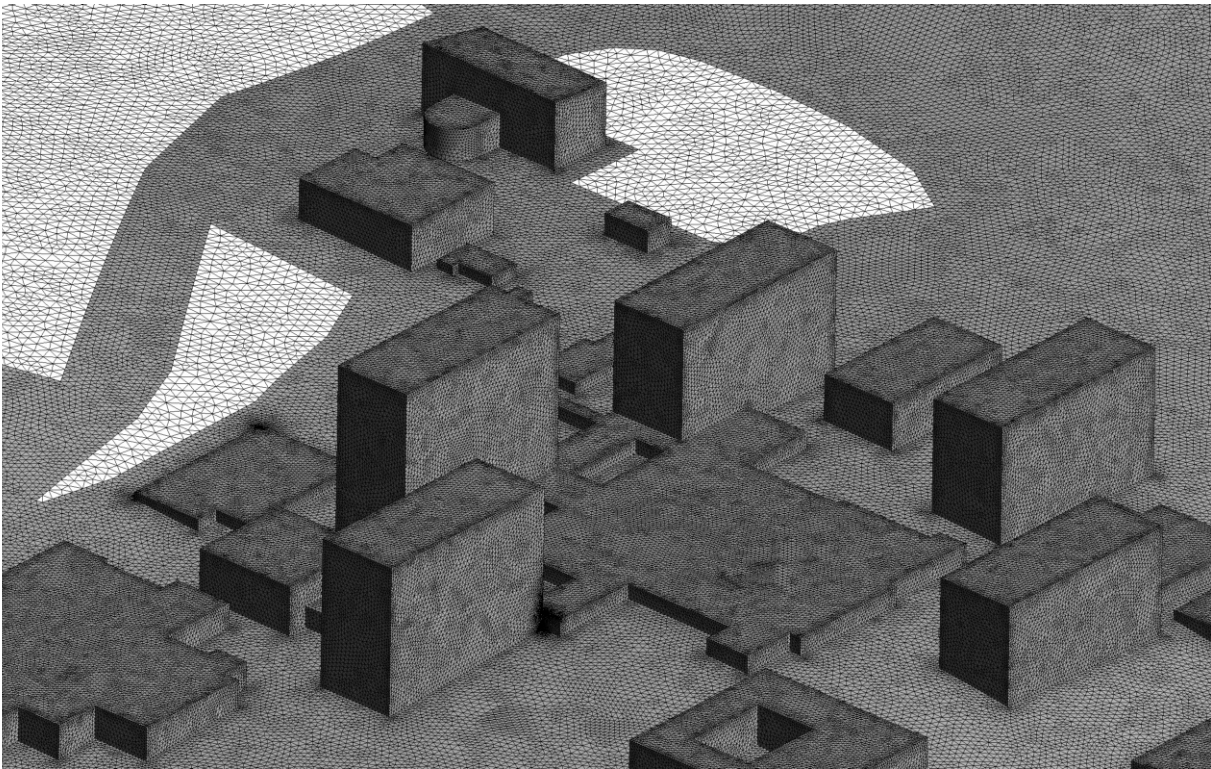


Figure 4.15: Meshed geometry with buildings, terrain and forested zones (light areas).

layers. The first cell layer height of the inflation layers amounts to 0.0005 m and fulfils the $y^+ \approx 1$ criterion so that the boundary layers are fully resolved. The growth rate of the cell layer heights to the normal grid is set to 1.2 according to Scaperdas and Gilham [110]. The number of the inflation layers is chosen to ensure a smooth transition between the inflation layers and the normal grid. The inflation layers consist of prismatic cells, as recommended by Franke et al [41], and they also meet the requirement that on walls the grid lines should be perpendicular to the wall as proposed by Menter et al. [82]. The total number of inflation layers varies between 36 and 38 which meets the suggestion of at least 10 cells per building separation as suggested by Franke et al. [41]. The grid resolution is

2.9 m. Additional refinement zones are applied around all buildings using a resolution of 1.45 m. The exact values are the result of a grid convergence study, which is described in section 5.1. With a chosen turbulence length scale of 55 m the number of cells per length scale amounts to 40 which is in the recommended range of Kim et al. [66] for an LES grid. Note that the volume of a tetrahedron is eight-times smaller than a hexahedron so that a grid resolution of 2.9 m using tetrahedral cells corresponds to a grid resolution of 1.45 m using hexagonal cells. Fig. 4.15 shows the meshed geometry of the urban domain used in the simulations. For building walls a maximum cell size of 1.1 m and for building edges 0.73 m are used but minimum five cells per edge according to Franke et al. [41]. The cells on the building walls are set by the meshing algorithm. The maximum grid width of 1.1 m is equal for all buildings but the cells on the building wall can be locally finer. The terrain surface is approximated by cells of 1.75 m edge length. The vegetation blocks are meshed entirely with the same grid resolution as the airflow, thus the drag force of the vegetation model is calculated in each cell individually for a realistic flow in and out of the forest. As shown in fig. 4.15, the additional wall refinement is neglected in the vegetation blocks, because the fluctuations at the ground of the forest are assumed to be very low and damped by the vegetation model. The total number of cells varies for each mesh between 60 and 70 million cells. Depending on the studies the domain size is changed but the principle meshing parameters are maintained in every mesh. The critical skewness number of 0.95 is undercut for every grid, avoiding divergence or unphysical results.

5 Evaluation: Sensitivity Analysis

In the following, various simulation and environmental parameters are changed to investigate their influence on the numerical results and the flow pattern. In particular, meshing parameters and different sizes of the computational domain are analysed. Regarding environmental parameters, the tree height and the leaf area density of the forest and the atmospheric turbulence intensity is investigated. Furthermore, the influence of surrounding buildings on the flow pattern is analysed.

5.1 Mesh convergence study

In this chapter, a mesh convergence study is performed in which the influence of meshing parameters such as the solid wall boundary layer resolution and the cell sizes at the surfaces of the buildings and the terrain and the cell width in the flow field are investigated.

5.1.1 Simulation setup

Initially, the size of the domain is $(15.6 \times 10 \times 6.25)H_{b,\max}$ according to the best practice guide for urban simulations [41] where $H_{b,\max}$ is 50 m and corresponds to the height of the tallest building. The upwind length L_u is $6.6 H_{b,\max}$ and the downwind length L_d is $9 H_{b,\max}$. The domain height is adapted for complex terrain. Fig. 5.1 illustrates the computational domain including the buildings used in the mesh convergence study. The minimum and maximum relative terrain height z is -39.7 m and 41.3 m, respectively resulting in a difference in altitude of 81 m. The forested zones are not considered in this study. The simulated wind direction at the test site in Tübingen is 245° and consequently, the domain and the inflow plane are oriented towards that direction. The mesh is generated according to the description in chapter 4.6.

The simulations are carried out with a turbulence intensity of 7% according to a neutral Atmospheric Boundary Layer (ABL) and a turbulence length scale L of 55 m. The power law

$$u(z) = \left(\frac{z}{10 \text{ m}}\right)^{0.19} \cdot u_{\text{ref}} \quad (5.1)$$

is used as a velocity profile and is applied at the inflow boundary plane, wherein u_{ref} is 4 m/s. For the side and the upper surfaces of the domain the so-called 'symmetry'

boundary condition was used in Fluent, that means all variables are forced to be parallel to the boundary plane at the surface. For the outlet a pressure-outlet boundary condition is used. The terrain and the building surfaces are all treated as no-slip walls. For the Courant number $Co = 0.25$ is chosen.

In total, the influence of three different parameters is investigated: the cell size, the

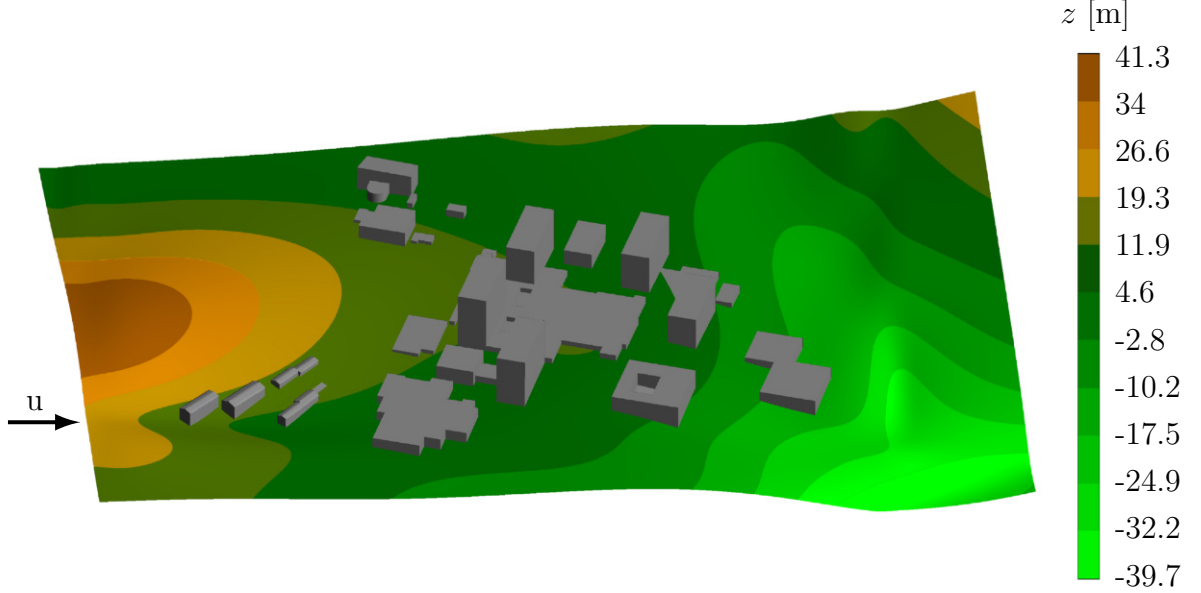


Figure 5.1: Computational domain of the simulations used in the mesh convergence study. Relative height (z) of the complex terrain with the buildings.

resolution at the building surfaces combined with the resolution of the terrain surface, and the number of the inflation layers.

5.1.2 Influence of meshing parameters

The flow field is evaluated by a pressure $c_{p,b}$ which is averaged over all buildings and their surfaces. Compared to the conventional definition of the $c_{p,b}$ coefficient, known from the pressure distribution, e.g., over a blade [123], the velocity of approach u_∞ is replaced by the reference velocity u_{ref} used in the inlet velocity profile, because a uniform velocity, such as u_∞ of approach does not exist in the ABL. Thus, the $c_{p,b}$ coefficient for buildings is defined as follows

$$c_{p,b} = \frac{p - p_\infty}{\frac{\rho}{2} \cdot u_{\text{ref}}^2}, \quad (5.2)$$

where p is the local pressure and p_∞ is the atmospheric pressure.

For the study of cells sizes, 1.2 m, 1.5 m, 2.25 m and 3 m are used, resulting in total cell numbers from 12.2 million to 73.3 million cells. Table 5.1 gives an overview of the meshing parameters of the simulations. The skewness of a numerical cell is an important parameter to assess the mesh quality. The skewness ranges from 0 to 1, wherein a value of 0 indicates an equilateral cell (best) and a value of 1 indicates a completely degenerate

Cell size Δ [m]	Total cell number [-]	Mean skewness s_{av} [-]	Maximum skewness s_{max} [-]
3	12.203.073	0.244	0.939
2.25	17.510.847	0.235	0.941
1.5	39.811.570	0.223	0.895
1.2	73.267.561	0.220	0.933

Table 5.1: Mesh properties of the simulations with various cell sizes.

cell (worst) [14]. The skewness s of a numerical cell is defined as [14]

$$s = \max \left[\frac{\theta_{\max} - \theta_e}{180^\circ - \theta_e}, \frac{\theta_e - \theta_{\min}}{\theta_e} \right], \quad (5.3)$$

where θ_e is the angle for an equiangular face or cell, θ_{\max} is the largest angle in the face or cell and θ_{\min} is the smallest angle in the face or cell.

As an effect of smaller cell sizes the mean skewness decreases which can improve the qual-

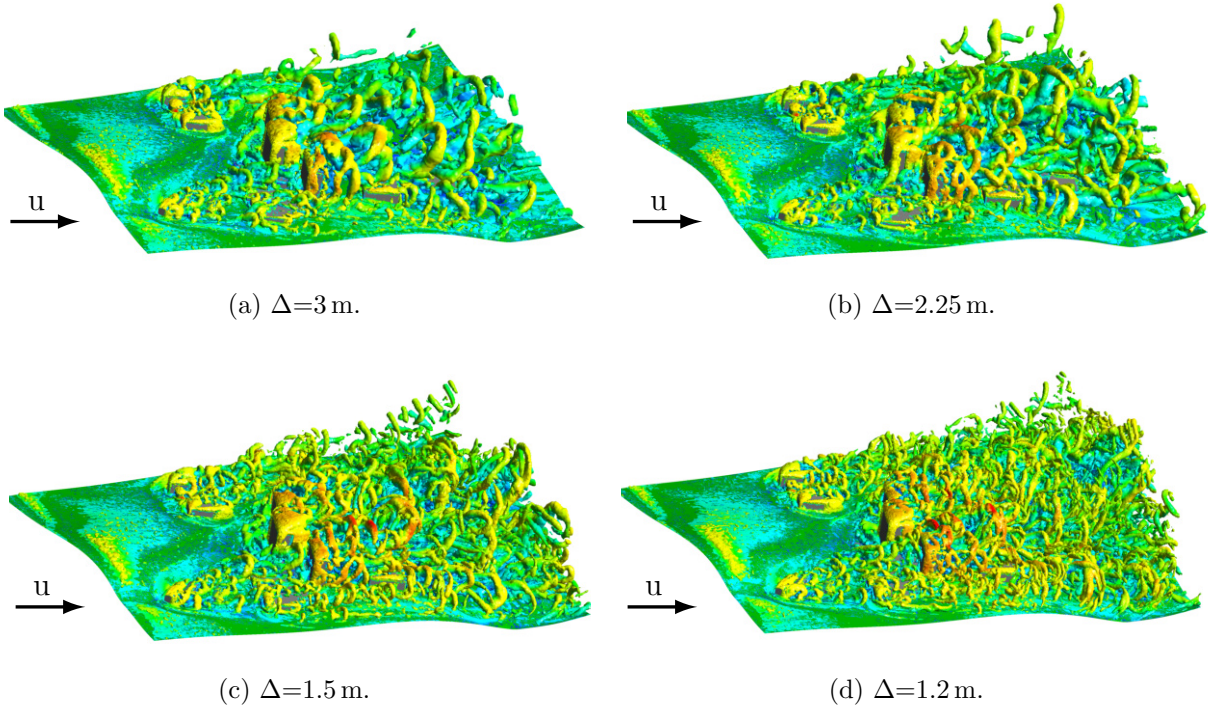
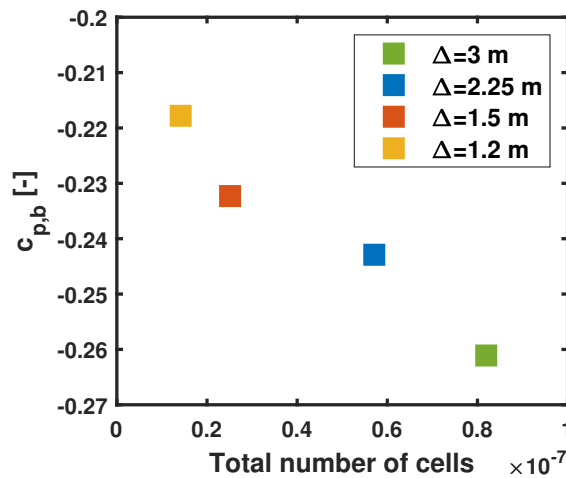


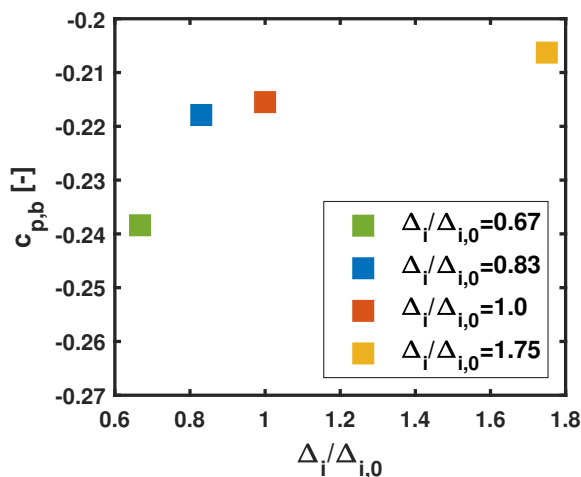
Figure 5.2: Iso-surfaces of the λ_2 criterion, obtained from the simulations with different cell sizes Δ and coloured by the velocity magnitude from blue (0 m/s) to red (11 m/s).

ity of simulation results. Fig. 5.2 illustrates the iso-surfaces of the λ_2 criterion for each simulated cell width. As described in chapter 2.2, the cell size is the threshold value for filtering the turbulent structures in a DES simulation in ANSYS Fluent. This effect can be clearly observed when comparing the structures with the smallest and largest cell size.

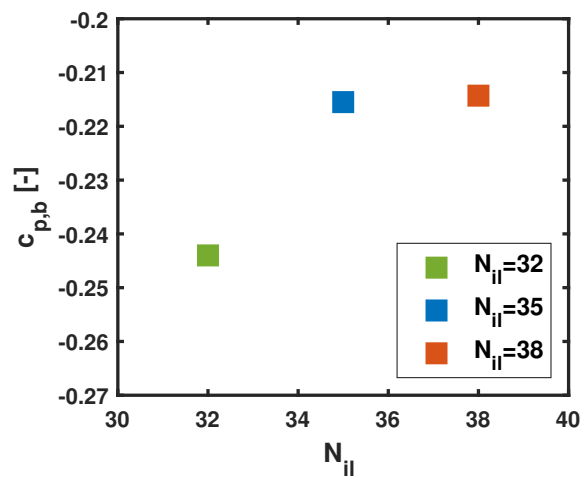
Fig. 5.2a shows the resolved structures in the simulation with a cell size of 3 m. Starting with the coarsest mesh, the turbulent structures become more detailed with increasing mesh resolution. Even when further reducing the cell size from 1.5 m down to 1.2 m, the turbulent structures are still noticeably finer. Fig. 5.3a shows the $c_{p,b}$ coefficient which is averaged over all buildings and their surfaces. The developing of the pressure coefficients shows that a finer mesh results in higher $c_{p,b}$ values. A strong rise of the $c_{p,b}$ values in relation to the total cell numbers is observed for coarser meshes when the cell size is reduced from 3 m to 2.25 m. As can be seen in fig. 5.3a, a mesh convergence is not reached, but due to computational resources a further reduction in the cell width Δ was not possible. Furthermore, the influences of the resolution of the terrain, the building surfaces and the



(a) Mean $c_{p,b}$ values for different cell widths Δ



(b) Mean $c_{p,b}$ values for different resolutions of building surfaces Δ_{bs} and edges Δ_{be} and terrain surfaces Δ_t



(c) Mean $c_{p,b}$ values for different numbers of inflation layers N_{il}

Figure 5.3: $c_{p,b}$ values averaged over all buildings for different meshing parameters.

building edges are investigated in the mesh convergence study. Table 5.2 gives an overview of the simulated resolutions and the mesh quality, described by the skewness. Starting

with a terrain resolution of $\Delta_t = 3$ m and a building surface resolution of $\Delta_{bs} = 2.75$ m, which corresponds to a building edge resolution of $\Delta_{be} = 100$ %, each resolution is reduced to 83 % and 67 % and increased to 175 %, respectively. The different resolutions do not af-

Resolution terrain Δ_t [m]	Resolution building surfaces Δ_{bs} [m]	Resolution building edges Δ_{be} [%]	Total cell number [-]	Mean skewness s_{av} [-]	Maximum skewness s_{max} [-]	$\Delta_i/\Delta_{i,0}$ [-]
4.5	4.13	67	23.566.485	0.228	0.935	0.67
3.6	3.31	83	24.295.029	0.228	0.945	0.83
3	2.75	100	26.372.728	0.228	0.923	1.0
1.7	1.57	175	39.088.736	0.228	0.888	1.75

Table 5.2: Mesh properties of the simulations with various cell resolutions of the terrain and building surfaces and building edges.

fect the mean skewness of the entire mesh, but the maximum skewness is reduced by 6 %. That is, the resolutions of the walls and the building edges affect the maximum skewness much more than the general cell size. The resolution depending mean $c_{p,b}$ coefficients are illustrated in fig. 5.3b where Δ_0 refers to the reference resolution of 100 %. Similar to the cell size study, the $c_{p,b}$ coefficient is noticeably lower for the lowest resolution and approximates the value of -0.2. Thus, finer resolutions of the terrain and building surfaces and building edges do not improve the simulation results. The reason for that is that finer resolutions of the terrain and building surfaces, when the general grid size remains equal, may lead to a jump in the cell size in the transition region from the inflation layers to the main mesh. It should be noted that in the simulations listed in table 5.2 the cell size of the main mesh is 1.8 m due to limited computational resources.

Moreover, it is investigated how the number of inflation layers N_{il} affects the flow field.

Number of inflation layers N_{il} [-]	Total inflation layer thickness [m]	Total cell number [-]	Mean skewness s_{av} [-]	Maximum skewness s_{max} [-]
32	0.26	26.069.428	0.228	0.937
35	0.44	26.372.728	0.228	0.923
38	0.76	26.785.898	0.230	0.940

Table 5.3: Mesh properties of the simulations with various numbers of inflation layers.

Inflation layers are applied near solid walls to resolve the entire boundary layer due to the $y^+ = 1$ criterion. The inflation layers are parallel layers to the terrain and building surfaces, and the thickness of each individual layer increases by a factor of 1.2 with increasing

distance from the ground. The number of inflation layers should be set to have a smooth transition of the cell sizes. In total, 32, 35 and 38 layers are used for the study with a total thickness of 0.26, 0.44 and 0.76 m as listed in table 5.3. Simulations with less than 32 layers show poor simulation results and diverged in the simulations so that they are not further considered in this study. The reason for that is that the jump in the cell size at the transition region is too large. It is noted that jumps in cell sizes in a mesh should be avoided in general. Both the mean and the maximum skewness are barely affected by the inflation layers. The mean $c_{p,b}$ values depending on the number of inflation layers are illustrated in fig. 5.3c. For the mesh with the building resolution of $\Delta_{be} = 100\%$ from table 5.2 the $c_{p,b}$ value obtained with 32 inflation layers is lower compared to the $c_{p,b}$ value using 35 and 38 inflation layers, because the transition from the inflation layer mesh to the main mesh is larger. When 35 and 38 inflation layers are applied to the mesh, the $c_{p,b}$ values reach a plateau and more inflation layers do not improve the simulation results.

A mesh convergence study is performed in which the sensitivity of meshing parameters such as the cell size of the main mesh, the resolution of the terrain, of the building walls and of the building edges, and the sensitivity of the inflation layers are investigated. The flow field is evaluated with the $c_{p,b}$ coefficient adapted for buildings. Smaller cell sizes of the main mesh and a higher resolution of the terrain, of the building walls and of the building edges result in higher $c_{p,b}$ coefficient of the buildings and are considered in the further simulations. Regarding the inflation layers, their influence on the flow field goes to zero, when a smooth transition between the inflation layers and the main mesh is obtained and the distance between the inflation layers is kept constant. For further simulations a cell size of 1.45 m with 38 inflation layers and a resolution of the building wall surfaces of 1.1 m with the corresponding resolution of building edges was chosen.

5.2 Domain size analysis

In the following, the wind flow is simulated with different heights and widths of the computational domain and their influence on the wind field is analysed.

5.2.1 Simulation setup

The domain sizes used in the domain size analysis are described in the respective sections. For the sake of simplicity, the forested zones are not considered in this study. The simulated wind direction at the test site in Tübingen is 245° and consequently, the domain and the inflow plane are oriented towards that direction. For the turbulence length scale $L = 55$ m is chosen. The mesh is generated according to the description in chapter 4.6.

The simulations are carried out with a turbulence intensity of 7% according to a neutral ABL. The power law in equ. 5.1 is used as a velocity profile and is applied at the inflow boundary plane. For the side and the upper surfaces of the domain the so-called 'symmetry' boundary condition was used in Fluent, that means all variables are forced to be parallel to the boundary plane at the surface. For the outlet a pressure-outlet boundary condition is used. The terrain and the building surfaces are all treated as a no-slip walls. The Co number amounts 0.25.

5.2.2 Domain height

The wind flow at the test site in Tübingen is simulated using different heights of the computational domain to investigate how various domain heights affect the flow field. According to the best practice guide for urban simulations [41] the size of the domain is $(15.6 \times 10 \times 6)H_{b,max}$. The upwind length L_u is $5.2H_{b,max}$ and the downwind length L_d is $10.4H_{b,max}$. Fig. 5.4 illustrates the computational domain including the buildings used in the domain size analysis. The minimum and maximum relative terrain height is -39.7 m and 41.3 m, resulting in a difference of altitude of 81 m. Regarding the domain

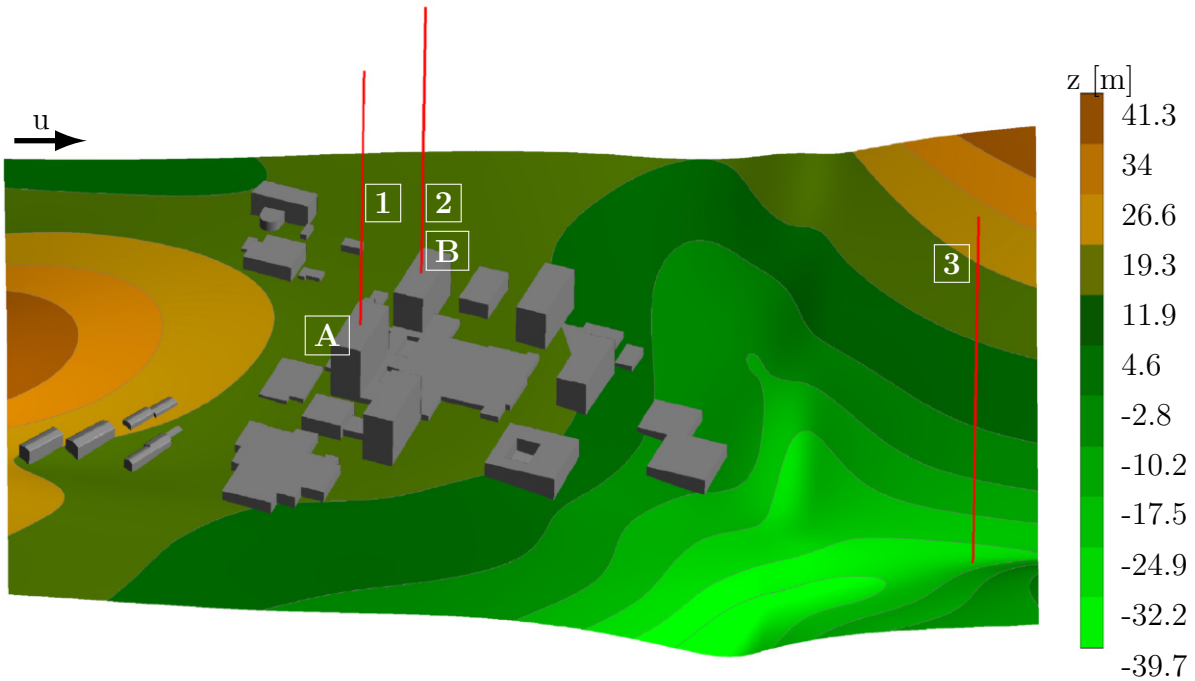


Figure 5.4: Computational domain used in the domain height study. The vertical evaluation lines are highlighted in red. Relative height (z) of the complex terrain with all buildings included.

height, some best practice guides exist in the literature recommending domain sizes of urban wind field simulations. For example, for a simulation of a single building Franke et

al. [41] suggest a domain height smaller than $5 H_{b,\max}$, and $10 H_{b,\max}$ for large blockages. Mochida et al. [86] propose a domain height of at least $5 H_{b,\max}$, where $H_{b,\max}$ is the maximum height of the building. However, when several buildings are considered in the domain, the crucial parameter is the blocking ratio ζ of the domain which is defined by

$$\zeta = 1 - \frac{A_{cs}}{A_{cs,\max}}, \quad (5.4)$$

where A_{cs} are cross-sectional areas of the domain and the buildings for varying x -values and $A_{cs,\max}$ is the largest cross-sectional area of the domain, wherein A_{cs} and $A_{cs,\max}$ are perpendicular to the inflow direction, marked by the arrow in fig. 5.4. When several buildings are taken into account, the domain height should be set according to ζ and ζ should be smaller than 0.03 to avoid artificial acceleration since otherwise the flow is not able to pass the side surfaces of the domain [20, 130]. The blockage of the flow is not

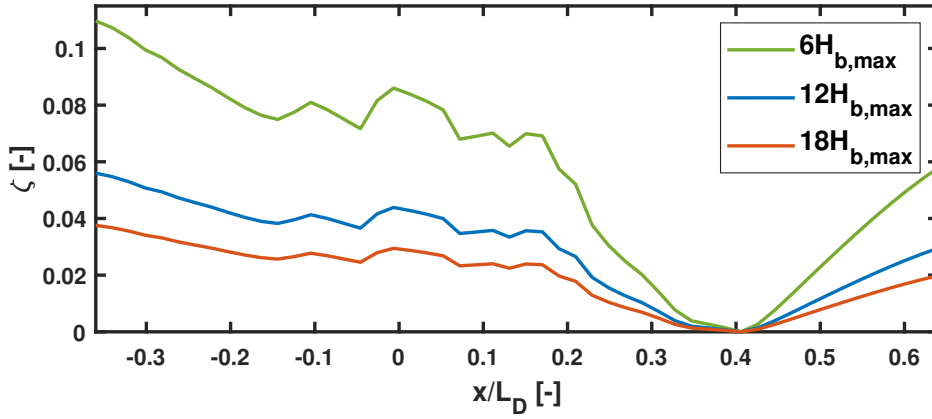


Figure 5.5: Blockage ratio ζ of the computational domain with a height of $6 H_{b,\max}$, $12 H_{b,\max}$ and $18 H_{b,\max}$ over the domain length L_D .

only caused by the buildings but also by hills and mountains of a terrain. However, in the mentioned studies, the complex terrain is not considered. Due to the high variety in terrains, the minimum domain height has to be determined for each test site in a previous study.

The simulated domain heights are $6 H_{b,\max}$, $12 H_{b,\max}$ and $18 H_{b,\max}$. Fig. 5.4 shows the computational domain with the buildings (grey) and the contour lines of the terrain. Furthermore, fig. 5.4 shows the vertical evaluation lines of the wind field which are marked red for the vertical lines. The vertical lines 1 and 2 are located above the buildings of interest which are building A and B, as shown in fig. 5.4. Line 3 is located in a valley, downstream behind the buildings. With increasing domain heights, ζ is reduced because the terrain and the buildings are of less consequences.

Fig. 5.6 shows the horizontal evaluation line of the wind field in the computational domain which is marked blue. Fig. 5.5 shows the distribution of the blockage ratios of the three simulated domains over the domain length L_D . The plane $x = 0$ is located shortly behind building A accompanied by an increase of the blocking ratio. The blocking ratio at the

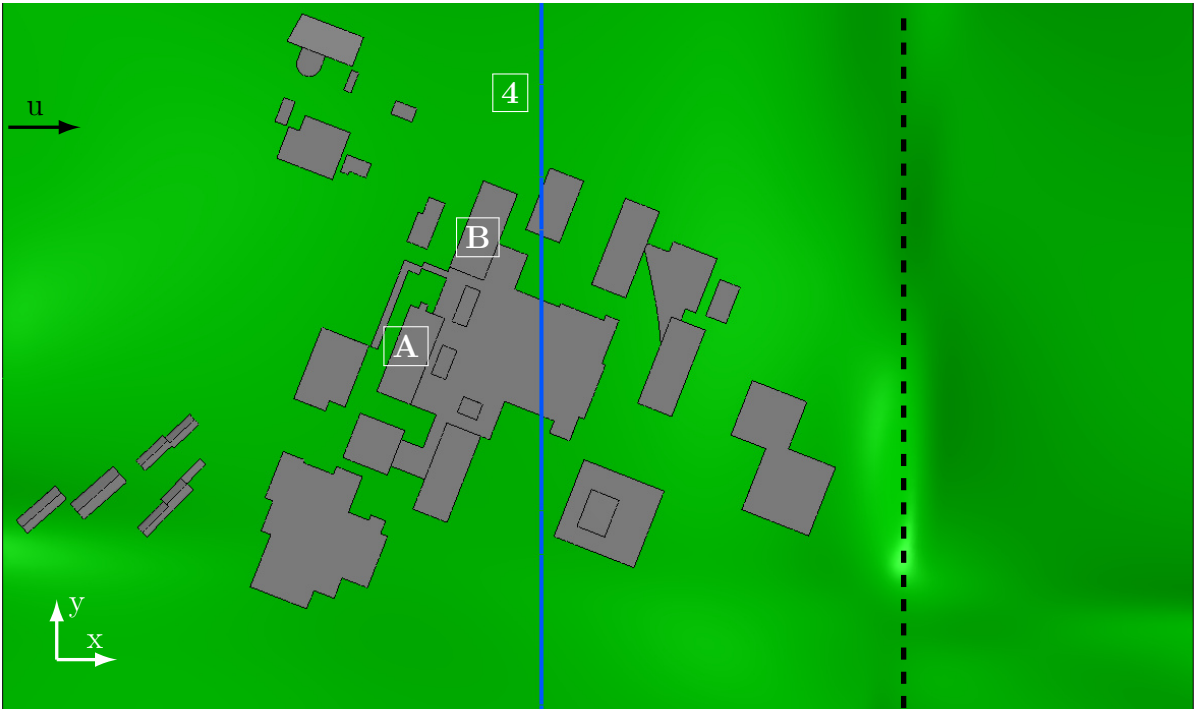


Figure 5.6: Computational domain used in the domain height study with the horizontal evaluation line which is highlighted in blue. Largest cross-sectional area of the domain $A_{cs,max}$ is indicated by the dashed line.

inflow plane is reduced from 0.11 for a domain height of $6 H_{b,max}$ to 0.056 for $12 H_{b,max}$ until to 0.038 for $18 H_{b,max}$. The highest blockage ratio is obtained at the inlet due to the high terrain and at the built area due to the high-rise buildings, especially the buildings A and B. The blockage ratio turns to zero, when A_{cs} reaches the size of $A_{cs,max}$ which has the largest cross-sectional area. The location of $A_{cs,max}$ is obtained at $x/L_D=0.4$ and is indicated by the black dashed line in 5.6.

The time-averaged velocity magnitude, evaluated along the horizontal line 4, indicated as blue line in fig. 5.6, is shown in fig. 5.7. Line 4 is located at a height of $z = 200$ m corresponding to $4 H_{b,max}$ and $x = 70$ m. The velocities obtained in the simulations using $12 H_{b,max}$ and $18 H_{b,max}$ are very similar. In comparison to that, higher wind speeds for the half of the domain with negative y values and higher wind speeds for the half of the domain with positive y values are obtained in the simulation using $6 H_{b,max}$. The part of the domain with positive y values has a higher blockage.

Fig. 5.8 shows the time-averaged velocity magnitude evaluated at the vertical lines 1 - 3 for different simulated domain heights. The sub-figures in fig. 5.8 show detailed sections of the plotted velocities. The differences in the wind speed above buildings A and B, represented by the lines 1 and 2, respectively, are quite small and can be neglected. The evaluation line 3 is located in a valley behind the buildings. Hence, the flow is decelerated when it enters the valley, similar to a diffuser effect. With increasing domain height the flow deceleration and the diffuser effect reduces which is quite noticeable for a domain height of $18 H_{b,max}$. This effect is more pronounced at lower domain heights since the

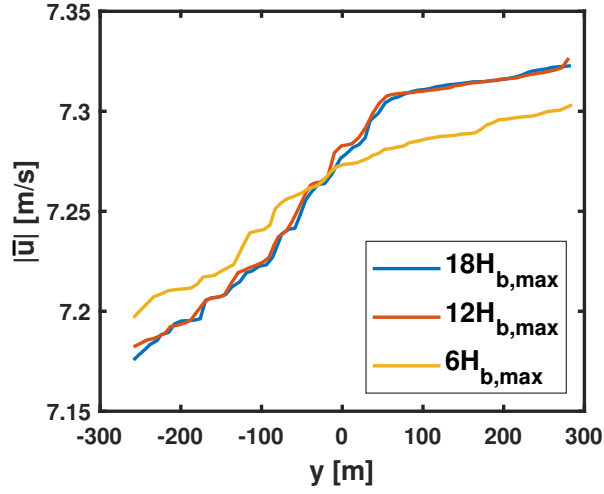


Figure 5.7: Time-averaged velocity magnitude $|\bar{u}|$ evaluated at the horizontal line 4 indicated as blue line in fig. 5.6 which is perpendicular to the main wind direction.

relative change in altitude related to the domain height is higher for lower domain heights. In a distance of 85 m to the terrain, the wind speed is slightly lower when a domain height of $6 H_{b,\max}$ is applied.

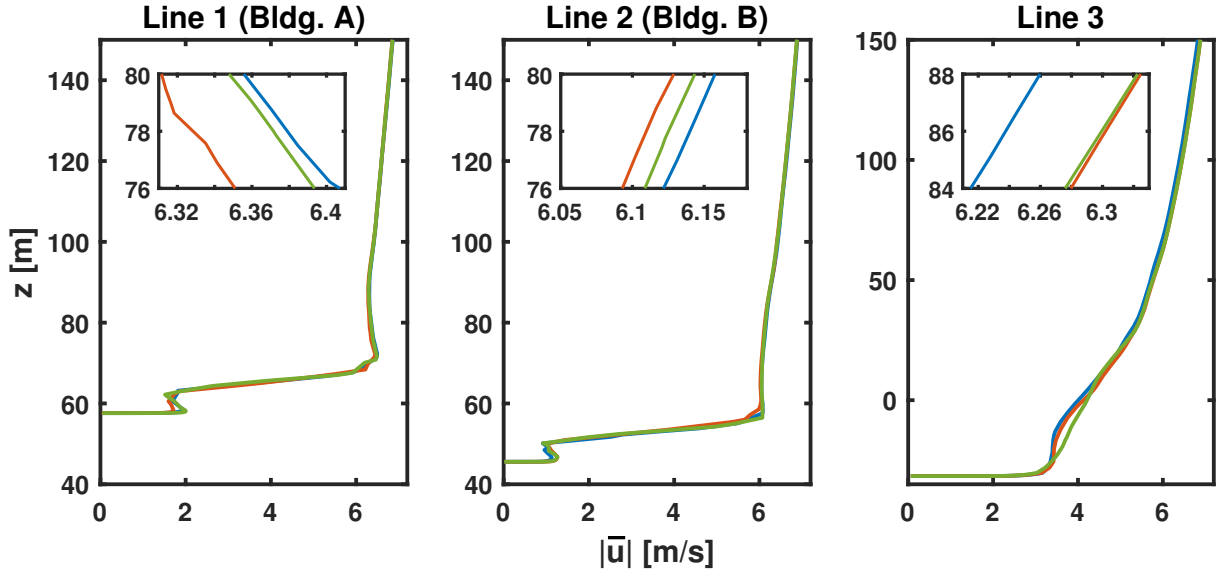


Figure 5.8: Time-averaged velocity magnitude $|\bar{u}|$ evaluated at vertical lines 1 - 3 using different domain heights, wherein line 1 is above building A and line 2 is above building B. Blue: $6 H_{b,\max}$, red: $12 H_{b,\max}$, green: $18 H_{b,\max}$.

A domain size analysis is performed in which the sensitivity of the domain height is investigated. Domain heights of $6 H_{b,\max}$, $12 H_{b,\max}$ and $18 H_{b,\max}$ are considered. Small but noticeable effects are observed when $6 H_{b,\max}$ is used in the simulations, but between a used height of $12 H_{b,\max}$ and $18 H_{b,\max}$ the differences in the wind speeds can be neglected. Thus, at least a domain height of $12 H_{b,\max}$ is taken for further simulations in this work corresponding to a blockage ratio of 0.055 at the inflow plane.

5.2.3 Domain width

In addition to the domain height, the test site in Tübingen is also simulated with two

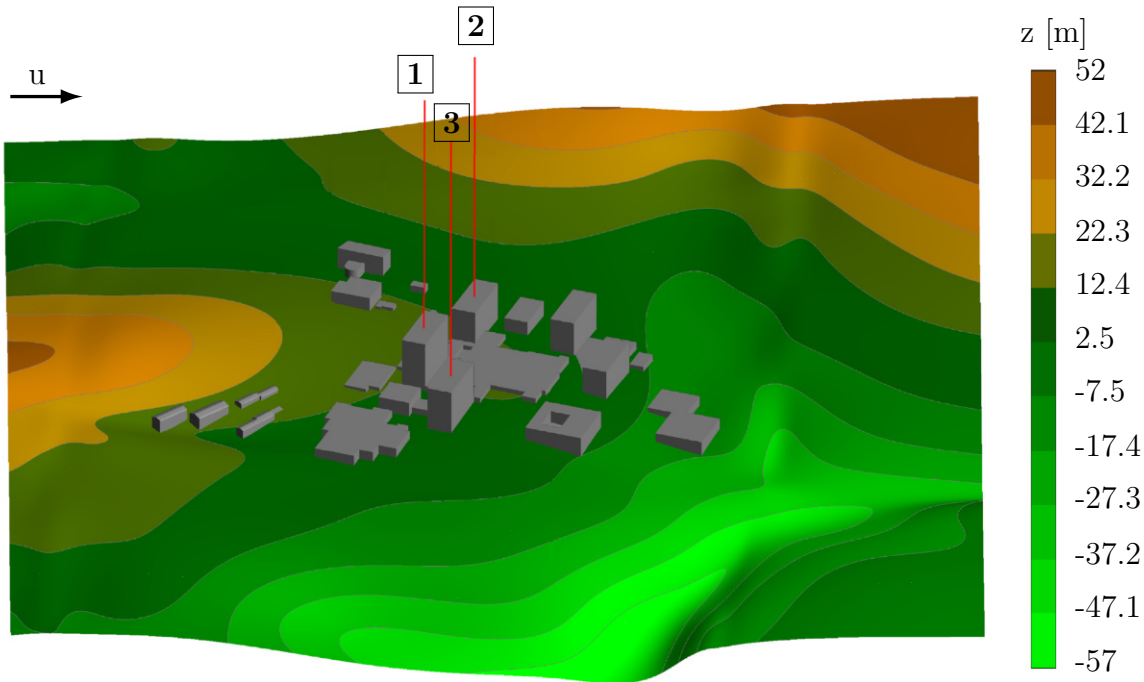


Figure 5.9: Computational domain with a width of $10 H_{b,\max}$. The vertical evaluation lines are highlighted in red. Relative height (z) of the complex terrain with all buildings included.

different domain widths to investigate how the lateral extension of the domain affects the flow field. The initial size of the domain is $(18.7 \times 10 \times 12)H_{b,\max}^3$, the upwind length L_u is $8.3 H_{b,\max}$ and the downwind length L_d is $10.4 H_{b,\max}$. Regarding best practice guides, Tominaga et al. [130] and Bartzis et al. [22] suggests a lateral extension to the side walls of the domain of at least $5 H_{b,\max}$ when just a single building is simulated. Franke et al. [41] figured out that a lateral extension to each side of $5 H_{b,\max}$ is sufficient. It should be noted that complex terrain is not considered in the statements of the best practice guides. Hence, a domain width depending study with complex terrain is performed.

The domain widths used in the simulations are $10 H_{b,\max}$ and $16 H_{b,\max}$. Fig. 5.9 shows the computational domain using the smallest width including the buildings (grey) and the contour lines of the terrain. The wind field is evaluated along horizontal lines, indicated in blue in fig. 5.10 and vertical lines which are marked in blue in fig. 5.9. The vertical lines 1 - 3 are located above the buildings A, B and C respectively.

Fig. 5.11 shows the time-averaged velocity magnitude evaluated along the lines 1 - 3 for the two used domain widths. Both velocities agree qualitatively and quantitatively quite well and show just minor differences. Both simulations show the same flow pattern above the buildings, and the recirculation bubble is predicted equally in its size and wind speed.

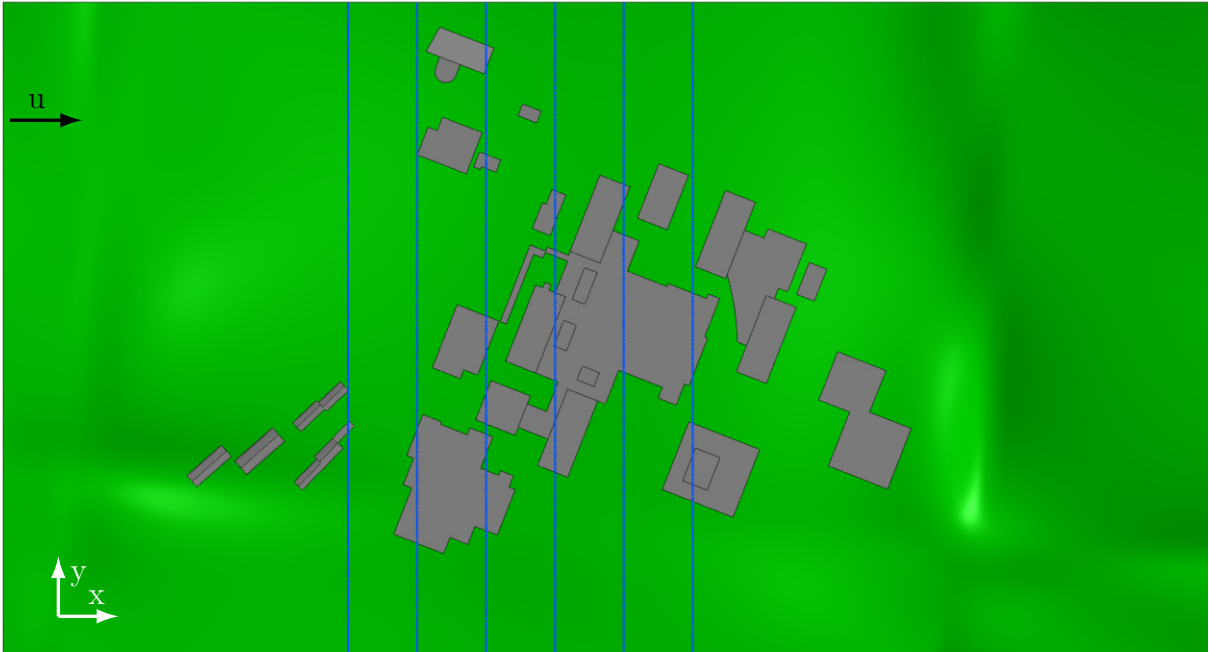


Figure 5.10: Computational domain with the horizontal evaluation lines highlighted in blue.

Also the height of the detached flow is predicted equally. Above the high-rise buildings, the wind flow is not affected by the domain widths.

The velocities are evaluated along the horizontal lines which are highlighted in blue in

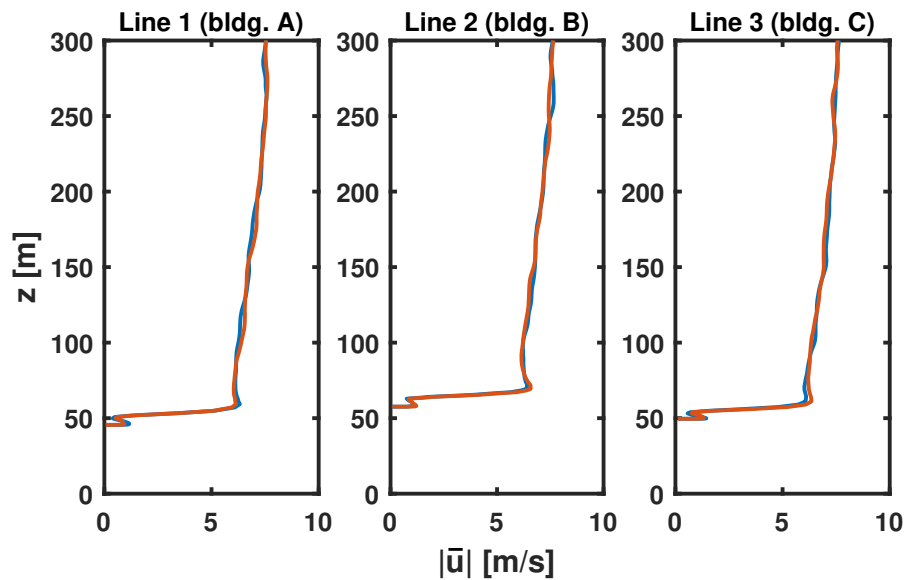


Figure 5.11: Time-averaged velocity magnitude evaluated at vertical lines 1 - 3 using different domain widths, wherein line 1 is above building A, line 2 is above building B and line 3 is above building C. Blue: $10 H_{b,\max}$ and red: $16 H_{b,\max}$

fig. 5.10 in a height of 70 m and a distance of 50 m to each other. The lines are arranged to evaluate the flow in the inflow region to the the buildings and over the buildings. As

observed along the vertical lines, the wind speed is predicted equally in both simulations in the inflow region and over the buildings. The influence of the buildings appears from $x = -50$ m. The velocity deficits are caused by the recirculation bubble on top of the buildings, wherein each deflection can be assigned to one of the buildings A, B and C.

A domain size analysis is performed in which the sensitivity of the domain width is

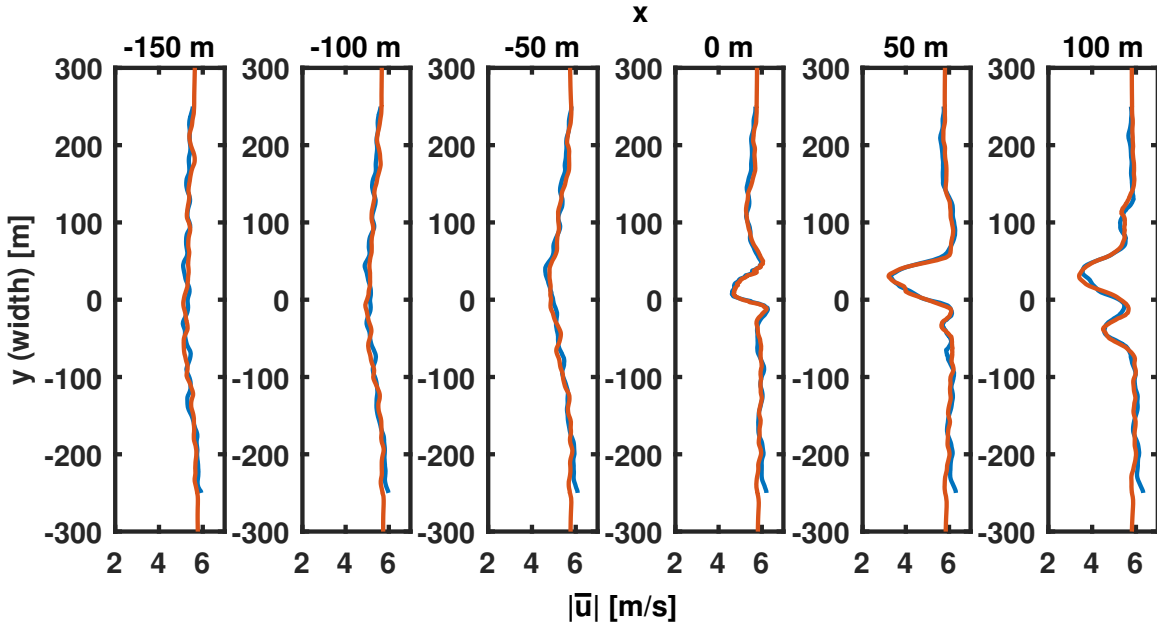


Figure 5.12: Time-averaged velocity magnitude evaluated at horizontal lines in y -direction as shown by the blue lines in fig. 5.9 in a height of 70 m. Blue: $10 H_{b,\max}$ and red: $16 H_{b,\max}$

investigated. Simulations using domain widths of $10 H_{b,\max}$ and $16 H_{b,\max}$ are performed. No noticeable effects are observed which would justify a lateral extension by more than $10 H_{b,\max}$. Thus, at least a domain width of $10 H_{b,\max}$ is taken for further simulations within this work.

5.3 Influence of environmental conditions

In this chapter, the flow field is simulated with different values of environmental parameters such as the tree height and the leaf area density of the forested zone. Furthermore, various values of the atmospheric turbulence intensity are applied at the inflow plane.

5.3.1 Simulation setup

As already mentioned in the introduction, there is a lack of sensitivity studies of atmospheric and vegetational parameters in urban wind flow. It is one objective of this work

to investigate how various types of vegetation depending on the foliation and the tree height influence the flow field around the buildings of interest. With different foliations in the forested zones seasonal effects can be considered in the simulation e.g., summer or winter. It should be noted that buildings A and B are directly located downstream of the vegetation zone. Hence, any changes of the parameter are supposed to be visible in the velocities and turbulent structures around these buildings.

The atmospheric layer can have three different states: the neutral, stable and unstable layer. An appropriate parameter to define the atmospheric stability is the Richardson number Ri , which is defined as the Gradient Richardson Number [46]:

$$Ri = \frac{g \cdot \frac{d\Theta}{dz}}{\Theta \cdot \left(\frac{du}{dz}\right)^2}, \quad (5.5)$$

where g is the gravitational acceleration and Θ is the virtual potential temperature [46]. The Richardson number may be interpreted as the ratio between the thermic and the mechanical atmospheric turbulence. In the neutral layer, the vertical temperature change corresponds to the dry adiabatic temperature change. That is, a defined air volume is hovering and not climbing or descending [79]. The Richardson number turns to zero. That means, that mechanical turbulence predominates. A stable atmospheric layer oc-

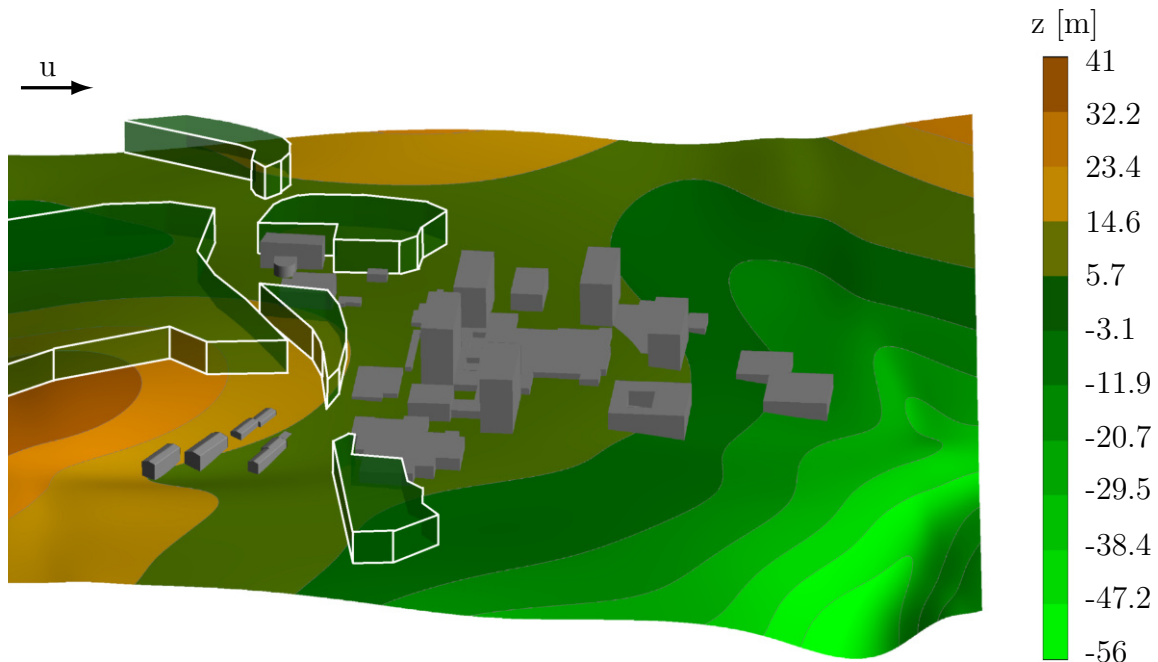


Figure 5.13: Computational domain for the simulations of different environmental conditions.

urs usually at night and is defined when the temperature change in the atmosphere is smaller than the dry adiabatic temperature change. That is, the defined air volume is descending [79]. The Richardson number is larger than zero and the turbulent exchange

is suppressed. An unstable layer occurs normally during the day when the air is heated up by the sun. The temperature change of the atmosphere is larger than the dry adiabatic temperature change. That is, the defined air volume is climbing [79]. The Richardson number is negative and thermic turbulence predominates. The type of layer also affects the turbulence intensity of the atmosphere. Under stable conditions low turbulence intensities are expected while the turbulence intensity increases during unstable conditions due to strong mixing in the air. That means, the turbulence intensity decreases with increasing stability [42].

Since the temperatures are not considered in this work, just neutral layers are simulated. But to consider the effect of unstable layers, a sensitivity study with different atmospheric turbulence intensities is performed.

The size of the domain is $(14 \times 14 \times 13)H_{b,\max}$ in length \times width \times height with an upwind length L_u of $7H_{b,\max}$ and a downwind length L_d of $7H_{b,\max}$. The quadratic ground area is taken for a better calculation of the AEP which is described in a later chapter. Fig. 5.13 illustrates the computational domain including the buildings as used in the domain size analysis. The minimum and maximum relative terrain height is $z = -55.7$ m and 41.3 m, resulting in a difference in altitude of 97 m. Thus, the domain height is adapted to $13H_{b,\max}$ which is higher than the outcome of the domain size analysis. The forested zones are considered in this study and represented by the transparent green bodies as shown in fig. 5.13. The tree height H_t ranges between 10 m and 30 m and the average tree height $H_{t,\text{av}}$ is 20 m. The forested zones are modelled as described in chapter 4.4. The simulated wind direction at the test site in Tübingen is 240° and consequently, the domain and the inflow plane are oriented towards that direction. Since the forested zones are considered now in the simulations, the turbulence length scale is changed from $L = 55$ m to 50 m. The mesh is generated according to the description in chapter 4.6. The simulations are carried out with a turbulence intensity of 10% according to a neutral Atmospheric Boundary Layer (ABL). Compared to the previous setting the turbulence intensity is increased from 7% to 10% due to the forested zones in the inflow region. The turbulence is synthetically generated at the inlet plane. The power law

$$u(z) = \left(\frac{z}{10 \text{ m}} \right)^{0.21} \cdot u_{\text{ref}} \quad (5.6)$$

is used as a velocity profile and is applied at the inflow boundary plane where u_{ref} is 2.95 m/s. Within the forest at the inlet plane, the velocity profile of equ. 4.3 is taken. The reference velocity is taken for the university campus in Tübingen according to the wind atlas of Baden-Württemberg [3]. For the side and upper surfaces of the domain the so-called 'symmetry' boundary condition is used in Fluent, that means all variables are forced to be parallel to the boundary plane at the surface. For the outlet a pressure-outlet boundary condition is used. The terrain and the building surfaces are all treated as no-slip walls. The Co number amounts to 0.25. The stabilization time is 147 s and the averaging

time is 240 s.

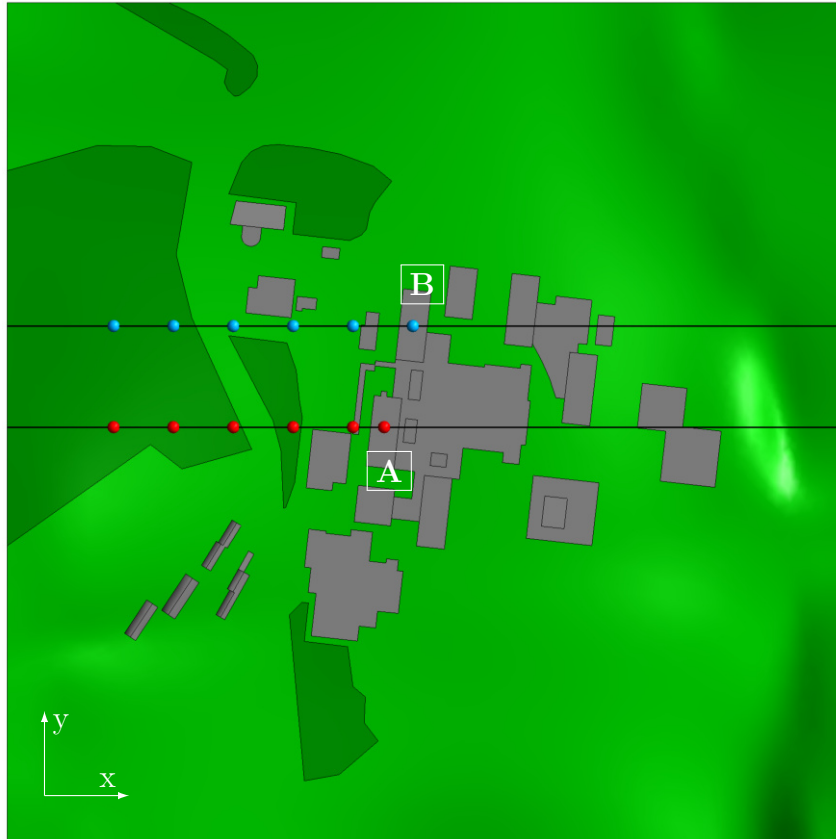


Figure 5.14: Vertical evaluation lines in front of building B at $y=80$ m (blue) and in front of building A at $y=-4.5$ m (red).

5.3.2 Investigation of different atmospheric turbulence intensities

In this subchapter, the influence of the inlet turbulence intensity is investigated. In total, three different values are simulated: 10 %, 20 % and 30 %. The turbulence intensity I is applied at the inlet plane via the inlet boundary condition. As part of the evaluation of the simulation results, it has been verified that only cells in areas 1 m above ground level are modeled in URANS mode. The rest of the flow field is completely simulated in LES mode to resolve the turbulent structures. The parameters are evaluated vertically in front of building B at the locations indicated by the blue points in fig. 5.14 and in front of building A at the locations indicated by the red points. The vertical evaluation lines are located at a respective distance of 50 m in x-direction to each other. The time-averaged velocity magnitude for the flow towards building B is shown in fig. 5.15, wherein the green curve represents the velocity obtained with $I=10$ %, the blue curve the velocity at $I=20$ % and the red curve the velocity at $I=30$ %. The black dashed lines represent

the upper and the lower tree height of the forest. As can be observed at $x=-261$ m and -211 m the velocities obtained with higher turbulence intensities are slightly increased in the crown region of the forest, at $z=30$ m. Due to higher velocity fluctuations, the

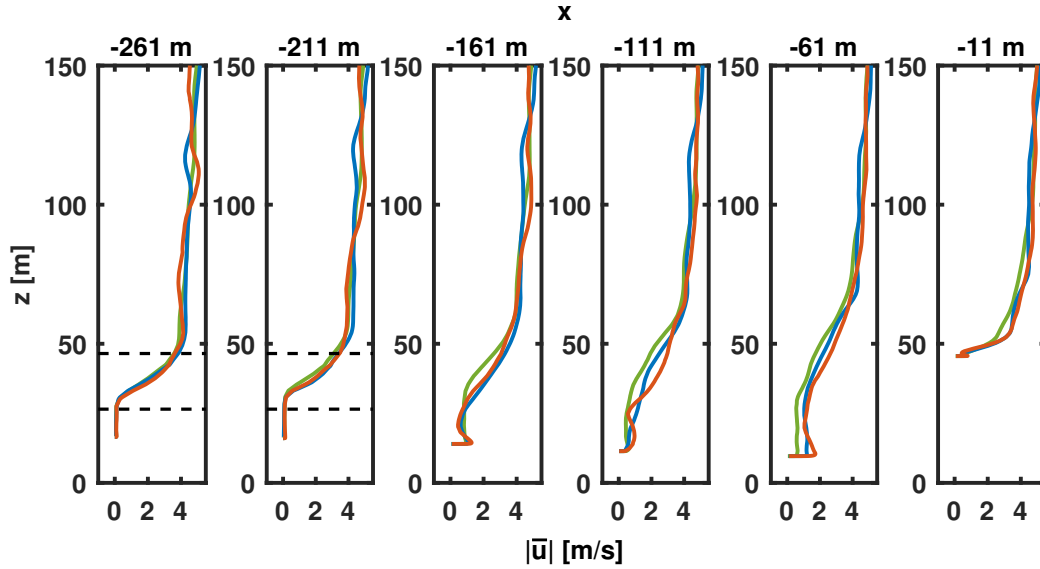


Figure 5.15: Time-averaged velocity magnitude evaluated in front of building B at $y=80$ m with an inlet turbulence intensity of 10 % (green), 20 % (blue) and 30 % (red).

turbulent eddies dive deeper into the upper part of the trees, resulting in higher overall velocities. This effect is also visible when the flow passes the forested zone from $x=-161$ m to $x=-111$ m which is divided by a road. After the flow is detached at the road like in a step flow, higher turbulence intensities lead to an increased vorticity of the part of the flow which is closer to the terrain. Thus, higher velocities are obtained at lower heights with increased turbulence intensities. At $x=-61$ m the velocity is increased by about 1.5 m/s at a turbulence intensity of 30 % compared to 10 % at the ground. Observing the wind speed at the top of building B, the velocity at $I=10$ % is reduced by 1 m/s compared to the velocities at $I=20$ % and 30 %. Hence, a higher atmospheric turbulence intensity increases the wind speed and the energy yield of a wind turbine on building B.

The velocity differences at $x=-261$ m above 50 m are caused by the synthetic turbulence generation method. Fig. 5.16 visualises the turbulent kinetic energy evaluated along the same evaluation lines as the velocity magnitude at $y=80$ m using equal legend colours. The different applied turbulence intensities can be obviously seen at the evaluation line at $x=-261$ m close to the inlet. Due to the synthetic turbulence generation, the k curve shows a wavy pattern. The high k values near the treetop appear also in this case caused by the rough surface of the tree top due to the local tree heights. The lower the atmospheric turbulence is, the disproportionately higher is the produced k in the crown region of the forest. That means that consequently the damping in the crown region increases with higher k values due to the forest model. But related to the k values obtained in the

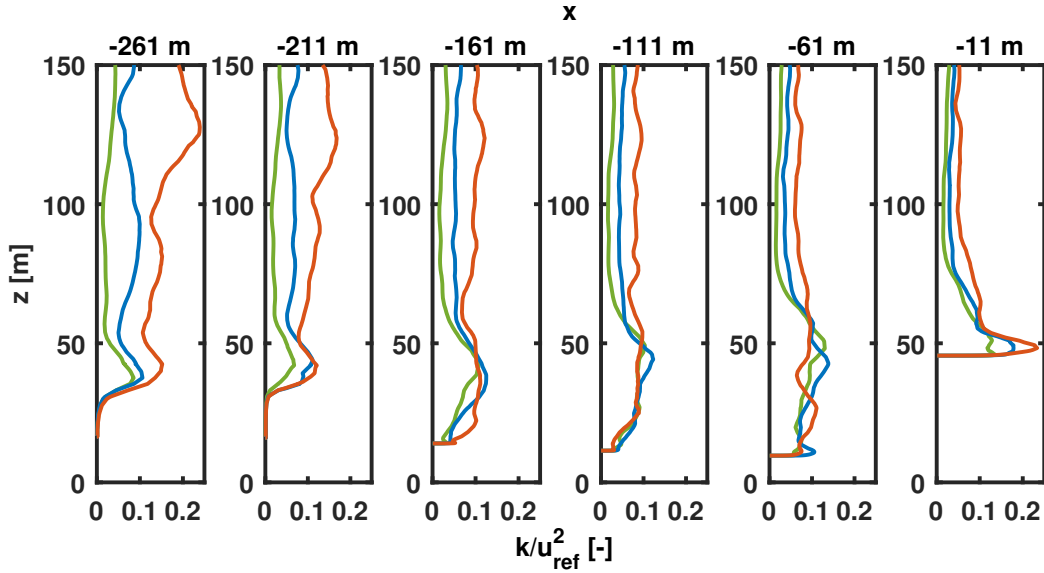


Figure 5.16: Turbulent kinetic energy evaluated in front of building B at $y=80$ m with an inlet turbulence intensity of 10 % (green), 20 % (blue) and 30 % (red).

farfield, the high k values are of less consequence at $x=-261$ m and -211 m. When the flow leaves the forest behind, the turbulent structures close to the terrain ($x=-161$ m) increase again, and they increase faster at a higher atmospheric turbulence intensity. At $x=-111$ m the flow is affected by an adjacent building, so for all turbulent intensities except for 20 % similar k values are obtained until $z=50$ m. At the top of building B the peak in k is more pronounced according to the applied turbulence intensity and almost doubled for $I=30$ % compared to 10 %.

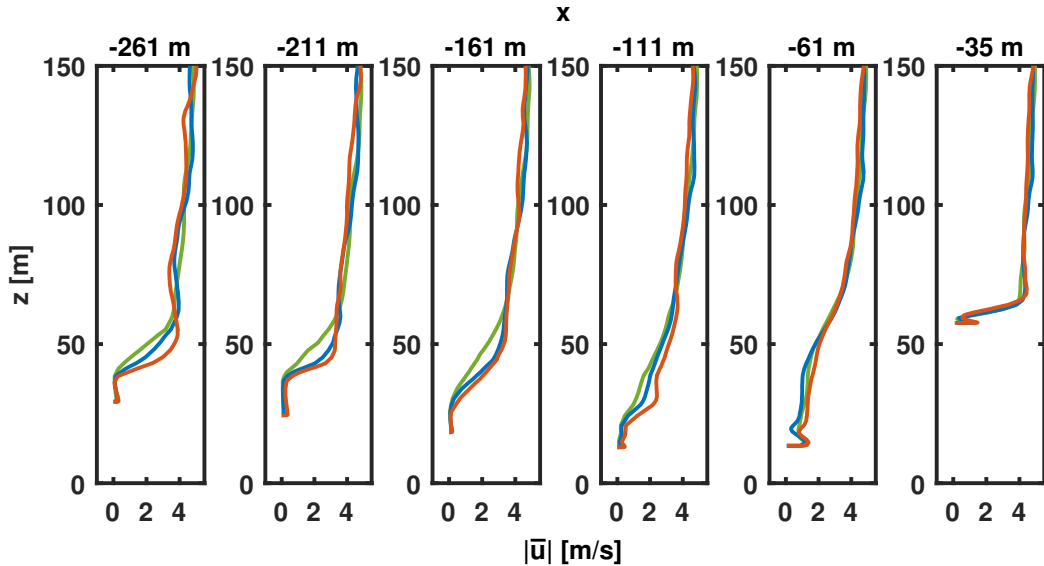


Figure 5.17: Time-averaged velocity magnitude evaluated in front of building A at $y=-4.5$ m with an inlet turbulence intensity of 10 % (green), 20 % (blue) and 30 % (red).

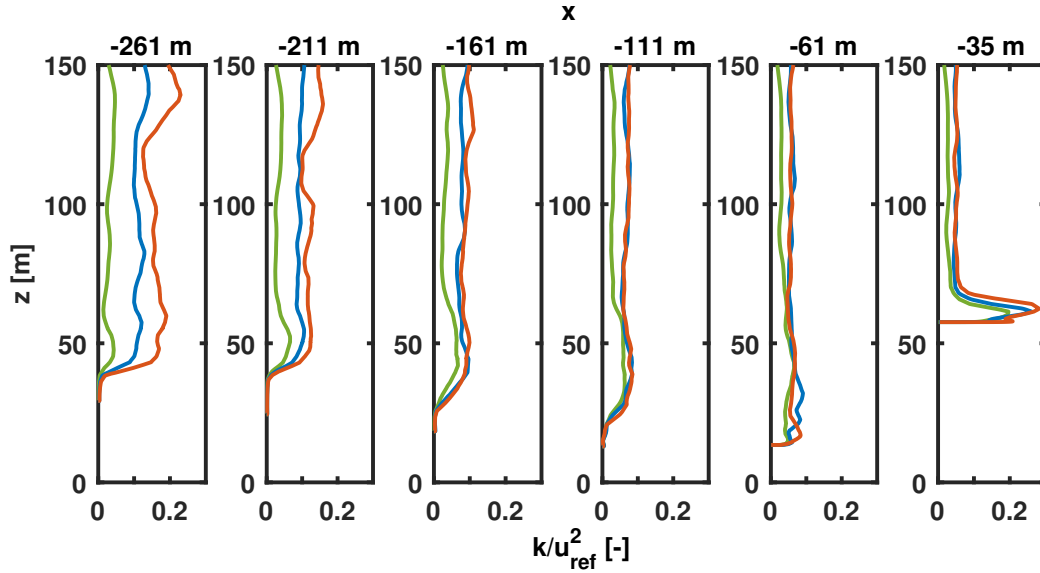


Figure 5.18: Turbulent kinetic energy evaluated in front of building A at $y=-4.5$ m with an inlet turbulence intensity of 10 % (green), 20 % (blue) and 30 % (red).

The time-averaged velocity magnitude in front of building A, indicated by the red points in fig. 5.14, is visualised in fig. 5.17. Combined with a more declining terrain, the effect of higher wind speeds at lower heights in forested zones for higher atmospheric turbulence intensities is more developed than compared to the inflow to building B. But within the forested zone a higher turbulence intensity does not lead to higher k values due to the damping of the forest. At $x=-111$ m the wind speed increases faster at $I=30\%$ when it hits the second forested zone which is located behind the dividing road. This is due to the effect similar to the step flow as described above. After leaving the forest, the wind speed is approximately 1 m/s higher for $I=30\%$ than lower turbulence intensities. The difference in wind speed disappears at a height of $z=50$ m. Since the roof of building A is located higher than $z=50$ m, the increased wind speed is not noticeable above the building. Thus, the wind speed above the high-rise buildings does not depend on the atmospheric turbulence intensity.

Fig. 5.18 visualises the turbulent kinetic energy evaluated along the same evaluation lines as the velocity magnitude at $y=-4.5$ m. Note, that the turbulent kinetic energy in the far field decreases when the wind flows through the domain. This occurs due to numerical dissipation and because turbulence scales larger than 50 m are not considered in the simulation due to the inflow condition. Larger turbulence scales would need more time to dissipate because they contain more energy. In and above the forested zone, the same characteristics are observed as in the inflow region to building B. The forested zone does not give any additional contribution to the turbulent kinetic energy at $I=30\%$. At $x=-111$ m and -61 m the influence of the atmospheric turbulence intensity can be neglected until a height of 50 m above the ground, since the vegetation and the buildings dominate the air flow. At the building A, k increases with the atmospheric turbulence intensity

in the recirculation zone, unlike the velocity magnitude k . As a result the height of the recirculation zone above the building increases with I . That means that the gradient of k towards the far field remain constant for various I .

5.3.3 Investigation of different vegetation modelling

Another simple way to consider a forest in a simulation is to represent the forest by solid bodies which are not meshed, so the flow has to pass around. This method is simulated and compared to simulations in which the forest is modelled by the vegetation model and without any forest considered. For the numerical setup of these simulations it is referred to chapter 6.2. The reference height z_{ref} is 240 m and the reference velocity u_{ref} is 8 m/s, since the reference velocity could be directly measured at that height. The following subsection is extracted and partially modified from a previous publication of von der Grün et al. [50].

In the following study, different evaluation lines are used. The lines are placed in the topography from $x/H_{t,\text{max}}=-10$ to $x/H_{t,\text{max}}=-4$ and at $y = 0$, as shown in Fig. 6.5. The inflow plane is located at $x/H_{t,\text{max}}=-12$. In contrast to the previous study about the investigation of the turbulence intensity, the time-averaged streamwise velocities are evaluated. These are shown in fig. 5.19 over the height evaluated along lines located at $x/H_{t,\text{max}} = -10$ to 0 which in front of building B. The variable $H_{t,\text{max}}$ describes the maximal tree height which is 25 m. The forested zone extends up to around $x/H_{t,\text{max}} = -7$. While the red line represents the velocity without any considered forested zone, the black line shows the velocity distribution obtained with the forest modelled by the vegetation model and the green line represents the simulation with the forest modelled as a solid body, as illustrated in fig. 6.3. In the evaluation only the flow until $x/H_{t,\text{max}}=0$ is considered because behind the high-rise buildings the flow is mainly affected by the buildings. In the centre of the forest at $x/H_{t,\text{max}}=-10$, the impact of the forest is quite significant. Without the forest the velocity profile adopts a simple power law. As mentioned in section 5.3.2, the velocity curve inside the forest, modelled by the vegetation model, has a mirrored shape as the drag force implemented according to the a -curve in fig. 4.3. However, in the forest, modelled as a solid body, the velocity curve is just a shift in z -direction from the simulation without the forest. The flow above the trees is much slower in the forest, modelled by the vegetation model, since local tree heights are considered causing a rougher surface. A similar behaviour can be observed at $x/H_{t,\text{max}}=-8$ for the green and red curve. The velocity in the forest, modelled by the vegetation model, is more damped inside the forest and the boundary layer above the trees is pronounced thicker. The evaluation line at $x/H_{t,\text{max}}=-6$ is already located behind the forested zones. In all cases a small recirculation zone at the ground is observed which is due to the influence of a nearby building

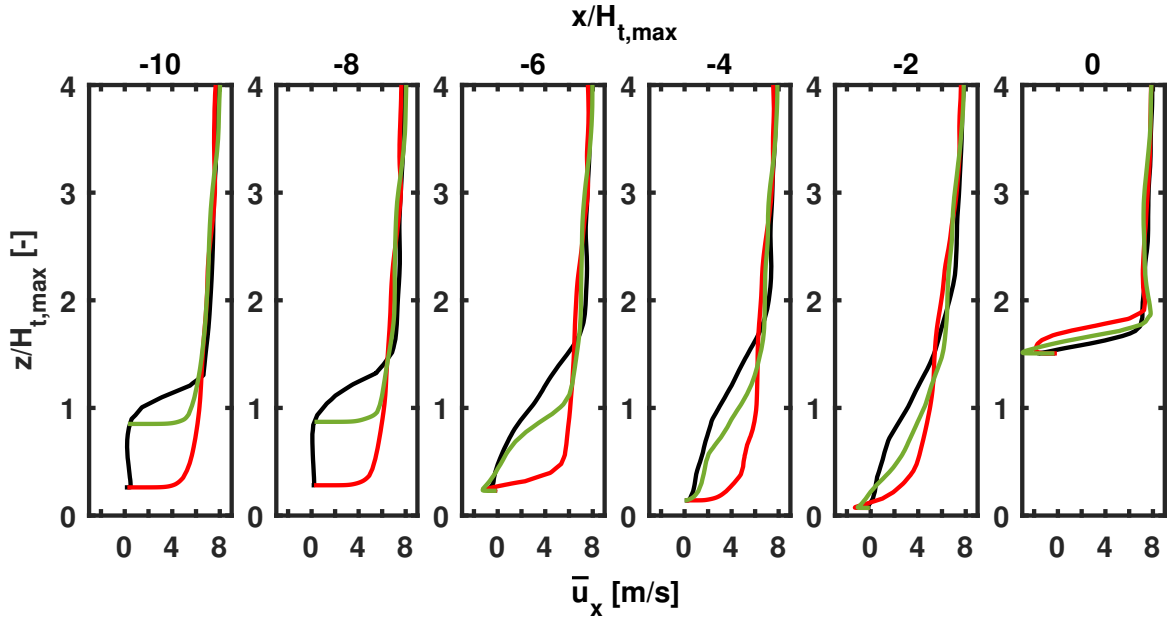


Figure 5.19: Time-averaged streamwise velocities u_x plotted over height with different types of forests: volume force modelled forest (black), solid body modelled forest (green) and without forest (red), based on [50].

and the wake behind the forest. Once the flow leaves the vegetation behind, its influence is still visible until $z/H_{t,max}=1.5$ and 1.0 for the solid body forest. At $x/H_{t,max}=-4$ the flow is more decelerated due to the sloping terrain. The recirculation zone at the ground at $x/H_{t,max}=-2$ is generated due to a flat building located upstream of the evaluation line. At a height of $z/H_{t,max}=2$ the velocities are higher when the forest is included in the simulations due to local blockage effects of the forest. Above the high-rise building at $x/H_{t,max}=0$, the flow is detached in the recirculation zone, followed by a high velocity gradient and an acceleration zone due to the sharp edge of the building which is also confirmed by El Bahlouli et al. [36]. The higher the tree heights, the higher the blockage ratio and the higher the velocity above the boundary layer. This leads to stronger velocity gradients and higher wind speeds at lower heights above the building at $x=0$.

Overall, the simulation with the solid body forest shows a more unrealistic velocity profile and higher wind speeds directly above the forest. On the top of a high-rise building a strong separation of the flow with high velocity gradients is observed. With regard to small wind turbines, the location has to be chosen carefully here. If it is mounted to low, directly on the roof top, the energy yield would be quite low, since there is a recirculation zone with low or even negative velocities. Increasing the height of the wind turbine, high velocity gradients lead to unbalanced loads and higher damages. A general statement is difficult to make because the location is always related to the specific terrain, building and vegetation.

A general prediction at what tree height a forested zone can be neglected in the simulation is very difficult because additionally, the complex terrain may influence the local flow field

besides the tree heights and the standard deviation of tree heights. But as a main result of the forest model study it is to say that permeable modelled vegetation clearly change the velocity field compared to vegetation modelled as solid bodies. This study further shows the importance of a permeable vegetation model. Thus, this model is used for the other simulations in this work.

5.3.4 Summer - winter comparison

The tree foliage can be set in the vegetation model via the LAI. In the simulation of the wind flow in the winter, a LAI of 0.5 [23] for deciduous trees is taken. However, in the simulations of the wind flow in the summer, a LAI of 3.5 [23] is taken. The profile of a over the tree height is adapted to the LAI as shown in fig. 4.3. The time-averaged

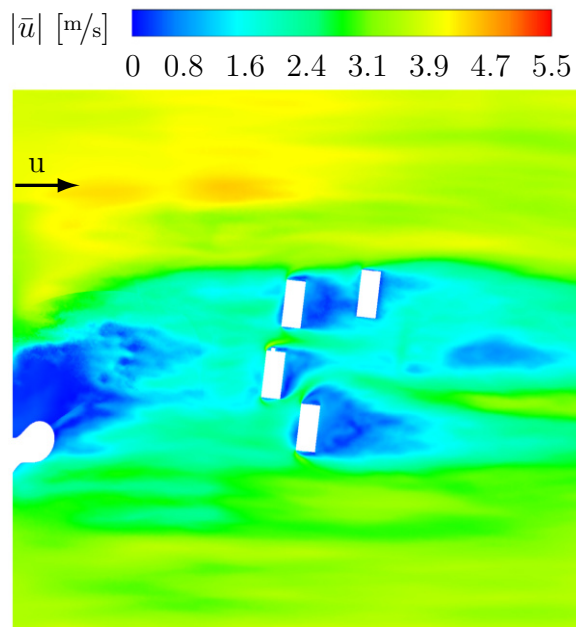


Figure 5.20: Time averaged velocity magnitude of the wind field with summer foliage in the forested zone (LAI=3.5).

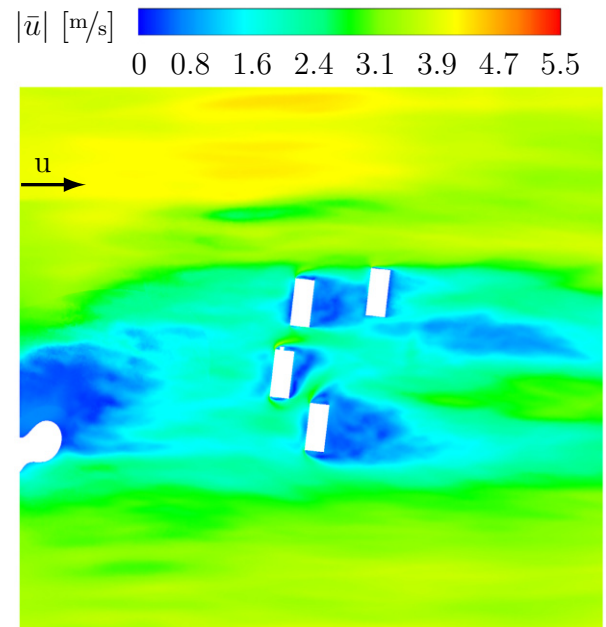


Figure 5.21: Time averaged velocity magnitude of the wind field with winter foliage in the forested zone (LAI=0.5).

velocity magnitude evaluated at a height of $z=15$ m for the summer and winter foliage is visualized in fig. 5.20 and 5.21. Obviously, in summer the velocities within the forested zone are lower due to the higher resistance caused by the leaves. Due to the higher blockage of the flow in the forested zones, the flow is turned around the forest, resulting in higher local wind speeds around forested zones.

In fig. 5.22 the time-averaged velocity magnitude which is evaluated over the height above the ground in front of building B at $y=80$ m is shown. The velocities obtained with the summer foliage is visualized in blue and with the winter foliage in red. The evaluation

lines at $x=-261$ m and $x=-211$ m are located within the forest. Thus, the different foliation directly affects the wind speed inside the forest. The wind speed is lower in the summer and higher in the winter inside the forest. However, due to the higher blockage in the summer the flow is accelerated above the forest at a height of 50 m compared to the flow in the winter. The evaluation lines further downstream at $x=-161$ m and $x=-111$ m are located between another forest and a building. Along these lines the flow is more accelerated like a nozzle flow due to the narrowing cross-section between the building and the forest. Consequently, higher wind speeds are reached in the summer due to the building and the higher blockage of the forest in the summer than in the winter. This

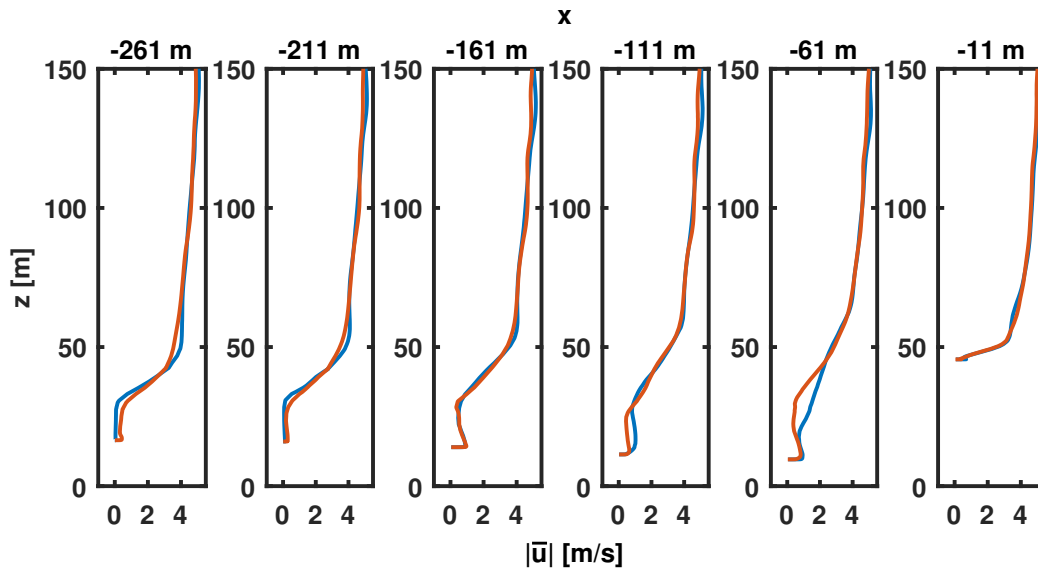


Figure 5.22: Time-averaged velocity magnitude evaluated in front of building B at $y=80$ m with summer foliation (blue) and winter foliation (red).

effect disappears when the height of the forest is reached. At $x=-61$ m this effect is more pronounced and shows higher velocities in the summer. The maximum difference in the wind speed between summer and winter amounts to around 1.5 m/s . With increasing height that difference vanishes due to the decreasing influence of the terrain, vegetation and buildings. At $x=-11$ m the velocities are evaluated in the center at the top of building B which is supposed to be a suitable location for wind turbines due to the height of the building. The effect of different foliation in the forest can be neglected because the differences in the wind speeds obtained in the summer and in the winter are just marginal. When the flow hits a high building, the flow is strongly dominated by the building itself and its shape.

The turbulent kinetic energy is evaluated along the same evaluation lines as the velocity magnitude using equal legend colours. The results are shown in fig. 5.23. A characteristic feature of the wind flow over a forested zone is the increase in k above the tree crone. This increase becomes stronger with increasing length of the forested zone since the k accumulates above the forest. In summer the k production over the forested zone is

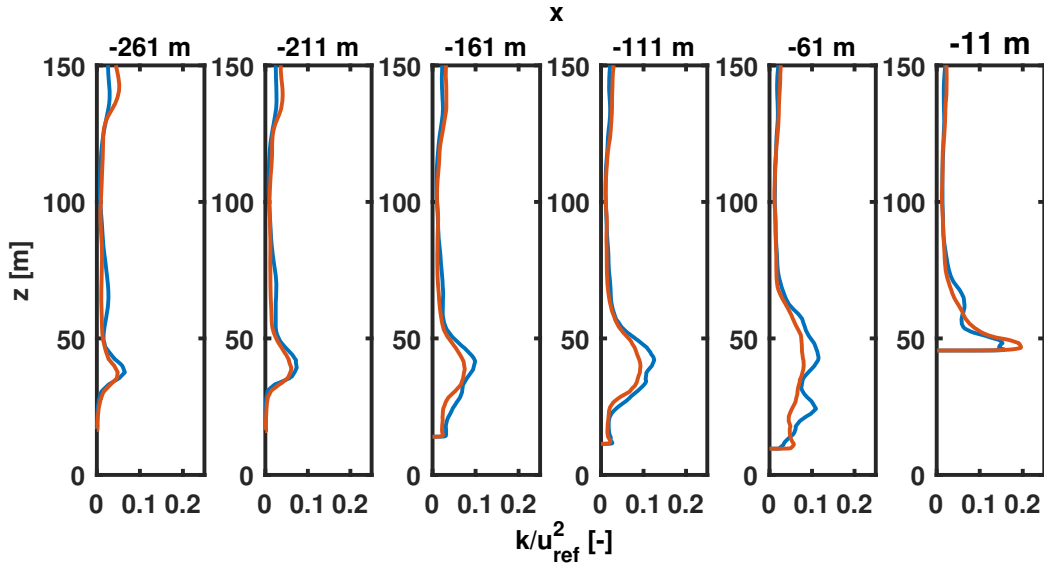


Figure 5.23: Turbulent kinetic energy evaluated in front of building B at $y=80$ m with summer foliage (blue) and winter foliage (red).

higher than in the winter. A reason for that is that the roughness on top of the trees caused by locally varying tree heights increases in summer due to the higher resistance in the summer caused by higher LAI values. The high k zone is carried with the flow towards the buildings, as observed at $x=-161$ m and $x=-111$ m. Furthermore, the high k zone is affected by an adjacent building which explains the wavy structure of k at $x=-61$ m in the summer. Above building B k increases strongly to its maximum within the boundary layer and decreases with increasing distance to the roof top. As mentioned above, the flow above the roof top of a high-rise building is more affected by the building itself than by an upstream located vegetation zone. Fig. 5.24 shows the time-averaged velocity magnitude

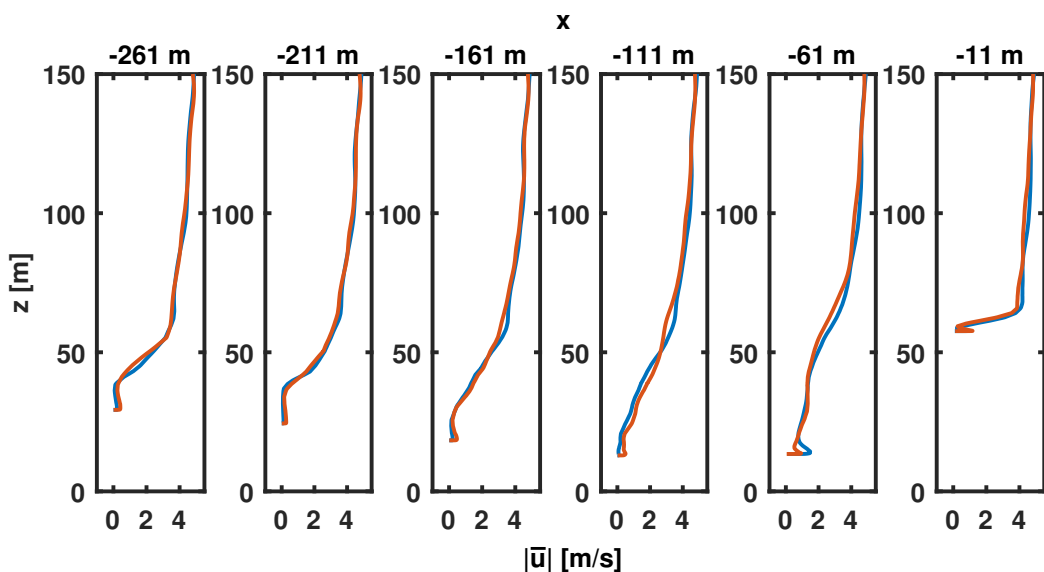


Figure 5.24: Time-averaged velocity magnitude evaluated in front of building A at $y=-4.5$ m with summer foliage (blue) and winter foliage (red).

evaluated vertically in front of building A at $y=-4.5$ m. The vertical evaluation lines are located at a respective distance of 50 m in x-direction to each other. The velocity obtained with the summer foliage is visualized in blue and with the winter foliage in red. The evaluation lines from $x=-261$ m to $x=-111$ m are located within the forest. Between $x=-161$ m and $x=-111$ m a road divides the forest. At $x=-261$ m the difference in the velocities is more developed than further downstream in the forest at $x=-161$ m because the flow is more decelerated the longer it flows through the forest. The velocity gradient near the top of the forest becomes smaller with increasing x-direction. Due to the decreasing terrain height a diffuser-like flow with an increasing cross-sectional area is developed in which the velocity of the flow increases slower over the height. For example, at $x=-261$ m the wind speed increases from 0 to 4 m/s within a height of 20 m and at $x=-111$ m the wind speed needs approximately 50 m in height to reach 4 m/s . The influence of the denser foliage is also visible in the second part of the forested zone which is divided by the road, resulting in higher wind speeds of 0.5 m/s . Similar to the flow in front of building B, a zone with higher wind speeds in summer is observed, which occurs due to the higher blockage in the forest, as mentioned above. When this zone hits building A, the wind speed is slightly increased 10 m over the rooftop. Thus, higher wind speeds and energy yields are observed in summer. Fig. 5.25 visualise the turbulent kinetic energy evaluated along the same

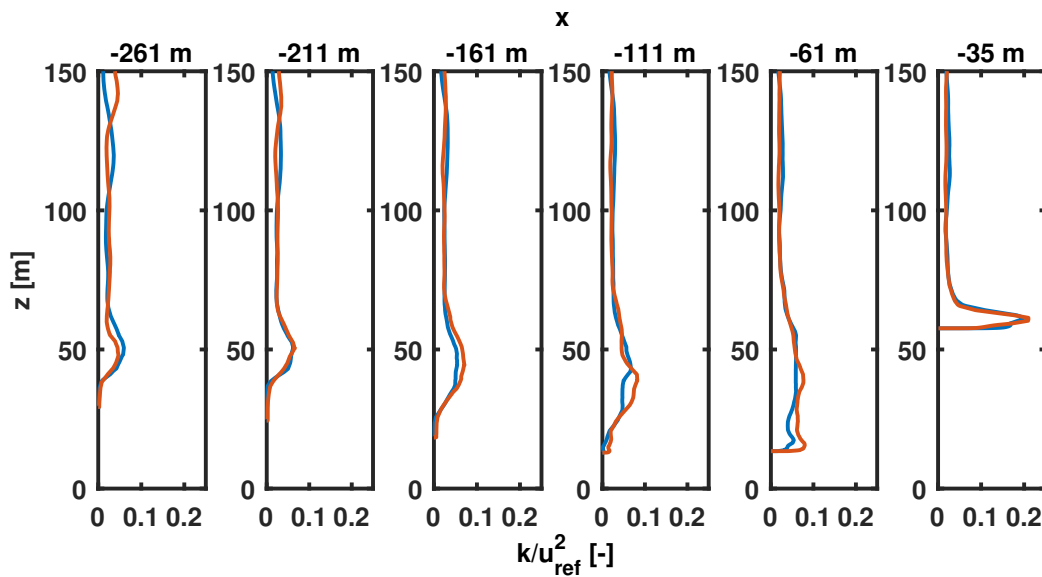


Figure 5.25: Turbulent kinetic energy evaluated in front of building A at $y=-4.5$ m with summer foliage (blue) and winter foliage (red).

evaluation lines as the velocity magnitude at $y=-4.5$ m. As can be observed in fig. 5.23 k is reduced to zero within the forested zone since the velocity fluctuations are damped due to the increased resistance within forested zones. At $x=-261$ m the k values over the treetop are higher in summer time because the rough upper surface of the forest gets more solid due to the higher resistance in the forest model in summer. This effect vanishes at $x=-211$ m and turns to the opposite at $x=-161$ m. At $x=-111$ m the flow is evaluated after

passing the road, what produces additional k in summer and winter time. Within the forested zone the fluctuations are increased in winter due to lower damping. Since the higher fluctuations are carried with the flow, k is also higher near the terrain at $x=-61$ m. Above the rooftop of building A no noticeable effect can be observed in k between summer and winter foliage because the flow is mainly affected by the building itself.

The effect of different foliations of the forests associated to the corresponding season can be neglected when the focus is on the wind flow above buildings nearby. There is almost no change in the wind speed and in the turbulent kinetic energy on top of the buildings A and B.

5.3.5 Investigation of different tree heights

In this subchapter, the influence of local tree heights is investigated. For this, the original local tree heights within all forested zones are multiplied by a factor of 0.5 and 1.5. The profile of a is adjusted accordingly. So, tree heights of 50 % and 150 % are used in the investigation. The maximum tree height for the 50 % case amounts to 12.5 m and 37.5 m for the 150 % case. The time-averaged velocity magnitude is evaluated at a height of $z=15$ m for the 50 % and 150 % of the local tree heights and illustrated in a plane view in fig. 5.26 and fig. 5.27, respectively. As expected, the increased tree heights show a large influence on the flow field. Due to the higher blockage of the forested zone at a tree

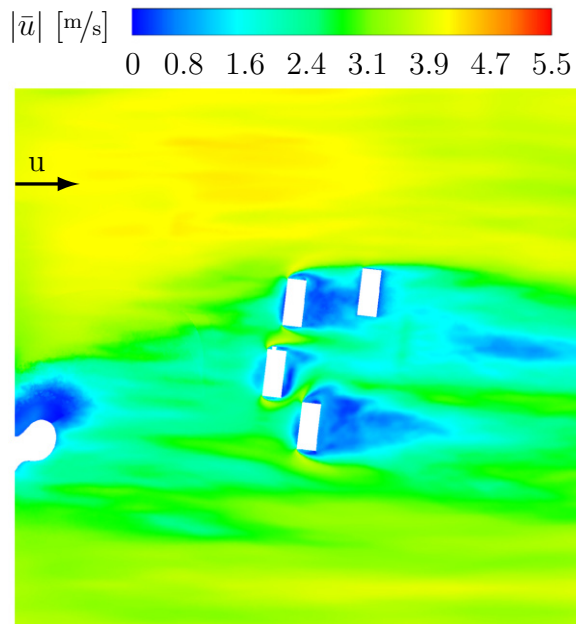


Figure 5.26: Time-averaged velocity magnitude of the wind field with 50 % of the tree height.

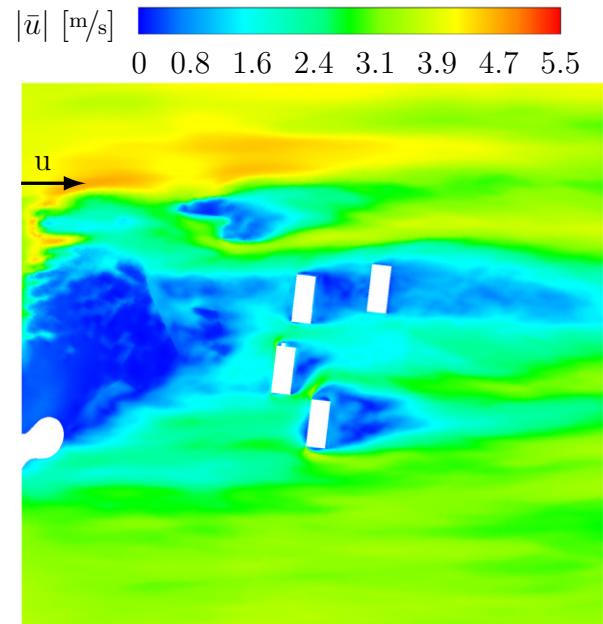


Figure 5.27: Time-averaged velocity magnitude of the wind field with 150 % of the tree height.

height of 150 %, the flow is deflected significantly around the forested zones and wakes behind them are formed. The wind speeds are 1 m/s higher around the forested zones. The

wakes are larger at a tree height of 150% so that the buildings are now included in the wake, resulting in lower wind speeds around the buildings. The time-averaged velocity magnitude in front of building B is visualised in fig. 5.28 along the same evaluation lines as above. Fig. 5.28 clearly shows that the velocity profiles are shifted upwards at the increased tree heights which is shown, e.g. at $x=-261$ m and -211 m. The blockage caused by forested zones increases with the tree heights so that the acceleration zone above the forest is more developed with higher wind speeds. This zone is carried with the flow but is fade out with increasing distance in x -direction to the forest. At $x=-111$ m the interaction between the adjacent building and the second forested zone causes a recirculation bubble with higher velocity magnitudes at the ground. The comparison of the velocities at $x=-261$ m and -61 m shows that the difference in the wind speed reduces from 4 m/s to 2 m/s and the influence of the tree heights vanishes with increasing distance in x -direction to the forest.

Above building B the wind shows an expected flow pattern, and lower tree heights lead to higher wind velocities. In the case of 50% of the original tree height, a small recirculation zone is formed at the rooftop which is not visible in the other cases. Fig. 5.29 visualises the turbulent kinetic energy evaluated along the same evaluation lines as the velocity magnitude at $y=80$ m using equal legend colours. Looking at the two evaluation lines in the forest, the characteristic high k values are shifted upwards corresponding to the height of the forest and the maximum value increases with the height. Since locally adapted tree heights are used in the forested zones and multiplied with a factor for this study the difference between the highest and lowest tree becomes higher and the top of the forested zones becomes rougher so that more k is produced. Only in the case of 150% of the original tree height, the high k values are carried with the flow over the surrounding buildings.

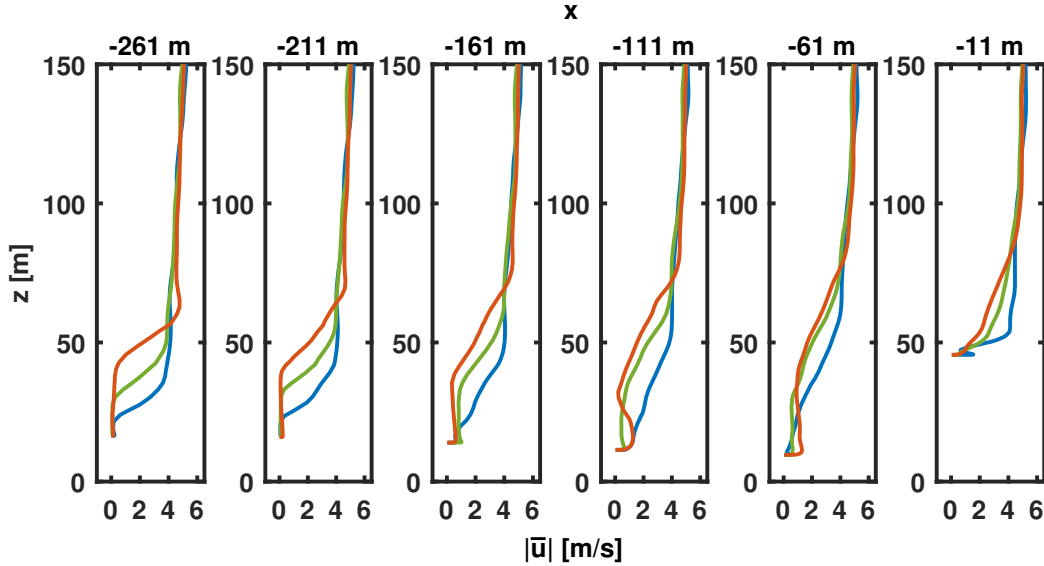


Figure 5.28: Time-averaged velocity magnitude in front of building B at $y=80$ m with tree heights of 50 % (blue), 100 % (green) and 150 % (red) related to the original tree heights.

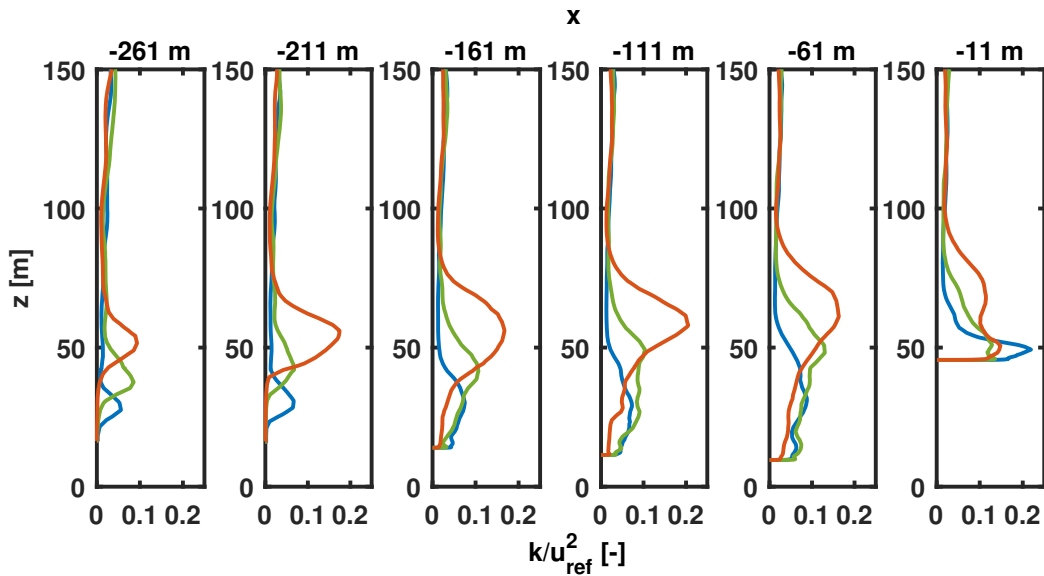


Figure 5.29: Turbulent kinetic energy evaluated in front of building B at $y=80$ m with tree heights of 50 % (blue), 100 % (green) and 150 % (red) related to the original tree heights.

However, from $x=-161$ m to $x=-61$ m the flow is affected by the buildings up to a height of $z=30$ m. The high k values generated above the forested zones are entirely damped at $x=-61$ m when 50 % of the original tree height is used in the simulations. The main contributor to the k values at the top of building B are the high k values generated above the forested zones at a tree height of 100 % and 150 %. In the case of 50 % of the tree heights, the peak of k at the rooftop of building B is caused by the strong velocity increase as shown in fig. 5.28.

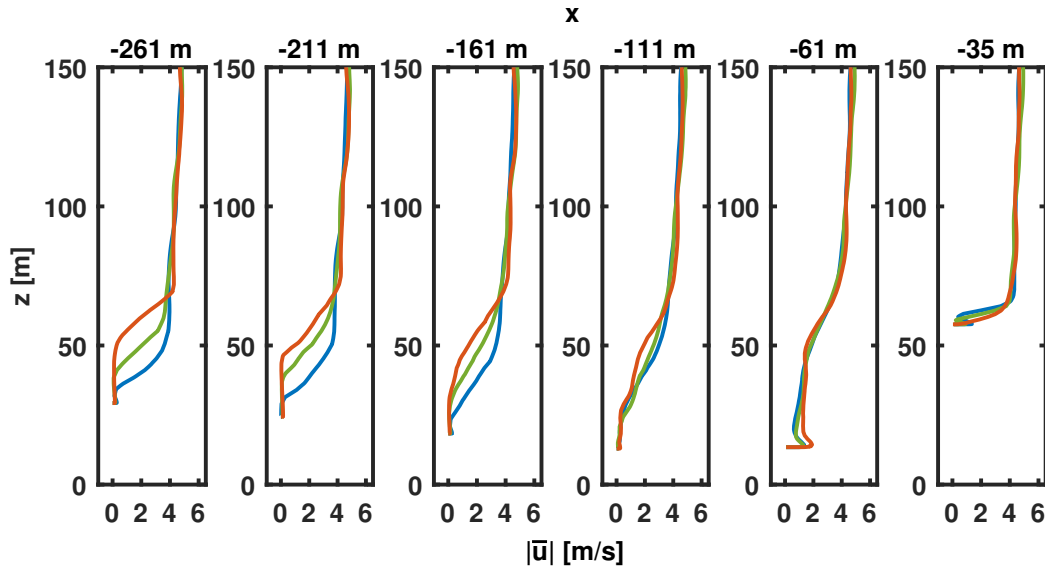


Figure 5.30: Time-averaged velocity magnitude in front of building A at $y=-4.5$ m with tree heights of 50 % (blue), 100 % (green) and 150 % (red) related to the original tree heights.

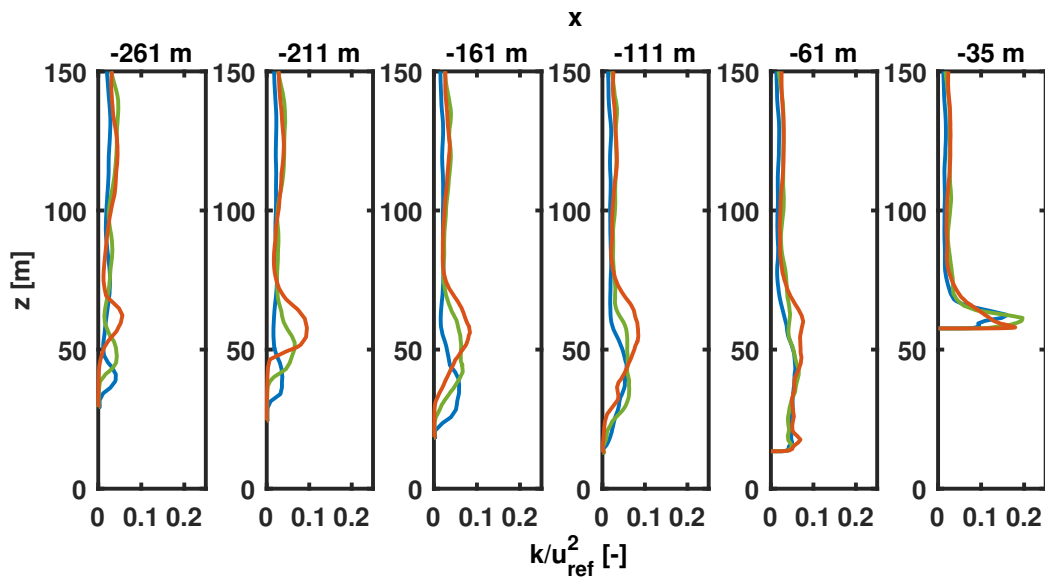


Figure 5.31: Turbulent kinetic energy evaluated in front of building A at $y=-4.5$ m with tree heights of 50 % (blue), 100 % (green) and 150 % (red) related to the original tree heights.

The wind speeds in front of building A along the vertical evaluation lines are illustrated in fig. 5.30. The flow shows a similar pattern as the flow towards building B and the same effects induced by various tree heights also occur here, such as the shifted upwards velocity profiles and the acceleration zone above the forest. At $x=-111$ m the influence of the tree height is almost vanished and it decreases stronger than in front of building B. The reason is that the flow is dominated by the declined terrain and is characterised by a diffusion-like flow pattern. The flow above building A can be divided into a first zone closer to the roof and a second zone more distant to the roof. In the first zone, higher wind

speeds at higher tree heights are obtained since at lower tree heights a small recirculation zone at the roof top is formed preventing higher wind speeds. However, in the second zone, higher wind speeds are obtained at lower tree heights.

Fig. 5.31 visualises the turbulent kinetic energy evaluated along the same evaluation lines as the velocity magnitude at $y=-4.5$ m. Along the evaluation lines located in the forest ($x=-261$ m to $x=-161$ m) the same characteristic flow features as in the inflow region to building B are observed. At $x=-111$ m the high k values generated above forested zones are transported with the flow, but in the first 20 m above the ground the influence of the tree height is lower and at $x=-61$ m it is almost vanished. Above building A, the major part of k is produced in the shear layer between the centre of the recirculation bubble and the farfield. The shear layer is characterised by high velocity gradients as shown in fig. 5.31. But with higher tree heights a zone with high k values is developed above the recirculation zone. The height of the zone increases with the tree heights.

The tree height of the forest highly affects the wind speeds and the turbulent kinetic energy above the forest and also on the buildings A and B. Thus, a correct determination and the inclusion of tree heights in the simulations are crucial for precise predictions of the wind field above buildings and confirms the importance of the consideration of local tree heights in the simulations. As a consequence, the local tree heights are considered in the simulations which will be used to determine the local AEP values.

5.4 Simulation of surrounding buildings

In this section, surrounding buildings outside the area of interest are added to the existing buildings in the computational domain. The influence of the surrounding buildings on the flow pattern is investigated by comparing the wind flow with and without the surrounding buildings.

5.4.1 Site information

In fig. 4.1 the surrounding buildings and the buildings of interest are shown. The objective of this study is to investigate how the surrounding buildings influence the flow and the energy yield in the area of interest, especially at the buildings A and B. For that, 48 surrounding buildings are considered additionally in the simulations and should be prepared according to the building preparation steps described in chapter 4.2 and the meshing procedure described in chapter 4.6. To avoid these inefficient manual preprocessing steps, the 48 surrounding buildings are modelled by the building model described in chapter 4.5.

A further objective of the study is to improve the simulation results. By adding the surrounding buildings to the domain the inflow towards the area of interest becomes more

realistic. Hence, the prediction of the energy yield is expected to be more reliable. A precise prediction of the wind flow is crucial for a location decision of wind turbines. Due to the fact that the wind power increases with the third power of the wind velocity, an error of 10% in the wind velocity prediction leads to an error of 30% in the energy yield prediction. It has to be noted that the additional buildings will only improve the results from these wind directions from which the buildings are located in the inflow regions of these wind directions.

For the literature related to surrounding buildings and their influences on the flow field it is referred to chapter 1. The main statement is that the influence depends on local conditions of the simulated site and it has to be investigated individually.

5.4.2 Simulation setup

The left part of fig. 5.32 visualises the computational domain used in the simulations within this study. Herein, the geometries of the surrounding buildings are shown as represented by the building model. The surrounding buildings are coloured by their height. For comparison the right part of fig. 5.32 shows all buildings as solid geometries and also emphasizes how accurate the building geometries are captured by the building model. Note that simulations are only performed with the surrounding buildings modelled by the building model as shown in the left part of fig. 5.32.

The size of the domain corresponds to the domain shown in fig. 5.13 as it is used in

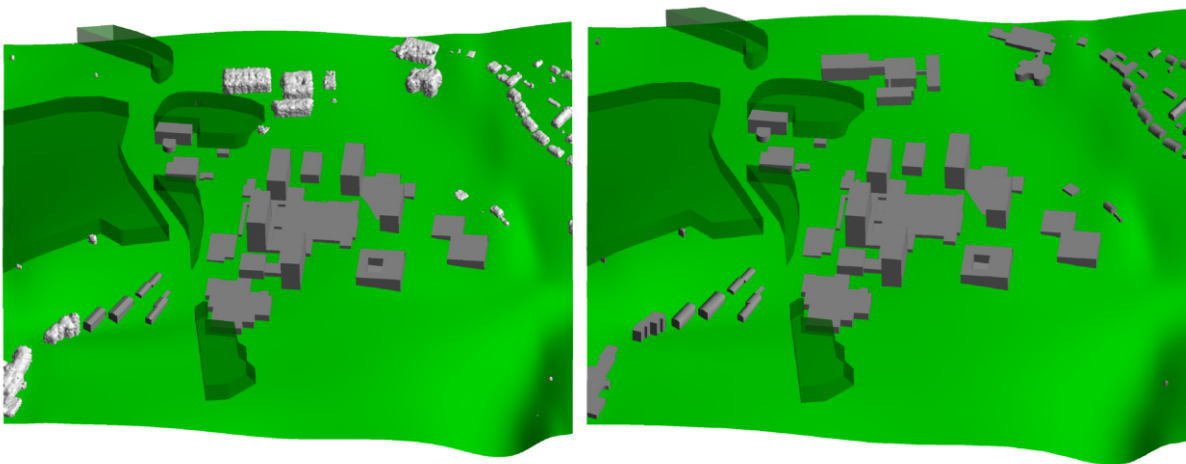


Figure 5.32: University campus Tübingen with modelled surrounding buildings (left) and surrounding buildings with solid geometries (right).

the sensitivity study of environmental parameters. The forested zones are considered in the study and represented by the transparent green bodies in fig. 5.32. The forested zones are modelled as described in chapter 4.4. To consider the effect of additional surrounding buildings from different wind directions, the simulations are performed from

a wind direction of 60° , 120° , 240° and 330° . Due to the quadratic ground area of the domain, the same mesh can be used for all simulated wind directions. The synthetic turbulence generation method requires a flat inflow plane, thus a polygonal inflow plane can not be used in this case. A turbulence length scale of $L = 50$ m is chosen. The mesh is generated according to the description in chapter 4.6 resulting in a total cell number of approximately 65 million cells.

The simulations are carried out with a turbulence intensity of 10 % according to a neutral ABL. The turbulence is synthetically generated at the inlet plane. The power law

$$u(z) = \left(\frac{z}{10 \text{ m}} \right)^{0.21} \cdot u_{\text{ref}} \quad (5.7)$$

is used as a velocity profile and is applied at the inflow boundary plane where u_{ref} is 2.95 m/s. The reference velocity for the university campus in Tübingen is taken according to the wind atlas of Baden-Württemberg [3]. For the side and the upper surfaces of the domain the so-called 'symmetry' boundary condition is used in Fluent, that means all variables are forced to be parallel to the boundary plane at the surface. For the outlet a pressure-outlet boundary condition is used. The terrain and the building surfaces are all treated as no-slip walls. The Co number amounts to 0.25. The stabilization time is 147 s and the averaging time is 240 s.

5.4.3 Wake flow analysis

For the sake of brevity only the results of the wind field simulations using wind directions of 240° and 330° are presented. In fig. 5.32 the wind direction of 240° corresponds to the direction when the wind enters the left side of the domain. The wind direction of 330° corresponds to the direction when the wind enters the upper side of the domain. The time-averaged velocity magnitude is evaluated at a height of $z=15$ m and illustrated in a plane view in fig. 5.33 for a simulated wind direction of 240° . The left figure shows the velocity field obtained when surrounding buildings (highlighted in silver) are included and the right figure shows the velocity field without the surrounding buildings. The characteristic differences in the flow field described in the following refer to the marked numbers shown in fig. 5.33. At point 1, the velocity is higher when the surroundings buildings are not considered in the simulation. The surrounding buildings located between a hill and a forested zone block the flow, so that the velocities are lower in the wake behind the buildings and the air is forced to flow over the surrounding building. That leads to lower velocities behind the hill at point 1. The higher the buildings or the more the cross-section between the hill and the forested zone is blocked by the surrounding buildings the more the wind speed is decreased in the wake and the wider is the wake. However, when there would be only residential buildings like single family homes instead of big office buildings, as in this case, the effect is less pronounced and higher energy yields could

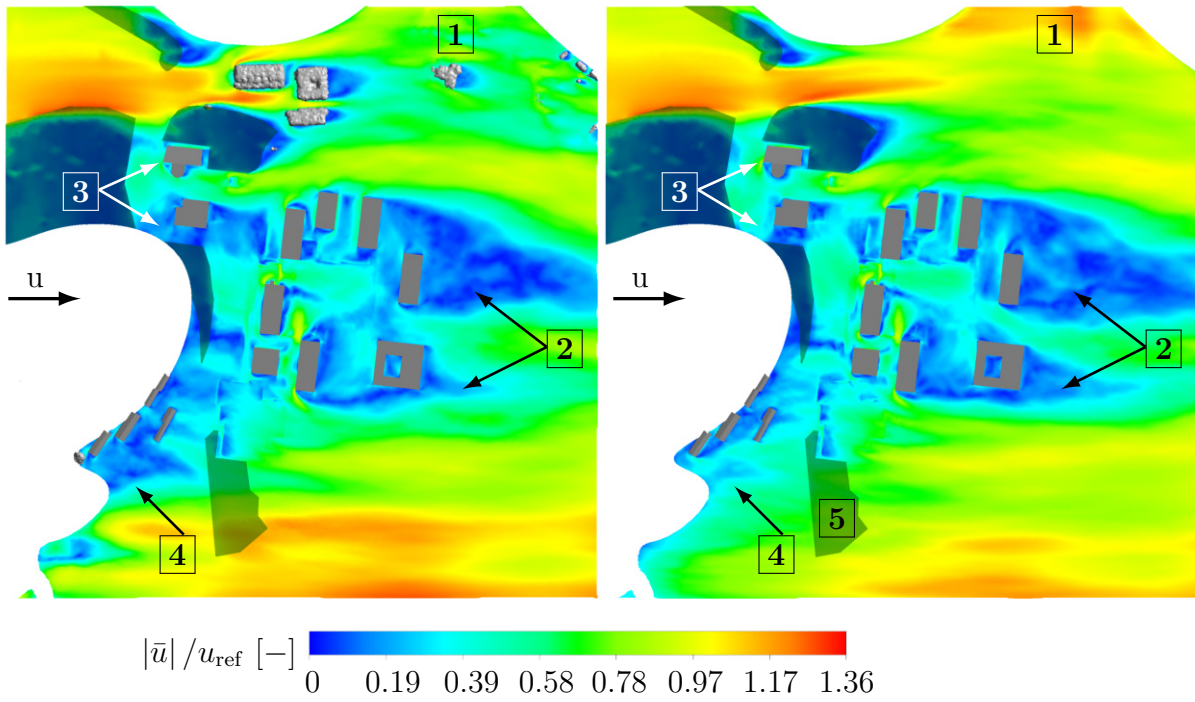


Figure 5.33: Time-averaged velocity magnitude with a simulated wind direction of 240° , evaluated at $z=15$ m with surrounding buildings included (left) and without surrounding buildings (right).

be observed at point 1. In location 2, the wakes are formed by the central buildings. Basically, the surrounding buildings are located in the upper and the lower part of fig. 5.33 which increases the blockage in the upper and lower part. That leads the flow more to the central buildings. Thus, higher velocities are obtained above the central buildings resulting in lower wake lengths behind the central buildings. In this case, the height of the surrounding buildings and the projected cross-section of the buildings towards the inflow direction play a crucial role for the blockage. For example, a long sleek building causes a much higher blockage when it is oriented in its longitude direction perpendicular to the wind direction compared to the case when it is oriented in line with the wind direction. In zone 3, higher wind speeds are obtained without the surrounding buildings. The upper arrow in fig. 5.33 points towards a building edge with higher velocities. The zone, to which the lower arrow points, shows higher wind speeds, too. The reason for that is that due to the blockage of the buildings added in the upper part the higher wind velocities are shifted to higher heights with lower velocities near the terrain as already mentioned in the analysis of points 1.

The area around point 4 becomes a big wake zone with low velocities when the surrounding upstream building is considered in the simulation. This building slows down the flow around the adjacent buildings. Especially high or dominant surrounding buildings can cause huge wakes which let the wind speed decrease over buildings which are located within or close to these wakes. When high or dominant surrounding buildings are not included in the simulations and in the energy yield calculation, the prediction of the energy

yield would fail.

The forest around point 5 does not affect the velocity field because the tree heights are too low. The time-averaged velocity magnitude is illustrated in a plane view in fig. 5.34 for a

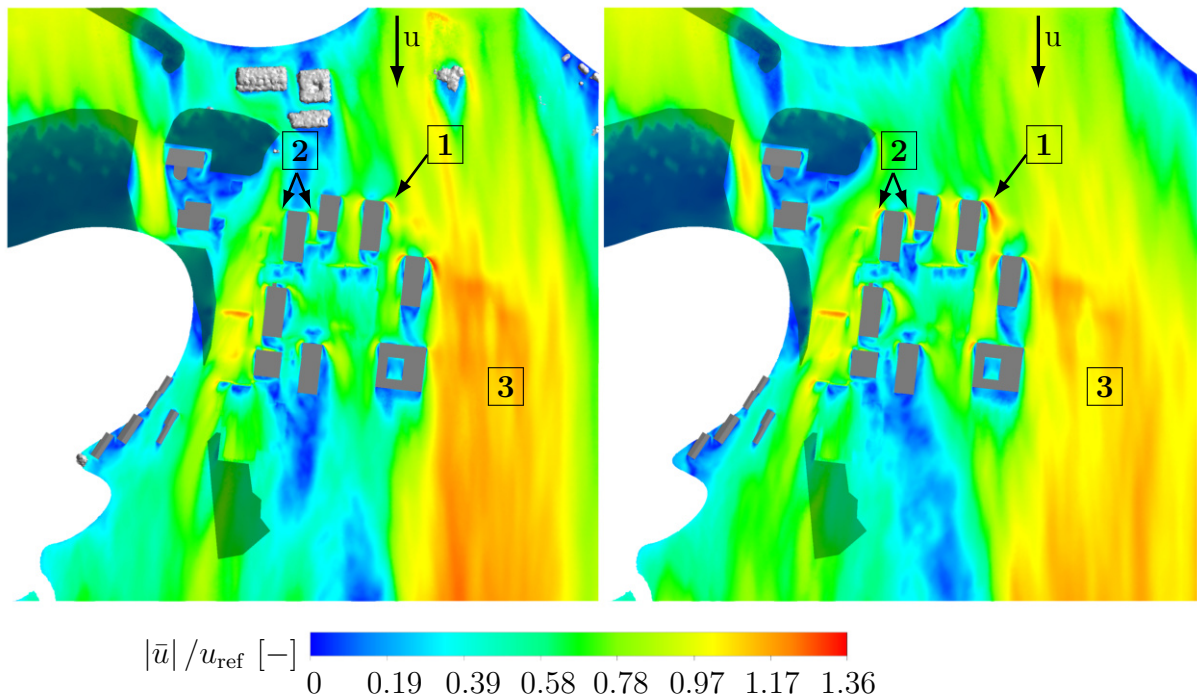


Figure 5.34: Time-averaged velocity magnitude with a simulated wind direction of 330° , evaluated at $z=15$ m with surrounding buildings included (left) and without surrounding buildings (right).

simulated wind direction of 330° . The left figure shows the velocity field obtained when the surrounding buildings (highlighted in silver) are included and the right figure shows the velocity field without the surrounding buildings. The locations used in the following to describe the characteristic differences are marked by numbered arrows in fig. 5.34.

Looking at the simulation results when the surrounding buildings are not included, point 1 could be considered as a good position for a wind turbine with locally increased wind speeds. But when the surrounding buildings are included in the simulation, it turns out that the velocity decreases from 4 m/s to 3.4 m/s . Consequently, it results in a wind energy loss of 62%. The reason for the velocity drop is the presence of the three big surrounding buildings in the upstream direction of the centre buildings. They cause a huge wake with reduced wind speeds which still affects the building edge at point 1. Smaller or lower surrounding buildings with a smaller wake would lead to higher wind speeds here.

Point 2 marks the edges of a building which is located directly downstream behind the three surrounding buildings. The building is now in the centre of the wake of the three surrounding buildings. When a succeeding building is located in a wake of a preceding building, the ratio of the sizes between the succeeding and the preceding building is important. For instance, when just a small shed would be located in front of a high building, then the shed can be neglected in the simulations. But in the opposite a high building,

located in front of the shed, highly affects the wind flow since the shed is located in the large wake of the high building. So it is not the building itself that matters, but the height ratio between the shed and the high building. But in this case the wind speed is dropped from 3.3 m/s to 2.7 m/s which leads to a loss in the energy yield of 82.5 %. That shows that surrounding buildings can significantly change the predicted energy yield when they are considered in the simulations.

The area around location 3 shows high wind speeds because this region is located in a valley which is enclosed by two hills at the inlet. So the flow is accelerated like a nozzle-like flow due to the narrowing cross-sectional area between the two hills. The surrounding buildings, located at the right side along the hill, further narrow the cross-sectional area of the valley and further increase the wind speed. Here, the complex terrain and the buildings interact and intensify the acceleration of the wind flow. This emphasizes the significance of the complex terrain in the simulations.

Since the buildings A and B are in the focus of the energy yield evaluation, the wind speeds on these buildings are analysed in the following for the simulated wind directions of 60° , 150° , 240° and 330° . The time-averaged velocity magnitude evaluated vertically in the centre of building A is shown in fig. 5.35 and of building B in fig. 5.36 with (red) and without (blue) surrounding buildings separately for each wind direction. It is noticeable that the velocity profiles differ from each other. When the wind comes from the direction of 60° and 240° a recirculation bubble is formed on the rooftop on the buildings A and B in comparison to the other wind directions. The reason for that is that building A extends much more in the direction of 150° and 330° and the wind flow attaches at the roof top of the building behind the recirculation bubble at the roof edges.

Note that the surrounding buildings are not located in the direct vicinity of the buildings A and B. That means that except for the wind direction of 330° at least another building or a forest is in between so that the wind field on building A and B is only influenced indirectly by the surrounding buildings. Regarding building A noticeable differences are observed from the simulated wind direction of 240° and in larger heights the wind direction of 330° . As mentioned in chapter 5.2.2 buildings, hills and forested zones can locally increase the blockage of the domain. Especially, high buildings and those which have a large projected area towards the wind direction are critical for blocking the domain. For the wind direction of 240° the blockage of the surrounding buildings located at the top and at the bottom in fig. 5.32 increase the blockage at the outer portions of the domain. The flow is guided and accelerated towards the central buildings, namely A and B. In consequence, higher wind speeds are obtained at lower heights above the rooftop.

Regarding the wind direction of 330° the surrounding buildings are located in the direct inflow behind a hill and towards building A and B as written above. Thus, a certain amount of air flows over the surrounding buildings with higher wind speeds and hits building B so that an increase of 1 m/s in the wind speed is observed directly at the roof top, which will have an impact on the estimated energy yield of a small wind turbine.

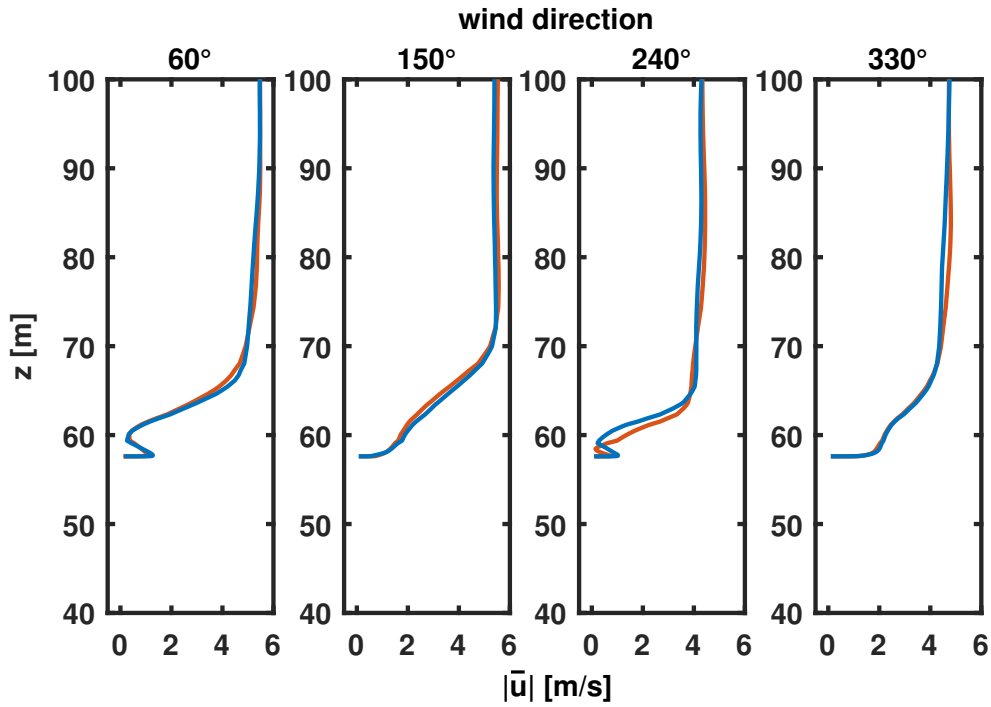


Figure 5.35: Time-averaged velocity magnitude on building A with surrounding buildings (red) and without surrounding buildings (blue).

However, this effect becomes visible on building A only at a height of 20 m above its roof. For small wind turbines here the difference between the models (with vs. without surrounding buildings) is not relevant.

Regarding the wind direction of 60° only on building B a noticeable effect is observed. The changes in wind speed is mainly caused by the location of the surrounding buildings around the hill, shown in the top right corner of fig. 5.32. Their blockage reduces the wind speed directly above the roof but increases the wind speed 25 m above the roof.

When the wind comes from 150° wind direction the wind speed does not change in the first 15 m above the roof on building B. Further up the wind speed increases due to the blockage of the surrounding buildings which are shown in the outer right and left areas of fig. 5.32. The surrounding buildings guide the flow towards the centre of the domain and accelerate the wind. But due to the fact that the increase in wind speed is observed from a height of 15 m above the roof, the differences between the models (with or without surrounding buildings) are not relevant for the estimated power production of a possible wind turbine. Underneath, the energy yield estimation for this wind direction is not affected. However, when the annual energy production is calculated, the wind speeds from several wind directions have to taken into account. This will be described in chapter 7.

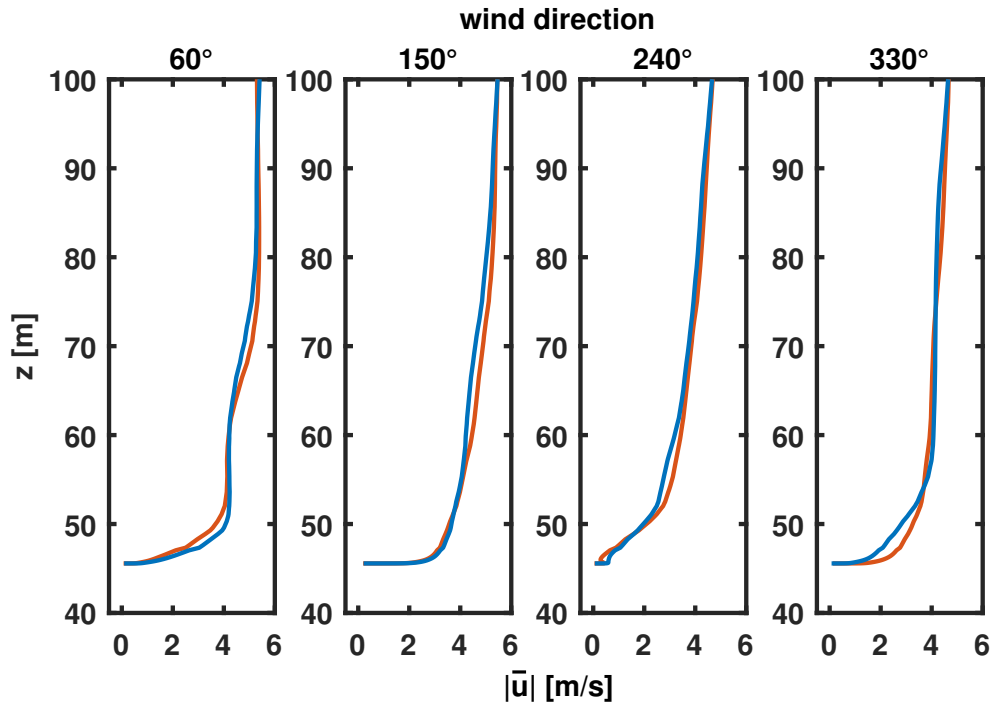


Figure 5.36: Time-averaged velocity magnitude on building B with surrounding buildings (red) and without surrounding buildings (blue).

The time-averaged velocity magnitudes obtained in the simulations using a wind direction of 240° and 330° are evaluated at the test site in Tübingen, wherein in the first simulations surrounding buildings are included in the domain and in the second simulations the surrounding buildings are neglected. The inclusion of surrounding buildings leads to different velocities, which will have an impact on the predicted energy yield. For that reason, surrounding buildings are considered in the calculation of the annual energy production.

5.5 Summary

In summary, at least the following values for the meshing parameters are chosen for the future numerical setup: A cell size of the main mesh of $\Delta = 1.5\text{ m}$ and a ratio of $\Delta_i/\Delta_{i,0} = 1$ is chosen, that means a terrain resolution of $\Delta_t = 3\text{ m}$, a building surface resolution of $\Delta_{bs} = 2.75\text{ m}$ and a building edge resolution of $\Delta_{be} = 2\text{ m}$. The number of inflation layers N_{il} is chosen to achieve a smooth transition between the inflation layers

and the main mesh.

For the domain height at least $12 H_{b,\max}$ and for the domain width at least $10 H_{b,\max}$ is taken for further simulations. The tree foliation is chosen according to the season in which the validation measurements (chap. 6) were performed. Due to the large effects of the local tree heights, these are considered in the simulations which will be used to determine the local AEP values. Furthermore, the surrounding buildings are considered in the calculation of the annual energy production due to the better prediction of the energy yield.

6 Evaluation against LiDAR Measurement Data

The following subchapter is extracted and partially modified from a previous publication of von der Grün et al. [50]. The numerical setup including terrain and the vegetation model from chapter 4.4 is compared with on-site LiDAR data. The surrounding buildings as described in chapter 5.4 are not considered in this study since none of the surrounding buildings is in the inflow. On-site planar wind field LiDAR data are utilized to define the inflow boundary condition. The required preprocessing steps of the LiDAR data are explained in detail and their assumptions which are made to interpolate the data onto the numerical inflow plane. Further simulations are performed using a uniform tree height and forested zones which are modelled as solid bodies.

6.1 Preparation and filtering of LiDAR measurement data

The Stuttgart Chair of Wind Energy (SWE) conducted an on-site LiDAR measurement campaign at the test site in Tübingen. The measurement device was located at the high-rise building B on the campus. Three points in width (-250, 0, 250 m) and four points in height (40, 140, 240 and 340 m) on a plane were measured in various distances, so this data set is used for the inflow boundary condition and for the comparison further downstream. The influence of the terrain is considered already at the computational inflow plane by the measurement of lateral depending wind profiles. This gives a more realistic inflow condition than a 1D-data set from a single met mast. The three-dimensional velocity components are determined from the measured line of sight velocity. In order to detect, sort out and replace extrem and unphysical measurement data an extended version of a non-linear median filter is applied which is widely-used in image data processing [59]. In the following the function and the extensions of the filter will be explained briefly. The filter is applied by running through the signal entry by entry. Assuming the following signal

$$M(i) = [\dots \quad 1 \quad [2 \ 102 \ 4] \quad 5 \ 6 \quad \dots] \quad (6.1)$$

with 102 as the number which should be replaced, so $g(x) = 102$.

Each value $g(x)$ is replaced by the median $g'(x)$ of the values in a window around $g(x)$, here the width of the window, marked with squared brackets is 3 and $g'(x) = 4$ and the signal turns to

$$M(i) = [\dots \ 1 \ 2 \ 4 \ 4 \ 5 \ 6 \ \dots]. \quad (6.2)$$

Fig. 6.1 shows the measured velocity signal in streamwise direction of a measurement point over the sampling time of 60 min. The black line shows the unfiltered velocity against the same velocity (red line) filtered by the median filter, as explained above.

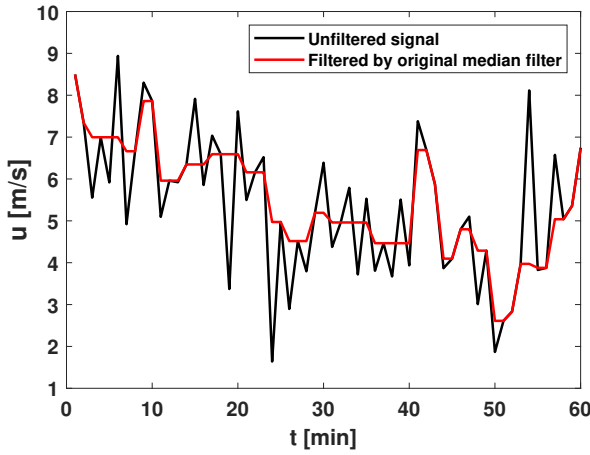


Figure 6.1: Velocity in streamwise direction u over time - unfiltered and filtered by the original median filter, von der Grün et al. [50].

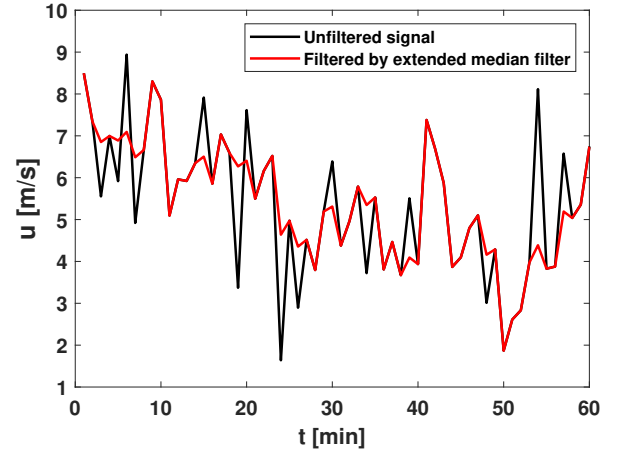


Figure 6.2: Velocity in streamwise direction u over time - unfiltered and filtered by the extended version of the median filter, von der Grün et al. [50].

Since not only the outliers are filtered but also the small fluctuations of the velocity signal, some extensions are added to the median filter. In order to avoid that even values with small deviations compared to $g(x)$ are replaced, a threshold value c triggers the replacement of $g(x)$ by $g'(x)$

$$|g'(x) - g(x)| > c, \quad (6.3)$$

which is set to 0.8 m/s . Additionally, a weighting function is applied to the filter. In case of replacement, the values within the window are updated by

$$M(i) = (g(x) - g_{\pm 1}(x)) \cdot w_m + g_{\pm 1}(x), \quad (6.4)$$

where $g_{\pm 1}(x)$ are the neighboring values and the weighting factor w_m is set to 0.1. Subsequently, the filter is applied using the new window elements. That means that the qualitative fluctuations remain in the signal and the new value $g'(x)$ is damped according to the weighting function. The updated signal versus the unfiltered signal are plotted in fig. 6.2 which show a good improvement with more smaller fluctuations remaining in the

signal. The median filter is applied to the signal of every measurement point and the signal is averaged over one hour.

Since the LiDAR measuring device was not able to capture the signal properly at the upper points of the measurement plane at 340 m due to fog or low clouds and the lower points due to the vicinity of the forest, some assumptions are made and explained in the following. Schatzmann et al. [112] addressed the issues to extrapolate measured planar wind field data onto the numerical inflow plane but just gave a solution for linear wind profiles in urban areas.

A previous simulation confirmed that the influence of the hilly terrain can be neglected at a height above $z_{\text{hom}} = 330$ m and lateral homogeneity can be assumed. The extrapolation scheme is divided into two parts depending on z_{hom} and a power law approach is taken for the overall velocity profile:

$$u(z) = \left(\frac{z}{z_{\text{ref}}} \right)^\alpha \cdot u_{\text{ref}}, \quad (6.5)$$

where u_{ref} is the measured velocity at the reference height z_{ref} and the exponent α depends on the surface roughness according to Davenport [34]. For $z > z_{\text{hom}}$ α is uniformly set to 0.21 due to the lateral homogeneity and u_{ref} is the velocity measured at $z_{\text{ref}} = 340$ m. For $z < z_{\text{hom}}$ the exponent $\alpha(y)$ is adapted to the local terrain height and calculated by

$$\alpha(y) = \frac{\ln\left(\frac{u(z_{\text{hom}})}{u_{\text{ref}}}\right)}{\ln\left(\frac{z_{\text{hom}}}{z_{\text{ref}}}\right)} \quad (6.6)$$

The velocity $u(z_{\text{hom}})$ obtained from equ. (6.5) and z_{hom} are used as boundary conditions for equ. (6.6) to determine $\alpha(y)$. In equ. (6.6) u_{ref} is the velocity measured at $z_{\text{ref}} = 240$ m. The values between the three lateral measurement points are interpolated linearly and are fed into the simulation on the inflow plane.

6.2 Numerical setup and inflow conditions

The size of the domain is $(15.0 \times 13.5 \times 14.6)H_{b,\text{max}}$ according to the best practice guide for urban simulations [41] where $H_{b,\text{max}}$ is the maximum building height which is approximately 50 m. The upwind length L_u is $6.3H_{b,\text{max}}$ and the downwind length L_d is $8.7H_{b,\text{max}}$. The domain height is adapted for complex terrain. The simulated wind direction at the test site in Tübingen is 245° and consequently, the domain and the inflow plane are oriented towards that direction. For the turbulence length scale $L = 55$ m is chosen. The mesh is generated according to the description in chapter 4.6.

The simulations are carried out with a turbulence intensity of 10 % according to a neutral ABL and higher turbulence due to scattered trees and buildings in the inflow zone

since the LiDAR measurements are conducted in the late winter and the weather was dominated by inversions. As inflow boundary condition, experimental LiDAR values are filtered by the median filter mentioned above and extrapolated onto the numerical inflow plane according to the equations (6.5) and (6.6). For the side and the upper surfaces of the domain the so-called 'symmetry' boundary condition is used in Fluent, that means all variables are forced to be parallel to the boundary plane at the surface. For the outlet a pressure-outlet boundary condition is used. The terrain and the building surfaces are all treated as a no-slip walls. For the Co number 0.25 is chosen.

The forested zone in the domain includes local tree heights depending on x and y which are the lateral and the longitudinal coordinate of the domain. The drag force is calculated with the $a(z)$ -profile depending on the local tree height for LAI=3 as shown in fig. 4.3. The foliage density remains constant over the computational domain.

6.3 Comparison with on-site LiDAR data

In the following section, the computational results will be analysed and discussed in detail. The inflow zone in the simulations includes forest vegetation, buildings and complex terrain. The results of the turbulent flow field are compared with on-site LiDAR wind data. Furthermore, the impact of the modelled forested zone is investigated on how it changes the wind direction and wind velocities. The geometries are normalized by the maximal tree height within the forest $H_{t,max}$ which is 30 m.

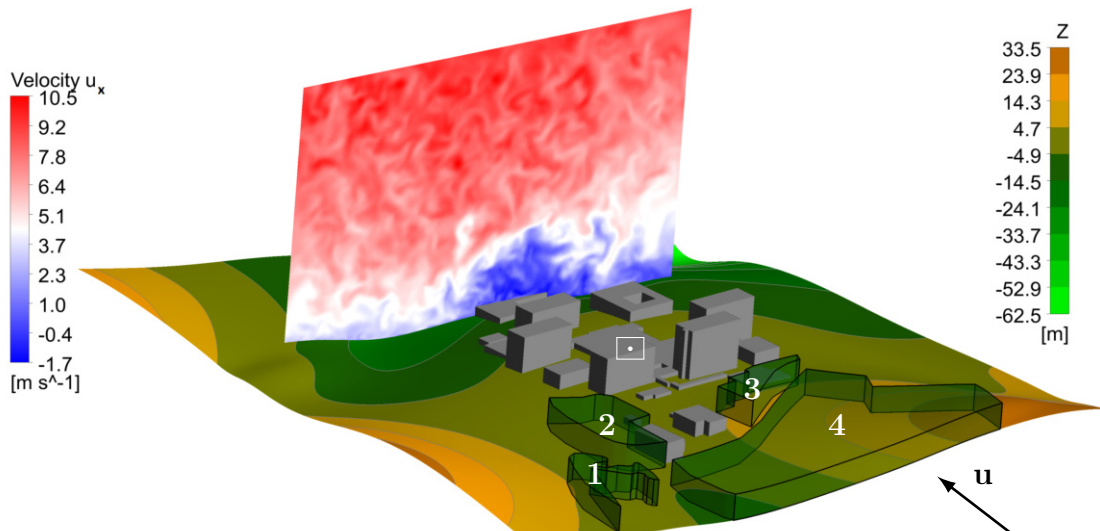


Figure 6.3: Height(z) of the complex terrain with forested zones, buildings and instantaneous streamwise velocity u_x from the simulation, von der Grün et al. [50].

Fig. 6.3 illustrates the computational domain with complex terrain, building geometries and forested zones. In total 18 buildings (grey) are considered in the simulations. The iso-lines show the different heights of the terrain. The maximum difference in altitude

amounts to 96 m. The figure also illustrates a plane with a snapshot of the instantaneous velocity in streamwise direction, showing a highly turbulent flow induced by the buildings. Negative velocities indicate backflow zones of detached flows behind the buildings. The numbers 1 to 4 represent the forested zones and show their positions in the domain. The black arrow at the bottom left part of the figure indicates the flow entering the domain. Hence, the forested zones are located in the inflow and the results presented in fig. 6.4 confirms the significance to consider the forest in the simulations. Without taking the forest into account in the simulations, the velocity profile over the height would correspond to a logarithmic wind profile. By taking the forest into account, the zero point of the logarithmic wind profile is shifted upwards by approximately one tree height. The white point within the rectangle represents the position of the LiDAR measurement device. Fig. 6.4 shows the simulated time-averaged velocity magnitude (red line) against the one obtained by the LiDAR measurement campaign (black squares) over the height at different downstream locations. The LiDAR velocities are averaged for 60 min while the numerical velocities are averaged for 4 min. Fig. 6.5 illustrates the placement of the evaluation lines in the topography from $x/H_{t,max}=-10$ to $x/H_{t,max}=-4$ and at $y=0$. The inflow plane is located at $x/H_{t,max}=-12$ and the inflow profile is based on LiDAR data, as explained above. An evaluation further downstream is not possible, because a minimal distance to the LiDAR measurement device is required to ensure good quality results. During the measurement campaign it was placed on the top of a building at $x/H_{t,max}=0$, as shown by the framed white dot in fig. 6.3. Area 1 in fig. 6.5 illustrates the zone in

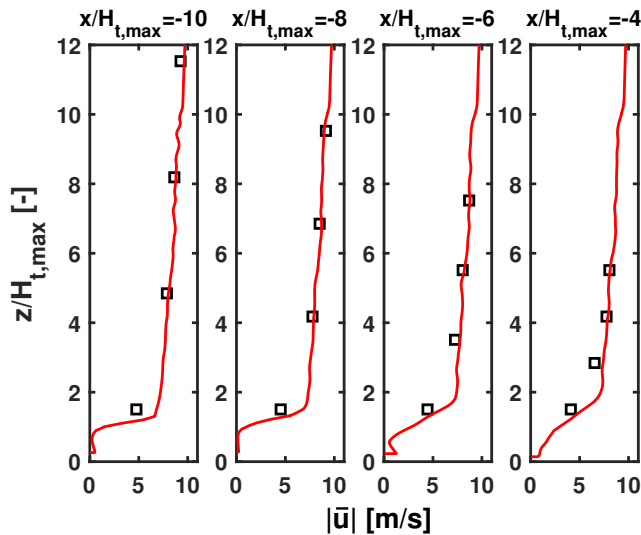


Figure 6.4: Simulated time-averaged velocity magnitude (red) compared with LiDAR data (black), see also [50].

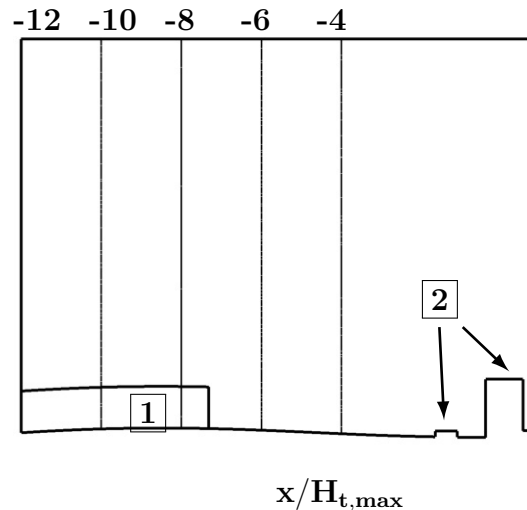


Figure 6.5: Section of the domain showing the locations of the evaluated lines, see also [50].

which the vegetation model is activated but area 1 does not show the local tree heights used in the simulations. Area 2 in fig. 6.5 represents some of the real buildings considered

in the simulations. For all measured positions a very good qualitative and quantitative agreement is achieved between the simulated and the on-site measured velocity magnitude. At the lowest measurement point the velocity magnitude in the simulations is a bit larger than the measured velocity magnitude. A possible explanation is the reconstruction process which calculates the 3D velocity components from the line of sight velocity. This may struggle with a highly turbulent flow induced by high surface roughness and obstacles. Furthermore, LiDAR does not measure a value at a certain point but measures the values within a control volume which can have a size of several meters. This can be problematic if the desired measurement point is close to forested zones or buildings.

Looking closer to the numerical velocity lines some characteristic phenomena are observed at the ground. The line at $x/H_{t,\max}=-10$ passes through the forested zone. The velocity magnitude inside the forest reflects the drag force according to the a -profile for LAI=3 in the model, see fig. 4.3. At the ground the velocity is higher due to a lower drag force because the foliage density of trees is lower towards the ground. With increasing foliage near the crown the velocity decreases due to higher drag forces. At the top of the forest a slight increase of the velocity is observed because local tree heights are considered in the model. Compared to a vegetation model with a uniform tree height, the top of the forest would be a plane resulting in a more sudden increase of the velocity. However, the adaption of the local tree height causes a much rougher surface at the top decelerating the flow. At $x/H_{t,\max}=-8$ the flow within the forest is almost damped to zero and the thickness of the boundary layer is increased above the trees due to a rougher surface because the local tree heights are considered. Further downstream at $x/H_{t,\max}=-6$ and -4 the velocity gradient levels out with increasing distance to the forest. Thus, the flow at the ground is getting faster and the edge in the curve is more flattened.

6.4 Summary

In this study the windfield in complex urban terrain is investigated at a test site in Tübingen. For that, a vegetation model is implemented in ANSYS Fluent which includes local tree height adaption based on Laser scan data. The local forest drag force and the associated wind speed reduction corresponds to the foliage density profile and depends on the x -, y - and z -direction. Measured on-site LiDAR data have been used to define the velocity profile of the inflow boundary condition. The required steps to preprocess the LiDAR data and their assumptions are explained in detailed. Therefore, a non-linear median filter is extended and adapted for LiDAR wind data to detect and replace outliers and unphysical measurement data.

Considering the modelled forested zones combined with complex terrain and real building geometries, simulations are performed. Their results are compared with on-site LiDAR data at various locations above forested zones. That means that besides the entire com-

putational setup also the vegetation model is validated and shows good results.

7 Windfield Evaluation and local Annual Energy Production

In this chapter, the windfield at the test site in Tübingen is simulated using four wind directions: 60° , 150° , 240° and 330° . The wind flows of the four wind directions are analysed and local wind statistics and the local annual energy production (AEP) are calculated by means of additional synthetic large scale wind statistics. Finally, locations for small wind turbines are evaluated and discussed.

7.1 Local site information

The test site is expected to be a suitable area for small wind turbines since the campus is located on a hill and is in an exposed position. Furthermore, few but exposed high-rise buildings onto which small wind turbines could be placed are built on the campus. In total, 23 buildings with a building height of up to 50 m are considered in the simulations. The simulated area of the campus is shown in fig. 7.1. The buildings used in the simulations are coloured in grey and the forested zones are coloured in dark green. The forested zones are modelled by the vegetation model described in chapter 4.4. The simulated wind directions are illustrated by the arrows as shown in fig. 7.1. The wind direction of 240° is the main wind direction at the campus Morgenstelle.

The local AEP is calculated for each building with and without the surrounding buildings included, so that the direct influence of the surrounding buildings on the AEP can be studied. The procedure of calculating the AEP is explained later in more detail.

Regarding the literature about the calculation of energy yields or other parameters to determine suitable wind turbine positions it is referred to chapter 1. But the main statement is that the energy yield depends on local site conditions and has to be investigated individually.

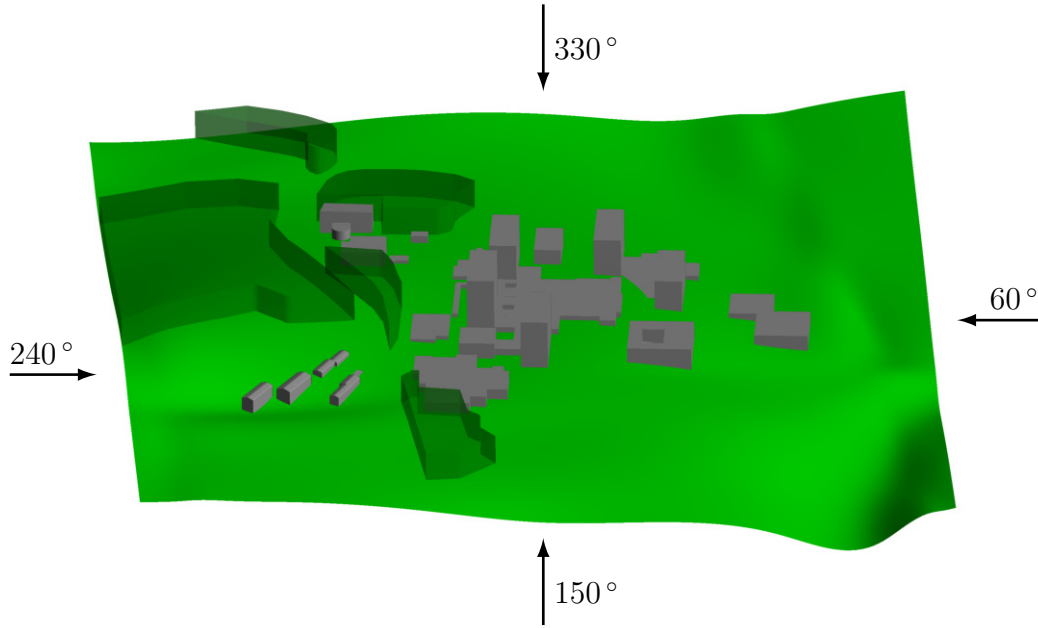


Figure 7.1: Computational domain with forested zones and buildings used for the calculation of the annual energy production. The four simulated wind directions are illustrated by the arrows.

7.2 Numerical setup and inflow conditions

The size of the computational domain is $(14 \times 14 \times 13)H_{b,\max}$ in length \times width \times height. In the domain, the buildings of interest are located in the centre so that the distances to the sidewalls are equal. Hence, the ground area of the domain enables the use of only one mesh for the simulations of all four wind directions. The mesh is generated according to the description in chapter 4.6 resulting in a total cell number of approximately 65 million cells.

The simulations are carried out with a turbulence intensity of 10 % according to a neutral Atmospheric Boundary Layer (ABL), and for the turbulence length scale $L = 50$ m is chosen. The turbulence is synthetically generated at the inlet plane using the Vortex Method, described in chapter 2.3. The power law

$$u(z) = \left(\frac{z}{10 \text{ m}}\right)^{0.21} \cdot u_{\text{ref}} \quad (7.1)$$

is used as a velocity profile and is applied to each inflow boundary plane and u_{ref} is 2.95 m/s . The reference velocity is taken for the university campus in Tübingen according to the wind atlas of Baden-Württemberg [3]. For the side and the upper surfaces of the domain the so-called 'symmetry' boundary condition is used in Fluent. For the outlet a pressure-outlet boundary condition is used. The terrain and the building surfaces are all treated as no-slip walls. For the Co number 0.25 is chosen. The profile for the leaf area density is taken according to $\text{LAI} = 3$ as shown in fig. 4.3. Seasonal effects in the foliage density of the forest can be neglected. The stabilization time is 147 s and the averaging

time is 240 s.

7.3 Flow analysis of the simulated wind directions

In the following, the wind flow from each of the four wind directions at the university campus Morgenstelle in Tübingen is simulated. The wind flow is evaluated by means of the time-averaged velocity magnitude and the turbulent kinetic energy at a height of $z=15$ m. Fig. 7.2 shows the evaluated time-averaged velocity magnitude in the left figure and the turbulent kinetic energy in the right figure from the 60° wind direction. The

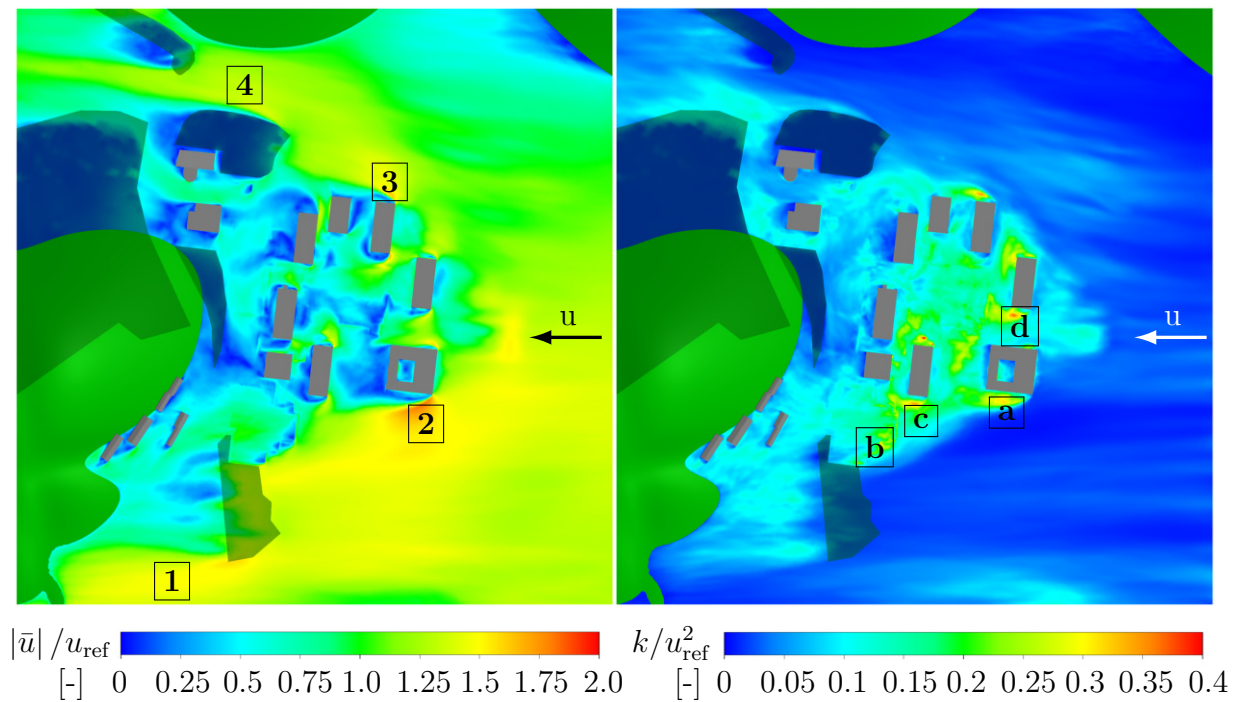


Figure 7.2: Time-averaged velocity magnitude (left) and turbulent kinetic energy (right) with a simulated wind direction of 60° and evaluated at $z=15$ m.

locations to which the discussions refers are indicated in the figures by numbers for the velocity and by letters for the turbulent kinetic energy. The wind flow enters the domain on the right side as indicated by the arrows in fig. 7.2. Since there are no obstacles, such as hills, forests or buildings, in the inflow region, higher wind speeds and higher k values than from other directions are obtained from this wind direction. At location 1, the flow is diverted and accelerated due to the blockage of the forested zone like a nozzle flow. Especially forested zones with high and dense trees increase the blockage. When the flow passes a forest on its sides, high wind speeds and energy yields can be obtained. At location 2, the highest wind speed at $z=15$ m is reached and the wind speed is almost twice the reference speed u_{ref} . the reason for that is when a flow hits an obstacle with sharp edges like a building, the flow detaches at their edges, since the flow cannot follow

the contour of the edge, and accelerates at the edges accompanied with a recirculation zone behind it. Since sharp edges are required for the detachment, this effect likely takes place at buildings and is less developed at forests. The same effect can also be observed at position 3. In general, very high wind speeds compared to the reference wind speed can be obtained at building edges. But the locations at vertical building edges strongly depend on the wind direction and thus are not recommended as a wind turbine position when the wind directions likely change. At position 4, a nozzle-like flow is formed between a forested zone and a hill due to a narrowing cross-section between the forested zone and the hill which cause the flow to accelerate. Usually, nozzle-like flows are formed between two hills, forested zones or buildings but are strongly wind direction dependent. When the wind comes from a direction which is perpendicular to the longitude of the natural nozzle, the wind speed would drop to zero. Depending on the annual variation of the wind directions, these locations can promise high energy yields or not.

Regarding locations with high k values in the wind flow, the locations 2 and a correlate with each other. Large velocity gradients, as observed in the locations 2 and a, and the associated high shear rates lead to high turbulent kinetic energy values. Location b is located several meters above an underlying building and shows high k values because of the underlying building. The reason for that is that the flow over a sharp edge rooftop is characterized by a detached flow with high velocity gradients and high k values and a region with increased wind speeds in contrast to an undisturbed flow. The locations c and d are close to vertical building edges at which the wind flow detaches. That causes one of the highest k values at $z=15$ m. Note that high k values lead to higher stresses at wind turbine blades and can reduce their life times. Furthermore, it is not recommended to mount wind turbines within zones with high vertical velocity gradients, e.g. at building roofs. For example, when the lower portion of a wind turbine is blown by a lower wind speed than the upper portion, it will cause unbalanced loads and bending stresses which can lead to shorter life cycles of the wind turbine.

Fig. 7.3 shows the evaluated time-averaged velocity magnitude in the left figure and the turbulent kinetic energy in the right figure from the 150° wind direction. The wind flow enters the domain on the lower side of fig. 7.1 indicated by the arrow on fig. 7.3. Since no obstacles, such as hills, forests or buildings, are located in the inflow region, higher wind speeds and higher k values are obtained from this wind direction as from the 60° wind direction. At location 1, the wind speed is increased due to a free undisturbed flow towards location 1 and the location is within an acceleration zone which is generated above a rooftop of an underlying building. As mentioned previously the flow over rooftops is usually accelerated and due to its height it can be more dominant and undisturbed from surrounding buildings which makes it less independent from wind directions. Thus, rooftops can be considered as possible locations with high energy yield potential. Fig. 7.3

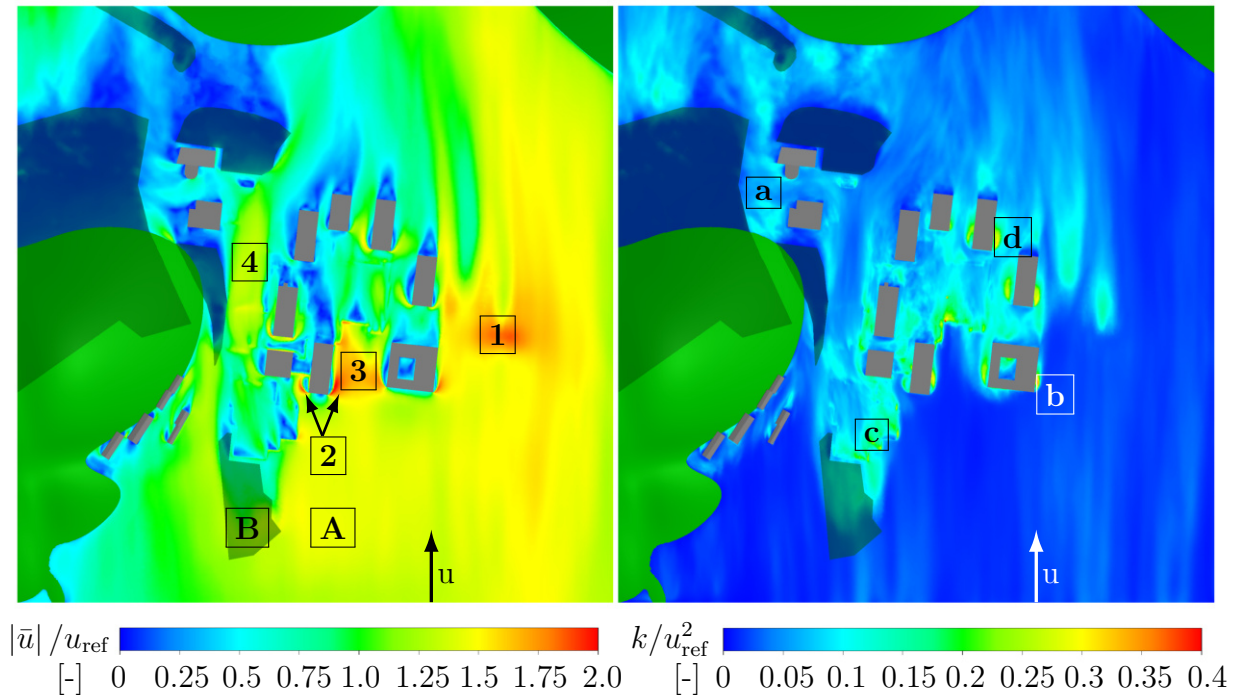


Figure 7.3: Time-averaged velocity magnitude (left) and turbulent kinetic energy (right) with a simulated wind direction of 150° and evaluated at $z=15$ m.

shows that the forested zone B separates the incoming flow into a left flow and a right flow A with higher wind speeds. The flow A hits the building 2 which separates the flow again including high acceleration zones around the vertical edges of building 2. Location 3 is within a canyon formed by two adjacent buildings so that the flow is accelerated in the canyon from $1.4 u_{\text{ref}}$ to $1.7 u_{\text{ref}}$. Due to the fact that the canyon is in line with the wind direction, location 3 strongly depends on the wind direction and would consequently not be a suitable position for wind turbines. When the wind changes the direction by some degrees, the wind speed could drop to zero or cause some backflow when crossing the canyon.

Evaluating the dimensionless k values in the wind flow, the locations a-d show increased k values in contrast to the surroundings. A high amount of turbulent kinetic energy is produced above the forested zone close to location a. As investigated above, crown regions of a forest produce high turbulent kinetic energies due to the rough top surface of a forest. These high k values are carried with the main flow so that behind forested zones usually higher k values are observed. High turbulent kinetic energies are caused by high velocity fluctuations which can negatively influence the blades of wind turbines due to the fluctuating loads and vibrations. Thus, locations downstream of forested zones should be avoided or taken with caution. Fig. 7.3 shows that at the locations b and d the flow is detached at vertical building edges. In contrast to round building edges, the flow can not follow the contour of the buildings and detaches at its sharp edges and separation bubbles are formed. Due to the blockage of the building, the flow is accelerated when the wind

flows past the building edges. This causes strong velocity gradients, high shear stresses and consequently high turbulent kinetic energies. Especially the shear stresses and the velocity gradients which can occur over the height of a wind turbine lead to high loads of the wind turbine blades. Despite the promising high wind speeds detachment zones at building edges are not recommended as suitable wind turbine locations. Another option is to adapt the design of the wind turbine accordingly to deal with high k values. Furthermore, small and long wind turbines which are mounted parallel to the building edges are preferred because the velocity gradients in the direction parallel to building edges are quite small unlike in the direction perpendicular to the building edges. At location c, the wind flow just passed a vegetation zone meanwhile a high amount of k is produced. Furthermore, location c is above a building and the rooftop acceleration zone produces additional k . The location c is characterized in that it is located downstream of a forest and above a building. First, the turbulent kinetic energy is produced in the crown region of the forest and carried with the flow downstream towards location c. Second, high k values are produced around the building edge at the roof similar to the locations b and d. But the building edge is oriented horizontally in this case and facing the upstream region of the flow. Since it is located in the wake of the flow, the associated increase in speed can be neglected in this case. So the interaction of both effects contribute to the high k values observed at location c. Since no increase of the wind speed unlike to the surroundings is observed, one only has the disadvantages of high k values which makes it to a non-recommendable place for small wind turbines, although the long, flat roof the roof facilitates the installation of the wind turbine.

Fig. 7.4 shows the evaluated time-averaged velocity magnitude in the left figure and the turbulent kinetic energy in the right figure from the 240° wind direction. The wind flow enters the domain on the left side of fig. 7.1 indicated by the arrow on fig. 7.4. Since a large hill and a long forested zone are located in the inflow region towards the university campus, lower wind speeds and lower k values are obtained from this wind direction in general. Furthermore, the buildings are located lower than the hill and the forested zone, and thus the buildings are in the wake of the hill and the forest. As expected, the wind speed is increased at location 1 due to a nozzle-like structure, which is formed by two forested zones on the one side and a hill and a forested zone on the other side. This arrangement and the interaction of the forests narrow the cross-section of the flow path like a nozzle or a cone shaped inflow. It is not like a real nozzle since the surface to the sky is open. But the narrowing cross-section is sufficient to accelerate the flow. Usually, the more the cross-section is narrowed, the more the flow is accelerated. But when the narrowing is too strong, the wind escapes over the open surface and the wind speed can drop to zero in the nozzle. Natural nozzle-like structures are only recommended for small wind turbines when the local flow is less wind direction dependent.

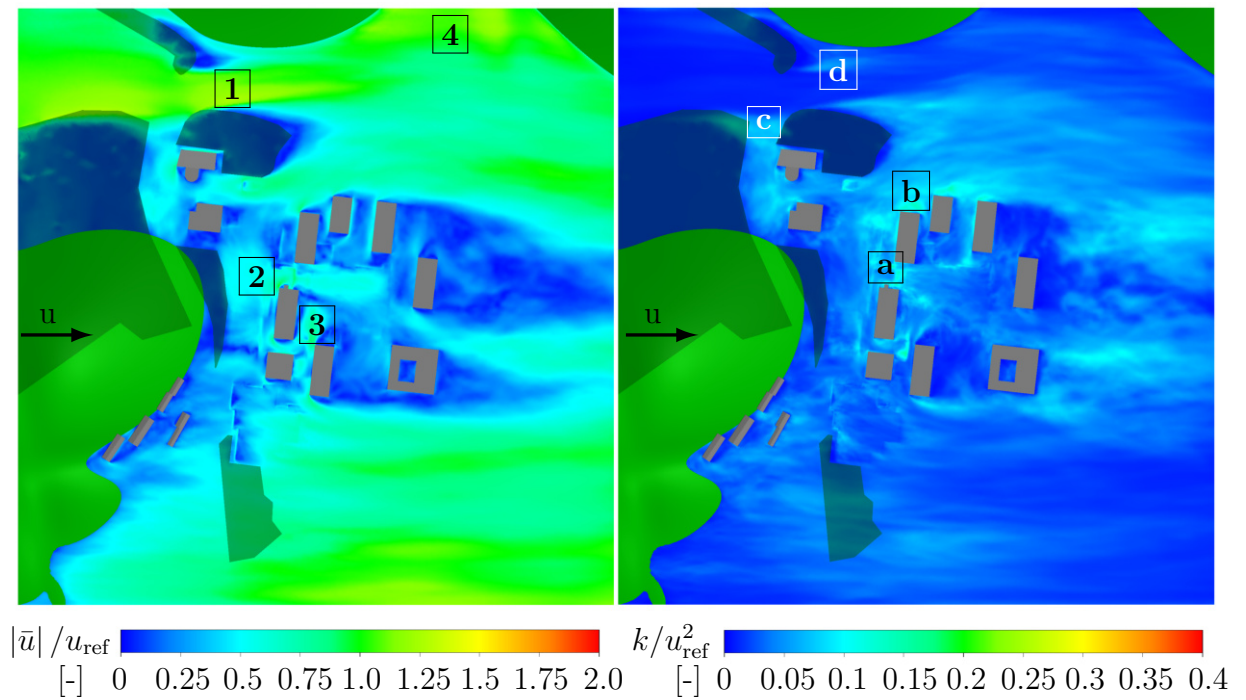


Figure 7.4: Time-averaged velocity magnitude (left) and turbulent kinetic energy (right) with a simulated wind direction of 240° and evaluated at $z=15$ m.

At point 2 one would expect a much lower wind speed because it is located downstream of a forested zone. The streamlines follow the sloping hill. The forest does not serve as a brake, but only as a height shift of the streamlines. The descending streamlines also continue behind the forest, so that this is not a classic wake after a forest with very low wind speeds. Furthermore, the following buildings (buildings A and B) are perpendicular to the flow direction and have a certain distance to each other, so that the flow is accelerated when passing between the buildings A and B similar to a nozzle but with an open surface to the sky.

The flow around location 3 is very complex and the wind speeds are higher than initially expected since this area is surrounded by high buildings. The flow enters a canyon formed by two buildings. Since the canyon is oriented in line with the main wind direction the flow is accelerated similar as in a nozzle due to the suddenly smaller cross-section caused by the two buildings. When the accelerated flow hits the next buildings, the flow is separated at the stagnation point in front of the next building. Since the path from the stagnation point towards the (in flow direction) left edge of the building is shorter than the path towards the (in flow direction) right edge, the resistance at the left edge is lower the amount of wind is higher at the left building edge. Due to the lower resistance the pressure is locally decreased and the wind is accelerated. Due to that specific flow between buildings and their interaction affecting the wind pattern, a small change of the wind direction can change the wind speed again. Thus, location 3 is not recommended for a wind turbine although it looks quite promising. At location 4, one may have expected

a lower wind speed when observing fig. 7.4 since location 4 is placed between two hills. But it should be noted that the hill, on the left of location 4, is pretty low. When the flow hits the small forested zone on the left of the hill, the flow is strongly decelerated in the forest. Thus, the main part of the flow is directed over the forest and is accelerated. Behind the forested zone, the accelerated flow reattaches at the hill and follows the slightly slopping terrain contour of the hill towards location 4. In addition to that, the wind is more accelerated at the boundaries of the domain, since the flow is blocked in the centre of the domain due to the high buildings.

Evaluating the turbulent kinetic energy, the locations 2 and a correlate with each other. Since location a is located downstream of a forest, above which a lot of turbulent kinetic energy is produced due to the rough tree surface, the k values are basically increased. When the flow hits the passage formed by the buildings A and B, the flow detaches at the vertical building edges, especially at the small protruding portion of building A which further reduces the cross-section of the passage. The detachment causes high velocity gradients and as a result high shear stresses around the building edges which increase the production of turbulent kinetic energy here.

The turbulent kinetic energy, produced above the forested zone, is carried with the flow towards location b. Additionally, turbulent kinetic energy is produced when the flow detaches at the edges of adjacent buildings. Here, the turbulent kinetic energy produced at different places superimpose here so that the k values are higher than in the surroundings. An interesting fact can be observed at the locations c and d. As reported previously, turbulent kinetic energy is produced above forested zones. But also when the flow passes the forested zone at its side, turbulent kinetic energy is produced and spreads in the wake of the forested zone like a cone. At location c it is further added, that the forested zone is towards its end. This favours the spreading of turbulent kinetic energy in a cone shape. Since every surface of a forested zone is rough, turbulent kinetic energy is produced when flowing over any surface of the forested zone. Thus, when high k values are not desired for small wind turbines, it is recommended to avoid the vicinity of forests, especially the wakes behind any high vegetation.

Fig. 7.5 shows the evaluated time-averaged velocity magnitude in the left figure and the turbulent kinetic energy in the right figure from the 330° wind direction. The wind flow enters the domain on the left side of fig. 7.1 indicated by the arrow on fig. 7.5. Since two hills and a small forested zone are located in the inflow region, lower wind speeds and lower k values are obtained from this wind direction. Location 1 is within a canyon like structure which is formed by the forested zone on the left side and by two buildings and the smaller forested zone on the right side, as shown in fig. 7.5. Since the canyon is in line with the simulated wind direction, the flow is accelerated. The forested zone, located upstream of location 1, has lower tree heights on the left side. That enables a straight path towards the canyon and contributes to higher wind speed in the canyon. As

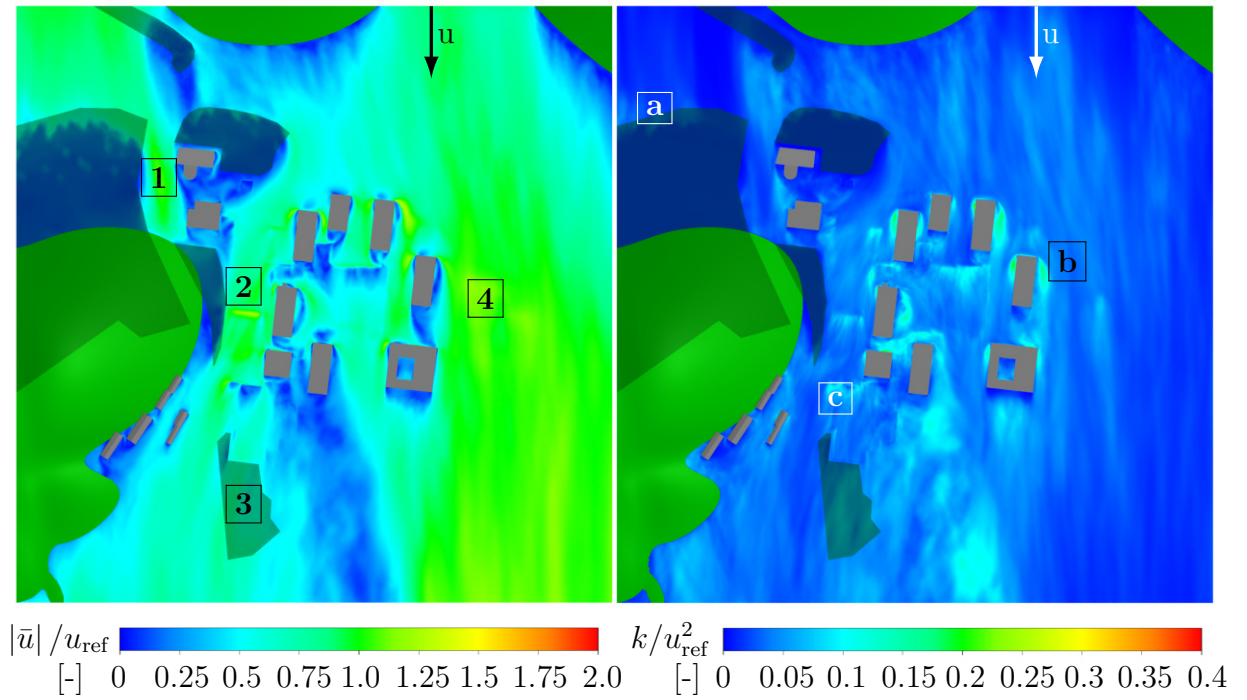


Figure 7.5: Time-averaged velocity magnitude (left) and turbulent kinetic energy (right) with a simulated wind direction of 330° and evaluated at $z=15$ m.

mentioned above, nozzle-like or channel-like flows strongly depend on the wind direction. This type of locations can only be recommended for wind turbines when this is the main wind direction without large deviations from it. When the wind comes from a direction perpendicular to the length direction of the canyon, backflow can occur and the velocity can drop to zero within the canyon.

A similar canyon effect takes place at location 2. In addition to that, the wind flows over a building roof which causes the wind to accelerate. This small flow acceleration is indicated in fig. 7.5 by the yellow longitudinal portion. The forested zone and the hill, located directly upstream of position 2, do not negatively affect the flow behaviour as would be obvious. When the wind flows over the hill and the forest, the streamlines approach the ground and the wind speed is increased. This increase amounts 50% compared to the reference wind speed which is a significant increase. But the negative aspects of canyon flows still remain. Since point 3 is placed within a forested zone, lower wind speeds might be expected. But due to the fact that the tree heights within this forested zone are lower than the height of the evaluation plane, the smaller wind speeds affected by the forest are below the evaluation plane. However, fig. 7.5 illustrates the velocity field above the real forest although it is still in the solid forest geometry box in which the vegetation model is enabled. This is the reason why the wind speeds are not slowed down significantly here. At location 4, high wind speeds are observed because of some reasons: first, straight upstream at the inlet plane there is a valley between two hills so that higher velocities are obtained at the inlet. Furthermore, no vegetation zones and buildings interfere with

the flow from the inlet plane to location 4. As not shown in fig. 7.5, there is a building below the evaluation plane, thus it intersects only the acceleration zone above the roof. As already mentioned above, the flow stagnates in front of a building and is forced to pass the building on its sidewalls and its roof. This causes a local acceleration close to the frontal building edges. The rooftop of the building at location 4 is indeed a highly promising place for an installation of small wind turbines because only the wind direction of around 240° is restricted by buildings. The wind from all the other wind directions has an almost unobstructed inflow to this building.

Evaluating the turbulent kinetic energy in the wind flow, there is one conspicuous area, where the flow hits the large forested zone at location a. As reported previously, turbulent kinetic energy is produced in the crown region of a forest and along its sidewalls. But in this case, turbulent kinetic energy is also produced in front of a forest, where the wind flow directly hits the forest. As also observed in front of some buildings, backflow and perturbation of the flow can occur in the region around the stagnation point of the building. In the case of the forest, the wind is not completely deflected as in the case of a building, but a part of it is strongly slowed down and still passes through the forest. Thus, this area is larger in front of this forest than in the case of a building.

The location b is close to a vertical building edge at which the flow detaches. Consequently, a recirculation zone is formed. The outer side of the recirculation zone is characterized by a strong increase in velocity which causes a strong velocity gradient, high shear stresses and high turbulence. Thus, especially these detachment zones are characterized by high k values. This must be taken into account in the search for suitable positions for small wind turbines.

Similar to point b, the flow detaches at a horizontal building edge at the roof at point c. The effect leading to high turbulence is equal to that in point b. But the shape of the roof and rounded building edges can change the turbulent kinetic energy production. For example, a rounded building edge reduces the recirculation zone and may also prevent the formation of the recirculation zone. That reduces the velocity gradient, the shear stresses and consequently the production of turbulent kinetic energy.

7.4 Procedure for calculating the local AEP

One of the most important key parameters in the wind energy field is the AEP. In urban areas, the wind field and the AEP assumed to strongly depend on local flow effects induced by buildings, vegetation, and the terrain [128, 32]. When the AEP of an on- or off-shore wind turbine in a non-built area is calculated, wind statistic data are obtained from a wind mast. Due to the strong local variation of the wind speed in urban areas, the validity of such wind statistics is spatially limited and many wind masts would have to be positioned in a fine raster in the urban area to capture all the local flow effects. To solve

this problem, local flow data from simulations are used in the calculation of the AEP. This promises more accurate results and less effort. The procedure of the calculation of the AEP is described in the following.

The method for calculating the local AEP is based on the simulation data of the four simulated wind directions and synthetic large scale wind statistic data which is available for entire Baden-Württemberg. The synthetic wind statistics are determined in a raster of 500 m x 500 m and provided by the Landesanstalt für Baden-Württemberg [3]. The wind statistic data include annual frequencies for wind directions and wind speeds. The annual frequencies of the wind speed and the wind direction are divided into bins which are called "wind velocity bins" and "wind direction bins" in the following. Each wind velocity bin includes a certain wind speed range and each wind direction bin a certain wind direction sector. Each bin contains the respective annual frequency for the wind speed range or the wind direction sector. The synthetic wind statistics will be explained later in more detail.

Since the computational domain is wider than one raster of the synthetic wind statistics, 14 wind statistics in total are used to cover the entire terrain of the computational domain. The method for calculating the local AEP values includes four steps. In a first step, the synthetic wind statistic data is interpolated by a bilinear interpolation method onto each computational cell. The interpolated wind statistic data does not depend on the z -coordinate of the computational domain. In a second step, new local wind statistics based on local flow data from simulations including wind speeds and wind directions are calculated for each computational cell. In a third step, the local AEP is calculated for each computational cell based on the local wind statistics calculated in the second step, and the local AEP is based on a power curve of a small wind turbine. In a fourth step, the local AEP calculated in the third step is corrected by power changes which are induced by the atmospheric turbulence intensity and the angle of attack of the small wind turbine.

7.4.1 Interpolation of the synthetic wind statistics onto the grid

This subsection describes the first step of the method for calculating the local AEP. Fig. 7.6 illustrates one of the 14 used synthetic large scale wind statistics at the university campus in Tübingen [3]. Fig. 7.7 illustrates the used synthetic large scale wind statistics represented by wind roses and the computational domain (black rectangle). The black dashed lines represent the raster width of the wind statistics. To cover the entire domain, in total 14 wind statistics are used. The synthetic wind statistics are obtained in large scale CFD simulations for whole Baden-Württemberg. The buildings were represented by roughnesses on the ground. The synthetic wind statistics corresponds to a height of 10 m above ground [3]. They include annual frequencies of wind speed ranges and wind

direction sectors, wherein the annual frequencies are classified into bins B_{WS} . Each bin has an upper and a lower limit.

Häufigkeitsverteilung der Windgeschwindigkeiten (m/s) und Windrichtungssektoren (°) in % (Klassenaufteilung nach TA Luft)										
Geschwindigkeit	0-1.3	1.4-1.8	1.9-2.3	2.4-3.8	3.9-5.4	5.5-6.9	7.0-8.4	8.5-10.0	> 10.0	
Richtung	m/s	m/s	m/s	m/s	m/s	m/s	m/s	m/s	m/s	Summe
346°-015°	2.22	0.83	1.78	0.29	0.00	0.00	0.00	0.00	0.00	5.12
016°-045°	2.74	1.46	2.84	3.29	0.03	0.00	0.00	0.00	0.00	10.36
046°-075°	5.32	1.40	2.82	2.12	0.02	0.00	0.00	0.00	0.00	11.69
076°-105°	3.64	0.88	1.73	0.18	0.00	0.00	0.00	0.00	0.00	6.43
106°-135°	2.62	0.69	0.69	0.04	0.00	0.00	0.00	0.00	0.00	4.04
136°-165°	2.23	0.05	0.08	0.14	0.00	0.00	0.00	0.00	0.00	2.51
166°-195°	1.73	0.08	0.12	0.31	0.05	0.00	0.00	0.00	0.00	2.29
196°-225°	3.82	1.79	1.48	5.57	1.55	0.00	0.00	0.00	0.00	14.21
226°-255°	6.02	4.26	2.20	7.05	3.49	0.01	0.00	0.00	0.00	23.03
256°-285°	4.18	1.35	1.36	1.56	0.79	0.00	0.00	0.00	0.00	9.24
286°-315°	3.49	0.10	0.73	0.16	0.16	0.00	0.00	0.00	0.00	4.64
316°-345°	6.35	0.02	0.07	0.00	0.00	0.00	0.00	0.00	0.00	6.44
Summe	44.35	12.92	15.90	20.73	6.09	0.01	0.00	0.00	0.00	100.00

Figure 7.6: One of the 14 used synthetic large scale wind statistics with frequencies (%) for wind direction sectors (°) and wind speeds (m/s) at the university campus in Tübingen [3].

Regarding fig. 7.6, the limits of the wind speed bins are 0, 1.35, 1.85, 2.35, 3.85, 5.45, 6.95, 8.45 and 10. The limits of the wind direction sectors are 15° plus 30° for each bin. The wind speed frequencies and the wind direction frequencies stored in the wind statistics have to be interpolated onto the numerical grid to get the information with which frequency the simulated flow behaviour from the simulated direction occurs in each cell. Since the wind statistic data does not depend on the height or the distance to the ground, it is two-dimensionally interpolated within the computational domain for each cell centre \vec{C}_c with x - and y coordinates. The bilinear interpolation method is used as follows:

$$f(\vec{C}_c) = w_2 \left(w_1 \cdot f(\vec{R}_1) + w_2 \cdot f(\vec{R}_2) \right) + w_1 \left(w_1 \cdot f(\vec{R}_3) + w_2 \cdot f(\vec{R}_4) \right) \quad (7.2)$$

where $f(\vec{R}_1)$ to $f(\vec{R}_4)$ are the statistic data of the points (\vec{R}_1) to (\vec{R}_4) which are the centre coordinates of the tiles of the raster of the synthetic wind statistics as illustrated in fig. 7.7. The parameters w_1 and w_2 are weightings and represent the ratio of the distances of the numerical cells to the points (\vec{R}_1) to (\vec{R}_4) .

Each wind direction bin has a range of 30° so that the entire range of 360° is covered by 12 bins. Consequently, the test site had to be simulated for each wind direction of the 12 bins to obtain the flow field for each of the 12 wind directions. Due to computational resources and to avoid interpolation errors between 12 different meshes only one quadratic mesh is generated to simulate four wind directions which are perpendicular to each other. These are 60° , 150° , 240° and 330° . For the simulated wind direction, the mean wind direction of the respective wind direction sector was assumed. The flow data of the lacking wind

directions is interpolated by the flow data of the simulated wind directions. For example, the wind speed for a wind direction of 90° is obtained by a rough approximation:

$$u_{90} = \frac{2}{3}u_{60} + \frac{1}{3}u_{150}, \quad (7.3)$$

where u_{60} is the wind speed for a wind direction of 60° and u_{150} is the wind speed for a wind direction of 150° .

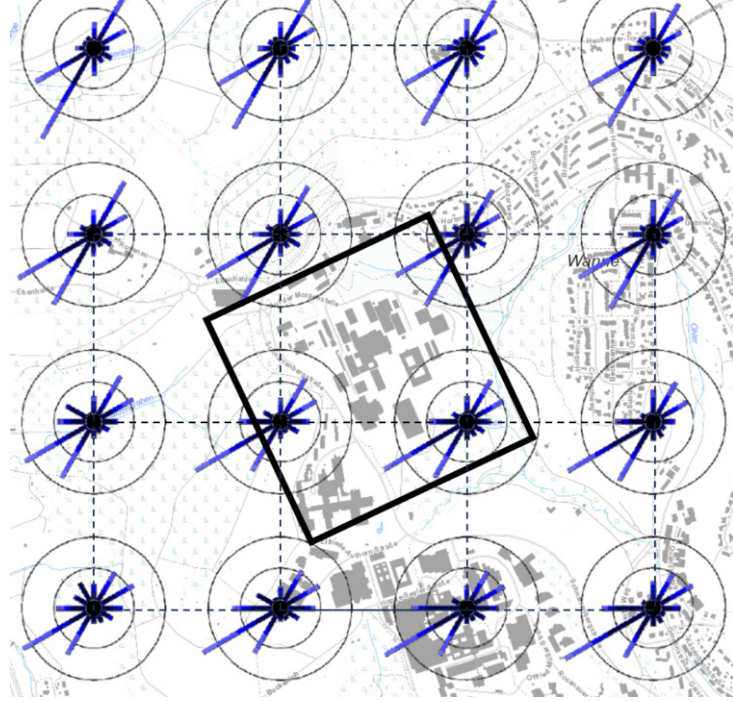


Figure 7.7: Large scale synthetic wind statistics at the university campus in Tübingen [3] (dashed lines) and the computational domain (black lines).

7.4.2 Calculation of local wind statistics

This subsection describes the second step of the method for calculating the local AEP. The yearly averaged wind velocity is indicated by \bar{u}_{WS} and already given in the synthetic wind statistics. In the case of fig. 7.6, \bar{u}_{WS} is 2.1 m/s but not shown in the figure. Similar to \bar{u}_{WS} , the simulated wind velocity \bar{u}_{sim} is averaged over the simulation time of 4 min. Since all wind directions are considered in \bar{u}_{WS} , the averaged wind velocity of each of the four simulated wind directions is taken into account and the average value \bar{u}_{sim} is calculated from this. New velocity bins B_{sim} based on the simulated wind speeds are calculated for each numerical cell to include the local wind speed and local flow effects. The new velocity bins B_{sim} are calculated by

$$B_{sim} = B_{WS} \cdot \psi(x, y, z), \quad (7.4)$$

where

$$\psi(x, y, z) = \frac{\bar{u}_{\text{sim}}}{\bar{u}_{\text{WS}}}. \quad (7.5)$$

The variable $\psi(x, y, z)$ is calculated for each numerical cell and consequently depends on x , y and z and defines the ratio between the simulated local wind speed \bar{u}_{sim} in a numerical cell and the yearly wind speed \bar{u}_{WS} from the synthetic wind statistics. Regarding equ. 7.4 each of the boundaries of B_{WS} is multiplied by $\psi(x, y, z)$. This results in a new scaling of the B_{sim} .

Since the wind speed bins are scaled new, also the frequencies have to be adapted according to the scaling. Otherwise, the frequencies would exceed 100%. To obtain the new adapted frequencies Φ_{sim} according to the new scaled wind speed bins B_{sim} , they are calculated by

$$\Phi_{\text{sim}} = \Phi_{\text{WS}} \cdot \frac{1}{\psi(x, y, z)}, \quad (7.6)$$

where Φ_{WS} are the frequencies given in the synthetic wind statistics.

Local wind directions in the simulations can differ from the main inflow wind direction. A building, a forested zone or other obstacles, may guide the flow towards another direction. To take this effect into account, an angle δ is introduced corresponding to the local wind direction in the simulations. The angle δ is defined as the angle between the unit vector of the northern direction \vec{n}_{nord} and the local flow direction because the northern direction corresponds to a wind direction of 0° . The angle δ is calculated for each numerical cell using the following equation

$$\delta = \arccos \left(\frac{\langle \vec{n}_{\text{nord}}, \vec{u}_h \rangle}{|\vec{u}_h|} \right), \quad (7.7)$$

wherein \vec{u}_h is the horizontal velocity vector. The local wind directions of the flow from non-simulated wind directions, such as 30° , 90° , 120° , 180° , 210° , 270° , 300° and 360° , are interpolated using the interpolation scheme of equ. 7.3 and the local wind directions of the flow from the simulated wind directions. With the help of δ , the new frequencies of the wind directions are calculated to investigate how the frequencies of the wind directions have been changed in comparison to those in the synthetic wind statistics.

The frequencies of the wind directions in the synthetic wind statistics are used as the frequencies of the local wind directions because these frequencies indicate how often the simulated main wind direction occurs and consequently the local wind comes from the local wind direction angle δ . For example, the simulated inflow wind direction is 240° with a frequency of 10% according to the synthetic wind statistics. Due to a building the flow is guided towards a local direction of 200° and the frequency of 10% is taken for the local wind direction. Note that the wind direction is not required for calculating the local AEP but important for the evaluation of the suitable positions for small wind turbines.

For the sake of visualization, the local wind directions are divided into the original wind direction bins used in the synthetic wind statistics as shown in fig. 7.6.

7.4.3 Calculation of the local AEP

In the third step, the local AEP is calculated using a powercurve of a real HAWT and a real VAWT with approximately the same rated power of 2.5 kW. For a HAWT, the Skystream 3.7 [5] wind turbine is taken and for a VAWT, the Turby B.V. [6] is taken. Both turbines are compared in table 7.1.

Type	HAWT	VAWT
Model	Skystream 3.7	Turby B.V.
Rated power [kW]	2.4	2.5
Rated wind speed [m/s]	13	14
Cut-in wind speed [m/s]	3.5	4
Cut-out wind speed [m/s]	25	14
Rotor diameter [m]	3.7	1.99

Table 7.1: Comparison of the horizontal and vertical wind turbines used in the calculation of the local AEP.

They mainly differ in the cut-out wind speed by 11 m/s. This is especially important for high wind speeds because the high wind speeds cannot be captured by the VAWT and converted into electrical power. It should also be noted that the HAWT starts to produce power at a lower wind speed (cut-in wind speed) and reaches its rated power at 13 m/s in contrast to 14 m/s obtained with the VAWT.

The local AEP is calculated for each numerical cell by the following equation:

$$\text{AEP} = 8760 \text{ h} \sum_{i=1}^9 \Phi_{\text{sim},i} \cdot \frac{P_{\text{u},i} - P_{\text{l},i}}{2}, \quad (7.8)$$

where 8760 h are the hours in a year. The frequencies $\Phi_{\text{sim},i}$ are calculated according to equ. 7.6. The power is taken from the respective power curve in accordance with the respective type of the wind turbine, presented in table 7.1. As mentioned above, each velocity bin B_{sim} has an upper and a lower velocity limit. The variable $P_{\text{u},i}$ indicates the power of the wind turbine according to the velocity of the upper velocity limit and $P_{\text{l},i}$ indicates the power of the wind turbine according to the velocity of the lower velocity limit.

7.4.4 Correction of the local AEP

The angle of attack γ of the wind turbine and the local atmospheric turbulence intensity can affect the power output of the wind turbine. To take these effects into account, the AEP is corrected in the fourth step. It should be noted that the power curve is adapted and the corrected AEP is calculated with the adapted power curve. Regarding the angle of attack, only the angle in the x - z -plane is taken into account. The angle γ is calculated for each numerical cell using the following equation

$$\gamma = \arccos \left(\frac{\langle \vec{n}_x, \vec{u}_{xz} \rangle}{|\vec{u}_{xz}|} \right), \quad (7.9)$$

wherein \vec{u}_{xz} is the velocity vector in the x - z -plane and \vec{n}_x is the unit vector in x -direction. To consider the effect of the angle of attack γ , the approach of Ferreira et al. [39] is used for VAWTs and the approach of Glauert [31] is used for HAWTs. The power curve of a VAWT is corrected using the ratio of the pressure coefficient of the current angle of attack $c_p(\gamma)$ to the pressure coefficient with a zero angle of attack $c_p(\gamma_0)$. This ratio is defined by Ferreria et al. [39] in the following equation

$$\frac{c_p(\gamma)}{c_p(\gamma_0)} = \left(\frac{\cos \gamma \cdot \left(\cos \gamma + \frac{\pi}{4} \cdot \frac{D_w}{H_w} \cdot \sin \gamma - 2 \sin \gamma \cdot \left(\beta_\gamma \cdot \frac{D_w}{4H_w} - \frac{L_\gamma}{H_w} \sin \beta_\gamma \cdot 0.5 \right) \right)}{\cos \gamma_0 \cdot \left(\cos \gamma_0 + \frac{\pi}{4} \cdot \frac{D_w}{H_w} \cdot \sin \gamma_0 - 2 \sin \gamma_0 \cdot \left(\beta_{\gamma_0} \cdot \frac{D_w}{4H_w} - \frac{L_{\gamma_0}}{H_w} \sin \beta_{\gamma_0} \cdot 0.5 \right) \right)} \right)^{1.5} \quad (7.10)$$

with the diameter D_w and the height H_w of the VAWT. Imagine a VAWT as a hollow cylinder which is inclined to the vertical axis of the cylinder, the parameters L_γ , β_γ and β_{γ_0} define the area of the hollow part of the surface.

For HAWTs the ratio of the pressure coefficients is defined according to Glauert [31] by

$$\frac{c_p(\gamma)}{c_p(\gamma_0)} = \frac{\sqrt{1-q} (2 \cos \gamma - q) \cdot (\cos \gamma - q)}{(1-q)^2}, \quad (7.11)$$

where q is the induction factor of a HAWT. The induction factor has to be determined for each HAWT individually. Fig. 7.8 illustrates the ratio of the pressure coefficients for the Turby B.V. VAWT and the Skystream 3.7 HAWT. For γ smaller than 30° the power output of the VAWT is even increased because the projected area in the angle of attack direction increases. That makes it a more suitable wind turbine for urban areas in which the flow is not necessarily horizontal and unidirectional. However, for the HAWT the power output is always reduced when the HAWT is not blown horizontally because the effective area of the wind turbine decreases in accordance with the projected area in the angle of attack direction. The power of the HAWT is reduced which is shown in fig. 7.9

in dependence of the angle of attack. For example, at an angle of attack of 30° the power output is reduced by 13%.

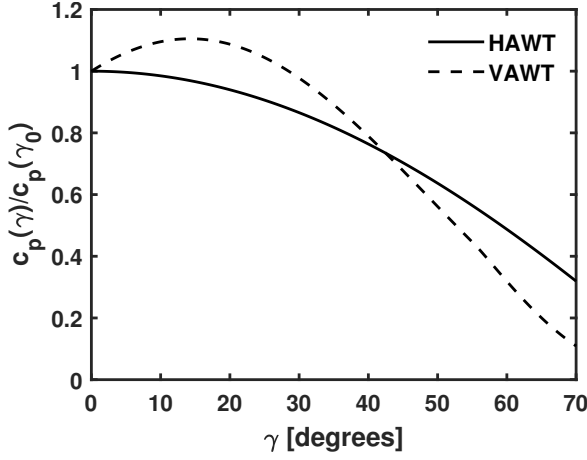


Figure 7.8: Pressure coefficient for the HAWT and the VAWT in dependence of γ .

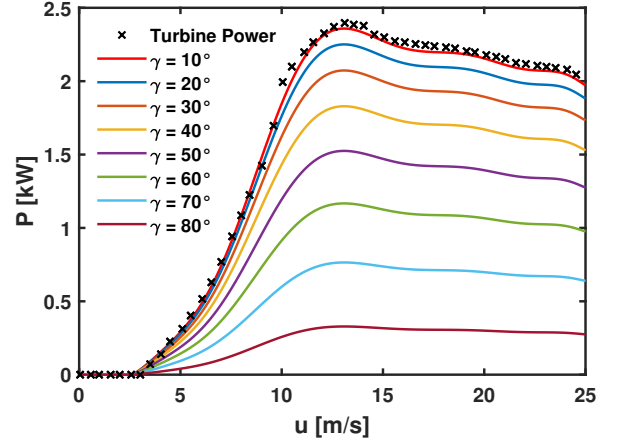


Figure 7.9: Power loss of the HAWT with increasing γ .

For the correction of the power curve regarding turbulence intensity, the approach by Albers et al. [17] is applied. The approach is based on the idea that the flow fluctuates around the time-averaged velocity. Since the power output of the wind turbine does not increase linearly with the time-averaged velocity, the fluctuations, which have a proportion of higher velocities, contribute more power than the fluctuations which have a proportion of lower velocities. The aerodynamic effects on the wind turbines due to turbulence intensity are not considered in this method since the aerodynamic effects are specific for each wind turbine and cannot be generalized. The basic equation of the corrected power $P_{\text{corr}}(u)$ is defined as

$$P_{\text{corr}}(u) = P(u) - P_{10\%TI}(u) + P_{\text{simTI}}(u). \quad (7.12)$$

The variable $P(u)$ is the measured power output according to the wind turbine manufacturer, assuming a turbulence intensity TI of 10%. The strong local variation of the fluctuations in the simulations are considered in $P_{\text{simTI}}(u)$, thus the power ratio according to $P_{10\%TI}(u)$ is subtracted and the power ratio according to $P_{\text{simTI}}(u)$ is added to the power equation. The fluctuations in the power ratios $P_{10\%TI}(u)$ and $P_{\text{simTI}}(u)$ are assumed to be Gaussian distributed [126]. The power ratio according to $P_{10\%TI}(u)$ is defined as

$$P_{10\%TI}(u) = \int_{u=0}^{\infty} P(u) \cdot f_{G10\%}(u) du, \quad (7.13)$$

where $f_{G10\%}(u)$ is the Gaussian distribution as a probability density function (pdf) and $P(u)$ is the power of the wind turbine. The standard deviation in the Gaussian distribution

is defined as

$$\sigma = I \cdot |\bar{u}| \quad (7.14)$$

with u as the time-averaged velocity magnitude $|\bar{u}|$ in each numerical cell and a turbulence intensity I of 10%. The power ratio according to $P_{\text{simTI}}(u)$ is defined as

$$P_{\text{simTI}}(u) = \int_{u=0}^{\infty} P(u) \cdot f_{G\text{sim}}(u) du. \quad (7.15)$$

In equ. 7.15 the turbulence intensity I obtained in the simulations is taken. The Gaussian distribution $f_{G\text{sim}}(u)$ is calculated with the standard deviation of the turbulence intensity from the simulations. Fig. 7.10 illustrates the effect of two different pdfs. The black line represents the power curve, the dashed line the mean velocity u and the dotted line the starting velocity of the wind turbine. Fig. 7.10 further shows two different pdfs with a turbulence intensity of 20% and 70% but with the same mean velocity. The pdf with $I=70\%$ has a larger proportion of high velocities and of high power than the pdf with $I=20\%$. Thus, higher turbulence intensities lead to higher power outputs. However, for higher mean velocities the opposite is the case and lower power outputs are obtained with higher turbulence intensities because the pdf spreads more into the low power range of the power curve. These effects are shown in fig. 7.11. Up to a wind speed of 9 m/s the power output increases with increasing turbulence intensity and above the wind speed of 9 m/s the power output decreases with increasing turbulence intensity.

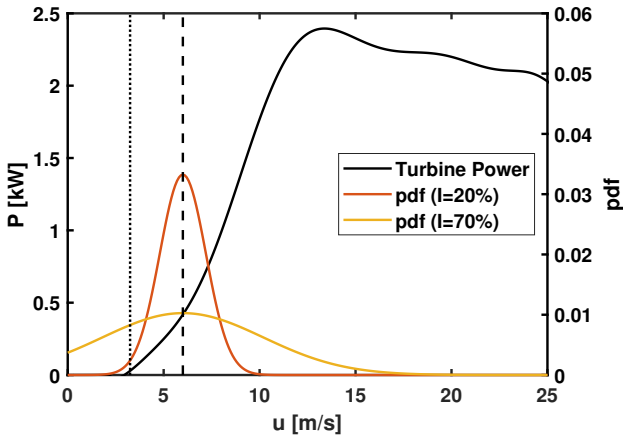


Figure 7.10: HAWT power curve with a pdf with $I=20\%$ and 70% .

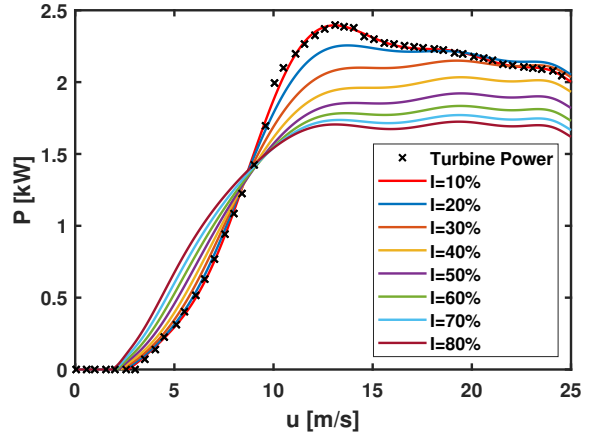


Figure 7.11: HAWT power curve affected by turbulence intensity.

7.5 Local wind statistics and local AEP

In the following, local wind statistics calculated based on the simulations according to the above mentioned method are presented and compared with the large scale synthetic wind statistics. Later the AEP calculated for each building using the HAWT and the VAWT

will be visualized and analysed.

Fig. 7.12 shows the local frequencies of the wind direction bins over the roof of building A compared to the frequencies in the synthetic large scale wind statistics. The local wind statistics are evaluated at 10 m over the roof and in the centroid of the top surface of the respective building to avoid the influence of aerodynamic effects at building edges such as cone vortices [58]. As the main difference to the synthetic wind statistics, the frequency in the sector of $226^\circ - 255^\circ$ is increased while the frequencies in the sectors of $16^\circ - 105^\circ$ are reduced. A possible reason for that could be the many buildings which are located in the inflow towards building 12, when the wind is coming from 60° wind direction. Fig. 7.13 illustrates the local frequencies of the wind speed bins determined at the same location as in fig. 7.12 compared to the frequencies in the synthetic large scale wind statistics. Lower wind speeds occur much more frequently in the synthetic wind statistics. Due to the fact that the location is above the roof of a building, the wind is accelerated above the roof top. As a result higher wind speeds occur much more frequently in the local wind statistics. For example, the frequency of the velocity in the range of $3.86 \text{ m/s} - 5.45 \text{ m/s}$ is 10 percentage points higher than in the synthetic wind statistics. Further locations with higher simulated wind speeds than in the synthetic wind statistics are especially above buildings and in larger heights. Using only the synthetic wind statistics for the calculation of the AEP would lead to a over-prediction. Thus, for a detailed and reliable wind energy yield calculation local wind statistics are essential and the simulation of different wind directions have to be taken into account for a precise location decision for small wind turbines in urban areas.

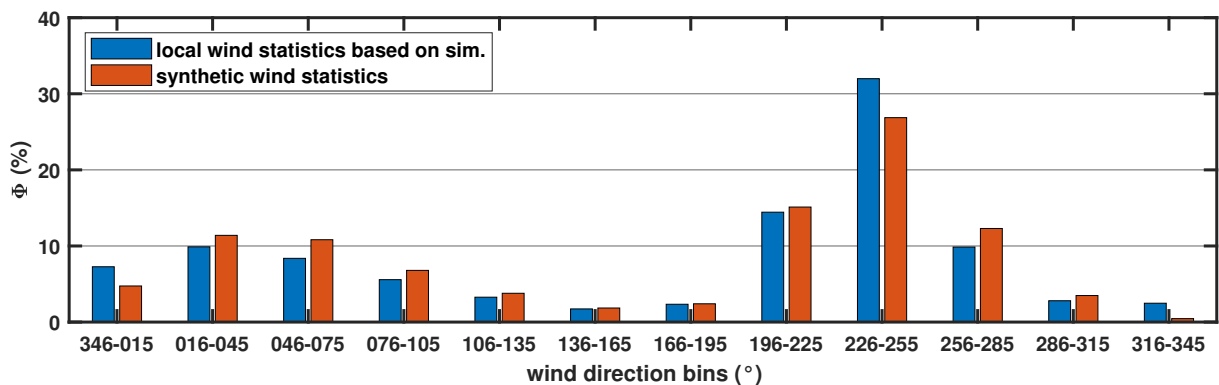


Figure 7.12: Frequencies Φ of local wind directions based on the simulations and synthetic wind statistics on building 12 with surrounding buildings in the simulations.

The AEP is determined using the Skystream 3.7 with 2.4 kW [5] as an example for the HAWT and using the Turby B.V. with 2.5 kW [6] as an example for the VAWT. The AEP is calculated according to the above mentioned method for each numerical cell. To associate the determined AEP values to each building, the cells within a height distance of 15 m to the building roof are associated to the respective building. The AEP values are averaged over a sphere with a radius of 1.86 m to avoid outliers and mesh induced errors.

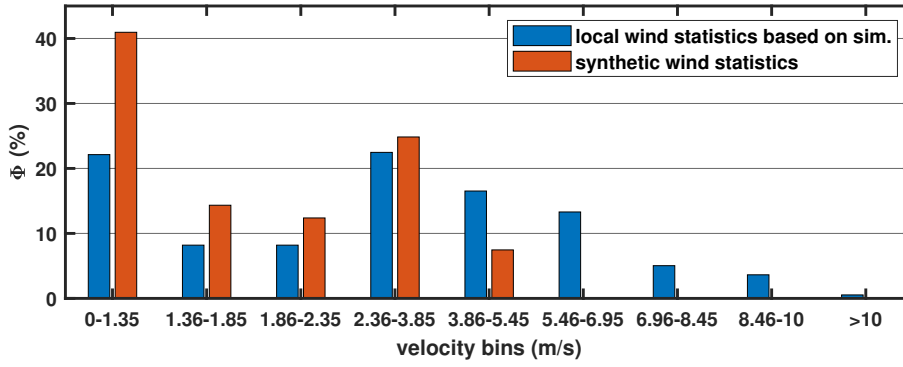


Figure 7.13: Frequencies Φ of local wind speeds based on the simulations and synthetic wind statistics on building 12 with surrounding buildings in the simulations.

The radius corresponds to the radius of the HAWT and half the height of the VAWT. Hence, it also gives a more realistic prediction of the energy yield which can be obtained with the HAWT or the VAWT. Fig. 7.14 shows the maximum value of all sphere-averaged AEP values associated to the respective building when the VAWT is used. The shown AEP values are both I - and γ -corrected. The term " I -corrected" means that the AEP is corrected by the method according to the equations 7.12-7.15. The term " γ -corrected" means that the AEP is corrected by the method according to the equations 7.10 or 7.11. The reference signs of the buildings used in the following refer to the reference signs shown in fig. 7.14.

The highest energy yield with a VAWT can be obtained on buildings 12 and 13 which are the buildings A and B, respectively and the highest buildings on the campus. But that does not mean that on every high building the energy yield is large. For example, the buildings 15, 17 and 22 are also high-rise buildings but show only around half the energy yield of building 13. The lowest energy yield is predicted for the buildings 5-8, 18 and 23. The buildings 5-8 are surrounded by forested zones and a hill. In the main wind direction, the forested zones and the hill are located in front of the buildings 5-8 and are consequently within the wake of the hill. This drastically lowers the obtainable energy yield. Additionally, the shape of the roof, namely the gable roof, of the buildings 5-8 leads to lower wind speeds than flat roofs, which is also confirmed by Ledo et al. [69]. The buildings 18 and 23 are surrounded by high-rise buildings shielding the wind from them. Regarding building 18, building 15 prevents the wind from the main wind direction from reaching building 18 directly. But also from the second main simulated wind direction, which is 150° , the building 18 is blocked by the adjacent building 17. But not all of the flat buildings show low energy yields, such as building 9, 11 and 21. Especially, the buildings 9 and 11 benefit from the almost free inflow from the 150° and 330° wind direction as shown by the location 2 in fig. 7.5 and location 4 in fig. 7.3. Building 21 benefits from the flow acceleration from the simulated second wind direction 150° at point 3, as shown in fig. 7.3. The flow is an undisturbed inflow in a canyon which is formed by the buildings 20 and 22. But in general, there is a trend towards that the amount of energy

yield increases with the building height since the building height makes the building less dependent by terrain and vegetational effects. Fig. 7.15 shows the maximum value of the

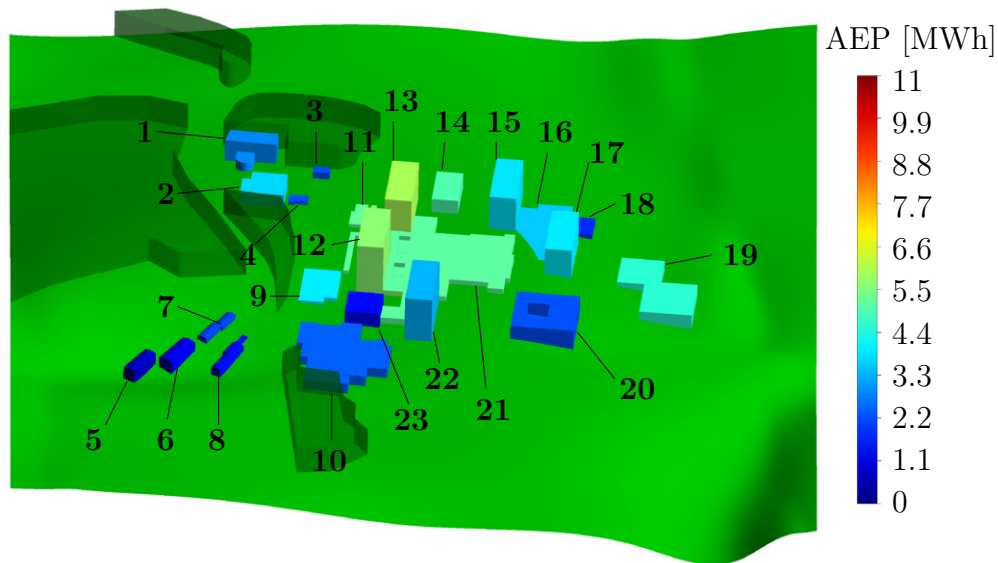


Figure 7.14: Calculated AEP associated to buildings at the university campus Morgenstelle in Tübingen for VAWT.

sphere-averaged AEP values for each building using the HAWT. The shown AEP values are both I - and γ -corrected. In total, higher AEP values are obtained with the HAWT due to a higher performance at lower wind speeds and a lower cut-in wind speed of 3.5 m/s in contrast to 4 m/s of the VAWT.

The highest energy yield with the HAWT can be obtained on building 13 with around 10 MWh compared to around 6 MWh with the VAWT. However, the energy yield on the buildings 5 and 6 is not significantly increased since these buildings are positioned too close to the hill so that they are often in the wake of said hill.

When considering the VAWT, on the buildings 13 and 22 a maximum AEP of 6.0 MWh and 3.3 MWh can be achieved, respectively. When the HAWT is used instead, the maximum AEP increases by 71 % to 10.2 MWh on building 13 and by 28 % to 4.3 MWh on building 22. Thus, it cannot be generally stated that the AEP increases at all locations by the same percentage when switching from the VAWT to the HAWT model. This can be caused by different angle of attacks because in contrast to the VAWT, an angle of attack larger than zero reduces the power output of the HAWT as shown in fig. 7.9. Even when both types of wind turbines have the same rated power, the AEP values do not increase by the same ratio. The higher performance of the HAWT in the lower wind velocity range and the lower cut-in speed certainly contributes to the AEP increase. The AEP associated to each building has to be investigated carefully and separately for each wind turbine model.

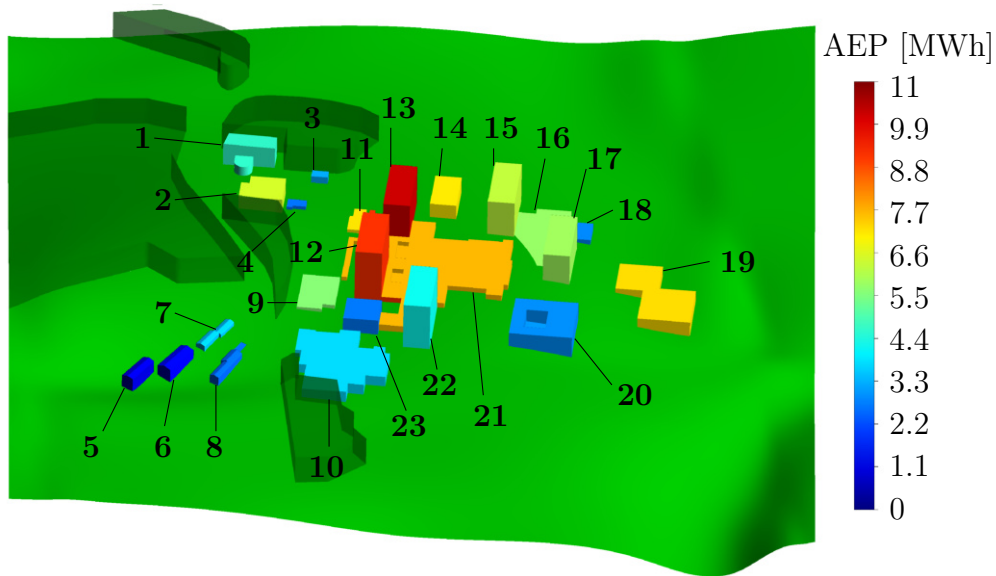


Figure 7.15: Calculated AEP associated to buildings at the university campus Morgenstelle in Tübingen for HAWT.

As expected, the buildings $12 \hat{=} A$ and $13 \hat{=} B$ are the buildings with the highest energy yield potential at the university campus Morgenstelle in Tübingen. Using the Skystream 3.7 with 2.4 kW [5] as a HAWT, the maximum AEP on building A is 9.1 MWh compared to 10.2 MWh on building B. Using the Turby B.V. model with 2.5 kW [6] as a VAWT, the maximum AEP on building A is 5.6 MWh compared to 5.9 MWh on building B.

Building No.	AEP uncorrected [MWh]	AEP I -corrected [MWh]	AEP γ -corrected [MWh]
1	0.34	2.72	2.87
2	0.33	3.52	3.72
3	0.37	2.08	2.24
4	0.12	2.01	2.20
5	0.12	0.53	0.57
6	0.13	1.12	1.16
7	0.59	1.91	2.04
8	0.94	1.38	1.49
9	1.26	3.78	3.94

10	1.03	2.27	2.42
11	0.88	4.90	5.20
12	1.71	5.42	5.63
13	2.42	5.78	5.95
14	1.59	4.77	4.98
15	2.14	3.76	3.87
16	1.04	3.49	3.55
17	1.61	3.70	3.93
18	0.8	1.76	1.84
19	1.02	4.40	4.59
20	0.17	2.14	2.25
21	1.45	4.93	5.13
22	1.17	3.09	3.33
23	0.65	1.32	1.45

Table 7.2: Comparison of the corrected and uncorrected AEP values using the VAWT.

Table 7.2 shows the calculated uncorrected, I -corrected and γ -corrected AEP values for each building obtained with the VAWT. First of all, the values have been strongly increased by the I -correction. A reason for that could be that only the area above the roof is considered. This area is characterized by a strong flow separation at the front edge of the roof in the case of a flat roof or on the gable roof ridge in the case of a gable roof. Consequently, the separation leads to a strong increase in the velocity gradient and high k and I values as already shown in 5.3. Referring to the figs. 7.10 and 7.11, the high I values lead to higher energy yields for the HAWT.

Related to the uncorrected AEP, the three highest AEP values are obtained on the buildings 12, 13 and 15. But the increase by the I -correction is on building 15 much less than on the buildings 12 and 13. This indicates that there the I values are higher which is due to the vicinity to the forested zones. When the wind comes from the main wind directions, the turbulent kinetic energy produced by these forested zones is transported with the flow towards the buildings 12 and 13 leading to higher I values.

It should be noted that due to the inertia of the wind turbine not all the wind speed

fluctuations can be captured by the wind turbine. That means, that not every short-term wind speed fluctuation changes the rotational speed and leads to higher or lower power outputs. As a result, the influence of the turbulence intensity may be lower in reality. Unfortunately, this influence could not be considered in this study since it depends on the used wind turbine model and has to be investigated specifically for each turbine. Since the correction changes the AEP values noticeable, this method must be considered in a detailed and accurate prediction of the AEP and must be part of detailed evaluation of possible locations for small wind turbines.

7.6 Influence of surrounding buildings on local AEP

In order to further investigate the influence of surrounding buildings, the AEP is calculated based on the simulations with surrounding buildings which are described in chapter 5.4. The same wind turbines as above are taken exemplarily to determine the AEP by means of the same method as described above.

Fig. 7.16 illustrates the maximum AEP values associated to the respective building using the VAWT and fig. 7.17 shows the maximum AEP values when the HAWT is used. When buildings, which surround the buildings of interest in the centre of the domain, are included in the simulations, the wind flow is influenced and may be blocked by the surrounding buildings. This influences the wind speed and the AEP values within the area of interest. To emphasize the significance of surrounding buildings for a precise AEP prediction, significant differences in AEP values are analysed.

The AEP values associated to the buildings 5 and 6 increase from 0.6 MWh and 1.2 MWh to 4.1 MWh and 5.1 MWh for the VAWT and from 1.0 MWh and 1.4 MWh to 6.8 MWh and 7.2 MWh for the HAWT. This strong increase is induced by the tall building close to building 5. The height of the tall building is around twice the height of building 5. The wind directions in the sector of 196° to 255° occurs with a frequency of 45%. When the wind comes from these wind directions, the wind flow is blocked by the tall surrounding building and deflected towards the upper direction in fig. 7.17. The deflected flow is accelerated when it passes the vertical edge of the taller building. Due to the larger height of the taller building the flow passes the roof of building 5. This effect improves also the AEP at building 6. Further downstream, the accelerated flow passes also the roof of building 8 so that the AEP at building 8 is improved by 107% for the VAWT and by 97% for the HAWT.

In the case, where the surrounding buildings are considered, the AEP increases by 27% on building 19 using the VAWT model compared to 51% using the HAWT model. The reason for that is that velocities from certain wind directions are increased, e.g., from 330° as illustrated in location 3 in fig. 5.34. Hence, the wind speeds exceed more often the cut-in speed limit during the *I*-correction, wherein the cut-in wind speed limit is higher in

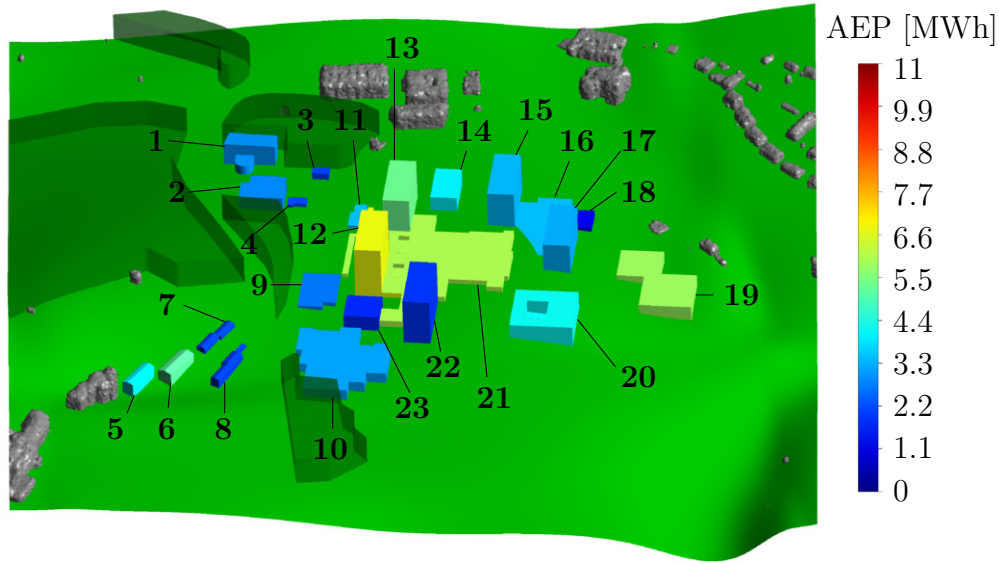


Figure 7.16: Calculated AEP associated to buildings at the university campus Morgenstelle in Tübingen for VAWT when the surrounding buildings are included in the simulations.

the HAWT in contrast to the VAWT. But the increase from the VAWT to the HAWT is larger, when the surrounding buildings have been taken into account. The reason for that is the lower cut-off wind speed of the VAWT of 14 m/s and a higher turbulence intensity above building 19. Especially, when the wind comes from the 60° and 150° wind direction, the buildings in the inflow towards building 19 cause higher I values. That means that in the I -correction the cut-off wind speed of the VAWT is likely exceeded and no electricity is produced when the cut-off wind speed is exceeded.

Another aspect is the different development of the electrical power on the buildings 22 and 23 when the surrounding buildings are considered in the simulation, although the buildings 22 and 23 are relatively close to each other. While on building 22 the electrical power decreases by about 50 %, on building 23 it increases by about one third. One reason for this is that the wind speed from 330° is lower, since the surrounding buildings are in the inflow. This has a greater effect on building 22 than on building 23, since the latter is in the wake of building 12 and therefore the wind speeds from this direction are very low for the building 23. On the other hand, if the situation from 240° is taken into account, a kind of blockade results from the surrounding buildings, through which the flow is directed more in the direction of building 23. As a result, the wind speeds increase on the roof of this building and not on the roof of building 22, since the latter is too high. The wind turbine is now longer in operation and contributes more power to the AEP. In the wind directions of 240° and especially at 330° , the velocity over the building 19 increases as shown in fig. 5.33 and 5.34.

The AEP associated to building 12 increases by 19% using the VAWT model while the

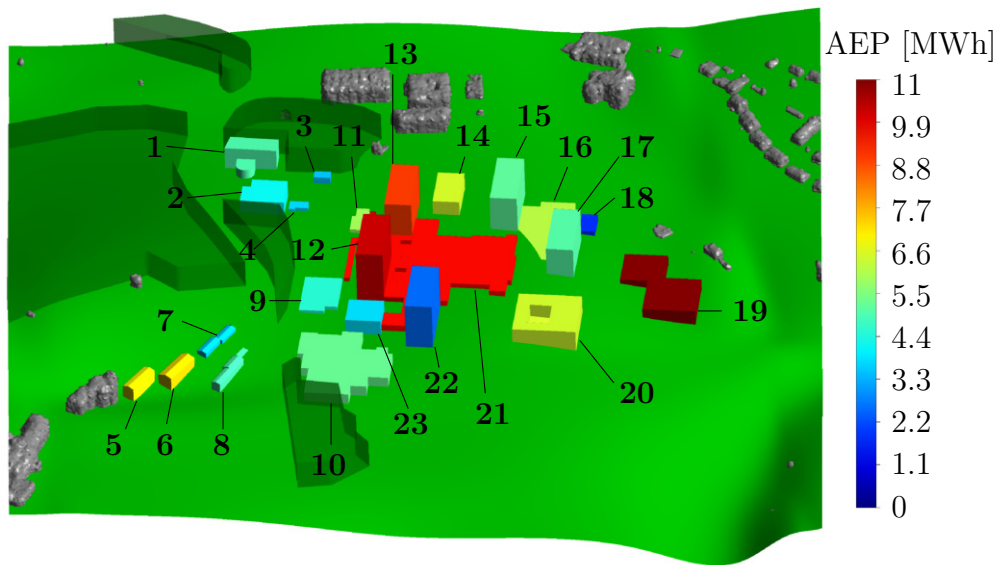


Figure 7.17: Calculated AEP associated to buildings at the university campus Morgenstelle in Tübingen for HAWT when the surrounding buildings are included in the simulations.

AEP using the HAWT model just increases by 11 % when the surrounding buildings are considered. The angle of attack over the rooftop is inclined due to curved streamlines associated with the characteristic detachment zone on a flat roof. A small angle of attack raise the power output of a VAWT while it reduces the power output of a HAWT.

The AEP associated to building 13 decreases by 10 % using the VAWT model while the AEP using the HAWT model is reduced by 11 % when the surrounding buildings are taken into account in the simulations. The reason for the different development of the AEP is due to the various building heights and their locations. Considering the main wind direction, the surrounding buildings are not located in the inflow region but more closer to the boundaries of the domain. Hence, the flow is decelerated at the boundaries of the domain and accelerated in the centre. The reason why the AEP on building 13 is reduced is that it is located closer to the surrounding buildings. When the wind is coming from the 330° or 60° wind direction, the surrounding buildings block the flow towards building 13. But due to the larger height of building 12, it is less affected by the blocking effect caused by the surrounding buildings.

7.7 Evaluation of locations for small wind turbines

In the following, suitable locations for small vertical and horizontal wind turbines will be discussed. Herein, only locations on buildings roofs will be analysed, locations between buildings, over vegetation zones or unbuilt terrain will be not considered. The buildings

12, 13, 19 and 21 are considered as suitable locations with an AEP of more than 8 MWh, wherein the buildings 12 and 13 are the highest buildings on the test site. The discussion is mainly based on the local wind statistics evaluated and the AEP values when the surrounding buildings are included in the simulations. The local wind statistics are evaluated as mentioned in chapter 7.5. For the sake of simplicity, the wind statistics in the following are only evaluated at the centroid. But depending on the evaluation point of a building, the frequencies in the local wind statistics can change again.

The load factor Ψ is introduced as a further parameter which is significant for customers and investors who are planning to operate a wind turbine. The load factor Ψ describes the ratio of the real obtained AEP to the theoretically maximum AEP of the wind turbine in one year. The load factor Ψ is given by

$$\Psi = \frac{\text{AEP}}{P_{\max} \cdot 8760 \text{ h}}, \quad (7.16)$$

wherein P_{\max} is the rated power of the wind turbine which is provided by the wind turbine manufacturer and 8760 h are the hours in one year.

Fig. 7.18, which is identical to figs. 7.12 and 7.13 in chapter 7.5, illustrates the local

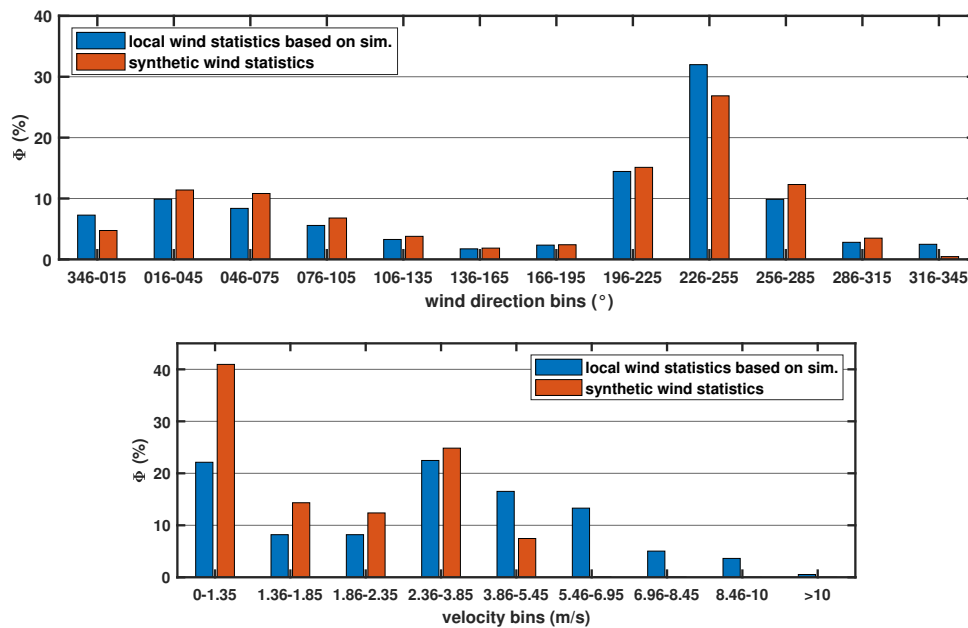


Figure 7.18: Local wind statistics including frequencies of wind directions and wind speeds compared to synthetic wind statistics for building 12.

wind statistics with the frequencies of wind directions and wind velocities compared to the synthetic wind statistics associated to building 12 $\hat{=}$ A. The wind statistics show a main wind direction sector between 226° and 255° with a frequency of 30%. The frequencies for the other wind directions are mostly 10% or below. As the main difference to the synthetic wind statistics, the frequency in the sector of 226° - 255° is increased while the frequencies in the sectors of 16° - 165° are reduced. A possible reason for that could be the many buildings which are located in the inflow towards building 12, when the wind

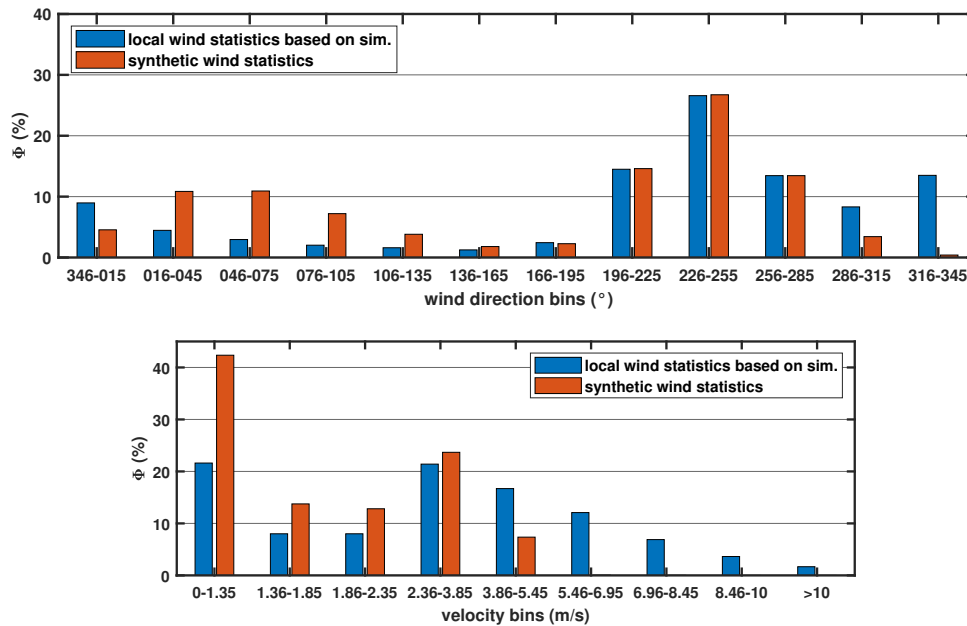


Figure 7.19: Local wind statistics including frequencies of wind directions and wind speeds compared to synthetic wind statistics for building 13.

is coming from the 60° wind direction. Lower wind speeds occur much more frequently in the synthetic wind statistics. Due to the fact that the location is above the roof of a building, the wind is accelerated above the roof top. As a result higher wind speeds occur much more frequently in the local wind statistics. For example, the frequency of the velocity in the range of $3.86 \text{ m/s} - 5.45 \text{ m/s}$ is almost twice as high as in the synthetic wind statistics.

The AEP using the VAWT is 6.7 MWh corresponding to a load factor of 0.32 and the AEP using the HAWT is 10.1 MWh corresponding to a load factor of 0.48. The lower load factor of the VAWT is due to the lower cut-off wind speed. The high AEP values are significantly improved by high turbulence intensity values. But turbulence intensity can further cause aerodynamic effects at the wind turbines. For example, they can affect the power performance and high fluctuating wind loads can also reduce the life time of wind turbines. These effects are not considered in this study. Together with the excellent load factor and the AEP it is one of the high-performance locations for small HAWTs on the university campus although it has to be assumed that the AEP in reality may be lower due to the fact that not all velocity fluctuations considered in the I -correction of the AEP lead to higher power outputs of the wind turbine.

Fig. 7.19 illustrates the local wind statistics with the frequencies of wind directions and wind velocities compared to the synthetic wind statistics associated to building 13. The wind statistics show a frequency of 26% for the main wind direction sector which is between 226° and 255° . The frequency distribution of the wind directions is a more equalized than that of building 12. The frequency of each wind direction bin between 16°

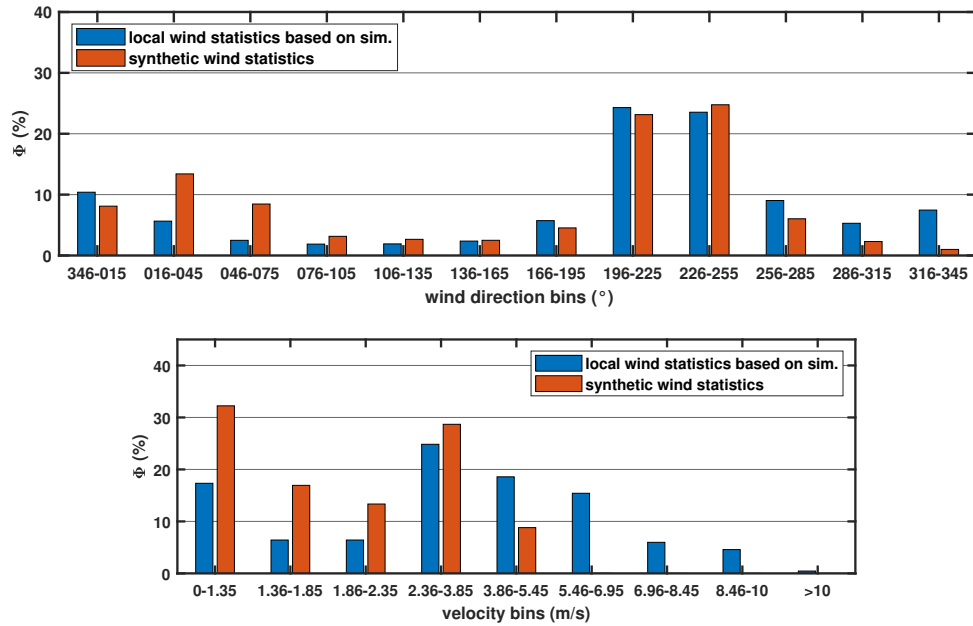


Figure 7.20: Local wind statistics including frequencies of wind directions and wind speeds compared to synthetic wind statistics for building 19.

and 195° is under 5%. The AEP using the VAWT is 5.3 MWh corresponding to a load factor of 0.25 and the AEP using the HAWT is 9.0 MWh corresponding to a load factor of 0.43.

Regarding the wind directions, the main difference to the synthetic wind statistics, is the shift in the frequency of the wind direction from the sector of $16^\circ - 105^\circ$ to the sector of $286^\circ - 15^\circ$. That means that the wind which is coming originally from 60° is now coming from 330° above building 13. Considering the orientation of building 13 it is more aligned towards the direction of 150° such that the wind is not directed towards 330° but towards 150° . That means that the wind comes now more often from the 330° wind direction. The orientation of the building 13 also affects the wind flow over its roof. Fig. 7.13 illustrates the local frequencies of the wind speed bins determined at the same location as in fig. 7.12 compared to the frequencies in the synthetic large scale wind statistics. When comparing the two frequency distributions of the wind speeds on buildings 12 and 13, you can see only small deviations. As also described for building 12, the location is above the roof of a building and due to the blockage of the building the wind is accelerated above the roof top. As a result higher wind speeds occur much more frequently in the local wind statistics. For example, the frequency of the velocity in the range of $2.36 \text{ m/s} - 3.85 \text{ m/s}$ is 10 percentage points higher than in the synthetic wind statistics.

Regarding the evaluation of the site, the location above building 13 shows a similar performance compared to building 12. The minor differences of the wind direction frequencies can be neglected, since such wind direction changes can be handled by both the VAWT and also the HAWT when equipped with a yaw control.

Fig. 7.20 illustrates the local wind statistics with the frequencies of wind directions and wind velocities compared to the synthetic wind statistics associated to building 19. Main wind direction sectors from 196° until 255° with a total frequency of approximately 50% are shown. The remaining wind directions have a frequency below 10% or even below 5%. Regarding the wind directions, the main difference to the synthetic wind statistics, is the shift in the frequency of the wind direction from the sector of $16^\circ - 105^\circ$ to the sector of $286^\circ - 15^\circ$. That means, that the wind which is coming originally from 60° is now coming from 330° above building 19. This is also the case above building 13. But here, the flow at the centroid of the top surface of building 19 is influenced only by the topography and the building itself and not by surrounding buildings when the flow comes from 60° . The streamlines from the 60° wind direction are diverted by the shape of the valley a bit to the north, so that they pass the roof surface near the outer edge of the building 19 which is the closest edge to the 60° inflow plane. Afterwards the streamlines approach the ground again and are directed more to 180° direction so that they pass the roof at its centroid of the building 19. A reason for that could be the stagnation region and the accumulation of streamlines near the north part of the building 19. Hence, the wind at the centroid of the roof surface of building 19 comes more from the 330° wind direction.

The AEP with a VAWT is 5.8 MWh corresponding to a load factor of 0.28 and the AEP with a HAWT is 10.9 MWh corresponding to a load factor of 0.52. A reason for the high AEP here are the high wind speeds from the main wind direction sector. The buildings 17 and 20 are arranged such that they squeeze the wind flow like in a nozzle flow accompanied by an acceleration of the wind flow. The centreline of the so-called nozzle points directly towards the centroid of building 19. The impressive load factor and the high AEP caused by the characteristic flow situation makes this location to a highly recommended and profitable position for the small HAWT.

Fig. 7.21 illustrates the local wind statistics with the frequencies of wind directions and wind velocities compared to the synthetic wind statistics associated to building 21. The wind statistics show a focus on the main wind direction sector between 226° and 255° with a frequency of almost 40%, while the frequencies of each wind direction bin between 286° and 165° is below 5%. The frequency reduction of the 60° wind direction sector is mainly caused by building 17 which blocks the flow towards the centroid of building 21. Regarding the wind direction of 330° , the wind flow is blocked by the surrounding buildings and the buildings 13 and 14. The reason for the high frequency from the 240° is that the buildings 12 and 13 are arranged such that they form a passage, so that the wind flows between the buildings 12 and 13 through this passage. The centreline of the passage points to the centre of the building 21 and directs the wind flow to it. Due to the narrowing cross-section of the passage, the flow is accelerated when the wind comes from

that direction.

The comparison of the synthetic and local wind statistics show an increase of the wind speed above building 21 due to the above mentioned local aerodynamic effects which are caused by the surrounding buildings, the terrain and the vegetation. The local wind statistics further show the largest idle time, that is the time, when the wind speed is below the cut-in wind speed of the wind turbine. The AEP using the VAWT is 6.0 MWh corresponding to a load factor of 0.29 and the AEP using the HAWT is 9.6 MWh corresponding to a load factor of 0.46.

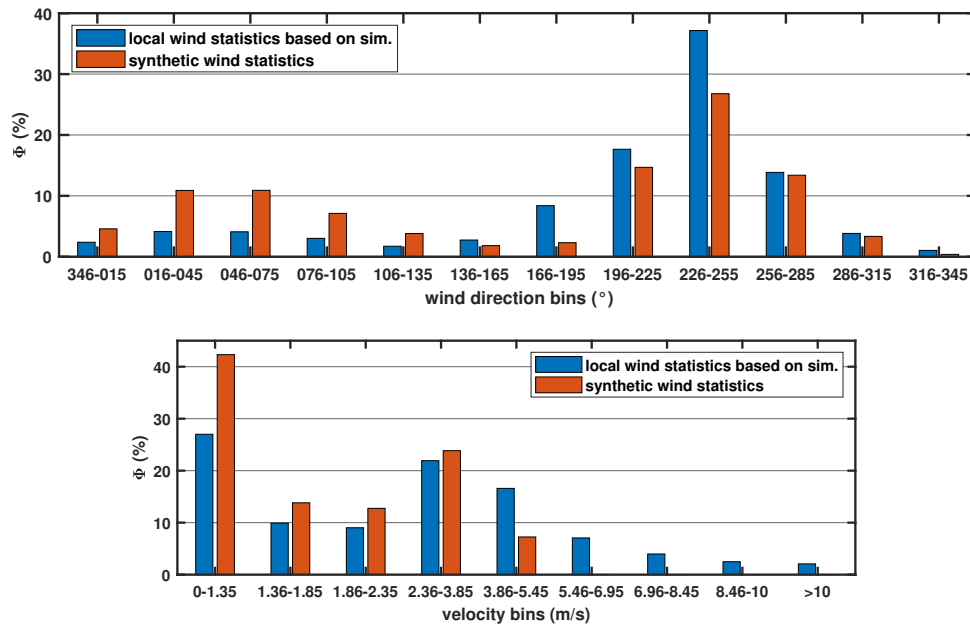


Figure 7.21: Local wind statistics including frequencies of wind directions and wind speeds compared to synthetic wind statistics for building 21.

In this case study, the Skystream 3.7 model (HAWT) [5] is the preferred wind turbine over the the Turby B.V. model (VAWT) [6]. Both wind turbines have the same rated power but the Skystream 3.7 shows a better performance at lower wind speeds and a lower cut-in wind speed. This gives the HAWT advantages in the AEP. In contrast to the VAWT the HAWT requires a sufficient yaw control due to varying wind directions.

Based on the locally determined wind statistics, the building 19 is the overall preferred location for a small wind turbine on the university campus Morgenstelle in Tübingen in comparison to the evaluated buildings 12, 13 and 21. But all of them take advantage of the accelerating effect of the wind on the roof. The total electricity consumption of the entire university in Tübingen, which includes further department buildings which are not located at the campus Morgenstelle, is 40 MWh. Keeping the disclaimer in mind, that the real AEP may be lower due to the not considered turbulence induced affects of a wind turbine, 25 % of total electricity consumption can be obtained with the HAWT

on the buildings 12 or 19. The highest AEP (10.9 MWh) amongst all buildings at the university campus can be achieved using the HAWT. Furthermore, the lowest ratio of idle time can be reached on building 19. The ratio of the idle time is defined by the sum of the frequencies of the velocity bins which are lower than the cut-in wind speed of the wind turbine. On building 12, the second highest AEP (10.1 MWh) can be achieved. The most balanced distribution of wind directions is on building 13. That requires a sufficient yaw control of the HAWT. The wind flow on building 21 shows the strongest focus on the main wind direction and the highest idle time amongst the four evaluated buildings.

It has to be noted that this study just includes a first recommendation for suitable wind turbine locations which is only based on local wind statistics. Further criteria have to be investigated such as the static load capacity of the buildings, the shadowing or the noise of the wind turbines which can affect the social acceptability of wind turbines. Potential power performance changes of wind turbines induced by the turbulence intensity have to be investigated and included into this study. But these are very specific and may differ much amongst wind turbine models.

The bottom line of this study is the consideration of several wind directions to obtain an entire view on the wind flow at the site. The local effects such as surrounding buildings, terrain and vegetation render the prediction of the wind flow and the AEP more precisely than simplified prediction methods. For a precise prediction of the AEP, the I - and γ -correction have to be included in the calculation method. The inflow condition in common studies is usually obtained from one wind measurement station which is located far from the focussed buildings without taking any wind statistics into account. Hence, these studies for determining suitable positions for small wind turbines in built areas neglected important information about the local site and, thus are lacking of preciseness and validity. Considering only one wind direction in the calculation of the annual energy yield would reflect only part of the reality and hide a large part of the wind situations that occur. Such a simplified procedure cannot lead to a reliable prediction of the annual energy yield. Neglecting surrounding buildings, terrain, and vegetation would inadequately reflect the local test site and omit local flow effects from the evaluation, making the prediction of annual energy yield of limited value.

7.8 Summary

The wind field at the test site in Tübingen is simulated using four wind directions: 60° , 150° , 240° and 330° . The simulated wind flows from the four wind directions are deeply analysed by means of characteristic flow phenomena. It is discussed how building arrangements, terrain and vegetation zones interact and change the local wind flows. Since the AEP is one of the most important key parameters defining suitable locations for wind turbines, a procedure for calculating local AEP values and local wind statistics is presented.

The calculation is based on large scale synthetic wind statistics which have been already available. The simulations are used to achieve local frequencies of wind directions and wind speeds. Power curves of a real VAWT and HAWT are used in the calculation. An already existing approach for correcting the wind turbine power curve by the atmospheric turbulence intensity and the angle of attack of the wind turbines is implemented in the procedure to give a more realistic and precise prediction of the energy yield. By means of this procedure, local AEP values and local wind statistics are calculated for each numerical cell with and without the surrounding buildings and are associated to each building. A comparison between the local and large scale synthetic wind statistics showed that the local statistics can differ in the frequencies of wind directions and especially of wind speeds from the large-scale synthetic wind statistics due to local effects. Thus, it is mandatory to determine local wind statistics and use them for a detailed location decision of small wind turbines.

The comparison of the local AEP values showed that the AEP values may change significantly when surrounding buildings are considered in the simulations. It also turned out that higher energy yields can be achieved using the HAWT model than the VAWT model even though they have the same rated power. This is due to the better performance at lower wind speeds and a smaller cut-in wind speed of the HAWT.

The highest AEP values are reached on the buildings 19 and 12 with 10.9 MWh and 10.2 MWh respectively when using the HAWT model. However, using the VAWT model, the AEP values are decreased to 5.8 MWh and 6.7 MWh on the buildings 19 and 12. According to the presented AEP calculation method, 25 % of the total electricity consumption of the entire university Tübingen can be covered by the HAWT on the buildings 19 and 12.

8 Conclusion and Outlook

This work investigates the urban wind field at the university campus Morgenstelle in Tübingen (southern Germany) with the focus on energy yields of small horizontal and vertical wind turbines using CFD simulations with ANSYS Fluent. Highly resolved IDDES simulations are performed which include building geometries, complex terrain and the vegetation. The building geometries are based on real 3D city models. A method for using 3D city models for urban CFD simulations from geometry optimisation to meshing requirements is used in this study. An already existing vegetation model by Shaw and Schumann [115] is extended to consider local tree heights. A sensitivity analysis is performed to study influences of different meshing parameters, domain sizes, atmospheric and environmental parameters. The numerical setup with the extended vegetation model is compared with on-site LiDAR data in Tübingen. A method for calculating local wind statistics and local annual energy productions based on four simulated wind directions and large scale synthetic wind statistics is presented. Local wind statistics and AEP values are calculated for each building and locations for small wind turbines are discussed.

Different turbulence models, shielding functions and synthetic turbulence generation methods in the numerical setup have been simulated and validated using a surface mounted cube in a boundary flow imitating a small scale high-rise buildings. The numerical results have been compared with DNS simulations by Saeedi et al. [104]. The results have illustrated the importance to choose shielding functions and turbulence models properly. The shielding function affects the time-averaged velocity and the dimensions of the recirculation zone because the shielding function prevents that the LES falls back into the RANS modelled boundary layer where the grid is too coarse to sufficiently resolve the fluctuations for LES. This thickens the boundary layer at the lateral surfaces of the cube. The best agreement with the wind tunnel data and DNS simulations are obtained using the $k-\omega$ SST turbulence model with the IDDES shielding function. Regarding the synthetic turbulence generation method, the validation study also indicates the dependency of the number of vortices in the VM which are applied at the inflow plane. Due to the constant size of the inflow area, more vortices lead to smaller turbulent structures which dissipate faster in the flow and increase the size of the recirculation zone behind the cube. Hence, the further simulations are performed with the combination of the IDDES shielding function and the $k-\omega$ SST turbulence model. The VM performed as the best turbulence

generation method and is chosen for the numerical setups of the following simulations. In this work, the number of vortices has to be adapted to the atmospheric boundary layer for urban wind flow.

The vegetation model of Shaw and Schumann [115] is extended to include local tree heights. A strong influence of standard deviations of tree heights on the flow field is shown since local tree heights increase the roughness in the top region of forested zones. That increases the turbulent kinetic energy which may also affect the flow within built areas. Based on the vegetation model, a new method for modelling buildings in urban wind simulations is presented and validated in real scale simulations. In the building model, the buildings are represented by an indicator function and modelled by a volume resistance force which is added to the momentum equations.

A mesh convergence study is performed to investigate the sensitivity of meshing parameters such as the cell size of the atmosphere, the resolution of the terrain, of the building walls and of the building edges, and the sensitivity of the inflation layers are investigated. The flow field is evaluated by means of the $c_{p,b}$ coefficient adapted for buildings. Finer resolutions of the atmosphere and of solid surfaces and edges increase the c_p coefficient of the buildings. For example, the sum of the $c_{p,b}$ coefficient of all buildings increases from -0.24 with a cell width of 2,25 m to -0,215 with a cell width of 1.2 m.

A domain size analysis is conducted to investigate the effects of the domain width and height on the urban flow field. Simulations using domain widths of $10 H_{b,max}$ and $16 H_{b,max}$ are performed. But no noticeable effects are observed which would justify a lateral extension by more than $10 H_{b,max}$. Thus, at least a domain width of $10 H_{b,max}$ is taken for further simulations in this work. The study has shown that a domain height of $6 H_{b,max}$ falsifies the flow field compared to $12 H_{b,max}$ and $18 H_{b,max}$ due to blockage induced accelerations and decelerations of the flow.

The sensitivities of environmental parameters on the flow field have been investigated. The environmental parameters include tree heights and seasonal effects by varying the tree foliations of forested zones and atmospheric turbulence intensities which are used at the inflow plane of the simulation. The tree foliations depending on the season show just a small influence on the flow field, also on top of the highest buildings A and B. The atmospheric turbulence intensity influences rather the flow above forested zones instead of the flow above the buildings. The largest influence shows the variation of tree heights which affect the velocity and increases the turbulent kinetic energy.

To study the effect of surrounding buildings, additional buildings surrounding the zone of interest at the university campus in Tübingen are included by the above mentioned building model. The simulation of the wind field with the surrounding buildings showed a misinterpretation of 82.5 % in the predicted energy yield compared to a simulation without the surrounding buildings. For that reason, it is important to consider the effect of surrounding buildings for a precise and reliable prediction of the wind energy yield.

Measured on-site LiDAR data have been used to define the velocity profile of the inflow

boundary condition. The required steps to preprocess the LiDAR data and their assumptions are explained in detail. A linear median filter is applied and adapted for LiDAR wind data to detect and replace outliers and unphysical measurement data.

The simulation results are compared with on-site LiDAR data at various locations above forested zones. A very good qualitative and quantitative agreement is achieved for all locations.

Further simulations with the vegetation model and a forest modelled as a solid body with an uniform tree height are compared with a simulation without any forested zone. The simulation with the solid forest body shows a more unreal velocity profile and higher wind speeds directly above the forest and emphasize the significance of a proper vegetation model. The simulation also shows high wind speed zones and flow detachment zones on the rooftop of high-rise buildings which could be of interest for small wind turbines. But the flow detachment zones are accompanied with high velocity gradients and high turbulent kinetic energy values. When the wind turbines is mounted in these zones, the velocity gradients can lead to unbalanced loads, higher damages and shorter lifetimes of wind turbines.

For the evaluation of the wind field and the calculation of local AEP values, the wind field at the test site in Tübingen is simulated using four wind directions: 60° , 150° , 240° and 330° . The simulated wind flows from the four wind directions are deeply analysed by means of characteristic flow phenomena, also regarding good position for small wind turbines. It is discussed how building arrangements, terrain and forested zones affect the local wind flow. Since the AEP is one of the most important key parameters defining suitable locations for wind turbines, a procedure for calculating local wind statistics and local AEP values is presented in this study. The calculation is based on large scale synthetic wind statistics which have been already available. The simulations of the four wind directions are added to achieve local probabilities of wind directions and wind speeds. Power curves of a real VAWT and a HAWT are used to determine the AEP. An already existing approach for correcting the AEP by the atmospheric turbulence intensity and the angle of attack of the wind turbines is implemented in the procedure to achieve a more realistic and precise prediction of the energy yield. By means of this procedure, local AEP values and local wind statistics are calculated for each numerical cell with and without the surrounding buildings and are associated to each building.

A comparison between the local and large scale synthetic wind statistics shows that both statistics can differ in the probabilities of wind directions and especially of wind speeds from the large-scale synthetic wind statistics due to local effects such as surrounding buildings, complex terrain and vegetation. Thus, it is highly recommended to use local wind statistics for a detailed location decision of small wind turbines. The comparison of the local AEP values showed that the AEP values may change significantly when surrounding

buildings are considered in the simulations. It also turned out that higher energy yields can be achieved using the HAWT model than using the VAWT model even though both have the same rated power. This is due to the better performance in the lower wind speed range and a smaller cut-in wind speed of the HAWT. The highest AEP values are reached on the buildings 19 and 12 with 10.9 MWh and 10.2 MWh, respectively when using the HAWT model. However, using the VAWT model, the AEP values are decreased to 5.8 MWh and 6.7 MWh on the buildings 19 and 12. According to the presented AEP calculation method, maximum 25 % of the total electricity consumption of the entire university Tübingen can be covered by the HAWT on the buildings 19 and 12. The real AEP may be lower since not all velocity fluctuations which are considered in the AEP calculation are captured by the wind turbine.

Future work may continue with an improved wind energy prediction model in built areas. The improved model could enable a classification of buildings and of building arrangements which are based on geometrical parameters. A geometrical parameter could be an angle defined by the distance and the height of surrounding buildings or a spreading angle describing the shadowing of a building. The geometrical parameter may also be the height, the aspect ratio or the dominance of a building. The model may include the probabilities of wind directions to weight the parameters. Such a model has the advantage to estimate the energy yield for a wide range of built areas without cost intensive simulations, just based on the arrangement and the building geometries. Based on this prior estimation, simulations can be performed to confirm or to specify the energy yield of the estimated wind turbine locations.

A new approach in urban wind field simulations is to estimate the energy yield of buildings in a new city quarter which are still in the planning phase [30]. The shape of planned buildings can be adapted to optimize the energy output of small wind turbines.

Furthermore, the simulation of thermal effects should be considered in the future work. For that, thermal models for heat storage in buildings, for shadowing and evaporation of vegetations and sun radiation have to be developed and included in the simulation. Especially in summer days, thermal effects may change the wind flow and an unstable atmospheric boundary layer with strong thermal turbulence is generated. That allows the additional simulation of unstable and stable atmospheric boundary layers. That can be relevant for small wind turbines which are basically installed closer to buildings.

For a better energy yield prediction, aerodynamic effects caused by the turbulent kinetic energy which affects the power performance of wind turbines should be considered in the simulations or in the method for calculating local AEP values. Based on the calculated local AEP values, small wind turbines should be installed on the buildings to validate the method for calculating local AEP values.

Bibliography

- [1] ANSYS Fluent. <https://www.ansys.com/de-de/products/fluids/ansys-fluent>. [Online; accessed: 2022-11-17].
- [2] European Wind Turbine Standards II. <https://cordis.europa.eu/project/id/JOR3950064/reporting>. [Online; accessed: 2022-09-16].
- [3] Landesanstalt für Umwelt Baden-Württemberg. <https://udo.lubw.baden-wuerttemberg.de/public/?highlightglobalid=synAKS>. [Online; accessed 2021-09-27].
- [4] Potentialstudie Kleinwindkraftanlagen auf Münchner Gebäuden. <https://stadt.muenchen.de/infos/regenerative-energiequellen-muenchen.html>. [Online; accessed: 2022-11-17].
- [5] Skystream 3.7 horizontal axis wind turbine. <https://www.directindustry.de/prod/southwest-windpower/product-20674-680643.html>. [Online; accessed: 2022-04-24].
- [6] Turby B.V. vertical axis wind turbine. <https://studylib.net/doc/8785752/catalogue-of-european-urban-wind-turbine-manufacturers>. [Online; accessed: 2022-04-24].
- [7] Windy Cities Programm. <http://windycities.de>. [Online; accessed: 2021-10-07].
- [8] World population prospects, UN department of economics and social affairs. <https://population.un.org/wpp/Graphs/Probabilistic/POP/TOT/900>. [Online; accessed: 2021-10-10].
- [9] I. Abohela, N. Hamza, and S. Dudek. Effect of roof shape, wind direction, building height and urban configuration on the energy yield and positioning of roof mounted wind turbines. *Renewable Energy*, 50:1106–1118, 2013.
- [10] ANSYS Fluent Theory Guide 18.1. 2017. [Online; accessed 2021-08-13].
- [11] ANSYS Fluent Theory Guide 2019R3. 2019. [Online; accessed 2021-08-13].
- [12] ANSYS Fluent User’s Guide 18.1. 2017. [Online; accessed 2021-08-13].
- [13] ANSYS Fluent User’s Guide 2019R3. 2019. [Online; accessed 2021-08-13].

- [14] ANSYS Meshing User’s Guide 2019R3. 2019. [Online; accessed 2022-01-29].
- [15] T. A. Adedipe, A. Chaudhari, and T. Kauranne. Impact of different forest densities on atmospheric boundary-layer development and wind-turbine wake. *Wind Energy*, 23(5):1165–1180, 2020.
- [16] C. Alanis Ruiz, I. Kalkman, and B. Blocken. Aerodynamic design optimization of ducted openings through high-rise buildings for wind energy harvesting. *Building and Environment*, 202:108028, 2021.
- [17] A. Albers. Turbulence and shear normalisation of wind turbine power curve. *European Wind Energy Conference and Exhibition 2010, EWEC 2010*, 6:4116–4123, 01 2010.
- [18] J. Allegrini, V. Dorer, and J. Carmeliet. Influence of morphologies on the microclimate in urban neighbourhoods. *Journal of Wind Engineering and Industrial Aerodynamics*, 144:108–117, 2015. Selected papers from the 6th International Symposium on Computational Wind Engineering CWE 2014.
- [19] U. Atila, I. R. Karas, M. K. Turan, and A. A. Rahman. *Automatic Generation of 3D Networks in CityGML and Design of an Intelligent Individual Evacuation Model for Building Fires Within the Scope of 3D GIS*, pages 123–142. Springer International Publishing, Cham, 2014.
- [20] F. Baetke, H. Werner, and H. Wengle. Numerical simulation of turbulent flow over surface-mounted obstacles with sharp edges and corners. *Journal of Wind Engineering and Industrial Aerodynamics*, 35:129–147, 1990.
- [21] F. Balduzzi, A. Bianchini, and L. Ferrari. Microeolic turbines in the built environment: Influence of the installation site on the potential energy yield. *Renewable Energy*, 45:163–174, 2012.
- [22] J. G. Bartzis, D. Vlachogiannis, and T. Sfetsos. Thematic area 5: Best practice advice for environmental flows. *The QNET-CFD Network Newsletter*, 2:34–39, 2004.
- [23] R. Bequet, M. Campioli, V. Kint, D. Vansteenkiste, Bart. Muys, and R. Ceulemans. Leaf area index development in temperate oak and beech forests is driven by stand characteristics and weather conditions. *Trees*, 25:935–946, 2011.
- [24] B. Blocken. 50 years of computational wind engineering: Past, present and future. *Journal of Wind Engineering and Industrial Aerodynamics*, 129:69–102, 2014.
- [25] B. Blocken. LES over RANS in building simulation for outdoor and indoor applications: A foregone conclusion? *Building Simulation*, 11:1–50, 2018.

- [26] B. Blocken, W.D. Janssen, and T. van Hooff. CFD simulation for pedestrian wind comfort and wind safety in urban areas: General decision framework and case study for the Eindhoven University campus. *Environmental Modelling and Software*, 30:15–34, 2012.
- [27] B. Blocken, S. Roels, and J. Carmeliet. Modification of pedestrian wind comfort in the silvertop tower passages by an automatic control system. *Journal of Wind Engineering and Industrial Aerodynamics*, 92:849–873, 2004.
- [28] M. Boudreau, G. Dumas, and J.-C. Veilleux. Assessing the ability of the DDES turbulence modeling approach to simulate the wake of a bluff body. *Aerospace*, 4(3), 2017.
- [29] J. Bourgeois, P. Sattari, and R. Martinuzzi. Alternating half-loop shedding in the turbulent wake of a finite surface-mounted square cylinder with a thin boundary layer. *Physics of Fluids*, 23, 2011.
- [30] M. Brennenstuhl, M. von der Gruen, S. Harbola, A. Koukofikis, R. Padsala, M. Schaaf, V. Coors, and U. Voss. CFD simulation and visualization based investigation of small wind turbine potential: A case study “Neuer Stöckach” for Stuttgart. *ISPRS Annals of the Photogrammetry, Remote Sensing and Spatial Information Sciences*, VIII-4/W1-2021:17–24, 2021.
- [31] T. Burton, N. Jenkins, D. Sharpe, and E. Bossanyi. *Aerodynamics of Horizontal Axis Wind Turbines*, chapter 3, pages 39–136. John Wiley and Sons, Ltd, 2011.
- [32] R. Dadioti. *Numerical Wind Resource Assessment in Urban Environments*. PhD thesis, De Montfort University Leicester, 2017.
- [33] R. Dadioti and S. Rees. Performance of detached eddy simulation applied to analysis of a university campus wind environment. *Energy Procedia*, 134:366–375, 2017.
- [34] A. G. Davenport and National Research Council Canada. Division of Building Research. *Wind Loads on Structures*. Technical paper - National Research Council of Canada, no. 088. National Research Council, 1960.
- [35] M. E. Deininger, M. von der Grün, R. Pieperit, S. Schneider, T. Santhanavanich, V. Coors, and U. Voß. A continuous, semi-automated workflow: From 3D city models with geometric optimization and CFD simulations to visualization of wind in an urban environment. *ISPRS International Journal of Geo-Information*, 9(11), 2020.
- [36] A. El Bahlouli and J. Bange. Experimental and numerical wind-resource assessment of an university campus site. In Lorenzo Battisti and Mosè Ricci, editors,

Wind Energy Exploitation in Urban Environment, pages 1–15, Cham, 2018. Springer International Publishing.

- [37] M. Elkhoury. Assessment of turbulence models for the simulation of turbulent flows past bluff bodies. *Journal of Wind Engineering and Industrial Aerodynamics*, 154:10–20, 2016.
- [38] N. N. Fedorova and S. A. Valger. Study of gas emission transfer processes in the city canyon based on numerical simulation data. *AIP Conference Proceedings*, 2351:030060, 2021.
- [39] C. Ferreira, G. van Bussel, and G. Kuik. An analytical method to predict the variation in performance of an H-Darrieus in skewed flow and its experimental validation. *Proceedings of the European Wind Energy Conference*, 2006.
- [40] J. H. Ferziger and M. Peric. *Numerische Strömungsmechanik*. Springer Berlin Heidelberg, 2008.
- [41] J. Franke, A. Hellsten, H. Schlünzen, and B. Carissimo. Best practice guideline for the CFD simulation of flows in the urban environment. *COST action*, 732:51, 2007.
- [42] K. Friedrich, J. K. Lundquist, M. Aitken, E. A. Kalina, and R. F. Marshall. Stability and turbulence in the atmospheric boundary layer: A comparison of remote sensing and tower observations. *Geophysical Research Letters*, 39(3), 2012.
- [43] A. Gagliano, F. Nocera, F. Patania, and A. Capizzi. Assessment of micro-wind turbines performance in the urban environments: An aided methodology through geographical information systems. *International Journal of Energy and Environmental Engineering*, 4:1–14, 2013.
- [44] M. Goude, U. Nilsson, and E. Holmström. Comparing direct and indirect leaf area measurements for scots pine and Norway spruce plantations in Sweden. *European Journal of Forest Research*, 138, 2019.
- [45] L. Grabowski, M. Sobek, and A. Baier. CFD analysis of a hybrid, Darrieus-Savonius, horizontal wind turbine, using static and moving mesh. *IOP Conference Series: Materials Science and Engineering*, 591(1):012049, 2019.
- [46] A. Grachev, E. Andreas, C. Fairall, P. Guest, and O. Persson. The critical Richardson number and limits of applicability of local similarity theory in the stable boundary layer. *Boundary-Layer Meteorology*, 147, 2012.
- [47] M. Gritskevich, A. Garbaruk, J. Schütze, and F. Menter. Development of DDES and IDDES formulations for the $k-\omega$ shear stress transport model. *Flow, Turbulence and Combustion*, 88, 2012.

- [48] C. Gromke, B. Blocken, W. Janssen, B. Merema, T. Hooff, and H. Timmermans. CFD analysis of transpirational cooling by vegetation: Case study for specific meteorological conditions during a heat wave in Arnhem, Netherlands. *Building and Environment*, 83, 2014.
- [49] U. Gruber. Official 3D spatial base data in Germany. *PFG*, 88:25–31, 2020.
- [50] M. von der Grün, P. Zamre, Y. Chen, T. Lutz, U. Voß, and E. Krämer. Numerical study and LiDAR based validation of the wind field in urban sites. *Journal of Physics: Conference Series*, 1618:042009, 2020.
- [51] S. Hajimirzaie, C. Wojcik, and J. Buchholz. The role of shape and relative submergence on the structure of wakes of low-aspect-ratio wall-mounted bodies. *Experiments in Fluids*, 53, 2012.
- [52] J. Hang, Y. Li, and M. Sandberg. Experimental and numerical studies of flows through and within high-rise building arrays and their link to ventilation strategy. *Journal of Wind Engineering and Industrial Aerodynamics*, 99(10):1036–1055, 2011.
- [53] S. R. Hanna, O. R. Hansen, M. Ichard, and D. Strimaitis. CFD model simulation of dispersion from chlorine railcar releases in industrial and urban areas. *Atmospheric Environment*, 43(2):262–270, 2009.
- [54] S. R. Hanna, S. Tehranian, B. Carissimo, R. W. Macdonald, and R. Lohner. Comparisons of model simulations with observations of mean flow and turbulence within simple obstacle arrays. *Atmospheric Environment*, 36(32):5067–5079, 2002.
- [55] B. Hong, H. Qin, and B. Lin. Prediction of wind environment and indoor/outdoor relationships for PM_{2.5} in different building–tree grouping patterns. *Atmosphere*, 9(2), 2018.
- [56] T. Hooff and B. Blocken. Coupled urban wind flow and indoor natural ventilation modelling on a high-resolution grid: A case study for the Amsterdam ArenA stadium. *Environmental Modelling and Software*, 25:51–65, 2010.
- [57] W. Huang and Z. Xibin. Wind field simulation over complex terrain under different inflow wind directions. *Wind and Structures An International Journal*, 28:239–253, 2019.
- [58] W.-H. Hucho. *Aerodynamik der stumpfen Körper - Physikalische Grundlagen und Anwendungen in der Praxis*. Vieweg und Teubner Verlag Wiesbaden, 2012.
- [59] B. Jähne. *Digitale Bildverarbeitung*. Springer Vieweg, Berlin, 7 edition, 2012.

- [60] Y.-H. Jang, S. I. Park, T. H. Kwon, and S.-H. Lee. CityGML urban model generation using national public datasets for flood damage simulations: A case study in Korea. *Journal of Environmental Management*, 297:113236, 2021.
- [61] A. P. R. Jeanjean, G. Hinchliffe, W. A. McMullan, P. S. Monks, and R. J. Leigh. A CFD study on the effectiveness of trees to disperse road traffic emissions at a city scale. *Atmospheric Environment*, 120:1–14, 2015.
- [62] A. P. R. Jeanjean, P. S. Monks, and R. J. Leigh. Modelling the effectiveness of urban trees and grass on PM_{2.5} reduction via dispersion and deposition at a city scale. *Atmospheric Environment*, 147:1–10, 2016.
- [63] J. Jeong and F. Hussain. On the identification of a vortex. *Journal of Fluid Mechanics*, 285:69–94, 1995.
- [64] Y.-H. Juan, C.-Y. Wen, W.-Y. Chen, and A.-S. Yang. Numerical assessments of wind power potential and installation arrangements in realistic highly urbanized areas. *Renewable and Sustainable Energy Reviews*, 135:110165, 2021.
- [65] A. G. Kalmikov, G. Dupont, K. Dykes, and C. P. Chan. Wind power resource assessment in complex urban environments: MIT campus case-study using CFD analysis. *American Wind Energy Association Wind Power Conference and Exhibition WINDPOWER2010*, 2010.
- [66] Y. Kim, P. Weihing, C. Schulz, and Th. Lutz. Do turbulence models deteriorate solutions using a non-oscillatory scheme? *Journal of Wind Engineering and Industrial Aerodynamics*, 156:41–49, 2016.
- [67] N. Kirchner-Bossi and F. Porté-Agel. Multi-rotor wind farm layout optimization. *Journal of Physics: Conference Series*, 1618(3):032014, 2020.
- [68] S. Krajnović, G. Minelli, and B. Basara. Partially-averaged Navier–Stokes simulations of two bluff body flows. *Applied Mathematics and Computation*, 272, 2015.
- [69] L. Ledo, P. Kosasih, and P. Cooper. Roof mounting site analysis for micro-wind turbines. *Renewable Energy*, 36:1379–1391, 2011.
- [70] D. Lee, P. Pietrzyk, S. Donkers, V. Liem, J. van Oostveen, S. Montazeri, R. Boeters, J. Colin, P. Kastendeuch, F. Nerry, M. Menenti, B. Gorte, and E. Verbree. Modeling and observation of heat losses from buildings the impact of geometric detail on 3D heat flux modeling. *Conference European Association of Remote Sensing Laboratories*, 2013.
- [71] H. Lehner and L. Dorffner. Digital geotwin Vienna: Towards a digital twin city as geodata hub. *PFG*, 88:63–75, 2020.

- [72] A. Leonard. Energy cascade in large-eddy simulations of turbulent fluid flows. In F. N. Frenkiel and R. E. Munn, editors, *Turbulent Diffusion in Environmental Pollution*, volume 18 of *Advances in Geophysics*, pages 237–248. Elsevier, 1975.
- [73] P. Letzgus, Th. Lutz, and E. Krämer. Detached eddy simulations of the local atmospheric flow field within a forested wind energy test site located in complex terrain. *J. Phys. Conf. Ser.*, 1037:072043, 2018.
- [74] C. Li, S. Zhou, Y. Xiao, Q. Huang, L. Li, and P. W. Chan. Effects of inflow conditions on mountainous/urban wind environment simulation. *Building Simulation*, 10:573–588, 2017.
- [75] J. Liu and J. Niu. CFD simulation of the wind environment around an isolated high-rise building: An evaluation of SRANS, LES and DES models. *Building and Environment*, 96:91–106, 2016.
- [76] S. Liu, W. Pan, X. Zhao, H. Zhang, X. Cheng, Z. Long, and Q. Chen. Influence of surrounding buildings on wind flow around a building predicted by CFD simulations. *Building and Environment*, 140:1–10, 2018.
- [77] L. Lu, T. Becker, and M.-O. Löwner. *3D Complete Traffic Noise Analysis Based on CityGML*, pages 265 – 283. Springer International Publishing: Berlin/Heidelberg Germany, 2017.
- [78] L. Lu and K. Ip. Investigation on the feasibility and enhancement methods of wind power utilization in high-rise buildings of Hong Kong. *Renewable and Sustainable Energy Reviews*, 13:450–461, 2009.
- [79] H. Malberg. *Meteorologie und Klimatologie: Eine Einführung*. Springer Berlin Heidelberg, Berlin, Heidelberg, 2007.
- [80] F. Mathey, D. Cokljat, J. P. Bertoglio, and E. Sergent. Specification of LES inlet boundary condition using vortex method. *4th International Symposium on Turbulence, Heat and Mass Transfer, Antalya, Turkey*, 2003.
- [81] F. Mathey, D. Cokljat, J. P. Bertoglio, and E. Sergent. Assessment of the vortex method for Large Eddy Simulation inlet conditions. *Progress in Computational Fluid Dynamics, an International Journal*, 6(1-3):58–67, 2006.
- [82] F. Menter. CFD best practice guidelines for CFD code validation for reactor-safety applications. *European Commission, 5th EURATOM Framework Programme, Report, EVOL- ECORA-D1*, 2002.
- [83] F. Menter, M. Kuntz, and R. B. Langtry. Ten years of industrial experience with the sst turbulence model. *Heat and Mass Transfer*, 4, 2003.

- [84] F. R. Menter. Two-equation eddy-viscosity turbulence models for engineering applications. *AIAA Journal*, 32(8):1598–1605, 1994.
- [85] A. Mochida, Y. Tabata, T. Iwata, and H. Yoshino. Examining tree canopy models for CFD prediction of wind environment at pedestrian level. *Journal of Wind Engineering and Industrial Aerodynamics*, 96:1667–1677, 2008.
- [86] A. Mochida, Y. Tominaga, S. Murakami, R. Yoshie, T. Ishihara, and R. Ooka. Comparison of various k- ϵ models and DSM applied to flow around a high-rise building - report on AIJ cooperative project for CFD prediction of wind environment. *Wind and Structures An International Journal*, 5:227–244, 2002.
- [87] M. A. Mohamed and D. Wood. Computational study of the effect of trees on wind flow over a building. *Renewables: Wind, Water, and Solar*, 2, 2015.
- [88] D. Monien, A. Strzalka, A. Koukofikis, V. Coors, and U. Eicker. Comparison of building modelling assumptions and methods for urban scale heat demand forecasting. *Future Cities and Environment*, 3:2:2363–9075, 2017.
- [89] H. Montazeri and B Blocken. CFD simulation of wind-induced pressure coefficients on buildings with and without balconies: Validation and sensitivity analysis. *Building and Environment*, 60:137–149, 2013.
- [90] M. Moradpour, H. Afshin, and B. Farhanieh. A numerical investigation of reactive air pollutant dispersion in urban street canyons with tree planting. *Atmospheric Pollution Research*, 2016.
- [91] H.-J. Niemann. *WtG-Merkblatt, Nr. WtG 001/1996, über - Windkanalversuche in der Gebäudeaerodynamik*, 1996.
- [92] J. Paik, F. Sotiropoulos, and F. Porté-Agel. Detached eddy simulation of flow around two wall-mounted cubes in tandem. *International Journal of Heat and Fluid Flow*, 30:286–305, 2009.
- [93] R. Pieperit, A. Beuster, M. von der Grün, U. Voß, M. Pries, and U. Wagner. Towards wind-simulation of virtual 3D city models in a collaborative VR environment. *Int. Arch. Photogramm. Remote Sens. Spatial Inf. Sci.*, XLII-4/W15:61–66, 2019.
- [94] R. Pieperit, M. Deininger, M. Kada, M. Pries, and U. Voß. A sweep-plane algorithm for the simplification of 3D building models in the application scenario of wind simulations. *Int. Arch. Photogramm. Remote Sens. Spatial Inf. Sci.*, XLII-4/W10:151–156, 2018.
- [95] M. Pontiggia, G. Landucci, V. Busini, M. Derudi, M. Alba, M. Scaioni, S. Bonvicini, V. Cozzani, and R. Rota. CFD model simulation of LPG dispersion in urban areas. *Atmospheric Environment*, 45:3913–3923, 2011.

- [96] S. B. Pope, P. J. Eccles, S. B. Pope, and Cambridge University Press. *Turbulent Flows*. Cambridge University Press, 2000.
- [97] Y. Qu, M. Milliez, L. Musson-Genon, and B. Carissimo. Numerical study of the thermal effects of buildings on low-speed airflow taking into account 3D atmospheric radiation in urban canopy. *Journal of Wind Engineering and Industrial Aerodynamics*, 104-106:474–483, 2012. 13th International Conference on Wind Engineering.
- [98] E. Robertson, V. Choudhury, S. Bhushan, and D. K. Walters. Validation of open-foam numerical methods and turbulence models for incompressible bluff body flows. *Computers and Fluids*, 123:122–145, 2015.
- [99] J. Rogelj, M. Meinshausen, M. Schaeffer, R. Knutti, and K. Riahi. Impact of short-lived non-CO₂ mitigation on carbon budgets for stabilizing global warming. *Environmental Research Letters*, 10(7):075001, 2015.
- [100] L. Romero Rodriguez, E. Duminil, J. Sanchez Ramosa, and U. Eicker. Assessment of the photovoltaic potential at urban level based on 3D city models: A case study and new methodological approach. *Sol. Energy*, 146:264–275, 2017.
- [101] B. Roscher, R. Schelenz, A. Werkmeister, Y. Shkara, L. Stössel, and G. Jacobs. Comparison of wind turbine loads inside a wake between engineering model and CFD calculation. *Journal of Physics: Conference Series*, 1037:072039, 2018.
- [102] C. Roy, L. DeChant, J. Payne, and F. Blottner. Bluff-body flow simulations using hybrid RANS/LES. *33rd AIAA Fluid Dynamics Conference and Exhibit*, 2003.
- [103] T. Ruohomäki, E. Airaksinen, P. Huuska, O. Kesäniemi, M. Martikka, and J. Suomisto. Smart city platform enabling digital twin. In *2018 International Conference on Intelligent Systems (IS), Funchal-Medeira, Portugal, 25-27 September 2018*, pages 155–161, 2018.
- [104] M. Saeedi, P. Lepoudre, and B.-C. Wang. Direct numerical simulation of turbulent wake behind a surface-mounted square cylinder. *Journal of Fluids and Structures*, 51, 2014.
- [105] Y. S. Saeedrashed and A. C. Benim. Validation methods of geometric 3D-CityGML data for urban wind simulations. *E3S Web Conf.*, 128:10006, 2019.
- [106] M. H. Salim, K. H. Schlünzen, and D. Grawe. Including trees in the numerical simulations of the wind flow in urban areas: Should we care? *Journal of Wind Engineering and Industrial Aerodynamics*, 144:84–95, 2015. Selected papers from the 6th International Symposium on Computational Wind Engineering CWE 2014.

- [107] J. Santiago, A. Martilli, and F. Martin. CFD simulation of airflow over a regular array of cubes. Part I: Three-dimensional simulation of the flow and validation with wind-tunnel measurements. *Boundary-Layer Meteorology*, 122:609–634, 2007.
- [108] J. L. Santiago, R. Borge, F. Martin, D. de la Paz, A. Martilli, J. Lumbreras, and B. Sanchez. Evaluation of a CFD-based approach to estimate pollutant distribution within a real urban canopy by means of passive samplers. *Science of The Total Environment*, 576:46–58, 2017.
- [109] P. Sattari, J. Bourgeois, and R. Martinuzzi. On the vortex dynamics in the wake of a finite surface-mounted square cylinder. *Experiments in Fluids*, 52, 2011.
- [110] A. Scaperdas and S. Gilham. Thematic area 4: Best practice advice for civil construction and HVAC. *The QNET-CFD Network Newsletter*, 2(4):28–33, 2004.
- [111] M. Schäfer. *Computational Engineering - Introduction to Numerical Methods*. Springer Berlin Heidelberg, 2006.
- [112] M. Schatzmann and B. Leitl. Issues with validation of urban flow and dispersion CFD models. *Journal of Wind Engineering and Industrial Aerodynamics*, 99:169–186, 2011.
- [113] G. Schrotter and C. Hürzeler. The digital twin of the city of Zürich for urban planning. *PFG*, 88:99–112, 2020.
- [114] C. Schulz, L. Klein, P. Weihing, Th. Lutz, and E. Krämer. CFD studies on wind turbines in complex terrain under atmospheric inflow conditions. *Journal of Physics: Conference Series*, 524:012134, 2014.
- [115] R. Shaw and U. Schumann. Large-eddy simulation of turbulent flow above and within a forest. *Boundary-Layer Meteorology*, 61:47–64, 1992.
- [116] R. F. Shi, G. Cui, Z. S. Wang, C. X. Xu, and Z. Zhang. Large eddy simulation of wind field and plume dispersion in building array. *Atmospheric Environment*, 42:1083–1097, 2008.
- [117] T.-S. Shih, W. W. Liou, A. Shabbir, Z. Yang, and J. Zhu. A new k- ϵ eddy viscosity model for high reynolds number turbulent flows. *Computers and Fluids*, 24(3):227–238, 1995.
- [118] M. Shur, P. Spalart, M. Strelets, and A. Travin. A hybrid RANS-LES approach with delayed-DES and wall-modelled LES capabilities. *International Journal of Heat and Fluid Flow*, 29:1638–1649, 2008.

- [119] C. R. Sonawane, R. Sawant, K. Patel, R. Sonawala, A. Pawar, P. Agrawal, and V. Mathur. Numerical investigation of vertical axis c-shaped Savonius wind turbine. *Journal of Physics: Conference Series*, 1706:012215, 2020.
- [120] P. Spalart and S. Allmaras. A one-equation turbulence model for aerodynamic flows. *AIAA*, 439, 1992.
- [121] P. Spalart, S. Deck, M. Shur, K. Squires, M. Strelets, and A. Travin. A new version of detached eddy simulation, resistant to ambiguous grid densities. *Theoretical and Computational Fluid Dynamics*, 20:181–195, 2006.
- [122] P. Spalart, W.-H. Jou, M. Strelets, and S. Allmaras. Comments on the feasibility of LES for wings, and on a hybrid RANS/LES approach. *Advances in DNS/LES: Direct numerical simulation and large eddy simulation*, pages 137–148, 1997.
- [123] J. Spurk and N. Aksel. *Strömungslehre: Einführung in die Theorie der Strömungen*. Springer Berlin Heidelberg, 2019.
- [124] W. Steffen, J. Rockström, K. Richardson, T. M. Lenton, C. Folke, D. Liverman, C. P. Summerhayes, A. D. Barnosky, S. E. Cornell, M. Crucifix, J. F. Donges, I. Fetzer, S. J. Lade, M. Scheffer, R. Winkelmann, and H. J. Schellnhuber. Trajectories of the earth system in the anthropocene. *Proceedings of the National Academy of Sciences*, 115(33):8252–8259, 2018.
- [125] T. Stoesser, F. Mathey, J. Fröhlich, and W Rodi. LES of flow over multiple cubes. *ERCOFTAC Bulletin 32*, pages 15–19, 2003.
- [126] K. Sunderland, T. Woolmington, J. Blackledge, and M. Conlon. Small wind turbines in turbulent (urban) environments: A consideration of normal and Weibull distributions for power prediction. *Journal of Wind Engineering and Industrial Aerodynamics*, 121:70–81, 2013.
- [127] D. D. Tjahjana, A. T. Halomoan, A. Wibowo, D. A. Himawanto, and Y. A. Wicaksono. Wind potential assessment in urban area of Surakarta city. *AIP Conference Proceedings*, 1931(1):030070, 2018.
- [128] F. Toja-Silva, T. Kono, C. Peralta, O. Lopez-Garcia, and J. Chen. A review of computational fluid dynamics (CFD) simulations of the wind flow around buildings for urban wind energy exploitation. *Journal of Wind Engineering and Industrial Aerodynamics*, 180:66–87, 2018.
- [129] F. Toja-Silva, C. Peralta, O. Lopez-Garcia, J. Navarro, and I. Cruz. On roof geometry for urban wind energy exploitation in high-rise buildings. *Computation*, 3(2):299–325, 2015.

- [130] Y. Tominaga, A. Mochida, R. Yoshie, H. Kataoka, T. Nozu, M. Yoshikawa, and T. Shirasawa. AIJ guidelines for practical applications of CFD to pedestrian wind environment around buildings. *Journal of Wind Engineering and Industrial Aerodynamics*, 96:1749–1761, 2008.
- [131] Y. Tominaga, Y. Sato, and S. Sadohara. CFD simulations of the effect of evaporative cooling from water bodies in a micro-scale urban environment: Validation and application studies. *Sustainable Cities and Society*, 19, 2015.
- [132] Z. Tong, Y. Chen, and A. Malkawi. Defining the influence region in neighborhood-scale CFD simulations for natural ventilation design. *Applied Energy*, 182:625–633, 2016.
- [133] Y. Toparlar, B. Blocken, P. Vos, G. J. F. Heijst, W. D. Janssen, T. Hooff, H. Montazeri, and H. J. P. Timmermans. CFD simulation and validation of urban microclimate: A case study for Bergpolder Zuid, Rotterdam. *Building and Environment*, 83, 2014.
- [134] S. Trometer and M. Mensinger. *Simulation von Detonationsszenarien im urbanen Umfeld.*, pages 150 – 164. Wichmann, Berlin, 2014.
- [135] T. Uchida and K. Sugitani. Numerical and experimental study of topographic speed-up effects in complex terrain. *Energies*, 13:3896, 2020.
- [136] S. Valger and N. N. Fedorova. CFD methods in architecture and city planning. *Journal of Physics: Conference Series*, 1425:012124, 2019.
- [137] S. Valger, N.N. Fedorova, and A. Fedorov. Structure of turbulent separated flow in the neighborhood of a plate-mounted prism of square section. *Thermophysics and Aeromechanics*, 22:29–41, 2015.
- [138] D. Wagner, N. Alam, M. Wewetzer, M. Pries, and V. Coors. Methods for geometric data validation of 3D city models. *Int. Arch. Photogramm. Remote Sens. Spatial Inf. Sci.*, XL-1-W5:729–735, 2015.
- [139] B. Wang, L. Cot, L. Adolphe, S. Geoffroy, and J. Morchain. The impact of urban form on wind energy potential. *International Seminar on Urban Form: Our common future in Urban Morphology*, 2014.
- [140] B. Wang, L. D. Cot, L. Adolphe, S. Geoffroy, and S. Sun. Cross indicator analysis between wind energy potential and urban morphology. *Renewable Energy*, 113:989–1006, 2017.
- [141] B. Wang, S. Sun, and M. Duan. Wind potential evaluation with urban morphology - a case study in Beijing. *Energy Procedia*, 153:62–67, 2018.

- [142] Qiang Wang, Jianwen Wang, Yali Hou, Renyu Yuan, Kun Luo, and Jianren Fan. Micrositing of roof mounting wind turbine in urban environment: Cfd simulations and lidar measurements. *Renewable Energy*, 115:1118–1133, 2018.
- [143] D. C. Wilcox. *Turbulence modelling for CFD*. DCW Industries, La Cañada, 1993.
- [144] A. Yakhot, H. Liu, and N. Nikitin. Turbulent flow around a wall-mounted cube: A direct numerical simulation. *International Journal of Heat and Fluid Flow*, 27:994–1009, 2006.
- [145] A.-S. Yang, Y.-M. Su, C.-Y. Wen, Y.-H. Juan, W.-S. Wang, and C.-H. Cheng. Estimation of wind power generation in dense urban area. *Applied Energy*, 171:213–230, 2016.
- [146] R. Yoshie, A. Mochida, Y. Tominaga, H. Kataoka, K. Harimoto, T. Nozu, and T. Shirasawa. Cooperative project for CFD prediction of pedestrian wind environment in the Architectural Institute of Japan. *Journal of Wind Engineering and Industrial Aerodynamics*, 95:1551–1578, 2007.
- [147] S. Zheng, Y. Wang, Z. Zhai, Y. Xue, and L. Duanmu. Characteristics of wind flow around a target building with different surrounding building layers predicted by CFD simulation. *Building and Environment*, 201:107962, 2021.

A Appendix

A.1 Data sheet of horizontal axis wind turbine [5]



Made in the USA

Technical Specifications

Model	Skystream 3.7
Rated Capacity	2.4 kW
Weight	170 lb (77 kg)
Rotor Diameter	12 ft (3.72 m)
Swept Area	115.7 ft ² (10.87 m ²)
Type	Downwind rotor with stall regulation control
Direction of Rotation	Clockwise looking upwind
Blades	3-Fiberglass reinforced composite
Rated Speed	50 - 325 rpm
Maximum Tip Speed	216.5 ft/s (66 m/s)
Alternator	Slotless permanent magnet brushless
Yaw Control	Passive
Grid Feeding	Southwest Windpower inverter 120-240 VAC 50-60 Hz
Battery Charging	Battery sensor available for battery charging systems
Braking System	Electronic stall regulation with redundant relay switch control
Cut-in Wind Speed	8 mph (3.5 m/s)
Rated Wind Speed	29 mph (13 m/s)
User Control	Wireless 2 way interface remote system
Survival Wind Speed	140 mph (63 m/s)
Warranty	5 year limited warranty

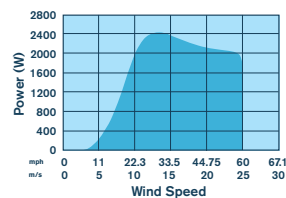
SKYSTREAM 3.7®

2.4 KW RESIDENTIAL POWER APPLIANCE

Skystream 3.7 is a breakthrough in a new generation of RPAs (Residential Power Appliances) that is changing the energy landscape of how homes and small businesses receive electricity. Skystream is the first fully integrated system that produces energy for less than the average cost of electricity in the United States and it produces usable energy in exceptionally low winds.¹

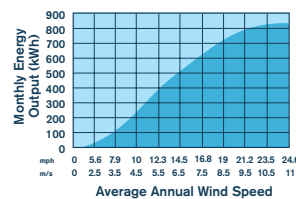
Skystream is available on towers ranging from 33 feet (10.2 m) to 110 feet (33.5 m)² tall. Its universal inverter delivers power compatible with any utility grid from 110-240 VAC. Skystream efficiently and quietly provides 40-90% of the energy needs for a home or small business. Any extra energy is fed into the grid spinning the meter backward.³

POWER



Data measured and compiled by USDA-ARS Research Lab, Bushland, TX

MONTHLY ENERGY



FIVE YEAR WARRANTY



Southwest Windpower

1801 W. Route 66 928.779.9463
 Flagstaff, AZ 86001 USA www.skystreamenergy.com

Makers of Skystream 3.7® / AIR / Whisper

1. Based on a 12 mph (5.4 m/s) wind and utility energy cost of \$.09/kWh
2. Taller towers are available
3. Assuming the Skystream 3.7 is producing more energy than the load is consuming

♻️ Printed on recycled paper using vegetable inks.

3-CMLT-1338-01 REV E 10-08

A.2 Data sheet of vertical axis wind turbine [6]

Turby B.V. VAWT 2,5 kW

Contact name: Dick Sidler
Address: Heuvelenweg 18, 7241 HZ Lochem
Telephone: +31 - 6-55822169
Country : Netherlands

Turby 2,5 kW references

Site	Use	Country
Amsterdam	Proof public building (former school)	Netherlands
Tilburg	Roof flat building	Netherlands
Den Haag	Roof town hall	Netherlands
Delft	Technical University	Netherlands

Turby 2,5 kW



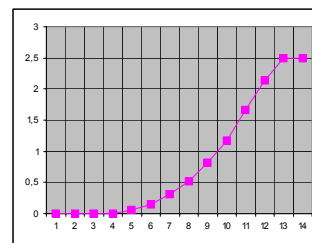
Technical information

POWER		Unit
1) Rated power	2,5	kW
2) Rated wind speed	14	m/s
3) Cut-in wind speed	4	m/s
4) Cut-out wind speed	14	m/s
5) Maximum wind speed the turbine can withstand	55	m/s
DIMENSIONS		
6) Rotor weight	135	kg
7) Rotor diameter	1,99	m
8) Rotor height (for VAWT only)	2,88	m
9) Swept area	5,3	m ²
10) Height of the mast	6 – 7,5	m
OTHER INFORMATION		
11) Maximum rpm	400	At rated wind speed
12) Gear box type	No gears	
13) Brake system	Electrical brake system	
14) Number of blades	3	
15) Blades material	Carbon epoxy composite	
16) Output voltage	230	V
17) Minimum operation temperature	- 20	°C
18) Maximum operation temperature	+ 40	°C
19) Acoustic levels at a distance of 20 m ? wind = 10 m/s)	45	DB
20) Lifetime	20	Years
21) Is the machine self-starting	No	
22) Use of an asynchronous generator	No	
23) Yaw control system	Independent	
24) Upwind or downwind	Both	

Calculated power curve

Wind speed (m/s)	Power (W)
1	0
2	0
3	0
4	6
5	56
6	155
7	310
8	527
9	812
10	1171
11	1659
12	2136
13	2500
14	2500
15	..

Power curve



Curriculum Vitae

Maximilian von der Grün

Address: Klarastr. 18, 80636 München

Email: maximilian.vondergruen@gmail.de

EDUCATIONAL BACKGROUND

10/08 - 09/12 **B.Sc** TU Darmstadt, Mechanical and Process Engineering

09/12 - 09/15 **M.Sc** TU Darmstadt, Mechanical and Process Engineering

10/16 - 06/21 **PhD** Institute of Aerodynamics and Gas Dynamics,
University of Stuttgart, and
Faculty C, Stuttgart University of Applied Sciences

EXPERIENCE

10/12 - 03/13 **Student assistant** TU Darmstadt,
and Institute for Fluid Mechanics
06/13 - 03/14 and Aerodynamics
04/14 - 09/14 **Internship** Airbus Defence and Space GmbH